

FACULTY OF PHYSICS, ASTRONOMY AND INFORMATICS



**Phase-based methods in optical coherence tomography  
for estimation selected physical parameters of biological tissues**

Metody fazowe w optycznej tomografii koherencyjnej  
do wyznaczania wybranych parametrów fizycznych tkanek

Ewelina Pijewska

*Doctoral dissertation under the supervision of*  
Maciej Szkulmowski, PhD, Prof. NCU

Toruń, 2022

Dziękuję wszystkim pracownikom  
Katedry Biofotoniki i Inżynierii Optycznej  
w szczególności mojemu promotorowi,  
dr. hab. Maciejowi Szkulmowskiemu, prof. UMK,  
dr hab. Iwonie Gorczyńskiej, prof. UMK,  
dr. Marcinowi Sylwestrzakowi,  
dr. Maciejowi Bartuzelowi,

oraz moim Rodzicom, którzy zawsze mnie wspierają.

## Table of contents

<b>1. Abstract in English.....</b>	<b>4</b>
<b>2. Abstract in Polish (Abstrakt w języku polskim) .....</b>	<b>6</b>
<b>3. Introduction.....</b>	<b>8</b>
<b>4. Optical coherence tomography (OCT).....</b>	<b>10</b>
4.1. Detection of interferometric fringes.....	10
4.2. Phase information of OCT signal.....	14
4.3. Artifacts related to phase analysis.....	16
4.4. Wrapped phase effect and known methods of unwrapping phase .....	19
<b>5. List of publications included in the doctoral thesis.....</b>	<b>21</b>
<b>6. Phase methods in selected applications.....</b>	<b>22</b>
6.1. Fast phase unwrapping algorithm (FPU) .....	22
6.2. Measurements of blood flow parameters in eye blood vessels .....	25
6.3. Measurement of light-induced retina activities.....	26
6.4. Measurement of biomechanical properties of biological tissues under compression .....	28
<b>7. Description of doctoral student's contribution.....</b>	<b>29</b>
<b>8. Summary.....</b>	<b>31</b>
<b>References.....</b>	<b>32</b>
<b>Appendixes.....</b>	<b>35</b>
Code 1. The code of FPU algorithm implemented in programming environment C/CUDA.....	35
Code 2. The FPU algorithm implemented in programming environment of the Matlab R2021a.	41
Code 3. The code of iterative FPU method for phase unwrapping with Volkov symmetrization .	43
<b>Manuscripts.....</b>	<b>46</b>
<b>Co-authorship declarations.....</b>	<b>136</b>

## 1. Abstract in English

Observation of changes in biological tissues allows evaluating the patient's health condition and also helps both in diagnosing and monitoring the progress of treatment of modern civilization diseases such as diabetic retinopathy, hypertension, glaucoma and cancer. These diseases reduce the patient's standard of living, and in their advanced stages prevent normal functioning and professional work.

Physicians are ready to test new methods for diagnosis, monitoring, and treatment of lifestyle diseases that are non-invasive and easy to implement in a clinic. A promising method is optical coherence tomography (OCT), a non-invasive method currently used in clinics for three-dimensional visualization of biological objects transparent to light. In this method, infrared or visible light is directed at the examined biological object. Part of the light is reflected by anatomical layers of tissue and can be registered by a detector and transformed into an image.

The OCT method has much greater diagnostic potential than visualization of structure based on the scattering properties of biological tissue. Tissues in living organisms are active, and optical methods allow us to monitor the physiological or pathological functioning of these tissues. Hence the name "functional testing", which includes phase-based data analysis methods.

The objective of the research proposed in this project is to develop methods for phase analysis of OCT signal allowing quantitative studies of selected physical parameters of tissues for medical diagnostic purposes.

In my work, I have demonstrated selected applications of these methods in Doppler OCT (used for quantification of blood flow in living tissues), OCT elastography (used for quantification of elastic properties of tissues) and optoretinography (used for quantification of the changes in nerve cell retinal layers in response to light stimulus). I focused on several problems associated with phase analysis: time required for data processing and memory requirements, limited range of measurable axial displacements, obtaining displacement information only in the beam axis, influence of object geometry on the measurement, motion artifacts unavoidable in a few-second measurement, phase artifacts resulting from combined analysis of OCT data. I have proposed methods for analysis of phase of OCT signal obtained with widely available spectral OCT systems, which would allow application of new methods with the use of already existing devices. The methods proposed in this thesis allow to reduce phase artifacts and make it possible to obtain reliable results. Experimental results were confirmed by simulations, experiments on real biological data *ex vivo* and *in vivo*. I have designed, optimized and implemented a phase unwrapping algorithm on graphics card processors to speed up computation time.



The projects presented in my dissertation are part of a broad research effort to develop phased methods and increase the functionality of OCT devices, which may in the future help develop biomarkers and accelerate the diagnosis of selected civilization diseases.

## 2. Abstract in Polish (Abstrakt w języku polskim)

Obserwacja zmian w tkankach biologicznych pozwala ocenić stan zdrowia pacjenta, a także pomaga zarówno w diagnozowaniu jak i w monitorowaniu postępów leczenia współczesnych chorób cywilizacyjnych, takich jak retinopatia cukrzycowa, nadciśnienie tętnicze, jaskra i nowotwory. Choroby te obniżają standard życia pacjenta, a w zaawansowanym stadium uniemożliwiają normalne funkcjonowanie i pracę zawodową.

Lekarze są gotowi do testowania nowych metod diagnostyki, monitorowania i leczenia chorób cywilizacyjnych, które byłyby nieinwazyjne oraz łatwe do wdrożenia w klinikach. Obiecującą metodą jest optyczna tomografia koherencyjna (OCT), nieinwazyjna metoda stosowana obecnie w klinikach do trójwymiarowej wizualizacji obiektów biologicznych przezroczystych dla światła. W tej metodzie światło podczerwone lub widzialne kierowane jest na badany obiekt biologiczny. Część światła odbija się od anatomicznych warstw tkanki i może być zarejestrowana przez detektor i przetworzona na obraz.

Metoda OCT ma znacznie większy potencjał diagnostyczny niż wizualizacja struktury na podstawie właściwości rozpraszających tkanki biologicznej. Tkanki w organizmach żywych są aktywne, a metody optyczne pozwalają na monitorowanie fizjologicznego lub patologicznego funkcjonowania tych tkanek. Stąd nazwa „badania funkcjonalne”, w skład których wchodzi metody analizy danych oparte na fazie.

Celem proponowanych w tym projekcie badań naukowych jest opracowanie metod analizy fazy OCT pozwalających na ilościowe badania wybranych parametrów fizycznych tkanek w celach diagnostyki medycznej.

W ramach pracy pokazałam wybrane zastosowania fazy OCT w Dopplerowskiej metodzie OCT (Doppler OCT, służąca do wyznaczania ilościowego przepływu krwi w żywych tkankach), elastografii OCT (OCE, używana do oceny ilościowej właściwości elastycznych tkanek) oraz optoretinografii (ORG, stosowana do ilościowej oceny zmian w warstwach komórek nerwowych oka pod wpływem bodźca świetlnego). Skupiłam się na kilku problemach towarzyszących analizie fazy: czasie potrzebnym na przetwarzanie danych i zapotrzebowanie na pamięć operacyjną, ograniczony zakres mierzalnych przesunięć osiowych, uzyskiwanie informacji o przesunięciu tylko w osi wiązki, wpływ geometrii obiektu na pomiar, artefakty ruchowe nieuniknione w kilku sekundowym pomiarze, artefakty fazowe wynikające z zespolonej analizy danych OCT. Pokazałam propozycje metod analizy danych fazowych uzyskanych za pomocą szeroko dostępnych układów do spektralnej OCT, co pozwoliłoby na zastosowanie nowych metod z wykorzystaniem już istniejących urządzeń. Zaproponowane w ramach niniejszej pracy doktorskiej metody pozwalają na zredukowanie artefaktów fazowych i umożliwiają uzyskanie wiarygodnego wyniku. Wyniki eksperymentów zostały potwierdzone symulacjami,

eksperymentami na rzeczywistych danych biologicznych *ex vivo* oraz *in vivo*. Zaimplementowałam algorytm odwijania fazy FPU na procesorach kart graficznych w celu przyspieszenia czasu obliczeń.

Przedstawione projekty w ramach mojej pracy doktorskiej wpisują się w szerokie badania nad rozwojem metod fazowych i zwiększeniem funkcjonalności urządzeń OCT, co może w przyszłości pomóc opracować biomarkery i przyspieszyć diagnostykę wybranych chorób cywilizacyjnych.

### 3. Introduction

Civilization diseases, such as diabetic retinopathy, hypertension, and glaucoma, reduce the standard of patients' lives and prevent normal functioning and professional work in their advanced stage. In addition, cardiovascular diseases and cancer are the most common cause of death. According to the demographic yearbook 2020 of The Central Statistical Office, between 2000 and 2018, in Poland, 20-25% of deaths were caused by cancer [1]. Cardiovascular diseases are the leading cause of death in Poland, accounting for between 30-40% of deaths between 2000-2018 [1]. An increasing number of patients requires constant medical care, social welfare, and help from their family members, which causes an increasing burden on the health care system and affects the economies of highly and moderately developed countries, including Poland. Therefore, these countries are making efforts to find effective methods of early diagnosis, treatment, and monitoring of these diseases and treatment progress.

Doctors are ready to test new methods of diagnosis and treatment, which would help to cope with the scourge of civilization diseases. In ophthalmology research, optical coherence tomography (OCT) has become the diagnostic standard for which the eye is an ideal object of study because it is an organ transparent to light. Infrared or visible light can easily reach deep layers of the eye, such as the retina or choroid. Some of the light is reflected by the anatomical layers of the eye and can be registered by a detector and processed into an image. In ophthalmology clinics and offices, OCT is mainly used for 3D visualization of the anterior chamber of the eye (cornea, lens) or retina. It also allows to create maps of the vascular network but without the information about the actual values of blood flow in the vessels.

OCT has much greater diagnostic potential than visualization of structure based on the scattering properties of biological tissue. Tissues in living organisms are active, and optical methods allow to monitor the physiological or pathological functioning of those tissues. Hence the name "function examinations" or "function tests", which include, among others, the Doppler OCT method [2-4], allowing for function examination of the circulatory system by measuring the blood flow velocity. Another branch of functional OCT methods is the study of tissue biomechanics. OCT elastography (OCE) deals with the study of the deformation of biological tissues under mechanical stimulus [5,6]. Optoretinography (ORG), on the other hand, allows for measuring the changes occurring in the nerve cell layers of the eye under the influence of a light stimulus [7,8]. We know from research conducted by scientists all over the world that civilization diseases, not only of the eye, but also systemic ones, manifest themselves as changes in the functioning of tissues [9,10], nerve cells [11,12], and vascular systems of the ocular fundus [9,13], often in the early stages of these diseases. For example, in diabetes, pathologies in the circulatory regulation of the brain, including the eye, appear earlier than

diabetic retinopathy[14,15]. Development of methods for quantitative analysis of OCT signal may allow early diagnosis of diseases, i.e., when they can be stopped, and lesions can still be cured.

These quantitative studies of retinal blood flow, nerve cell activity, and measurements of layer biomechanics can be performed by analyzing the phase of the OCT signal. Despite promising results, the transfer of OCT phase methods from research laboratories to clinics has been delayed. Before phase methods can be widely used, a number of problems must be solved, including: long data processing time and large memory requirements, limited range of measurable axial displacements and layer shuffling velocities, obtaining displacement information only in the beam axis, effect of object geometry on the measurement, motion artifacts unavoidable in a few seconds of *in vivo* measurement of biological objects, and phase artifacts resulting from composite analysis of OCT data.

The aim of the doctoral thesis was to address some of the abovementioned issues by **devising OCT phase methods allowing for quantitative examination of selected parameters of biological tissues for medical diagnostics**. The most important findings were described in publications [Pub 1-5](#), of which I am the lead author. During my doctoral studies, I was working on four research projects [P1-4](#), concerning the analysis of the OCT signal phase and its potential applications in medical diagnostics.

Research projects, depending on the application and the manner of phase analysis:

- [P1](#). Reduction of artifact resulting from OCT signal phase analysis involving phase wrapping. ([Pub. 1](#))
- [P2](#). Measuring blood flow parameters in eye blood vessels. ([Pub. 2, 3](#))
- [P3](#). Measuring light-induced retina activity. ([Pub. 4](#))
- [P4](#). Measuring biomechanical properties of biological tissues under compression. ([Pub. 5](#))

The information which serves as an introduction to the issues described in [Pub 1-5](#) is included in chapters §1-8 of this work. The experimental part, findings, and conclusions from individual works were presented in detail in [Pub 1-5](#), which are included in the doctoral thesis.

The doctoral thesis was written as a part of project POIR.04.04.00-00-2070/16-00, "FreeZEYE Tracker – ultrafast system for image stabilization in biomedical imaging" carried out within the TEAM TECH programme of the Foundation for Polish Science co-financed by the European Union under the European Regional Development Fund.

## 4. Optical coherence tomography (OCT)

### 4.1. Detection of interferometric fringes

Optical coherence tomography (OCT) is a technique of optical imaging allowing for three-dimensional observation of biological objects transparent for light. OCT was created in the 90's of the 20th century [16–18]. There are many types of optical coherence tomography, depending on the light source used and the manner of detection. Among them, there is the time method (TDOCT) [18], spectral method (SdOCT) [19,20], the method using short-cavity swept light sources (SS-OCT) [21,22] and the full field method (FFOCT) [23]. In my research, I focused mainly on the spectral domain optical coherence tomography (SdOCT). The method is easily available and relatively cheap. It is currently the most commonly used OCT method in eye clinics. Creating an additional functionality, apart from standard imaging, would merely require a software change in the already existing devices.

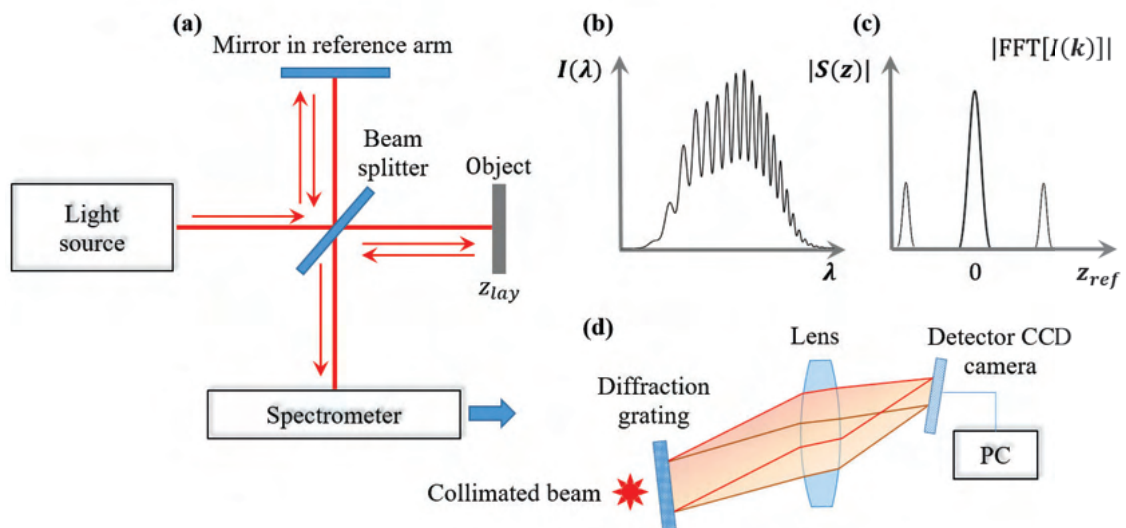


Fig. 1. a) Conceptual scheme of the OCT measuring system in the configuration of Michelson interferometer. A beam of light is split at the beam splitter. One part is directed to the reference arm, the other to the object arm. Detection of interferometric spectral fringes is conducted by means of a spectrometer (d). b) Graph of spectral interferometric fringes  $I(\lambda)$ . The modulation frequency is proportional to the difference of optical paths between the reference arm and the layers within the object. c) Fourier's transform of the optical signal from (b). The locations of peaks in the transform reflect the optical distances of the object's layers in reference to the length of the optical path of the light from the reference arm  $z_{ref}$ .

A device for spectral domain OCT uses an interferometer to measure the optical path difference between the reference arm and the object arm. A schematic of the spectral OCT (SdOCT) system in the

Michelson interferometer configuration is shown in Fig. 1(a). A beam of light with high spatial coherence and low temporal coherence is split at the beam splitter. A mirror of high reflectivity is placed in the reference arm. An object is placed in the object arm, usually consisting of multiple reflective layers. Light is reflected from the individual layers of the object and then runs to the detector, interfering with the beam reflected from the reference mirror. The detection of the spectrum of the light source modulated by interferometric fringes (Fig. 2(a)) is performed with the spectrometer equipped with a diffraction grating where each pixel of the line-scan camera detects a specific range of wavelengths.

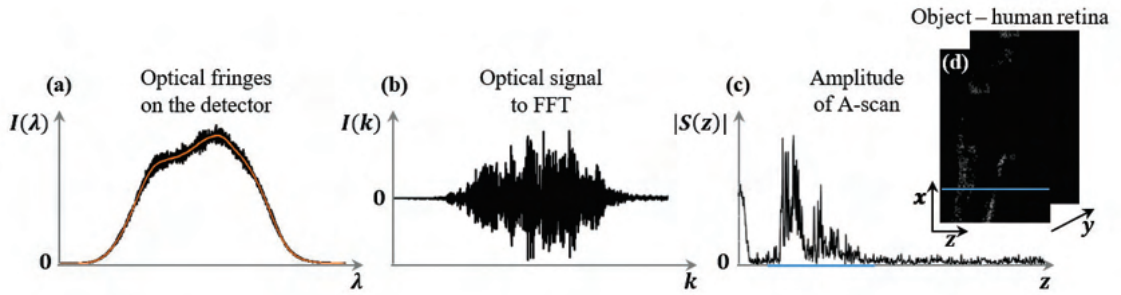


Fig. 2. a) Signal of interferometric fringes collected directly on the line-scan camera. b) The signal after the removal of background, compensation of dispersion, and after calibration from wavelengths to wavenumbers. c) Amplitude of signal after Fourier's transformation (b). One line of an image, called A-scan, obtained from one spectrum (a) recorded on the detector. d) Cross-section of the measured object – a human eye retina. B-scan presented on the greyscale with intensity proportional to the amplitude of the signal from (c). The lighter the object, the stronger the scattering properties of the measured retina layer. The blue line marks the A-scan reflecting the graph (c).

In the process of measurement using a spectrometer equipped with a diffraction grating, the spectrum is sampled in wavelengths  $\lambda$  and is non-linear in wavenumbers  $k$ . Additionally, different optical materials in the arms of the interferometer cause dispersion mismatch, and light reflexes from layers in the interferometer lead to parasitic terms in the signal. Therefore, before Fourier transforming the acquired signal, a number of preprocessing steps is required in the following order: (1) the fixed pattern noise removal to cancel the parasitic terms, followed by (2) resampling from wavelengths to wavenumbers, and (3) numerical compensation of dispersion mismatch [24]. After these steps, the signal ready for Fourier's transformation takes the following form:

$$I(k, t) \approx I_0(k) \sqrt{R_r R} \cos(2knz(t)), \quad (1)$$

where  $I_0(k)$  is the spectra density of the light source,  $R_r$  – mirror’s reflectance in the reference arm,  $R$  – reflectance of the object’s layer,  $n$  – refractive index of the object’s layer,  $t$  – time in which the interferometric fringe spectrum was recorded,  $z$  – the difference in the lengths of optical paths of the light between the object arm and the reference arm  $z_{ref}$ . An example of an optical signal prepared in this manner was demonstrated in Fig 2(b). Fourier’s transformation allows for moving from the domain of wavenumbers  $k$  to the domain of differences in the optical paths between the interferometer’s arms, usually denoted as  $z$ . Distances to subsequent layers in object,  $z_1, z_2, \dots, z_w$ , are measured from fringe zero, which denotes the distance equal to the optical distance to the reference mirror in the reference arm.

A line of OCT image is the result of Fourier’s transformation of the  $FT$  spectrum of interferometric fringes and is a complex signal:

$$FT[I(k,t)] = S(z,t) = A(z,t)\exp(j\varphi(z,t)), \quad (2)$$

with amplitude  $A(z, t)$  and phase  $\varphi(z, t)$ . Each point of the transform carries information about scattered light at the optical distance reflecting the location of that point. Amplitude  $A$  of the OCT signal, which is the value of Fourier’s transform at a given point, is related to the dispersing properties of those layers and proportional to the root of the reflection index [19,20,25]. This property is used in the creation of so-called structural OCT images, in which the source of contrast is the ability to scatter light. From a single interference spectrum, we obtain an image line that contains information about the distances between successive layers of the object and is called an A-scan. An example image line is shown in Fig. 2(c).

By using a galvanometer or resonance scanner to move a beam that forms A-scans over an object, a two-dimensional cross-section of the object can be obtained. This is called a B-scan and is composed of A-scans. An example B-scan is shown in Fig. 2(d) in the spatial variables  $(x, z)$ . In this notation, the coordinate  $z$  describes the direction along the light beam, while the coordinate  $x$  describes the direction of light beam displacement by the scanner. Using an additional galvanometric scanner, adding the ability to move the beam in a direction perpendicular to the motion set by the first scanner, a 3D tomogram of the object under study, composed of B-scans, can be obtained. The spatial variable, perpendicular to the B-scan plane, is denoted as  $y$  in Fig. 2(d). The Fourier’s transform of the interferometric fringes’ spectrum at any point  $(x, y, z)$  is described by the formula:

$$S(x, y, z, t) = S(\mathbf{r}, t) = A(\mathbf{r}, t)\exp(j\varphi(\mathbf{r}, t)), \quad (3)$$

with amplitude  $A(\mathbf{r}, t)$  and phase  $\varphi(\mathbf{r}, t)$ , of a point in space denoted by vector  $\mathbf{r}$  whose coordinates are  $(x, y, z)$ .



Issues related to optical coherence tomography have been thoroughly described in publications [17,19,20], in postdoctoral dissertation by Profesor Maciej Wojtkowski [26], and in doctoral theses by Maciej Szkulmowski, PhD, Prof. NCU [24], Anna Szkulmowska, PhD [25], and Marcin Sylwestrzak, PhD [27].

## 4.2. Phase information of OCT signal

The OCT signal is a complex signal described by expression (3). The amplitude  $A$  of the OCT signal, or the value of the Fourier transform modulus at a given point, is related to the scattering properties of the layers. The phase  $\varphi$  of the OCT signal, on the other hand, carries information about the position of the scattering layer small enough that it does not cause a change in the frequency of the interferometric striations large enough that it leads to a shift in the next peak of the Fourier transform. These small frequency changes manifest as a change in the initial phase of the OCT signal, as illustrated in Fig. 3.

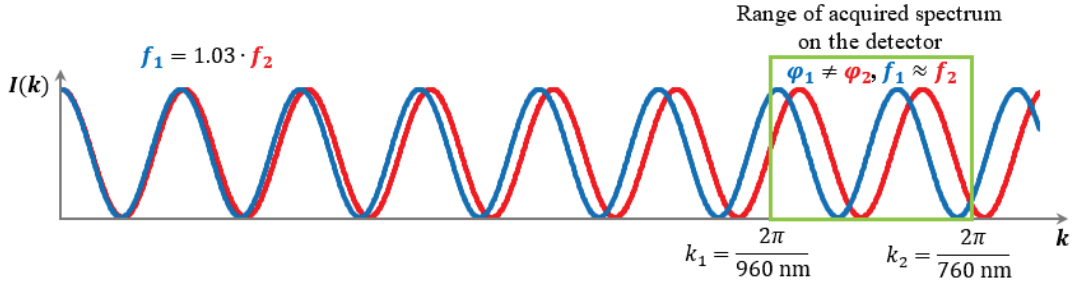


Fig. 3. Graph for two harmonic signals present in detected OCT signal with slightly different frequencies  $f_1$  and  $f_2$ . The green rectangle indicates the range of wave numbers  $k$  for which the signals are recorded on the detector, for a light source with a central wavelength of 860 nm and a half-width of 100 nm. In a typical OCT analysis, the frequencies of these signals are indistinguishable, while the change in phase offset (or initial phase for  $k_1$ ) is clearly visible.

When an object moves in time  $\Delta t$  at the velocity of  $v$ , it is possible to measure its relocation  $\Delta z = v\Delta t$  by measuring changes in the initial phase of the fringe reflecting the in-depth position  $z$ :

$$I(k, t + \Delta t) \approx I_0(k) \sqrt{R_r R} \cos(2knz(t + \Delta t)), \quad (4)$$

$$I(k, t) \approx I_0(k) \sqrt{R_r R} \cos(2knz(t) + 2kn\Delta z). \quad (5)$$

Since the change in  $\Delta\varphi$  phase between signals  $I(k, t)$  and  $I(k, t + \Delta t)$  for the frequency reflecting the location of  $z$  is equal to  $2kn\Delta z$  the relocation of the scattering center by  $\Delta z$  can be calculated in the following way:

$$\Delta z = \frac{\Delta\varphi}{2kn}. \quad (6)$$

In this way, directly from the phase difference of spectral fringes, it is possible to calculate the relocation for a single point in space – one depth from A-scan. After performing the Fourier's transformation and moving to space  $z$ , the same value of the phase change  $\Delta\varphi$  can be calculated for the whole 3D set of complex valued B-scans  $S'(\mathbf{r})$  for every spatial point with coordinates  $\mathbf{r} = (x, y, z)$ :

$$\Delta\varphi(\mathbf{r}) = \arctan\left[\frac{\text{Im}(S'(\mathbf{r}))}{\text{Re}(S'(\mathbf{r}))}\right], \quad (7)$$

where

$$S'(\mathbf{r}) = S(\mathbf{r}, t) \cdot S^*(\mathbf{r}, t + \Delta t) \quad (8)$$

defines the signal composed of OCT signals after Fourier's transformation, defined by formula (2), registered at two time instants  $t$  and  $t + \Delta t$ . The symbol \* denotes complex conjugate.

Making use of the fact that  $\Delta z = v\Delta t$ , it is possible to calculate the velocity of a moving object from the transformed formula (6):

$$v = \frac{\Delta\varphi}{2kn\Delta t}. \quad (9)$$

Information from different time instants and from the same location in the object can be recorded between A-scans, B-scans, and also between three-dimensional tomograms. It is necessary to fulfill the condition of comparing phase differences between points that contain part of the common information, i.e., during subsequent measurements the measuring beam must illuminate the same set of scattering particles in the object. Ideally, the beam should cover an identical area, but in practical cases, this is difficult to achieve, and only partial coverage is achieved. The effect of incomplete coverage is a decrease in the signal-to-noise ratio (SNR) because the phase information is countable only between those signal components that originate from the same scatterers. For studies of blood flow in OCT spectral systems in laboratory practice, it is sufficient that the displacement of the beam between consecutive spectra acquisitions is lower than half of the transverse beam profile [28,29]. Phase information for the same object then occurs between successive A-scans.

Phase changes can also be analyzed between B-scans and whole three-dimensional tomograms of the studied structure if the data processing or measurement protocol allows to eliminate the effect of signal decorrelation in time. The phase relation between signals from consecutive B-scans was the subject of research in my doctoral dissertation on optoretinography and OCT elastography described later in this paper and [Pub. 4, 5](#).

The issues related to the interpretation of phase in the OCT signal was exhaustively described in doctoral dissertations of Anna Szkulmowska, PhD [25] and Maciej Szkulmowski, PhD, Prof. NCU [24].

### 4.3. Artifacts related to phase analysis

Phase analysis can be applied to functional tissue studies using OCT. Although the first references to phased-based OCT methods were made several years after the development of OCT [2,30], the transfer of phased array methods from research laboratories to clinical practice is still ongoing.

In general, methods using phase information are more precise in estimating object relocations than methods using amplitude. This means that they are also sensitive to motion artifacts, unavoidable in in-vivo studies. For eye imaging, motion artifacts are mainly due to breathing, heartbeat, but also to the physiology of the visual process. One of the main eye movements that hinder measurement is microsaccades [31], which are a physiological phenomenon with the purpose of changing the gaze direction to allow stimulation of different photoreceptor cells. The chemical processes accompanying the process of vision are reversible. If there is a full rhodopsin bleaching in a photoreceptor outer segment optical signal cannot be processed by this nerve cell. Eye movements occur in both horizontal and vertical directions. Any eye movement during OCT measurement, which lasts from a few to several tens of seconds, causes phase signal decorrelation in time. There is a gradual decrease in sensitivity of the measurement until the useful information is completely dominated by phase noise.

Each phase measurement is limited from the bottom and from the top. The bottom limit is phase noise, consisting of shot noise which results from the particle nature of a photocurrent generated in a semiconductor detector [32,33]. In OCT, the shot noise is mainly related to the optical power of the incident light beam, detector quantum efficiency and acquisition time [34]. The variance of the photocurrent influences variance detected spectral optical fringes signal.

The top limit is fringes washout [29,35]. When an object is moving, the frequency of interferometric fringes changes. Minor changes in the frequency are observed on the detector in the form of phase shift. The detector records the electric signal reflecting the value of light intensity falling on the vision scan line camera during  $\Delta t_a$  acquisition. In the OCT spectra method, signal detection reflects the integration of interferometric fringes in  $\Delta t_a$  time. Let us consider equation (1) for the interferometric fringes spectrum. By integrating equations (1), we obtain a sinc function:

$$\int_0^{\Delta t_a} I_0(k) \sqrt{R_r R} \cos(2knz(t)) dt = I_0(k) \sqrt{R_r R} \frac{\sin(2knv\Delta t_a)}{2knv\Delta t_a} \Delta t_a. \quad (10)$$

For a given wavenumber  $k$ , the sinc function drops to zero, when the phase in the equation (9) equals  $\pi$ , meaning the object's velocity of  $v_{wash} = \pi / 2kn\Delta t_a$ . For this velocity, the amplitude of the signal recorded on the detector drops to the level of background noise, making speed measurement impossible.

The phase of the OCT signal required to recover velocity using equation (9) is obtained from the real and imaginary parts of the complex signal, according to equation (7). The counter-domain of the arcus tangent function of the real and imaginary parts of the complex number, covers the interval  $(-\pi, \pi)$ . In this range the maximal object velocity that can be determined by Doppler OCT is give by:

$$v_{wrap} = \pm \frac{\pi}{2kn\Delta t}, \quad (11)$$

where  $\Delta t$  – time between subsequent recorded signals for a given wavenumber  $k$ . In case the phase exceeds this range a phase wrapping artifact occurs. I devoted a separate chapter of this work (§4.4.) to the topic of phase unwrapping.

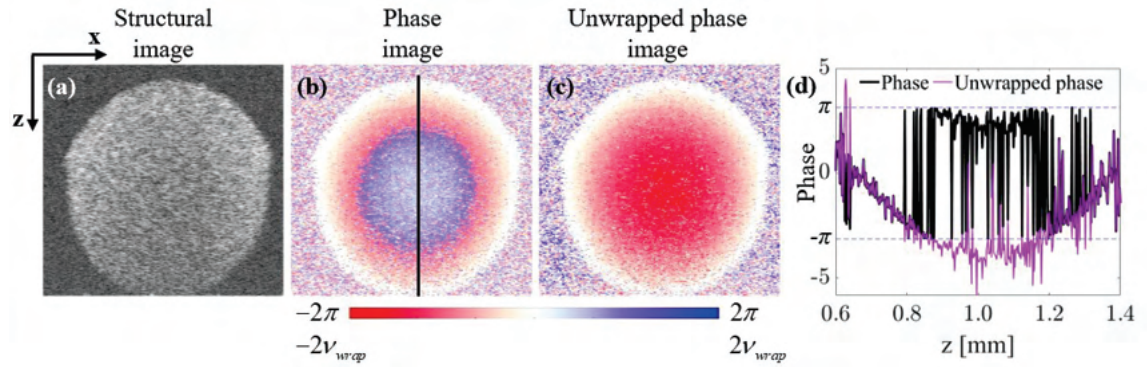


Fig. 4. Cross-section of a glass tube made using OCT. A glass tube with a diameter of 0.8 mm was filled with milk. The movement of the fat suspension was induced by pressing the piston of a syringe that was connected to the tube. a) Structural image shown in gray scale. b) Artefacted phase difference image corresponding to structural image (a). According to equation (5), the phase difference is proportional to the axial velocity of the fluid flow. The red shades represent the negative phase change, corresponding to the displacement of the object in the direction of the incident beam. The blue shades represent positive phase change values, which corresponds to particles moving against the direction of the incident beam. The white shade represents an object that did not move during the measurement. c) Phase difference image after removal of the phase wrap artifact, corresponding to structural image (a). d) Plot of the phase along the line marked in black line on phase image (b). Wrapped phase – black line, and unwrapped phase – purple line.

An example of the wrapped phase in Doppler OCT presents in Fig. 4. In the Doppler OCT experiment, I counted the axial velocity component of milk inside a glass tube with a 0.8 mm diameter. The movement of the fat suspension was induced by pressing the piston of a syringe that was connected to the tube. The structural OCT image of the glass tube shows in Fig. 4(a). In Fig. 4(b, c) the color scale from red to the blue codes velocity of the milk inside the tube. The red shades represent the negative phase change, corresponding to the displacement of the object in the direction of the

incident beam. The blue shades represent positive phase change values, which correspond to particles moving against the direction of the incident beam. In Fig. 4(b), one can see the discontinuity in wrapped phase, limited to the range  $(-\pi, \pi)$ . However, the flow inside the vessel is continuous, so the change in velocity direction is an artifact caused by the phase wrap effect. The unwrapped phase is presented in Fig. 4(c), the phase unwrapping discontinuities are removed and the parabolic velocity profile inside the vessel is revealed. In Fig. 4(d) a comparison of wrapped (black line) and unwrapped (purple line) phase from a single profile taken along the black line from Fig. 4(b, c) is shown.

Additional difficulties, especially important for clinical staff, are the need to collect and analyze large data sets (on the order of GB). Currently, full phase analysis is performed after measurement acquisition is finished and takes from several to several dozen seconds. Work is in progress to implement online calculation of selected biomarkers.

Difficulties related to the measurement protocol should also be mentioned. The phase allows the calculation of displacements in the beam axis, which means the influence of the test object's geometry on the measurement result. This is especially important when measuring blood flow in the blood vessels of the eye. Blood vessels in the eye are mainly arranged horizontally with respect to the incident beam, which in extreme cases makes measurement impossible when the angle between the light beam and the flow direction approaches  $\pi / 2$ . Therefore, techniques to cope with this limitation are used, most often involving a change in the spatial orientation between the object and the incident beam. The main methods include techniques using multiple measurement beams or introducing changes in measurement protocols and the way the object is scanned [36–38].

#### 4.4. Wrapped phase effect and known methods of unwrapping phase

The phase wrapping effect is an artifact resulting from complex analysis and occurs in many interferometric fields. The effect limits the possibility to unambiguously measure phase to the range  $(-\pi, \pi)$ . In the OCT spectral method, the limitation of the measured phase causes limitations in the measurement of object displacements and velocities, according to equations (9) and (11). An example of phase unwrapping is shown in Fig. 4(b). The goal of all phase unwrapping methods is to reconstruct the unwrapped phase waveform, which extends beyond the range  $(-\pi, \pi)$  corresponding to the wrapped phase.

According to equations (5) and (10), phase unwrapping is related to the wavenumber  $k$ , and thus also to the wavelength of the OCT source. One class of phase unwrapping methods are multi-wavelength methods [39–41], first applied to holography. In the case of OCT, for each wavelength, phase unwrapping will occur for a different value of measured object shift. Wraps can then be detected at the measurement stage or during the processing of already collected data, and unwrapping can be performed [42].

The phase unwrapping problem can be analyzed as a series of two-dimensional images. There are methods to look for pixels arranged in certain structures such as edges or signal jumps using methods borrowed from image processing [43,44].

There are a number of methods that are based on jump detection and breaking continuity by calculating a gradient or a derivative [45,46]. In order to reduce the noise-sensitivity of those methods, a combination of derivative and Laplace operators with Prewitt and Sobel operators [46] and other methods borrowed from the image-processing analysis.

Phase wrapping results from complex analysis, which is why the problem can be considered making use of the full information of complex OCT signal. The first algorithms used in interferometric radars [47,48] were based on the residue theorem as well as the search for the branch point and branch cut. Path-following methods make use of the residue theorem, which for phase unwrapping is described by the following equation:

$$\oint \Delta\varphi \cdot d\mathbf{r} = 2\pi \cdot \Omega, \quad (12)$$

where  $\Omega$  is the sum of charges of phase residues is not closed by the contour along which the integral is calculated. It is easy to see from equation (12) that balancing the residue charges in a certain region causes the integral along any closed contour to be zero. This means that phase unwrapping is possible if and only if the integration contour does not surround the unbalanced residue charges. The residue charge is balanced by combining residues of opposite polarity inside the cutting branch. Phase unwrapping can occur along the integration path but cannot cross unwrapping barriers called cut

branches. The unwrapping barriers must be defined by balancing the charge of the residues. Improving phase unwrapping methods with path-following methods boils down to increasing the efficiency of residue charge balancing and selecting the integration paths.

A separate class is formed by the methods based on searching for the minimum norm of the function. Let us consider the problem in two dimensions. Let  $D_{q,h+1/2} = \Delta\psi_{q,h+1} - \Delta\psi_{q,h}$ ,  $D_{q+1/2,h} = \Delta\psi_{q+1,h} - \Delta\psi_{q,h}$  for  $q = 1, \dots, N$  and  $h = 1, \dots, M$ . Unwrapped phase  $\Delta\psi$  is reflected by wrapped phase  $\Delta\varphi$ . In order to unwrap the phase, such a value of  $D$  function is sought for which the functional below reaches the minimum:

$$\sum_{q=1}^N \sum_{h=1}^{M-1} (\Delta\varphi_{q,h+1} - \Delta\varphi_{q,h} - D_{q,h+1/2})^2 + \sum_{q=1}^{N-1} \sum_{h=1}^M (\Delta\varphi_{q+1,h} - \Delta\varphi_{q,h} - D_{q+1/2,h})^2. \quad (13)$$

From mathematical analysis, a function reaches an extreme value when the derivative of that function is zero. Then, the phase unwrapping problem is reduced to a differential problem and the solution of Poisson's equation [48,49]. Poisson's equation can be solved in a number of ways, in phase unwrapping algorithms the most common ways are: least squares method [49], discrete cosine transform based method [48], Fourier transform based method [50]. This class of methods also includes fast phase unwrapping algorithm (FPU), implemented to OCT solutions.

Nowadays, there is a growing interest in artificial intelligence and its application in new technologies. Phase unwrapping methods based on neural networks have been developed [51,52].

There are also ways to process the phase that avoid the need for its unwrap depending on downstream applications. An example is the vector method used to calculate the deformation of tissue under compression, described in [Pub. 5](#). The deformation of a compressed object is proportional to the derivative of the phase difference. The phase differences, and hence the tissue deformation, are calculated from complex numbers, for which the phase wrapping effect occurs only after the transition from complex to real analysis. Another example is the phase method I used to measure the retinal response to a light stimulus ([Pub. 4](#)). In this method, the retinal layer shifts can be reconstructed from time samples for which no phase wrapping has occurred.



## 5. List of publications included in the doctoral thesis

The doctoral dissertation consists of a number of intermediate projects P1-P4. An abbreviated description of each of them was provided in chapter §6. The list of references describing the results of individual projects includes the following items:

**Pub. 1. Ewelina Pijewska**, Iwona Gorczynska, and Maciej Szkulmowski. "Computationally effective 2D and 3D fast phase unwrapping algorithms and their applications to Doppler optical coherence tomography." *Biomedical Optics Express* 10(3), 1365-1382 (2019).

<https://doi.org/10.1364/BOE.10.001365>

**Pub. 2. Ewelina Pijewska**, Marcin Sylwestrzak, Iwona Gorczynska, Szymon Tamborski, Mikołaj Pawlak, Maciej Szkulmowski. "Blood flow rate estimation in optic disc capillaries and vessels using Doppler optical coherence tomography with 3D fast phase unwrapping". *Biomedical Optics Express* 11(3), 1336-1353 (2020).

<https://doi.org/10.1364/BOE.382155>

**Pub. 3. Ewelina Pijewska**, Marcin Sylwestrzak, Krystian Wróbel, Iwona Gorczynska, Szymon Tamborski, Mikołaj Pawlak, Maciej Szkulmowski. "Blood flow rate estimation in optic disc capillaries and vessels using Doppler optical coherence tomography." *Biomedical Spectroscopy, Microscopy, and Imaging. SPIE Proceedings Vol. 11359. International Society for Optics and Photonics*, 113590Q (2020).

<https://doi.org/10.1117/12.2555754>

**Pub. 4. Ewelina Pijewska**, Pengfei Zhang, Michał Meina, Ratheesh K. Meleppat, Maciej Szkulmowski, and Robert J. Zawadzki, "Extraction of phase-based optoretinograms (ORG) from serial B-scans acquired over tens of seconds by mouse retinal raster scanning OCT system," *Biomed. Opt. Express* 12(12), 7849-7871 (2021).

<https://doi.org/10.1364/BOE.439900>

**Pub. 5. Jiayue Li, Ewelina Pijewska (shared first author)**, Qi Fang, Maciej Szkulmowski, Brendan Kennedy, "Analysis of strain estimation methods in phase-sensitive compression optical coherence elastography", *Biomed. Opt. Express* 13(4), 2224-2246 (2022).

<https://doi.org/10.1364/BOE.447340>

## 6. Phase methods in selected applications

### 6.1. Fast phase unwrapping algorithm (FPU)

Fast phase unwrapping algorithm (FPU) was first proposed by Schofield [50] for holographic purposes, as a proposal for estimation of unwrapped phase reflecting wrapped phase calculated from 2D interferometric fringes. He was using Laplace operator and reversed Laplace operator, replaced by Fourier's transformations.

It is necessary to provide a number of equations for the purpose of further analysis of the FPU method. The phase of any signal, both in the form of wrapped  $\Delta\varphi$  and unwrapped  $\Delta\psi$  is indistinguishable:

$$\exp(j\Delta\psi(\mathbf{r})) = \exp(j\Delta\varphi(\mathbf{r})) = P(\mathbf{r}), \quad (14)$$

where in the case of using it for an OCT signal,  $P(\mathbf{r}) = S'(\mathbf{r})/|S'(\mathbf{r})|$  can be obtained directly from the complex signals by means of equations (4) and (8). Vector  $\mathbf{r}$  reflects the coordinates  $(x, y, z)$  in the data volume. Using Laplace operator on each term of equation (14) and transforming the equation for the purpose of obtaining the estimation of  $\Delta\psi_{est}$  phase, we obtain a differential-integral formula:

$$\Delta\psi_{est}(\mathbf{r}) = \nabla^{-2} \operatorname{Im}\{P(\mathbf{r})^{-1} \nabla^2 P(\mathbf{r})\}. \quad (15)$$

After replacing Laplace's operator  $\nabla^2$  and inverse Laplace's operator  $\nabla^{-2}$  with Fourier's transformations according to the formulas included in works [50,53], we obtain the equation which allows for direct calculation of the unwrapped phase estimation based on the phase obtained from the measurement:

$$\Delta\psi_{est}(\mathbf{r}) = -(2\pi)^{-2} F^{-1} \left\{ \mathbf{K}^{-2} F \left[ \operatorname{Im} \left( -P(\mathbf{r})^{-1} (2\pi)^2 F^{-1} \left[ \mathbf{K}^2 F(P(\mathbf{r})) \right] \right) \right] \right\}, \quad (16)$$

where  $\mathbf{K}$  is the vector of Fourier's coordinates reflecting a spatial vector  $\mathbf{r}$  with coordinates  $(x, y, z)$ . Equation (14) was an implementation amendment, which allowed to speed up the calculation time twofold (Pub. 1).

Based on equation (15), several problems and limitations of the FPU method can be noticed. First of all, it is a differential-integral method, which means the possibility of random phase shift by the *offset*( $\mathbf{r}$ ) function (Pub. 1, 5). In addition, it is necessary to meet the boundary conditions and the conditions of continuity of the first and the second complex function  $P(\mathbf{r})$  derivative and the real

function  $\varphi(\mathbf{r})$  derivative. It means that there is an influence of input phase distribution on the algorithm's proper functioning.

FPU algorithm in its original form, used for 2D B-scan from Doppler OCT, did not perform in a satisfactory manner. It was necessary to use the algorithm in the 3D form, which analyzes the volumetric data. More details about the algorithm used for Doppler OCT, as well as a comparison of two-dimensional and three-dimensional methods, are described in [Pub. 1](#). publication contains the results of FPU algorithm tests on *in silico* and *ex vivo* data.

When measuring blood flow velocity in the blood vessels of the eye, I examine inherently symmetrical objects. The blood vessels are a circle or ellipse in cross-section, and the background of the measurement is tissue and background noise. In practice, this means that the blood vessels within which phase wrap occurs are surrounded by a medium that produce the signal close to zero, because the tissue moves only slightly during A-scan acquisition. The specificity of the Doppler OCT data caused the FPU algorithm to successfully unwrap the phase already with the direct application of equation (12), without any additional data preparation. The results of *in vivo* phase unwrapping of phase data obtained by Doppler OCT are further described in [Pub. 2](#). Implementation of FPU algorithm on graphic card processors allowed for unwrapping the phase of 1.5 GB of data within  $\sim 1$  s ([Pub. 1](#)). The algorithm I implemented, in C/CUDA language [Code 1](#) and in programming environment of Matlab [Code 2](#) has been attached to this paper.

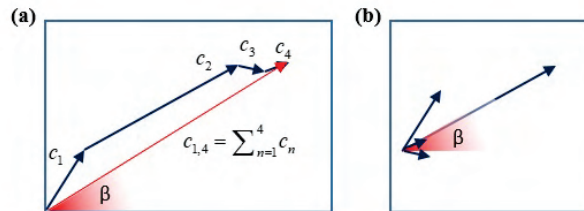


Fig. 5. Schematic showing the principle of the composite filter. Within a given window, I performed summation of the complex numbers  $c_1, \dots, c_4$ . The amplitude of the complex number acts as weights because a high amplitude value in the OCT corresponds to a high signal-to-noise ratio. Ultimately, the composite number  $c_{1,4}$  resulting from the windowed summation of the composite numbers takes on a phase value close to the dominant phase of the number with the largest amplitude, slightly corrected by the phase of the numbers  $c_1, c_3$ , and  $c_4$ .

The data in OCT elastography (OCE) show a different specificity ([Pub. 5](#)). Under compression on a homogeneous object, I expect a linear increase in the layer shift over time, which corresponds to a linearly increasing phase change. As a result of experiment and composite analysis, I obtain the input function for the FPU algorithm, which is in the form of ramp. The ramp does not satisfy the continuity condition on the edges. Martinez-Carranza *et al.* [54] proposed a solution to this problem

using the Volkov symmetrization [55]. I have demonstrated the application of Volkov symmetrization on three-dimensional OCE data. The application of Volkov symmetrization is not always sufficient. In addition, symmetrization results in an eightfold increase in volumetric data and increases the demand for working memory. The problem turns out to be not insignificant for tomographic data. Using the algorithm in three-dimensional form results in the need to allocate the GPU (graphics processing unit) or CPU (central processing unit) memory for up to tens of GB. When symmetrization is not enough, phase unwrapping can be completed successfully using an iterative approach. I also introduced a change in the iteration stop condition and an implementation change in the calculation of the correction in each iteration, which are described in more detail in [Pub. 5](#).

My analysis shows that for OCE data, reducing the number of iterations and also the sensitivity of the algorithm to noise can be achieved by using additional filters, for example, a median or complex filter. By its nature, the FPU algorithm does not use information from the signal amplitude. Calculations are performed using complex analysis, but assuming that all complex numbers have amplitude equal to one. The use of composite filtering, allows the amplitude information to be introduced into the phase analysis. The operation of the composite filter is schematically shown in Fig. 5.

## 6.2. Measurements of blood flow parameters in eye blood vessels

Diseases of the circulatory system manifest themselves in changes of vascularization and the mechanism of autoregulation of blood flow. We are able to observe part of the cerebral vessels optically without the need to perform invasive examinations. OCT of the eye is adapted for this purpose. In the last few decades, dynamic development of angiographic methods has been observed, which consists in imaging and tracking morphological changes of blood vessels in the retina and choroid [56–58]. In addition to angiographic methods, there is a separate class of Doppler OCT methods that allows measurement of the velocity of the scattering centers of the measured object. The determination of velocity is possible by measuring the Doppler frequency [30,59,60] or from phase analysis [61,62].

The main goal of the project was to obtain information on selected blood flow parameters such as axial velocity, volume flow, and the dependence of blood flow on vessel diameter as defined by Murray parameter. The main challenges of the project were to reduce the influence of blood vessel geometry on the measurement, to remove the phase wrapping artifact, and to reduce the time from experiment to complete data processing and obtain flow biomarkers.

As part of the [P2](#) project, I implemented the FPU phase unwrapping algorithm in the Doppler OCT method. In my research, I focused on retinal blood vessels of healthy volunteers. Example results of selected parameters of blood flow in human eye and description of experiments with measurement protocols are included in publications [Pub. 2, 3](#).

In [Pub. 3](#) we demonstrated the feasibility of determining resistivity and pulsatility index by OCT for healthy volunteers and compared these parameters for the middle cerebral artery obtained by transcranial Doppler ultrasonography (TCD). One of my goals was to develop a method and measurement protocols to determine resistivity and pulsatility parameters by noninvasive Doppler OCT.

In the future, I would like to study the differences between the blood flow velocity course between a cerebral vessel with a diameter of  $\sim 100 \mu\text{m}$  and a middle cerebral artery with a diameter of the order of mm. I have already performed some experiments on 40 patients at Oculomedica Clinic in Bydgoszcz in cooperation with doctor Bartłomiej Sikorski, MD. Data analysis and development of methods allowing for greater automation of the data analysis process, mainly segmentation of blood vessels, is ongoing. Together with the authors, we hypothesize that blood flow autoregulation pathologies occurring in smaller retinal vessels may precede changes in larger cerebral vessels, which may help develop new bio-markers for cardiovascular disease.

### 6.3. Measurement of light-induced retina activities

Another application area of the phase is nerve cell research. The biochemical processes involved in vision are still not well understood. Electroretinography (ERG) [63], an invasive method involving direct measurement of voltage shifts between the inside and outside of a nerve cell, has provided much valuable information about the changes occurring in retinal nerve cells under the influence of a light stimulus. The OCT method is adapted to measure the shifts without invasive use of electrodes. Optical methods for determining the retinal response to light stimulus are called optoretinography (ORG). Currently, attempts are being made to relate the changes observed in OCT to the results of ERG and physiological pathologies within the photoreceptors.

Due to the limited resolution of optical systems, the measurement of single photoreceptors is still the subject of much research, especially those related to adaptive optics [64]. Adaptive optics allows for the reduction of wavefront distortion thus reducing the influence of optical aberrations on the experimental outcome. Changes in single photoreceptors are manifested by changes within entire layers, which can be observed by means of spectral OCT.

The goal of the P3 project was to develop a method that would measure the response of nerve cells to a given luminous stimulus using a spectral OCT scanning system, without the use of adaptive optics and additional eye tracking systems. Studies of changes in retinal nerve cell layers under a luminous stimulus based on the scattering properties of biological tissue have already been conducted by other research groups [65–69]. These methods show low sensitivity to signal decorrelation over time, at the expense of the measurement accuracy of the measured layer relocations.

The project objective has been reached thanks to modification and application of a method based on phase analysis. It was possible due to data presentation by means of so called cross-spectra. The ORG signal, meaning the relocations of the retinal layers after the onset of a light pulse, is reconstructed in this method from the Knox-Thompson pathways based on the cross-correlation spectrum. The cross-correlation spectrum, in simple terms, represents the evolution of the signal difference between two retinal layers (Fig. 1 in Pub. 4). The method allows us to use the full information between each time sample, not just the differences between the first and subsequent time samples. The graphical presentation of the autocorrelation signal of the phase difference between the analyzed retinal layers, allows to develop weights and to separate the less correlated signal from the well-defined one. By running paths within the cross-correlation spectrum, it is possible to reconstruct the ORG signal, even in tens of seconds of measurement, as I have shown in Pub. 4 In this project, we tracked the shifts between the photoreceptor (inner and outer photoreceptors segments, IS/OS) and Bruch's membrane (BrM) layers in mouse retinas. Application of the phase method allowed us to increase the sensitivity of the measurement and to observe more subtle changes, unnoticeable in results obtained

with methods based on amplitude analysis. The study was conducted on anesthetized mice at the University of California, Davis Eyepod Imaging Laboratory. Following the collaboration of this project, after the completion of work on [Pub. 4](#), I completed a month-long research internship at the laboratories of the University of California, Davis under the supervision of Professor Robert Zawadzki, performing further experiments to continue research in optiretinography-related topics.

As the next steps, I plan to develop a phase-based ORG method by optimizing the selection of a pathway composed of Knox-Thompson pathways, which will enable the application of this method on humans in clinical conditions.

The details of the experiments and the proposed method were described in [Pub. 4](#).

#### 6.4. Measurement of biomechanical properties of biological tissues under compression

Precise measurements of sample's layer relocations in OCT measurements, also allow the use of phase methods to determine biomechanical properties of tissues. Changes in tissue stiffness accompany disease processes, including cancer. In this project, I studied changes in tissue stiffness modulus under the influence of tissue compression using a piston that gradually compresses tissue between successive OCT image recordings. Rigid tissue under compression deforms less than soft tissue. Tumor tissue is characterized by heterogeneous structure and stiffness, which allows to distinguish it from healthy tissue [70]. Measuring the stiffness modulus boils down to measuring the displacement of tissue layers between two piston positions [5,71].

The goal of this project was to propose a new method for calculating the deformation of objects using OCT elastography (OCE) and to present it in terms of two previously used methods: the vector method [72] and the weighted phase unwrapping method [73]. The new method was intended to reduce the amount of artifacts caused by phase wrapping. We also wanted to review the methods and analyze the algorithms in OCE applications.

I modified the FPU fast phase unwrapping algorithm for elastography applications. The main changes were the extension of the algorithm to analyze three-dimensional volumetric data, the development and application of Volkov symmetrization [55] for the case of three-dimensional data, and a change in the iteration stop condition and an implementation change in the calculation of the correction in each iteration (Fig. 1 in [Pub. 5](#)). The algorithm I implemented, in Matlab [Code 3](#) has been attached to this paper. I used the modified FPU in the procedure of defining the strain on the data from mice and pig tissue. This enabled the reduction of artifacts in strain imaging caused by phase unwrapping errors in the other two methods. Along with the other authors of [Pub. 5](#), I made a comparison between the previously used methods for calculating the stiffness modulus and the method using FPU. The FPU method was able to increase the dynamic range and thus improve the contrast in strain imaging at the cost of decreasing computational efficiency. In [Pub. 5](#), in collaboration with the University of Western Australia in Perth, we presented the advantages and disadvantages of each method, which can help in choosing the right one depending on the researcher's goal.

Details of the application of the FPU algorithm to OCE studies of mouse and pig tissue and a comparison of the results for the other methods of determining the stiffness modulus in OCE are described in [Pub. 5](#).



## 7. Description of doctoral student's contribution

The publications presented in this dissertation are part of the output of the research projects **P1-P3** projects where I was the main contributor in all the aspects, starting from the concept of the research, development of necessary tools, their implementation, design of experiments and data analysis. For obtaining the results from projects **P4-P5** I have reached to foreign partners with proposition of implementing the developed tools in their studies, made preliminary tests followed by close collaboration, where I prepared almost all the data analysis tools and processed the experimental data that led to the published results. Detailed description of the work done in the projects is given below.

In **P1** project, as a part of my research, I modified and implemented an algorithm for removing one of the most common artifacts occurring during phase analysis of OCT signal - phase wrap. I implemented, with the help of Marcin Sylwestrzak, PhD, FPU algorithm on GPUs in C/CUDA environment. I implemented simulation of flow phantom, allowing to change its orientation and to change parameters of internal flows. I made a number of tests of the FPU algorithm *in silico*. I prepared and performed OCT experiments on the flow phantoms. My tasks also included entire data processing and preparation of the final results.

In the **P2** project, I was responsible for implementing the FPU algorithm to remove phase wrap artifact in Doppler OCT measurements. I applied the algorithm to the study of blood flow in retinal vessels in the human eye in healthy patients. I was responsible for preparation of the experiment both formally and scientifically, including recruiting the volunteers, contact with the eye clinic, contact with patients, and direct execution of experiments on volunteers. I proposed post-measurement protocols and performed full data processing to obtain selected blood flow parameters such as flow velocity, volume flow, Murray parameter relating diameter to volume flow in the vessel, vascular resistance. In [Pub. 3](#) the time course of axial blood velocity pulsatility for selected retinal arterioles is also shown. I was responsible for the preparation and execution of the experiments, complete data processing and presentation of the final results. I compared pulsatility in retinal arterioles with blood velocity in middle cerebral artery obtained by transcranial Doppler (TCD) ultrasonography.

As part of the **P3** project, I demonstrated another way of presenting the phase signal along with the application of the phase method with Knox-Thompson pathways to measure light-induced retinal function using spectral OCT. I implemented the method and adapted it to the needs of optoretinography. I demonstrated the application of the method in real *in vivo* measurements on immobilized mice. I applied the phase method based on cross-correlation to widely available spectral OCT systems without the need for adaptive optics, an eye movement-induced motion artifact correction device, fast light sources, and high acquisition rates. My tasks included complete data processing and presentation and analysis of the final results.

As part of the P4 project, I once again modified the FPU algorithm and applied it to a new field, OCT elastography, for measuring the biomechanics of biological tissues. My modifications included extending the algorithm to analyze three-dimensional volumetric data, developing and applying Volkov symmetrization [54] for the case of three-dimensional data, changing the iteration stop condition, and an implementation change in computing the correction at each iteration. I was responsible for implementing FPU phase unwrapping for strain rate measurements on real *ex vivo* biological tissues. My tasks included the preparation of phase data and its processing by the FPU method. I was involved in comparing the calculated strains with results obtained using two methods previously used at OCE: the vector method and the weighted phase unwrapping method. I contributed to the analysis of results comparing the performance of three methods for calculating tissue strain in OCE.

In Pub. 1-4, which are part of the dissertation, I am the lead author. The text of the manuscripts of Pub. 1-4 were almost entirely written by me. I authored the tables, figures, and video files included as appendices to the publications. I was responsible for responses to reviewers and edits to the manuscript after reviews. In the publication Pub. 5, I share the lead authorship with Jiayue Li. I am the author of the results obtained using the FPU algorithm found in the tables and figures of this paper. I am the author of the illustration showing the operation of the modified FPU algorithm and the chapter on the FPU method. I was responsible for the responses to papers reviewers concerning the application of the modified FPU method in OCE.

## 8. Summary

Phase provides a range of interesting physiological information that could help in the diagnosis of selected modern civilization diseases. A prerequisite for the applicability of these methods is their reliability and obtaining information in a satisfactory time, adapted to real clinical conditions. Despite promising results, the transfer of phased-based OCT methods to clinics has been halted by a number of problems, which are still an open topic for researchers.

I have demonstrated selected applications of the OCT signal phase in Doppler OCT, OCT elastography and optoretinography. I focused on several problems accompanying phase analysis: the time required for data processing and the need for working memory, the limited range of measurable axial displacements, obtaining displacement information only in the beam axis, the influence of object geometry on the measurement, motion artifacts unavoidable in a measurement of a few seconds, phase artifacts resulting from the composite analysis of OCT data. I have shown proposals of methods for analysis of phase data obtained with widely available systems for spectral OCT, which would allow application of new methods using already existing devices.

The proposed methods allow to reduce phase artifacts and to obtain reliable results, what was confirmed by simulations and experimental data gathered *ex vivo* and *in vivo* from real biological samples. I have implemented FPU phase unwrapping algorithm on graphics card processors to speed up the computation time.

The projects presented in my dissertation are part of a broad research effort to develop phased-array methods and increase the functionality of OCT devices, which may help develop biomarkers and accelerate the diagnosis of selected diseases of civilization in the future.

## References

1. "Rocznik Demograficzny 2020," Główny Urząd Stat. Polska (2020).
2. Y. Zhao, Z. Chen, C. Saxer, S. Xiang, J. F. de Boer, and J. S. Nelson, "Phase-resolved optical coherence tomography and optical Doppler tomography for imaging blood flow in human skin with fast scanning speed and high velocity sensitivity," *Opt. Lett.* **25**(2), 114–116 (2000).
3. T. Schmoll and R. A. Leitgeb, "Heart-beat-phase-coherent Doppler optical coherence tomography for measuring pulsatile ocular blood flow," *J. Biophotonics* **6**(3), 275–282 (2013).
4. M. Szkulmowski, I. Gorczynska, and E. Pijewska, "Complex fast phase unwrapping method for Doppler OCT," in *Optical Coherence Tomography and Coherence Domain Optical Methods in Biomedicine XXIII*, J. A. Izatt and J. G. Fujimoto, eds. (SPIE, 2019), **10867**, p. 87.
5. J. M. Schmitt, "OCT elastography: imaging microscopic deformation and strain of tissue," *Opt. Express* **3**(6), 199–211 (1998).
6. B. F. Kennedy, K. M. Kennedy, A. L. Oldenburg, S. G. Adie, S. A. Boppart, and D. D. Sampson, "Optical coherence elastography - OCT at work in tissue biomechanics [Invited]," *Biomed. Opt. Express*, Vol. 8, Issue 2, pp. 1172-1202 **8**(2), 1172–1202 (2017).
7. J. B. Mulligan and D. I. A. Macleod, "In Search of an Optoretinogram," in *Vision Science and Its Application Topical Meeting* (1994).
8. G. Ma, T. Son, T.-H. Kim, and X. Yao, "Functional optoretinography: concurrent OCT monitoring of intrinsic signal amplitude and phase dynamics in human photoreceptors," *Biomed. Opt. Express* **12**(5), 2661 (2021).
9. M. W. Stewart, *Diabetic Retinopathy* (Springer, New York, NY, 2010).
10. S. JS, H. MR, A. AV, P.-K. T, P. CA, F. JG, and S. EA, "Optical coherence tomography: a new tool for glaucoma diagnosis.," *Curr. Opin. Ophthalmol.* **6**(2), 89–95 (1995).
11. H. A. Quigley, "Neuronal death in glaucoma," *Prog. Retin. Eye Res.* **18**(1), 39–57 (1999).
12. C. D. Dimitriou and D. C. Broadway, *Pathophysiology of Glaucoma* (Future Medicine, 2013).
13. L. Biscetti, M. Lupidi, E. Luchetti, P. Eusebi, R. Gujar, A. Vergaro, C. Cagini, and L. Parnetti, "Novel noninvasive biomarkers of prodromal Alzheimer disease: The role of optical coherence tomography and optical coherence tomography–angiography," *Eur. J. Neurol.* **28**(7), 2185–2191 (2021).
14. V. Patel, S. Rassam, R. Newsom, J. Wiek, and E. Kohner, "Retinal blood flow in diabetic retinopathy.," *Br. Med. J.* **305**(6855), 678–683 (1992).
15. Z. Burgansky-Eliash, A. Barak, H. Barash, D. A. Nelson, O. Pupko, A. Lowenstein, A. Grinvald, and A. Rubinstein, "Increased retinal blood flow velocity in patients with early diabetes mellitus," *Retina* **32**(1), 112–119 (2012).
16. J. A. Izatt, E. A. Swanson, J. G. Fujimoto, M. R. Hee, and G. M. Owen, "Optical coherence microscopy in scattering media," *Opt. Lett.* **19**(8), 590–592 (1994).
17. and J. G. F. U. Morgner, W. Drexler, F. X. Kartner, X. D. Li, C. Pitris, E. P. Ippen, U. Morgner, W. Drexler, X. Li, F. X. Kartner, C. Pitris, S. A. Boppart, E. P. Ippen, and J. G. Fujimoto, "Spectroscopic optical coherence tomography," *IQEC, Int. Quantum Electron. Conf. Proc.* **25**(2), 111–113 (2000).
18. D. Huang, E. A. Swanson, C. P. Lin, J. S. Schuman, W. G. Stinson, W. Chang, M. R. Hee, T. Flotte, K. Gregory, C. A. Puliafito, and J. G. Fujimoto, "Optical coherence tomography," *Science* (80-. ). **254**(5035), 1178–1181 (1991).
19. A. Kowalczyk, A. F. Fercher, M. Wojtkowski, and R. Leitgeb, "Full range complex spectral optical coherence tomography technique in eye imaging," *Opt. Lett.* Vol. 27, Issue 16, pp. 1415-1417 **27**(16), 1415–1417 (2002).
20. M. Wojtkowski, V. J. Srinivasan, T. H. Ko, J. G. Fujimoto, A. Kowalczyk, and J. S. Duker, "Ultra-high-resolution, high-speed, Fourier domain optical coherence tomography and methods for dispersion compensation," *Opt. Express* **12**(11), 2404 (2004).
21. Y. Yasuno, Y. Hong, S. Makita, M. Miura, and T. Yatagai, "Phase-insensitive optical coherence angiography of the choroid by 1-micrometer band swept-source optical coherence tomography," in *International Society for Optics and Photonics* (SPIE, 2007), **6429**, p. 642905.
22. A. Yasin Alibhai, C. Or, and A. J. Witkin, "Swept Source Optical Coherence Tomography: a Review," *Curr. Ophthalmol. Rep.* **6**(1), 7–16 (2018).
23. D. A and B. C, "Full-field OCT," *Med. Sci. (Paris)*. **22**(10), 859–864 (2006).
24. M. Szkulmowski, "Numeryczne Metody Zwiększania Jakości Obrazów w Spektralnej Tomografii Optycznej," Nicolaus Copernicus Univ. Fac. Physics, Astron. Informatics Toruń (2006).
25. A. Szkulmowska, "Analiza i wykorzystanie informacji fazowej w spektralnej tomografii optycznej z użyciem światła częściowo spójnego," Nicolaus Copernicus Univ. Fac. Physics, Astron. Informatics Toruń (2009).
26. M. Wojtkowski, "Obrazowanie za pomocą tomografii optycznej OCT z detekcją fourierowską," Nicolaus Copernicus Univ. Fac. Physics, Astron. Informatics Toruń (2010).
27. M. Sylwestrzak, "Analiza danych spektralnej tomografii optycznej OCT z wykorzystaniem wielordzeniowych kart graficznych," Nicolaus Copernicus Univ. Fac. Physics, Astron. Informatics Toruń (2013).
28. B. R. White, M. C. Pierce, N. Nassif, B. Cense, B. H. Park, G. J. Tearney, B. E. Bouma, T. C. Chen, and J. F. de Boer, "In vivo dynamic human retinal blood flow imaging using ultra-high-speed spectral domain optical Doppler tomography," *Opt. Express* **11**(25), 3490–3497 (2003).
29. E. Koch, J. Walther, and M. Cuevas, "Limits of Fourier domain Doppler-OCT at high velocities," *Sensors Actuators*

- A Phys. **156**(1), 8–13 (2009).
30. A. M. Rollins, J. A. Izatt, and S. Yazdanfar, "Imaging and velocimetry of the human retinal circulation with color Doppler optical coherence tomography," *Opt. Lett.* Vol. 25, Issue 19, pp. 1448–1450 **25**(19), 1448–1450 (2000).
  31. M. M. Bartuzel, K. Wróbel, S. Tamborski, M. Meina, M. Nowakowski, K. Dalasiński, A. Szkulmowska, and M. Szkulmowski, "High-resolution, ultrafast, wide-field retinal eye-tracking for enhanced quantification of fixational and saccadic motion," *Biomed. Opt. Express* **11**(6), 3164 (2020).
  32. J. Walther, G. Mueller, H. Morawietz, and E. Koch, "Signal power decrease due to fringe washout as an extension of the limited Doppler flow measurement range in spectral domain optical coherence tomography," *J. Biomed. Opt.* **15**(4), 041511 (2010).
  33. A. Szkulmowska, M. Szkulmowski, A. Kowalczyk, and M. Wojtkowski, "Phase-resolved Doppler optical coherence tomography—limitations and improvements," *Opt. Lett.* **33**(13), 1425 (2008).
  34. R. Leitgeb, C. K. Hitzenberger, and A. F. Fercher, "Performance of fourier domain vs. time domain optical coherence tomography," *Opt. Express* **11**(8), 889–894 (2003).
  35. H. C. Hendargo, R. P. McNabb, A.-H. Dhalla, N. Shepherd, and J. A. Izatt, "Doppler velocity detection limitations in spectrometer-based versus swept-source optical coherence tomography," *Biomed. Opt. Express* **2**(8), 2175 (2011).
  36. O. Tan, R. Konduru, X. Zhang, S. R. Sadda, and D. Huang, "Dual-Angle Protocol for Doppler Optical Coherence Tomography to Improve Retinal Blood Flow Measurement," *Transl. Vis. Sci. Technol.* **3**(4), 6 (2014).
  37. R. Haindl, W. Trasischker, A. Wartak, B. Baumann, M. Pircher, and C. K. Hitzenberger, "Total retinal blood flow measurement by three beam Doppler optical coherence tomography," *Biomed. Opt. Express* **7**(2), 287 (2016).
  38. Y. Wang, A. Lu, J. Gil-Flamer, O. Tan, J. A. Izatt, and D. Huang, "Measurement of total blood flow in the normal human retina using Doppler Fourier-domain optical coherence tomography," *Br. J. Ophthalmol.* **93**(5), 634–637 (2009).
  39. Y.-Y. Cheng and J. C. Wyant, "Two-wavelength phase shifting interferometry," *Appl. Opt.* **23**(24), 4539 (1984).
  40. K. Creath, "Step height measurement using two-wavelength phase-shifting interferometry," *Appl. Opt.* **26**(14), 2810 (1987).
  41. D. Parshall and M. K. Kim, "Dual-Wavelength Phase Unwrapping," *Appl. Opt.* **45**(3), 451–459 (2006).
  42. H. C. Hendargo, M. Zhao, N. Shepherd, and J. A. Izatt, "Synthetic wavelength based phase unwrapping in spectral domain optical coherence tomography," *Opt. Express* **17**(7), 5039–5051 (2009).
  43. P. Soille, "Morphological phase unwrapping," *Opt. Lasers Eng.* **32**(4), 339–352 (1999).
  44. M. Ma, P. Yao, J. Deng, H. Deng, J. Zhang, and X. Zhong, "A morphology phase unwrapping method with one code grating," *Rev. Sci. Instrum.* **89**(7), 073112 (2018).
  45. S. Pi, A. Camino, X. Wei, T. T. Hormel, W. Cepurna, J. C. Morrison, and Y. Jia, "Automated phase unwrapping in Doppler optical coherence tomography," *J. Biomed. Opt.* **24**(01), 1 (2019).
  46. Y. Lu, W. Zhao, X. Zhang, W. Xu, and G. Xu, "Weighted-phase-gradient-based quality maps for two-dimensional quality-guided phase unwrapping," *Opt. Lasers Eng.* **50**(10), 1397–1404 (2012).
  47. R. M. Goldstein, H. A. Zebker, and C. L. Werner, "Satellite radar interferometry: Two-dimensional phase unwrapping," *Radio Sci.* **23**(4), 713–720 (1988).
  48. D. C. Ghiglia and M. D. Pritt, *Two-Dimensional Phase Unwrapping: Theory, Algorithms, and Software* (1998).
  49. D. C. Ghiglia and L. A. Romero, "Direct phase estimation from phase differences using fast elliptic partial differential equation solvers," *Opt. Lett.* **14**(20), 1107–1109 (1989).
  50. M. a Schofield and Y. Zhu, "Fast phase unwrapping algorithm for interferometric applications," *Opt. Lett.* **28**(14), 1194–1196 (2003).
  51. W. Schwartzkopf, T. E. Milner, J. Ghosh, B. L. Evans, and A. C. Bovik, "Two-dimensional phase unwrapping using neural networks," in *Proceedings of the IEEE Southwest Symposium on Image Analysis and Interpretation* (Institute of Electrical and Electronics Engineers Inc., 2000), pp. 274–277.
  52. K. Wang, Y. Li, Q. Kema, J. Di, and J. Zhao, "One-step robust deep learning phase unwrapping," *Opt. Express* **27**(10), 15100 (2019).
  53. K. A. Nugent and T. E. Gureyev, "Phase retrieval with the transport-of-intensity equation. II. Orthogonal series solution for nonuniform illumination," *JOSA A*, Vol. 13, Issue 8, pp. 1670–1682 **13**(8), 1670–1682 (1996).
  54. J. Martinez-Carranza, K. Falaggis, and T. Kozacki, "Fast and accurate phase-unwrapping algorithm based on the transport of intensity equation," *Appl. Opt.* **56**(25), 7079–7088 (2017).
  55. V. V. Volkov, Y. Zhu, and M. De Graef, "A new symmetrized solution for phase retrieval using the transport of intensity equation," *Micron* **33**(5), 411–416 (2002).
  56. S. Makita, Y. Hong, M. Yamanari, T. Yatagai, and Y. Yasuno, "Optical coherence angiography," *Opt. Express* **14**(17), 7821 (2006).
  57. R. F. Spaide, J. G. Fujimoto, N. K. Waheed, S. R. Sadda, and G. Staurenghi, "Optical coherence tomography angiography," *Prog. Retin. Eye Res.* **64**(June 2017), 1–55 (2018).
  58. J. V. Migacz, I. Gorczynska, M. Azimipour, R. Jonnal, R. J. Zawadzki, and J. S. Werner, "Megahertz-rate optical coherence tomography improves the contrast of the choriocapillaris and choroid in human retinal imaging," *Biomed. Opt. Express* **10**(1), 50 (2019).
  59. J. S. Nelson, T. E. Milner, and X. J. Wang, "Characterization of fluid flow velocity by optical Doppler tomography," *Opt. Lett.* Vol. 20, Issue 11, pp. 1337–1339 **20**(11), 1337–1339 (1995).

60. A. Malekafzali, J. S. Nelson, M. J. C. van Gemert, S. Srinivas, T. E. Milner, X. Wang, and Z. Chen, "Noninvasive imaging of in vivo blood flow velocity using optical Doppler tomography," *Opt. Lett.* Vol. 22, Issue 14, pp. 1119-1121 **22**(14), 1119–1121 (1997).
61. J. A. Izatt and S. Yazdanfar, "Self-referenced Doppler optical coherence tomography," *Opt. Lett.* Vol. 27, Issue 23, pp. 2085-2087 **27**(23), 2085–2087 (2002).
62. M. Szkulmowski, A. Szkulmowska, T. Bajraszewski, A. Kowalczyk, and M. Wojtkowski, "Flow velocity estimation using joint Spectral and Time domain Optical Coherence Tomography.," *Opt. Express* **16**(9), 6008 (2008).
63. D. L. McCulloch, M. F. Marmor, M. G. Brigell, R. Hamilton, G. E. Holder, R. Tzekov, and M. Bach, "ISCEV Standard for full-field clinical electroretinography (2015 update)," *Doc. Ophthalmol.* **130**(1), 1–12 (2015).
64. D. R. Williams, D. T. Miller, and J. Liang, "Supernormal vision and high-resolution retinal imaging through adaptive optics," *JOSA A*, Vol. 14, Issue 11, pp. 2884-2892 **14**(11), 2884–2892 (1997).
65. Q. Zhang, R. Lu, B. Wang, J. D. Messinger, C. A. Curcio, and X. Yao, "Functional optical coherence tomography enables in vivo physiological assessment of retinal rod and cone photoreceptors," *Sci. Rep.* **5**(1), 1–10 (2015).
66. M. Azimipour, D. Valente, K. V. Vienola, J. S. Werner, R. J. Zawadzki, and R. S. Jonnal, "Optoretinography: Optical measurements of human cone and rod photoreceptor responses to light," *bioRxiv* 760306 (2019).
67. Vimal Prabhu Pandiyan, Aiden Maloney Bertelli, James A Kuchenbecker, B. Hyle Park, Daniel V Palanker, Austin Roorda, and Ramkumar Sabesan, "Optoretinogram: stimulus-induced optical changes in photoreceptors observed with phase-resolved line-scan OCT," *Invest. Ophthalmol. Vis. Sci.* **60**(9), 1426 (2019).
68. T. Son, T. H. Kim, G. Ma, H. Kim, and X. Yao, "Functional intrinsic optical signal imaging for objective optoretinography of human photoreceptors," *Exp. Biol. Med.* **246**(6), 639–643 (2021).
69. R. S. Jonnal, "Toward a clinical optoretinogram: a review of noninvasive, optical tests of retinal neural function," *Ann. Transl. Med.* **9**(15), 1270–1270 (2021).
70. A. A. Sovetsky, A. L. Matveyev, A. Y. Vorontsov, A. A. Plekhanov, D. A. Vorontsov, E. V. Gubarkova, E. V. Zagaynova, L. A. Matveev, M. A. Sirotkina, N. P. Pavlova, N. D. Gladkova, S. S. Kuznetsov, and V. Y. Zaitsev, "OCT-elastography-based optical biopsy for breast cancer delineation and express assessment of morphological/molecular subtypes," *Biomed. Opt. Express*, Vol. 10, Issue 5, pp. 2244-2263 **10**(5), 2244–2263 (2019).
71. K. M. Kennedy, C. Ford, B. F. Kennedy, M. B. Bush, and D. D. Sampson, "Analysis of mechanical contrast in optical coherence elastography," *J. Biomed. Opt.* **18**(12), 121508 (2013).
72. V. Y. Zaitsev, A. L. Matveyev, L. A. Matveev, G. V. Gelikonov, A. A. Sovetsky, and A. Vitkin, "Optimized phase gradient measurements and phase-amplitude interplay in optical coherence elastography," *J. Biomed. Opt.* **21**(11), 116005 (2016).
73. B. F. Kennedy, R. A. McLaughlin, K. M. Kennedy, L. Chin, A. Curatolo, A. Tien, B. Latham, C. M. Saunders, and D. D. Sampson, "Optical coherence micro-elastography: mechanical-contrast imaging of tissue microstructure," *Biomed. Opt. Express* **5**(7), 2113 (2014).

## Appendixes

### Code 1. The code of FPU algorithm implemented in programming environment C/CUDA

```
1. //CUDA 10.1, Visual Studio 2017
2. #define EXPORT_FCNS
3. #define Pi 3.141592654f
4. #include "helper.h"
5. #include "stdafx.h"
6. #include "CUDAprocessing.h"
7. #include <cuda.h>
8. #include <cuda_runtime.h>
9. #include <stdio.h>
10. #include <cuFFT.h>
11. #include <malloc.h>
12. #include <Windows.h>
13. #include "device_launch_parameters.h"
14. #include "device_functions.h"
15. #include "cuda_fp16.h"
16. #include <math.h>
17. #define BATCH 10
18. #define NRANK 3
19. #define Pi 3.141592654f
20.
21. int pix = 0;
22. int ascans = 0;
23. int bscans = 0;
24. int allPix = pix * ascans*bscans;
25. const float PI = 3.141592654f;
26. float* K_device = NULL;
27. #define LUT_FWHM_FUNCTIONS 80
28. cufftHandle plan1, plan2;
29. cufftComplex* dispAndShapeVector_dev = NULL;
30. //
31. // CUDA initialization
32. int InitCuda(void)
33. {
34. int count = 0;
35. int i = 0;
36. cudaGetDeviceCount(&count);
37.
38. if (count == 0) {
39. return 5001; // CUDA device is disconnected
40. }
41.
42. for (i = 0; i < count; i++) {
43. cudaDeviceProp prop;
44. if (cudaGetDeviceProperties(&prop, i) == cudaSuccess) {
45. if (prop.major >= 1) {
46. break;
47. }
48. }
49. }
50.
51. if (i == count) {
52. return 5002; // device does not support CUDA calculations
53. }
54. cudaError_t cudaStatus = cudaSetDevice(i);
55. if (cudaStatus != cudaSuccess) {
56. return 5003; // error with CUDA initialization
57. }
58. return 0;
```



```

59. }
60.
61. //
62. //          *****
63. //          P R O C E S S I N G Phase unwrapping FPU
64. __global__ void div_ComplexFloatD(cufftComplex *C, float *B) {
65. register int i_loc = blockIdx.x*blockDim.x + threadIdx.x;
66. C[i_loc].x = C[i_loc].x / B[i_loc];
67. C[i_loc].y = C[i_loc].y / B[i_loc];
68. //avoid division by zero
69. if (i_loc == 0) {
70. C[i_loc].x = 0;
71. C[i_loc].y = 0;
72. }
73.
74. __global__ void product_ComplexFloatD(cufftComplex *C, float *B) {
75. register int i_loc = blockIdx.x*blockDim.x + threadIdx.x;
76. C[i_loc].x = C[i_loc].x * B[i_loc];
77. C[i_loc].y = C[i_loc].y * B[i_loc];
78. }
79.
80. __global__ void Imag_zlbyz2(cufftComplex *A, float *B, float allPix_c) {
81. //imag(z1/z2) = im2rel-im1re2; when |z2|=1;
82. register int i_loc = blockIdx.x*blockDim.x + threadIdx.x;
83. A[i_loc].x = A[i_loc].y*cosf(B[i_loc]) / allPix_c -
    A[i_loc].x*sinf(B[i_loc]) / allPix_c;
84. A[i_loc].y = 0;
85. }
86.
87. __global__ void unwrap(float *W, cufftComplex *PSI, float PI2, float all-
    Pix_c) {
88. register int i_loc = blockIdx.x*blockDim.x + threadIdx.x;
89. W[i_loc] = W[i_loc] + PI2 * round((PSI[i_loc].x / allPix_c - W[i_loc]) /
    (PI2));
90. }
91.
92. __global__ void P_vec(cufftComplex *P, float *W){
93. register int i_loc = blockIdx.x*blockDim.x + threadIdx.x;
94. P[i_loc].x = cosf(W[i_loc]);
95. P[i_loc].y = sinf(W[i_loc]);
96. }
97.
98. // Fast Phase Unwrapping (FPU) with timing
99. int FPU3d(float *wrapped, float *unwrapped) {
100. LARGE_INTEGER countPerSec, tim1, tim2, tim3, tim4, tim5, tim6, tim7,
    tim8, tim9, tim10, tim11;
101. QueryPerformanceFrequency(&countPerSec);
102. cufftHandle plan1 = NULL, plan2 = NULL;
103. int err;
104. cudaError_t status;
105. cufftResult_t e;
106. float* data_in = NULL;
107. cufftComplex* P = NULL;
108.
109. /* Create a 3D FFT ComplexToComplex plan. */
110. int n[3] = { bscans, ascans, pix };
111. int n1[3] = { pix, ascans, bscans };
112. e = cufftPlan3d(&plan1, bscans, ascans, pix, CUFFT_C2C);
113. cudaMalloc((void**)&data_in, allPix * sizeof(float));
114. cudaMalloc((void**)&P, allPix * sizeof(cufftComplex));
115.
116. if ((P == NULL) || (data_in == NULL) ) {
117. return 5004; // error with CUDA malloc

```



```

118. }
119.
120. dim3 block(pix, 1, 1);
121. dim3 grid(ascans*bscans, 1, 1);
122. QueryPerformanceCounter(&tim1);
123. status = cudaMemcpy(data_in, wrapped, allPix * sizeof(float), cudaMemcpy-
HostToDevice);
124. QueryPerformanceCounter(&tim2);
125. P_vec << < grid, block >> > (P, data_in);
126. cudaDeviceSynchronize();
127. err = cudaGetLastError();
128. QueryPerformanceCounter(&tim3);
129. //1
130. e = cufftExecC2C(plan1, P, P, CUFFT_FORWARD);
131. cudaDeviceSynchronize();
132. QueryPerformanceCounter(&tim4);
133. product_ComplexFloatD << < grid, block >> > (P, K_device);
134. cudaDeviceSynchronize();
135. err = cudaGetLastError();
136. QueryPerformanceCounter(&tim5);
137. //2
138. e = cufftExecC2C(plan1, P, P, CUFFT_INVERSE);
139. cudaDeviceSynchronize();
140. QueryPerformanceCounter(&tim6);
141. Imag_zlbyz2 << < grid, block >> > (P, data_in, allPix);
142. cudaDeviceSynchronize();
143. err = cudaGetLastError();
144. QueryPerformanceCounter(&tim7);
145. //3
146. e = cufftExecC2C(plan1, P, P, CUFFT_FORWARD);
147. div_ComplexFloatD << < grid, block >> > (P, K_device);
148. cudaDeviceSynchronize();
149. err = cudaGetLastError();
150. //4
151. QueryPerformanceCounter(&tim8);
152. e = cufftExecC2C(plan1, P, P, CUFFT_INVERSE);
153. cudaDeviceSynchronize();
154. QueryPerformanceCounter(&tim9);
155. unwrap << < grid, block >> > (data_in, P, 2 * PI, allPix);
156. cudaDeviceSynchronize();
157. err = cudaGetLastError();
158. QueryPerformanceCounter(&tim10);
159. status = cudaMemcpy(unwraped, data_in, allPix * sizeof(float), cudaMemcpy-
cpyDeviceToHost);
160. QueryPerformanceCounter(&tim11);
161. double j[12];
162. j[0] = (double) (tim2.QuadPart - tim1.QuadPart)/countPerSec.QuadPart*1000;
163. j[1] = (double) (tim3.QuadPart - tim2.QuadPart)/countPerSec.QuadPart*1000;
164. j[2] = (double) (tim4.QuadPart - tim3.QuadPart)/countPerSec.QuadPart*1000;
165. j[3] = (double) (tim5.QuadPart - tim4.QuadPart)/countPerSec.QuadPart*1000;
166. j[4] = (double) (tim6.QuadPart - tim5.QuadPart)/countPerSec.QuadPart*1000;
167. j[5] = (double) (tim7.QuadPart - tim6.QuadPart)/countPerSec.QuadPart*1000;
168. j[6] = (double) (tim8.QuadPart - tim7.QuadPart)/countPerSec.QuadPart*1000;
169. j[7] = (double) (tim9.QuadPart - tim8.QuadPart)/countPerSec.QuadPart*1000;
170. j[8] = (double) (tim10.QuadPart -tim9.QuadPart)/countPerSec.QuadPart*1000;
171. j[9] = (double) (tim11.QuadPart-tim10.QuadPart)/countPerSec.QuadPart*1000;
172. j[10] = (double) (tim11.QuadPart-tim1.QuadPart)/countPerSec.QuadPart*1000;
173. j[11] = (double) (tim10.QuadPart-tim2.QuadPart)/countPerSec.QuadPart*1000;
174.
175. cudaFree (P);
176. cudaFree (data_in);
177. cudaFree (K_device);
178. cufftDestroy(plan1);

```

```

179. return 0;
180. }
181.
182. __global__ void kernel_ifftShift_3(float* data_copmplex_dev)
183. {
184. register int index = blockIdx.x * blockDim.x + threadIdx.x;
185. register int offset = blockDim.x * gridDim.x;
186. float re = data_copmplex_dev[index];
187. data_copmplex_dev[index] = data_copmplex_dev[index + offset];
188. data_copmplex_dev[index + offset] = re;
189. }
190.
191. int ifftShift_3(float* data_copmplex_dev)
192. {
193. int nThreads = pix;
194. dim3 nBlocks(ascans*bscans/ 2);
195. kernel_ifftShift_3 << <nBlocks, nThreads >> > (data_copmplex_dev);
196. cudaError_t cudaStatus1 = cudaGetLastError();
197. cudaError_t cudaStatus2 = cudaDeviceSynchronize();
198. if ((cudaStatus1 != cudaSuccess) && (cudaStatus2 != cudaSuccess)) {
199. return 11;
200. }
201. return 0;
202. }
203.
204. __global__ void kernel_ifftShift_1(float* data_complex_dev)
205. {
206. register int index = blockIdx.y * 2 * blockDim.x * gridDim.x + blockIdx.x
      * 2 * blockDim.x + threadIdx.x;
207. register int offset = blockDim.x;
208. float re = data_complex_dev[index];
209. data_complex_dev[index] = data_complex_dev[index + offset];
210. data_complex_dev[index + offset] = re;
211. }
212. int ifftShift_1(float* data_complex_dev)
213. {
214. int nThreads = pix / 2;
215. dim3 nBlocks(ascans, bscans, 1);
216. kernel_ifftShift_1 << <nBlocks, nThreads >> > (data_complex_dev);
217. cudaError_t cudaStatus1 = cudaGetLastError();
218. cudaError_t cudaStatus2 = cudaDeviceSynchronize();
219. if ((cudaStatus1 != cudaSuccess) && (cudaStatus2 != cudaSuccess)) {
220. return 11;
221. }
222. return 0;
223. }
224.
225. __global__ void kernel_ifftShift_2(float* data_complex_dev)
226. {
227. register int index = blockIdx.y * blockDim.x * 2 * gridDim.x + blockIdx.x
      * blockDim.x + threadIdx.x;
228. register int offset = blockDim.x * gridDim.x;
229. float re = data_complex_dev[index];
230. data_complex_dev[index] = data_complex_dev[index + offset];
231. data_complex_dev[index + offset] = re;
232. }
233. int ifftShift_2(float* data_complex_dev)
234. {
235. int nThreads = pix;
236. dim3 nBlocks(ascans / 2, bscans, 1);
237. kernel_ifftShift_2 << <nBlocks, nThreads >> > (data_complex_dev);
238. cudaError_t cudaStatus1 = cudaGetLastError();
239. cudaError_t cudaStatus2 = cudaDeviceSynchronize();

```

```

240. if ((cudaStatus1 != cudaSuccess) && (cudaStatus2 != cudaSuccess)) {
241. return 11;
242. }
243. return 0;
244. }
245.
246. __global__ void kernel_calc_matrix_K(float* K_dev)
247. {
248. //k - threadIdx.x
249. //j - blockIdx.x
250. //i - blockIdx.y
251. //pix - blockDim.x
252. //ascans - gridDim.x
253. //bscans - gridDim.y
254. int index = blockDim.x * gridDim.x * blockIdx.y + blockIdx.x * blockDim.x
+ threadIdx.x;
255. K_dev[index] = (1.0 / (float(blockDim.x - 1))*(-float(blockDim.x) / 2 +
threadIdx.x)) * (1.0 / (float(blockDim.x - 1))*(-float(blockDim.x) / 2 +
threadIdx.x))
256. + (1.0 / (float(gridDim.y - 1))*(-float(gridDim.y) / 2 + block-
Idx.y))* (1.0 / (float(gridDim.y - 1))*(-float(gridDim.y) / 2 + blockIdx.y))
257. + (1.0 / (float(gridDim.x - 1))*(-float(gridDim.x) / 2 + block-
Idx.x))* (1.0 / (float(gridDim.x - 1))*(-float(gridDim.x) / 2 + blockIdx.x))
+ 2.0e-16;
258. //for (int i = 0; i < bscans; i++)
259. //for (int j = 0; j < ascans; j++)
260. // for (int k = 0; k < pix; k++) {
261. // K_dev[k + j * pix + i * ascans*pix] = powf(1.0 / (float(pix - 1))*(-
float(pix) / 2 + k), 2)
262. // + powf(1.0 / (float(bscans - 1))*(-float(bscans) / 2 + i), 2)
263. // + powf(1.0 / (float(ascans - 1))*(-float(ascans) / 2 + j), 2) +
2.0e-16;
264. // }
265. }
266. int calc_matrix_K(float* K_dev)
267. {
268. int nThreads = pix;
269. dim3 nBlocks(ascans, bscans, 1);
270. kernel_calc_matrix_K <<<nBlocks, nThreads >>> (K_dev);
271. cudaError_t cudaStatus1 = cudaGetLastError();
272. cudaError_t cudaStatus2 = cudaDeviceSynchronize();
273. if ((cudaStatus1 != cudaSuccess) && (cudaStatus2 != cudaSuccess)) {
274. return 21;
275. }
276. return 0;
277. }
278.
279. //void frequency_vec_K(float *vec_K) {
280. //
281. //for (int i = 0; i < bscans; i++)
282. // for (int j = 0; j < ascans; j++)
283. // for (int k = 0; k < pix; k++) {
284. // vec_K[k + j * pix + i * ascans*pix] = powf(1.0 / (float(pix - 1))*(-
float(pix) / 2 + k), 2)
285. // + powf(1.0 / (float(bscans - 1))*(-float(bscans) / 2 + i), 2)
286. // + powf(1.0 / (float(ascans - 1))*(-float(ascans) / 2 + j), 2) +
2.0e-16;
287. // }
288. //int i = 0; int j = 0; int k = 0;
289. //float p, a, b;
290. //p = 1.0 / (float(pix))*((float(pix) / 2) + 0);
291. //a = powf(1.0 / (float(ascans))*(-float(ascans) / 2 + j), 2);
292. //b = powf(1.0 / (float(bscans))*(-float(bscans) / 2 + i), 2);

```

```

293. //}
294. EXPORTED_FUNCTION int Initialization(int _ascans, int _bscans, int _pix)
295. {
296. ascans = _ascans;
297. bscans = _bscans;
298. pix = _pix;
299. allPix = ascans * bscans*pix;
300. int error = 0;
301. error = InitCuda();
302. if (error != 0)
303. return error;
304. cudaDeviceReset();
305. cudaMalloc((void**)&K_device, allPix * sizeof(float));
306. int status=0;
307. //status = cudaMemcpy(K_dev, K_c, allPix * sizeof(float), cudaMemcpy-
    HostToDevice);
308. calc_matrix_K(K_device);
309. if (error == 0)
310. error = ifftShift_3(K_device);
311. if (error == 0)
312. error = ifftShift_2(K_device);
313. if (error == 0)
314. error = ifftShift_1(K_device);
315. return 0;
316. }
317.
318. EXPORTED_FUNCTION int FPU(float *wrapped, float *unwrapped)
319. {
320. FPU3d( wrapped, unwrapped);
321. return 0;
322. }

```

**Code 2. The FPU algorithm implemented in programming environment of the Matlab R2021a**

```

1. %                               Fast phase unwrapping algorithm (FPU)                               %
2. %                               %                               %                               %
3. % wrapped                        input array with wrapped phase                        %
4. % -----                        -----                        %
5. % estimated_psi                  output array with unwrapped phase                  %
6. %                               %                               %                               %
7. %                               %                               %                               %
8. %                               %                               %                               %
9.
10. function [unwrapped_psi] = fpu_base(wrapped_fi)
11.
12.     S = size(wrapped_fi);
13.     dim = length(S);
14.
15. % estimated unwrapped phase psi using 4 FFTs
16.
17.     complex_buf = exp(1i*wrapped_fi);
18.     complex_buf = fftn(complex_buf);
19.     K = calc_K;
20.     complex_buf = K.*complex_buf;
21.     clear K
22.     complex_buf = ifftn(complex_buf);
23.     complex_buf = complex_buf./exp(1i*wrapped_fi);
24.     real_buf = imag( complex_buf );
25.     complex_buf = fftn(real_buf);
26.     real_buf = calc_K;
27.     complex_buf = complex_buf./real_buf;
28.     real_buf = real(ifftn(complex_buf));
29.     clear complex_buf
30.
31.     estimated_psi = real_buf;
32.
33. % estimated unwrapped phase psi using 4 FFTs
34. % estimated_psi = ...
35. %     ifftn(fftn(imag(ifftn(K.*fftn(exp(1i*wrapped_fi))))...
36. %     ./exp(1i*wrapped_fi)))./K);
37.
38. % estimated unwrapped phase psi using 6 FFTs
39. % estimated_psi = ...
40. %     ifftn(fftn(((cos(wrapped_fi).*ifftn(K.*fftn(sin(wrapped_fi))))...
41. %     - sin(wrapped_fi).*ifftn(K.*fftn(cos(wrapped_fi))))))./K);
42.
43. % estimated unwrapped phase psi using 8 FFTs
44. % estimated_psi = ...
45. %     ifftn( fftn(cos(wrapped_fi).*(ifftn(K.*fftn(sin(wrapped_fi)))))./K ) ...
46. %     -ifftn( fftn(sin(wrapped_fi).*(ifftn(K.*fftn(cos(wrapped_fi)))))./K );
47.
48.     Q = round( (estimated_psi - wrapped_fi)/(2*pi) );
49.     unwrapped_psi = wrapped_fi + 2*pi*(Q);
50.     unwrapped_psi = real(unwrapped_psi);
51.
52.
53. function K = calc_K()
54.
55.     fx = 1/(S(1)-1)*[-S(1)/2:S(1)/2-1];
56.     fy = 1/(S(2)-1)*[-S(2)/2:S(2)/2-1];
57.
58.     % K is Fourier-space conjugate of the vector r [x,y] or r [x,y,z]
59.

```

```
60.     if dim == 2
61.         [X, Y] = meshgrid(fy, fx);
62.         K = X.^2 + Y.^2 + eps;
63.
64.     elseif dim == 3
65.         % additional coordinates for third spatial dimension
66.         fz = 1/(S(3)-1)*[-S(3)/2:S(3)/2-1];
67.
68.         [X, Y, Z] = meshgrid(fy, fx, fz);
69.         K = X.^2 + Y.^2 + Z.^2 + eps;
70.
71.     elseif dim == 1
72.         K = fx.^2 + eps;
73.
74.     end
75.     K = fftshift(K);
76.     tic();
77.     t1 = tic;
78. end
79.
80. end
```

**Code 3. The code of iterative FPU method for phase unwrapping with Volkov symmetrization**

```

1. %      Fast phase unwrapping algorithm (FPU) with Volkov symmetrization      %
2. %      _____ %
3. %      wrapped                input array with wrapped phase %
4. %      threshold              stop parameter to iteration %
5. %      iter                   stop limit of iterations %
6. %      path                   main path to input file %
7. %      filename               file name with input file %
8. %      ----- %
9. %      estimated_psi          output array with unwrapped phase %
10. % %
11. %      _____ %
12.
13.
14. close all
15. clear all
16.
17. global S dim SK
18.
19. threshold = 1.5;
20. iter = 1e3;
21.
22. % folder with file
23. path = 'C:\MainpathToFile\';
24.
25. % path to file
26. filename = ['filename.m'];
27.
28.     wrapped = read3DleeS([path filename]);
29.     S = size(wrapped);
30.     dim = length(S);
31.     SK = S*2;
32.
33. wrapped = flip(wrapped,3);
34. p = isnan(wrapped);
35. [rr1,rr2]=find(p>0);
36. wrapped(p)=0;
37.
38.
39. % symmetrization
40. ex_wrapped = cat(1,wrapped,flip(wrapped,1));
41. ex_wrapped = cat(3,ex_wrapped,flip(ex_wrapped,3));
42. ex_wrapped = cat(2,ex_wrapped,flip(ex_wrapped,2));
43.
44.
45. % first estimation of unwrapped phase
46. [ex_estimated_psi] = estimation(ex_wrapped);
47. estimated_psi = ex_estimated_psi(1:S(1),1:S(2),1:S(3));
48.
49. clear ex_estimated_psi ex_wrapped wrapped
50.
51. i = 0;
52. if i <= iter
53. if th <= threshold
54.
55.     % correction of estimation
56.     Q2 = angle(exp(1i*wrapped).*exp(-1i*estimated_psi));
57.
58.     % noise can be calculaten in ROI or global
59.     th = std(std(std(angle(Q2))));

```

```

60.
61.
62.     % Volkov symmetrization
63.     ex_Q = cat(1,Q2,flip(Q2,1));
64.     clear Q2
65.     ex_Q = cat(2,ex_Q,flip(ex_Q,2));
66.     ex_Q = cat(3,ex_Q,flip(ex_Q,3));
67.
68.
69.     % estimation of correction
70.     [est_Q2] = estimation(ex_Q);
71.     Q = est_Q2(1:S(1),1:S(2),1:S(3));
72.
73.         clear ex_Q est_Q2
74.
75.     % corrected estimation psi
76.     estimated_psi = estimated_psi + Q;
77.
78. i = i + 1;
79. end
80. end
81.
82.
83. function [output_phase] = estimation(input_phase)
84.
85.     SK = size(input_phase);
86.
87.     real_buf = GenSaveKtesty(SK);
88.     K = real_buf;
89.
90.     complex_buf = single(input_phase);
91.
92.     % estimated unwrapped phase psi using 4 FFTs
93.
94.     complex_buf = exp(1i*complex_buf);
95.     complex_buf = single(complex_buf);
96.     complex_buf = fftn(complex_buf);
97.
98.     complex_buf = real_buf.*complex_buf;
99.     complex_buf = ifftn(complex_buf);
100.
101.     complex_buf = complex_buf./exp(1i*ex_wrapped);
102.
103.     clear ex_wrapped
104.
105.     real_buf = imag( complex_buf );
106.     complex_buf = fftn(real_buf);
107.
108.     complex_buf = complex_buf./K;
109.
110.     clear K
111.
112.     real_buf = real(ifftn(complex_buf));
113.
114.     clear complex_buf
115.
116.     output_phase = real_buf;
117.
118. end
119.
120.
121. function [array_data] = read3Dlees(path)
122.

```



```

123. file1 = fopen(path,'r'); % open file to read
124. size = fread (file1,3,'int32', 'ieee-le'); % read 3-dimentional data
125. data = fread (file1,'single','ieee-le'); % read data in single precision
126. fclose('all'); % close file
127.
128. % reshape data to matlab 3-dim array
129. array_data = reshape(data,[size(1),size(2),size(3)]);
130.
131.end
132.
133.
134.function K = GenSaveKtesty(SK)
135.
136. global dim
137.
138. ER = 0.01;
139.
140. fx = [-SK(1)/2:SK(1)/2-1];
141. fx = single(fx);
142. fy = [-SK(2)/2:SK(2)/2-1];
143. fy = single(fy);
144.
145. % K is Fourier-space conjugate of the vector r [x,y] or r [x,y,z]
146.
147. if dim == 2
148. [X, Y] = meshgrid(fy, fx);
149. clear fz ty
150. K = X.^2 + Y.^2 + ER;
151. clear X Y Z
152.
153. elseif dim == 3
154.
155. % additional coordinates for third spatial dimension
156. fz = [-SK(3)/2:SK(3)/2-1];
157.
158. [X, Y, Z] = meshgrid(fy, fx, fz);
159.
160. clear fz fy fz
161. X = single(X);
162. Y = single(Y);
163. Z = single(Z);
164.
165. K = X.^2 + Y.^2 + Z.^2 + ER;
166. clear X Y Z
167. end
168. K = fftshift(K);
169. tic();
170. t1 = tic;
171.end

```

## **Manuscripts**

The original publications [Pub. 1-5](#) are included in this chapter. Publications [Pub. 1-2](#) and [Pub. 4-5](#) are available from the Biomedical Optics Express (JIF 3.92 in 2019 and JIF 3.73 in 2020) website <https://opg.optica.org/boe> as Open Access journals. Publication [Pub. 3](#) is available on the SPIE website <https://www.spiedigitallibrary.org/conference-proceedings-of-spie> with an online conference presentation presented in SPIE Photonics Europe 2020.



# Computationally effective 2D and 3D fast phase unwrapping algorithms and their applications to Doppler optical coherence tomography

EWELINA PIJEWSKA, IWONA GORCZYNSKA, AND MACIEJ SZKULMOWSKI\*

*Institute of Physics, Faculty of Physics, Astronomy and Informatics, Nicolaus Copernicus University in Torun, Grudziadzka 5, 87-100 Torun, Poland*

\*[maciej.szkulmowski@fizyka.umk.pl](mailto:maciej.szkulmowski@fizyka.umk.pl)

**Abstract:** We propose a simplification for a robust and easy to implement fast phase unwrapping (FPU) algorithm that is used to solve the phase wrapping problem encountered in various fields of optical imaging and metrology. We show that the number of necessary computations using the algorithm can be reduced compared to its original version. FPU can be easily extended from two to three spatial dimensions. We demonstrate the applicability of the two- and three-dimensional FPU algorithm for Doppler optical coherence tomography (DOCT) in numerical simulations, and in the imaging of a flow phantom and blood flow in the human retina *in vivo*. We introduce an FPU applicability plot for use as a guide in the selection of the most suitable version of the algorithm depending on the phase noise in the acquired data. This plot uses the circular standard deviation of the wrapped phase distribution as a measure of noise and relates it to the root-mean-square error of the recovered, unwrapped phase.

© 2019 Optical Society of America under the terms of the [OSA Open Access Publishing Agreement](#)

## 1. Introduction

Optical coherence tomography (OCT) is a micrometer-scale imaging technique [1, 2] most commonly used in medical diagnostics to visualize structures and detect the functions of biological tissues and cells. OCT relies on the principle of white light interferometry. Analysis of the interference signals originating from backscattered light within the tissue and backreflected from the reference mirror of an interferometer provides information about the spatial distribution of scattering structures within the object. The broader the spectrum of the light is, the higher the axial imaging resolution is. In the case of the Fourier-domain variant of the OCT technique (FdOCT), the interference signal is recorded in the wavelength space. Interference spectra are acquired, digitized, and numerically processed (calibrated in the wavenumber domain, corrected for dispersion, spectrally shaped, and Fourier transformed) to generate complex OCT signals that contain information about the object. One of the advantages of the inherent access to the amplitude and phase of the interference signals is the possibility to devise methods for motion or flow detection and measurement. The motion/flow detection methods are typically used in biomedical OCT imaging for the visualization of the circulatory systems within the living tissues. Their most common application is the use of blood motion to generate contrast for the visualization of vessels using a family of techniques known as optical coherence angiography (OCA or OCTA) [3-5]. However, motion detection techniques can be also augmented with data analyses to provide quantitative information about at least one component of the flow velocity vector [6-11]. Most frequently, the flow measurement is performed with Doppler OCT techniques that either use the Doppler effect directly [12-16], or analyze the phase differences among complex OCT signals [17-21]. Quantitative motion detection and the Doppler OCT methods are often jointly referred to as OCT velocimetry.

Doppler OCT methods can provide information similar to OCTA techniques, i.e., about the 3D architecture of active vascular systems [13, 22-24]. However, they can also enable the quantification of parameters characterizing the blood flow in the vessels of various organs, such as the eye [21, 23], or the brain [21, 25-27]. Doppler OCT can therefore provide information that is important for the research and clinical diagnosis of pathologies affecting specific tissues or the entire circulatory system. However, there are a few practical limitations associated with this technique. One of the most often discussed limitations is the range of axial flow velocity values which can be measured. If the flow is too slow, it cannot be distinguished from the noise attributed to the phase stability of various components of the OCT system [19, 28-34]. If the flow is fast enough to introduce a phase change among the complex signals that exceeds  $2\pi$ , a phase wrapping occurs that renders the estimation of the flow velocity obscured [24, 32]. The same effect is encountered in electron holography, magnetic resonance imaging (MRI), radar interferometry, and other interferometric techniques [35-38]. If the flow is too fast, i.e., much faster than the imaging speed of the OCT system, interference fringe wash-out occurs [32, 39-41], and the flow cannot be detected. However, the severity of this effect depends on the degree of averaging of the interference fringes. In practice, it is prominent in the spectral-domain OCT systems and often negligible in the swept-source OCT systems.

Since the phase wrapping problem is commonly encountered in various imaging and detection techniques, several data analyses methods have been developed to solve it [38]. The simplest algorithm adds or subtracts  $2\pi$  whenever the phase difference between consecutive phase values exceed  $\pi$ . Calculations of phase differences directly make this algorithm highly sensitive to noise and unpractical for use in most real life applications. More sophisticated algorithms were proposed by Goldstein [35] and Itoh [42]. These methods search for phase discontinuities by calculating phase gradients either directly or with use of Laplace operators, or by comparing phase distributions at different wavelengths. Therefore, these algorithms require numerous, time consuming calculations. To improve the efficiency of the computations, a fast phase unwrapping (FPU) method was developed by Schofield et al. [43]. The calculation of the phase derivatives with Laplace operators was replaced by Fourier transformations. This method has also been used in MRI for quantitative magnetic susceptibility mapping (QSM) [44], MRI venography [45], MRI flow estimation methods [46], magnetic resonance elastography [47], electron holography [48], and digital holographic microscopy [49].

The main reason for the failure of the phase unwrapping methods is attributed to the low signal-to-noise ratio (SNR) of reconstructed phase images. A phase unwrapping method for Doppler OCT must meet additional requirements, e.g., it must work in low SNR cases, and must also be insensitive to spatial variations of the SNR, including variations in depth (sensitivity roll-off), across the vessels (interference fringe wash-out at increasing flow velocities), or across the imaged pathology (weak OCT signal due to developing pathology). This method should also work in the presence of speckle noise and preferably operate in real time. To the best of our knowledge, to-this-date, the only methods that have been used for phase unwrapping in OCT are synthetic wavelength phase unwrapping [50] and various phase gradient analyses methods [51-53].

In this study, we have adapted the fast phase unwrapping (FPU) algorithm for spectral-domain Doppler OCT imaging, and demonstrate its applicability in data obtained with the joint spectral and time domain OCT (STdOCT) method [12]. We present the FPU method in a unified notation for multidimensional signals and propose a methodology to improve the calculation speed. The algorithm in the presented form has three properties that make it attractive for the OCT data processing. First, it uses the basic properties of Fourier transformations and postulates no assumptions on the input signal. Secondly, the method can be easily applied to either 2D or 3D data analyses. Lastly, it can be applied directly to OCT complex data without the need to extract the phase of the signal before its input to

the algorithm. We compare the phase unwrapping performances of the FPU algorithm following its applications in numerical simulations and in data obtained from Doppler OCT or STdOCT imaging of a flow phantom which used a milk solution as the fluid flowing through a glass capillary. We demonstrate the applicability of the 2D and 3D FPU for Doppler OCT imaging of the human retina *in vivo*. We finally introduce a method to estimate the performance of the algorithms directly from the wrapped phases.

## 2. Methods

### 2.1 Fast phase unwrapping

The common observation in phase unwrapping methods is that the phase has to be corrected when an abrupt change occurs in the analyzed data (e.g., wrapping over a  $2\pi$  range). One of the strategies used to correct the phase wraps is to calculate the phase derivatives and then compute the integral of the result. This leads to the estimation of the unwrapped phase, as will be explained in detail in a subsequent section. Depending on the data dimensionality, one, two, or three partial spatial derivatives have to be calculated. In the approach presented by Schofield et al. [43], a two-dimensional (2D) phase derivative calculation was performed using 2D Laplace operators. The key observation in this popular algorithm was that the use of Fourier transformations simplifies and speeds up the computations. Therefore, the name fast phase unwrapping (FPU) was used. Herein, we outline the FPU algorithm for data with an arbitrary number of spatial dimensions before we introduce the optimizations in the next section. The dataflow in the algorithm is depicted in Fig. 1.

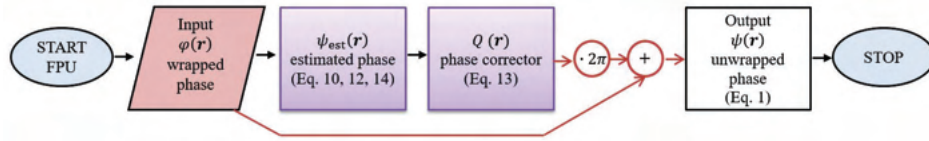


Fig. 1. Graphical representation of the data flow in the fast phase unwrapping (FPU) algorithm. The wrapped phase distribution,  $\varphi(\mathbf{r})$ , is the input data. It is used to calculate the phase estimate  $\psi_{est}(\mathbf{r})$ . The phase correcting function  $Q(\mathbf{r})$  is computed as the difference between the phase estimate and the input phase scaled by  $2\pi$  and rounded to the nearest integer numbers, i.e., it is an integer map of  $2\pi$  phase wraps. The phase wrap map is multiplied by  $2\pi$  and added to the input phase to yield the output unwrapped phase distribution  $\psi(\mathbf{r})$ .

If the spatial phase distribution  $\varphi(\mathbf{r})$  in the acquired data has phase wraps, a correcting function  $Q(\mathbf{r})$  needs to be identified to obtain the unwrapped phase distribution  $\psi(\mathbf{r})$ :

$$\psi(\mathbf{r}) = \varphi(\mathbf{r}) + 2\pi \cdot Q(\mathbf{r}), \quad (1)$$

where  $\mathbf{r}$  denotes the spatial coordinates, and  $Q(\mathbf{r})$  is a function used to correct the wrapped phase using an integer number of  $2\pi$  radians. The estimate of  $Q(\mathbf{r})$  can be calculated as,

$$Q'(\mathbf{r}) = (2\pi)^{-1} (\psi_{est}(\mathbf{r}) - \varphi(\mathbf{r})). \quad (2)$$

$Q'(\mathbf{r})$  is a function of real numbers (can be fractional, positive, and negative). Accordingly,  $\psi_{est}(\mathbf{r})$  is the unwrapped phase estimate which should be identified using only wrapped phase information. This can be done by integrating the derivatives of the phase, and in practice, by applying the Laplace operator  $\nabla^2$  and its inverse  $\nabla^{-2}$ :

$$Q'(\mathbf{r}) = (2\pi)^{-1} \nabla^{-2} (\nabla^2 \psi_{est}(\mathbf{r}) - \nabla^2 \varphi(\mathbf{r})). \quad (3)$$

Schofield proposed to solve this equation for  $\nabla^2 \psi_{est}(\mathbf{r})$  by defining a function  $P(\mathbf{r})$  such that

$$P(\mathbf{r}) = \exp(j\psi_{est}(\mathbf{r})) = \exp(j\varphi(\mathbf{r})), \quad (4)$$

where  $j$  is the imaginary unit. This function has a key property in that it has the same values for wrapped and unwrapped phase, i.e., it is insensitive to phase wraps. The Laplacian of the  $P(\mathbf{r})$  function can be expressed as,

$$\nabla^2 P(\mathbf{r}) = \nabla(P(\mathbf{r})j\nabla\psi_{est}(\mathbf{r})) = -P(\mathbf{r})(\nabla\psi_{est}(\mathbf{r}))^2 + jP(\mathbf{r})\nabla^2\psi_{est}(\mathbf{r}), \quad (5)$$

which can be used to find  $\nabla^2\psi_{est}(\mathbf{r})$ :

$$\nabla^2\psi_{est}(\mathbf{r}) = \text{Im}\{P(\mathbf{r})^{-1}\nabla^2 P(\mathbf{r})\}. \quad (6)$$

In the above formula, the Laplacian of the unwrapped phase distribution is expressed with the use of function  $P(\mathbf{r})$  which can be obtained from the known (measured) wrapped phase distribution. In the original approach, Schofield et al. [43] used Eq. 4 and Euler's formula to derive the Laplacian of the unwrapped phase,

$$\begin{aligned} \nabla^2\psi_{est}(\mathbf{r}) &= \text{Im}\{\exp(-j\varphi(\mathbf{r}))\nabla^2\exp(j\varphi(\mathbf{r}))\} = \\ &= \cos\varphi(\mathbf{r})\nabla^2\sin\varphi(\mathbf{r}) - \sin\varphi(\mathbf{r})\nabla^2\cos\varphi(\mathbf{r}). \end{aligned} \quad (7)$$

Application of the inverse Laplace operator to both sides of this equation leads to an expression for the unwrapped phase estimate,

$$\psi_{est}(\mathbf{r}) = \nabla^{-2}[\cos\varphi(\mathbf{r})\nabla^2\sin\varphi(\mathbf{r})] - \nabla^{-2}[\sin\varphi(\mathbf{r})\nabla^2\cos\varphi(\mathbf{r})]. \quad (8)$$

The Laplace operators of an arbitrary function  $g(\mathbf{r})$  can be calculated using Fourier transformations (FT) [54],

$$\begin{aligned} \nabla^2 g(\mathbf{r}) &= -(2\pi)^2 F^{-1}\{\mathbf{K}^2 F\{g(\mathbf{r})\}\} \\ \nabla^{-2} g(\mathbf{r}) &= -(2\pi)^{-2} F^{-1}\{\mathbf{K}^{-2} F\{g(\mathbf{r})\}\}, \end{aligned} \quad (9)$$

where  $\mathbf{K}$  is Fourier space conjugate of the vector  $\mathbf{r}$ , and  $F\{\}$  and  $F^{-1}\{\}$  are forward and inverse Fourier transformation operators. With this observation, Eq. 8 can be rewritten as,

$$\begin{aligned} \psi_{est}(\mathbf{r}) &= F^{-1}\{\mathbf{K}^{-2} F\{\cos\varphi(\mathbf{r}) \cdot F^{-1}\{\mathbf{K}^2 F\{\sin\varphi(\mathbf{r})\}\}\}\} + \\ &\quad - F^{-1}\{\mathbf{K}^{-2} F\{\sin\varphi(\mathbf{r}) \cdot F^{-1}\{\mathbf{K}^2 F\{\cos\varphi(\mathbf{r})\}\}\}\}. \end{aligned} \quad (10)$$

The above version of Schofield's algorithm (Eq. (10)) requires eight Fourier transformations, and constitutes a computational challenge if the phase distribution is multidimensional. A straightforward improvement in the numerical efficiency arises from the simple rearrangement of Eq. (8), as proposed by Jeught et al. [37]:

$$\psi_{est}(\mathbf{r}) = \nabla^{-2}[\cos\varphi(\mathbf{r})\nabla^2\sin\varphi(\mathbf{r}) - \sin\varphi(\mathbf{r})\nabla^2\cos\varphi(\mathbf{r})], \quad (11)$$

which leads to a simplified version of Eq. (10) with six (instead of eight) Fourier transformations,

$$\psi_{est}(\mathbf{r}) = F^{-1}\{\mathbf{K}^{-2} F\{\cos\varphi(\mathbf{r}) \cdot F^{-1}\{\mathbf{K}^2 F\{\sin\varphi(\mathbf{r})\}\} - \sin\varphi(\mathbf{r}) \cdot F^{-1}\{\mathbf{K}^2 F\{\cos\varphi(\mathbf{r})\}\}\}\}. \quad (12)$$

If the periodic boundary conditions required for the existence of the Fourier transforms are not fulfilled, phase unwrapping errors arise, thus preventing direct use of the estimate  $\psi_{est}(\mathbf{r})$  as the final unwrapped phase distribution. To overcome this issue, Schofield proposed the use of the phase correcting function defined as a difference between unwrapped and wrapped phase distributions, scaled by  $2\pi$ , and rounded to the nearest integer values,

$$Q(\mathbf{r}) = \text{round}\left((2\pi)^{-1}(\psi_{est}(\mathbf{r}) - \varphi(\mathbf{r}))\right) = \text{round}(Q'(\mathbf{r})). \quad (13)$$

$Q(\mathbf{r})$  can be thought of as an integer map of  $2\pi$  phase wraps. The phase correcting function was subsequently used in Eq. (1) to calculate the unwrapped phase.

### 2.2 Optimized FPU algorithm

We propose the modification of the FPU algorithm based on the application of Laplace operators directly on the function  $P(\mathbf{r})$ . This enables the calculation of the unwrapped phase estimator  $\psi_{est}(\mathbf{r})$  from Eq. (6) with complex signals (Eq. (4)) as the input data. The Laplace operators can be computed again using Fourier transformations,

$$\psi_{est}(\mathbf{r}) = F^{-1}\left\{\mathbf{K}^{-2}F\left\{\text{Im}\left\{P(\mathbf{r})^{-1} \cdot F^{-1}\left\{\mathbf{K}^2F\{P(\mathbf{r})\}\right\}\right\}\right\}\right\}. \quad (14)$$

The clear advantage of our approach is a reduction of the number of required Fourier transformations to only four (4FT).

### 2.3 Computational efficiency of FPU algorithms

The proposed calculation scheme can be used for phase unwrapping in any phase-sensitive imaging or detection technique. Equations 10, 12, and 14, can be applied to solve multidimensional phase unwrapping problems. Additionally, the 3D phase distribution can be unwrapped either by the use of the 3D version of the algorithm, or the use of the 2D version applied to each of the 2D data slices. This property makes the approach attractive for Doppler OCT, whereby 3D data is acquired as a sequence of 2D images. Its advantage in Doppler optical coherence tomography is attributed to the readily available complex function  $P(\mathbf{r})$ , as it will be shown in the next sections. The 2D version requires the computation of two-dimensional Fourier transformations (FT), whereas in the 3D option, the three-dimensional FT is calculated. In this work, we have implemented two-dimensional (2D) and three-dimensional (3D) versions of the FPU method. To make the implementation as clear as possible (see Code 1 in Ref. [55]) we decided to use MATLAB but without any optimizations. Therefore, all the Fourier transforms are implemented as complex Fast Fourier Transforms (FFTs). Although full optimization of the algorithms is beyond the scope of this article, we can make one remark on this topic. The previously reported versions of the FPU algorithm [30, 32] calculated Laplacians on real-value input data. This allowed the calculation of Fourier transformations that led to Hermitian functions. This was followed by the multiplication with a real-valued, symmetrical coordinate function. The latter operation does not alter the phase of the transform, and the subsequent inverse Fourier transformation transforms the Hermitian function to a real-valued function. Therefore, each of the Laplacian calculations can be performed with the use of two real Fourier transformations that in principle require half of the operations needed by the complex Fourier transformation [56]. In the previous versions of the algorithm eight or six real Fourier transformations are required. In contrast, in our approach only one of the Laplacians is applied to real-valued function, while the second one is applied to complex-valued function and is calculated with the use of complex Fourier transformation. In Table 1 we compare our proposed 4FT FPU method with previously published approaches.

If we assume that real the FT requires half the calculation time compared to the complex FT of the same size, one can immediately notice that our approach requires exactly the same number of calculations as the version with six real FTs. It has to be noted, however, that in practical applications, the code that implements the real FT requires additional steps to obtain the results, and is in general less efficient than the complex FT. This is true in principle for most data sizes and available FFT libraries [57]. Therefore, it is in general better to use complex FTs instead of real FTs. Accordingly, we believe that our approach has potential in outperforming the previous implementations.



Experiments performed on the same simulated data sets with all three implementations of the FPU algorithms (using [Code 1](#) run on MATLAB R2016b) showed that the obtained results are practically identical. The number of voxels with different values after phase unwrapping was in the range of 0.01% of the total number of voxels in tested data sets. All the results presented in the following sections were obtained with the 4FT version of the algorithm.

**Table 1. Comparison of fast phase unwrapping (FPU) algorithms**

Algorithm	Number of multidimensional Fourier Transforms (FT)	Formula** for the unwrapped phase distribution $\psi_{est}$ with a given wrapped phase $\varphi$
Original FPU [43] – Eq. (10)	Eight real FTs	$\psi_{est} = \nabla^{-2} (\sin \varphi \cdot \nabla^2 \cos \varphi) - \nabla^{-2} (\cos \varphi \cdot \nabla^2 \sin \varphi)$
Re-arranged FPU [37] – Eq. (12)	Six real FTs	$\psi_{est} = \nabla^{-2} (\sin \varphi \cdot \nabla^2 \cos \varphi - \cos \varphi \cdot \nabla^2 \sin \varphi)$
4FT FPU – this article Eq. (14)	Two real FTs + two complex FTs	$\psi_{est} = \nabla^{-2} \text{Im}\{\exp(-j\varphi)\nabla^2 \exp(j\varphi)\}$

\*\*Note that each Laplacian operator,  $\nabla^2$  and  $\nabla^{-2}$ , requires two Fourier transformations. MATLAB implementation of the algorithms (with all FTs calculated as complex FTs for simplicity) can be found in [Code 1](#).

In the case of the 3D version of the algorithm, the computational times for the same dataset ( $256 \times 256 \times 256$  voxels) are  $1.07 \pm 0.03$  s,  $1.77 \pm 0.02$  s, and  $2.30 \pm 0.03$  s, while for the 2D version of the algorithm (applied to all the B-scans) the computation times are  $0.64 \pm 0.06$  s,  $0.93 \pm 0.15$  s, and  $1.20 \pm 0.26$  s, for 4FT, 6FT, and 8FT, respectively. This shows a linear dependence of the calculation time on the number of Fourier transforms for the 2D and 3D versions of the algorithms.

#### 2.4 Doppler OCT

In the Fourier-domain OCT, an image line (A-scan) is obtained via the Fourier transformation of the interference signal collected in the wavelength space and linearized in the wavenumber space. 2D or 3D datasets are obtained by the lateral scanning of the object. Most frequently, a raster scan is performed in which the beam of light is scanned along the x- and y- axes of the Cartesian coordinates system. Fourier transformed FdOCT data can be represented at any given time  $t$  and for any spatial position  $\mathbf{r}$ , using a complex amplitude  $A$ ,

$$A(\mathbf{r}, t) = |A(\mathbf{r}, t)| \exp(j\varphi(\mathbf{r}, t)), \quad (15)$$

where  $\varphi(\mathbf{r}, t)$  is the phase of the interference pattern, and  $|A(\mathbf{r}, t)|^2$  is proportional to the light intensity backscattered at position  $\mathbf{r}$  in the object at time  $t$ . To perform Doppler OCT analyses, a series of A-scans needs to be collected from the same spatial location in the object. In practice, the beam position changes are not greater than half of the beam's spot diameter [26, 29, 30, 58]. The phase differences  $\varphi_D$  between the pairs of A-scans are proportional to the axial component  $v_z$  of the velocity vector  $\mathbf{v}$ ,

$$\varphi_D(\mathbf{r}, \Delta t) = \text{Im}\{\ln(A(\mathbf{r}, t) A^*(\mathbf{r}, t + \Delta t))\} = 2k_z n v_z(\mathbf{r}) \Delta t, \quad (16)$$

where  $k_z$  is the wavenumber, and  $n$  is the index of refraction of the moving medium. The phase wrapping occurs when the time lapse  $\Delta t$  between the acquisition of the A-scan pairs involved in the Doppler OCT analysis exceeds the limit

$$\Delta t_{\max} = \frac{\pi}{2k_z n v_{z, \max}}, \quad (17)$$



where  $v_{z \max}$  is the maximum measurable axial velocity at  $\Delta t_{\max}$ . The measurements of the velocities exceeding the  $v_{z \max}$  value require the implementation of phase unwrapping algorithms.

Given the representation of the FdOCT signal (Eq. (15)) and the representation of the phase differences in Doppler OCT (Eq. (16)), the function  $P(\mathbf{r})$  used to estimate the unwrapped phase in the FPU algorithm (Eq. (14)) can be defined as,

$$P(\mathbf{r}, \Delta t) = \frac{A(\mathbf{r}, t) A^*(\mathbf{r}, t + \Delta t)}{|A(\mathbf{r}, t) A^*(\mathbf{r}, t + \Delta t)|} = \exp(j\varphi_D(\mathbf{r}, \Delta t)). \quad (18)$$

The complex amplitudes  $A$  are obtained directly from the Fourier transformation of the interference spectra acquired in the FdOCT imaging. Our modified FPU algorithm is therefore naturally suited for the unwrapping of the phase differences in Doppler OCT.

### 2.5 Numerical simulations

To perform the tests of the FPU method and generate reference data for Doppler OCT imaging, a numerical model of the FdOCT signal corresponding to the flow of a scattering medium through a cylindrical tube was created. A laminar flow through a vessel with a circular lumen has a parabolic velocity distribution, changing from maximum in the center of the pipe to zero at the capillary walls according to

$$v_z(\mathbf{r}) = \begin{cases} v_{\max} - (v_{\max}/R^2)|\mathbf{r}|^2 & \text{for } |\mathbf{r}| < R \quad (\text{inside the capillary}) \\ 0 & \text{for } |\mathbf{r}| \geq R \quad (\text{outside the capillary}) \end{cases} \quad (19)$$

where  $|\mathbf{r}|$  is the radial distance from the center of the tube,  $R$  is the radius of the tube lumen, and  $v_{\max}$  is the maximum axial velocity in the center of the tube.

In the simulation, the phase differences ( $\varphi_D$ ) were computed from the spatial velocity distribution with a given  $v_{\max}$  according to Eq. (17). The noise was simulated as a complex amplitude that changed randomly across the spatial and temporal coordinates according to  $A_n(\mathbf{r}, t) = A_{nRe}(\mathbf{r}, t) + jA_{nIm}(\mathbf{r}, t)$  with a normal ( $N$ ) probability distribution ( $p$ ) of the real ( $A_{nRe}$ ) and imaginary ( $A_{nIm}$ ) parts, where  $p(A_{nRe}) = N(\mu, \sigma)$ , and  $p(A_{nIm}) = N(\mu, \sigma)$ . The mean of the normal distribution is  $\mu = 0$  and the standard deviation  $\sigma$  sets the noise level. Pairs of complex OCT amplitudes at each location  $\mathbf{r}$  separated in time  $\Delta t$  were simulated as sums of the complex signal  $A_s$  and complex noise  $A_n$  according to

$$A(\mathbf{r}, t) = A_s(\mathbf{r}, t) + A_n(\mathbf{r}, t) = |A(\mathbf{r}, t)| \exp[i\varphi(\mathbf{r}, t)] + A_n(\mathbf{r}, t), \quad (20)$$

$$A(\mathbf{r}, t + \Delta t) = A_s(\mathbf{r}, t + \Delta t) + A_n(\mathbf{r}, t + \Delta t) = |A(\mathbf{r}, t)| \exp[i\varphi(\mathbf{r}, t) + i\varphi_D(\mathbf{r}, \Delta t)] + A_n(\mathbf{r}, t + \Delta t). \quad (21)$$

These signals were used to compute  $P(\mathbf{r}, \Delta t)$  according to Eq. (18) and applied in the fast phase unwrapping algorithm.

### 2.6 Measures of error

In our experiments we have analyzed the performance of the FPU algorithms depending on the noise level in the input data. To provide a measure of the noise, we use a circular standard deviation of the phase distribution  $\sigma_{circ}$  [59] according to,

$$\sigma_{circ}(\varphi(\mathbf{r}, t)) = \sqrt{2 \ln \left( 1 / \left| \sum_{\mathbf{r} \in S} p(\varphi(\mathbf{r}, t)) \exp(i\varphi(\mathbf{r}, t)) \right| \right)}, \quad (22)$$

where the sum spans the spatial coordinates  $\mathbf{r}$  in the area  $S$  where  $\sigma_{circ}$  is calculated, and  $p(\varphi)$  is a probability density function which we have approximated with the histogram of the phase

distribution. The key property of  $\sigma_{circ}$  is its independence with respect to the phase wraps. Therefore, it can be used as a measure of phase variability of the wrapped input data. Care must be taken when choosing the area  $S$  to ensure that the variability of the phase is not dominated by phase gradients. In other words, Eq. (22) must be calculated within a range in which the velocity does not vary. Since the value of  $\sigma_{circ}$  goes to infinity when the phase distribution approaches a uniform distribution, this parameter is sensitive to low-SNR conditions, where none of the methods will correctly unwrap the phase.

We have used the root-mean-square error (*RMSE*) as an error metric of the FPU algorithm outcomes, which measures the deviation of the unwrapped phase  $\psi(\mathbf{r})$  from the reference phase  $\varphi_{D,ref}(\mathbf{r})$ ,

$$RMSE(\psi) = \sqrt{M^{-1} \sum_{\mathbf{r}} (\psi(\mathbf{r}) - \varphi_{D,ref}(\mathbf{r}))^2}, \quad (23)$$

where  $M$  is the number of pixels in the analyzed region-of-interest (ROI) in the dataset. In the absence of phase unwrapping errors, *RMSE* depends only on the noise level in the simulated data, and increases linearly at increasing circular standard deviations of the phase  $\sigma_{circ}(\varphi)$ . Errors in phase unwrapping, i.e., in  $\psi(\mathbf{r})$ , increase the *RMSE*. This leads to deviations from its expected linear dependence on  $\sigma_{circ}(\varphi)$ .

To analyze the influence of noise on the outcomes of the FPU algorithms, we have generated a diagram in which we have plotted the *RMSE* values of the unwrapped phase  $\psi(\mathbf{r})$  as a function of the  $\sigma_{circ}$  values computed from the corresponding wrapped phase  $\varphi(\mathbf{r})$  distribution for a series of simulated data at increasing noise levels, as shown in Fig. 2.

In the simulations, the reference phase  $\varphi_{D,ref}(\mathbf{r})$  is identical to the arbitrarily given, noise-free and phase-wrap-free  $\varphi_D(\mathbf{r})$ . However, in the data obtained from the Doppler OCT imaging experiments ( $\varphi_{exp}$ ), the true phase distribution that is undisturbed by wraps introduced during the OCT detection, is not known. In other words, *RMSE*( $\psi_{exp}$ ) cannot be calculated because of the lack of a reliable reference phase  $\varphi_{D,ref}(\mathbf{r})$ . Therefore, the scatterplot of *RMSE*( $\psi_{exp}$ ) vs.  $\sigma_{circ}(\varphi_{exp})$  cannot be generated. However, the circular standard deviation  $\sigma_{circ}(\varphi_{exp})$  can still be calculated from the experimental data and referred to the simulated *RMSE* scatterplot to predict the outcome of the FPU algorithms for a particular noise level given by the same value of  $\sigma_{circ}(\varphi)$ . Such analysis can provide insights into the possibility of error-free phase unwrapping to enable the selection of the FPU algorithms that should be used for the output data that are least affected by errors.

### 2.7 Spectral-domain OCT experimental setup

Experiments were performed with a spectral domain OCT setup developed in our laboratory [60]. The light was emitted by a superluminescent diode ( $\lambda_c = 860$  nm,  $\Delta\lambda = 135$  nm, Broadlighter T860, Superlum) providing an axial imaging resolution in tissue of  $\sim 3$   $\mu\text{m}$ . The imaging system was designed to provide a lateral resolution 17  $\mu\text{m}$  in the experiments with the flow phantom and 7.3  $\mu\text{m}$  in eye imaging. The repetition times of the CMOS camera used in the spectrometer were adjusted to obtain phase wrapping in the acquired data. The flow phantom contained 0.5 % fat milk, which was pumped through a glass capillary (600  $\mu\text{m}$  lumen) with a syringe pump (neMESYS 290N, CETONI GmbH). The *in vivo* imaging of the human eye was performed in a healthy volunteer (I.G). Informed consent was obtained prior to the imaging in compliance with the Declaration of Helsinki [61]. The details of the imaging protocols are listed in Table 2.

**Table 2. Imaging protocols applied for the experiments with the use of the flow phantom and human eye.**

	Flow phantom	Human eye
A-scans $\times$ B-scans	500 $\times$ 800	600 $\times$ 700
Transverse scan range (x, y)	1.6 $\times$ 0.9 mm	0.9 $\times$ 0.9 mm
Camera repetition time ( $\Delta t_{\max}$ in Eq. (16))	10 $\mu$ s (20 $\mu$ s)	30 $\mu$ s
$v_{\max}$ (Eq. (17))	21.5 mm/s (10.75 mm/s)	7.2 mm/s

For the Doppler OCT computations we have used joint spectral and time domain OCT [5] in the fast flow detection regime, i.e., the flow velocity was calculated among groups of adjacent A-scans. To calculate flow based on the imaging of the human eye we have used groups of four A-scans. In the imaging of the flow phantom we have used groups of seven A-scans.

### 3. Results

#### 3.1 Simulation of Doppler OCT in a cylindrical tube

We have simulated 3D Doppler OCT data of laminar flow in a cylindrical tube with the procedure described in Section 2.4. The time interval  $\Delta t_{\max}$  and flow velocity were chosen to generate one phase wrap. One hundred different values of standard deviations  $\sigma$  of the normal probability distribution  $N(\mu=0, \sigma)$  were used to simulate increasing noise levels. One hundred datasets were generated at each noise level. The 2D and 3D 4FT FPU algorithms were executed in all the simulated datasets. The *RMSE* values of the unwrapped phase distributions  $\psi(\mathbf{r})$  were calculated and plotted against the circular standard deviation  $\sigma_{\text{circ}}$  which was computed from the phase-wrapped input data  $\varphi(\mathbf{r})$ , as shown in Fig. 2(a). These metric pairs were calculated in the ROI located in the center of the simulated cylindrical tube. The size of the ROI was selected to include the largest possible flow area with no phase wraps. Herein, we have arbitrarily selected a rectangular window and manually placed it in the center of the tube. However, other shapes of ROIs can be considered or even automatically determined. Regardless of the method of ROI selection, it should be kept in mind that it is used to calculate the local standard deviation of the phase distribution characteristic of the blood flow in the analyzed vessel. If the ROI area is too small, then the  $\sigma_{\text{circ}}$  values will exhibit increased dispersion due to noise. If the ROI area is too large, the phase distribution will no longer be characteristic of the local flow. Instead, it may attain all the values within the  $(-\pi, +\pi)$  range and rapidly increase. In the limit case of pure phase noise, when the phase distribution in the ROI includes with equal probability values form  $(-\pi, +\pi)$  range the value of  $\sigma_{\text{circ}}$  will be infinite.

For the phase-wrap-free input data (the simulated phase distribution with increasing noise but with no phase wraps), the dependence between the *RMSE* and  $\sigma_{\text{circ}}$  is linear (blue line in Fig. 2(a)). Their values increase proportionally at increasing noise levels. This idealized case serves as a reference for the analysis of more realistic scenarios in which the existing phase wraps have to be removed in the presence of noise. For low-noise levels (small  $\sigma_{\text{circ}}$  values), the 2D and 3D versions of the 4FT FPU method yield correct unwrapped phase distributions. Example images obtained with  $\sigma_{\text{circ}}=0.69\text{--}1.04$  are shown in Fig. 2(b). The plots of *RMSE* ( $\psi$ ) vs.  $\sigma_{\text{circ}}$  ( $\varphi$ ) follow the reference line, i.e., the *RMSE* ( $\psi$ ) is only affected by noise. At increasing noise levels, phase unwrapping errors begin to emerge in the case of the 2D 4F FPU algorithm. Patches of incorrect phase values appear within and outside the images of the tube. Their numbers and total areas increase at increasing  $\sigma_{\text{circ}}$  values. As a consequence, the *RMSE* ( $\psi$ ) vs.  $\sigma_{\text{circ}}$  ( $\varphi$ ) plot deviates considerably from the reference line. The 3D 4FT FPU method produces phase unwrapping errors at considerably higher noise levels. The *RMSE* ( $\psi$ ) vs.  $\sigma_{\text{circ}}$  ( $\varphi$ ) plot deviates from the reference line at higher  $\sigma_{\text{circ}}$  values. The 3D version of the algorithm is therefore more immune to noise compared to the 2D variant. It enables reliable phase unwrapping at higher noise levels. The standard deviation of the *RMSE*

values, which is a measure of the repeatability of the outcomes of the algorithm, is considerably smaller in the case of the 3D 4FT FPU (dashed lines in Fig. 2(a)). We postulate that this is caused by the additional number of data from the third dimension which allows more precise derivatives calculations in the presence of noise.

It has to be noted that we did not threshold the Doppler OCT images (based on intensity) as it is commonly done to reject the phase noise from the areas with no OCT signal, neither in the simulated nor in the experimental data. This was because our intention was to demonstrate the influence of the FPU methods on all the components of the Doppler OCT image, including the detected flow, and the stationary parts of the object and noise (where there was no signal from the object).

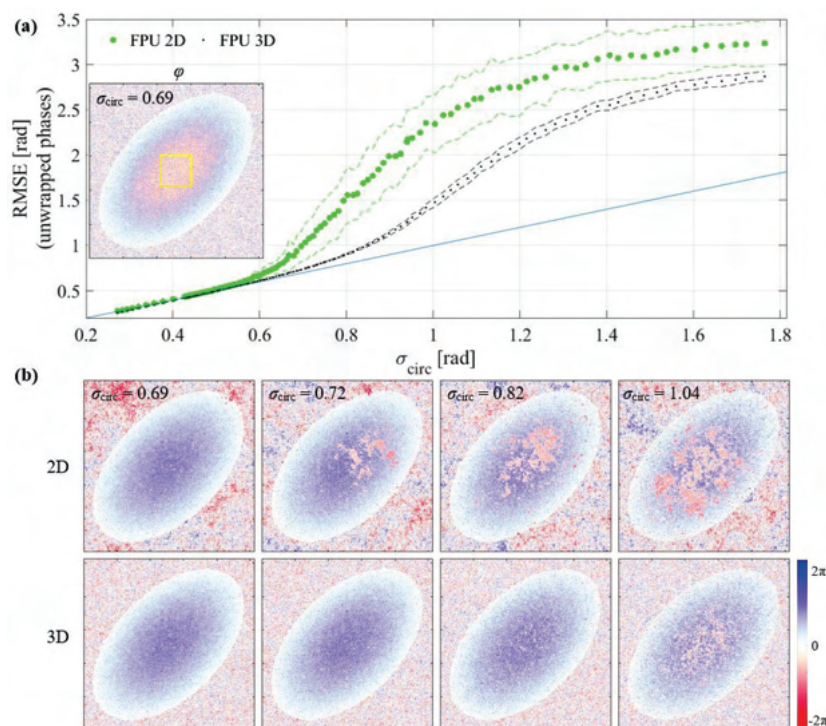


Fig. 2. Result from the applications of 2D and 3D fast phase unwrapping in a set of simulated 3D Doppler OCT data at increasing noise levels. (a) A plot of phase unwrapping error metrics ( $RMSE(\psi)$ ) vs. phase noise metrics ( $\sigma_{circ}(\varphi)$ ). Dots represent mean  $RMSE(\psi)$  values computed from data sets comprising 100 data points each. Dashed lines indicate the standard deviations of the mean  $RMSE$  [2D FPU algorithm (green) and 3D FPU algorithm (black) outcomes]. The blue plot shows a linear dependence of the  $RMSE(\psi)$  on  $\sigma_{circ}(\varphi)$  in the absence of phase unwrapping errors in  $\psi(\mathbf{r})$ , i.e.  $RMSE(\psi)$  is only affected by the noise level. The deviations of the 2D and 3D FPU  $RMSE$  plots from this reference line indicate an increasing probability of phase unwrapping errors in  $\psi(\mathbf{r})$ . The inset presents an example of phase-wrapped input data  $\varphi(\mathbf{r})$ . Yellow rectangle denote the region-of-interest used to calculate  $\sigma_{circ}$ . (b) Example cross-sectional images of the unwrapped phase  $\psi(\mathbf{r})$  extracted from four selected 3D data sets. The values of the circular standard deviation  $\sigma_{circ}(\varphi)$  in the input data are listed in the top left corners. The top row of images shows the results of the 2D FPU method, and the bottom row demonstrates the outcomes of the 3D FPU algorithm. The Doppler OCT images were intentionally not thresholded for noise elimination to demonstrate the influences of the 4FT FPU algorithms on the noise areas. The results of the algorithms for all the data points in the plots on the top are presented in Visualization 1.



Similar simulations were performed to explore the performance of the algorithms in the case of multiple wraps in the simulated Doppler OCT data. The results are presented in Fig. 3(a-b), with an example of unwrapped phase image presented in Fig. 3(c). It can be observed that an increasing number of wrapping errors appear following unwrapping at lower  $\sigma_{circ}$  values compared to the case of single wraps, as shown in Fig. 2(a). Once again, the 3D 4FT FPU algorithm performs better at lower  $\sigma_{circ}$  values compared to 2D 4FT FPU.

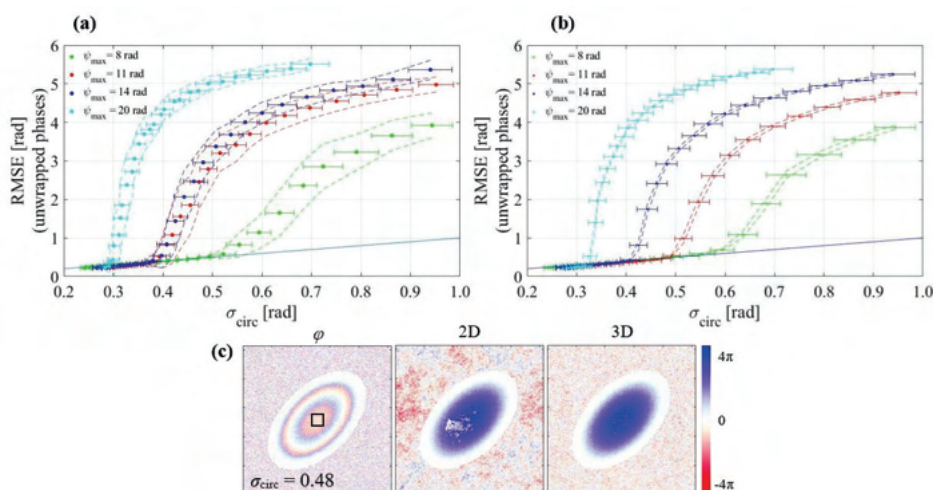


Fig. 3. Phase unwrapping using the 4FT FPU algorithm for multiple phase wraps in four sets of data at different maximum values of unwrapped phases  $\psi_{max}$ . (a, b) Plots of phase unwrapping error metric ( $RMSE(\psi)$ ) as a function of phase noise metric ( $\sigma_{circ}(\phi)$ ) for 3D Doppler OCT data simulated at increasing noise levels. (a) 2D 4FT FPU and (b) 3D 4FT FPU. Dots represent the mean  $RMSE(\psi)$  values computed from data sets comprising 100 data points each. Dashed lines indicate the standard deviations of the mean  $RMSE$ . Colors represent different maximum values of unwrapped phases  $\psi_{max}$ . The blue solid line shows a linear dependence of the  $RMSE(\psi)$  on  $\sigma_{circ}(\phi)$  in the absence of phase unwrapping errors in  $\psi(\mathbf{r})$ , i.e.,  $RMSE(\psi)$  is only affected by the noise level. The deviation of the 2D and 3D FPU  $RMSE$  plots from this reference line indicates increasing probability of phase unwrapping errors in  $\psi(\mathbf{r})$ . As the number of phase wraps increases, the sensitivities of the algorithms to noise also increase. (c) An example of phase-wrapped input data  $\phi(\mathbf{r})$  for  $\sigma_{circ} = 0.48$  rad. 2D: Phase unwrapped using 2D 4FT FPU, and 3D: phase unwrapped using 3D 4FT FPU. Black rectangle denote the region-of-interest used to calculate  $\sigma_{circ}$ .

### 3.2 Doppler OCT imaging of a flow phantom

The OCT experiments with a flow phantom were performed with the imaging parameters listed in Table 2 with  $\Delta t_{max}$  equal to 10  $\mu$ s. The value of  $v_{zmax}$  was selected to provide one phase wrap in the Doppler OCT data. In Fig. 4(b), we present OCT and Doppler OCT images of the glass tube with 0.5 % fat milk as the circulating fluid. The tube was tilted along the Z-axis to ensure a nonzero axial component of the flow velocity vector. As a result, the image appears at increasing depths in subsequent B-scans. Given that the imaging sensitivity of the spectral-domain OCT system exhibits an inherent decay as a function of depth, the signal-to-noise ratio decreases along the Z-axis. We have exploited this property in the analyses of the performances of the 2D and 3D 4FT FPU algorithms. Phase unwrapping was performed in the images of the glass tube cross-sections at increasing depth positions, i.e., at decreasing SNR values. Consequently, the circular standard deviation  $\sigma_{circ}$ , which we calculated in the center of the tube, increases in subsequent images, as illustrated by the yellow rectangles in Fig. 4(b). The results are similar to the simulation outcomes. Phase unwrapping errors become evident as  $\sigma_{circ}$  increases, first in the 2D version of the algorithm and in the 3D

variant, at larger  $\sigma_{circ}$ . Thus, the experiment confirms higher immunity to noise in the case of the 3D 4FT FPU algorithm.

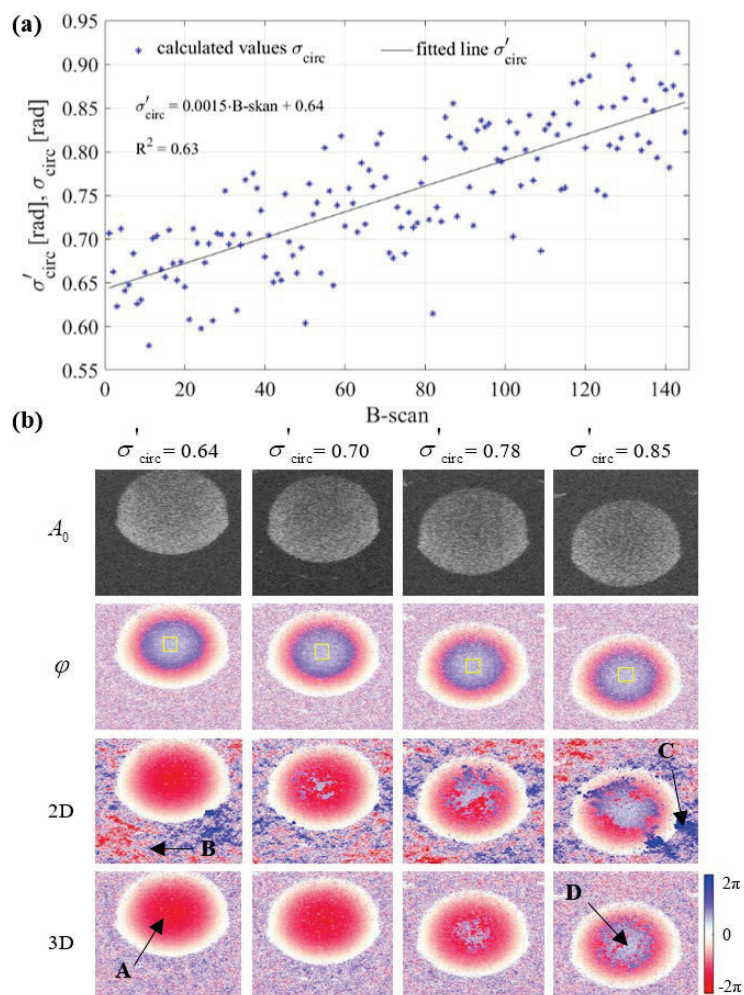


Fig. 4. Phase unwrapping in the flow phantom. (a) Plot of the circular standard deviation values ( $\sigma_{circ}$ ) in subsequent B-scans. The values were calculated based on the regions-of-interest indicated by the yellow rectangles in the wrapped phase images in (b); black line: linear fit to the data points. (b)  $A_0$ : cross-sectional structural OCT images of the glass tube with milk as the circulating fluid at four locations in the 3D data set;  $\varphi$ : wrapped phase; 2D: phase unwrapped with the 2D 4FT FPU method, arrows B and C indicate the phase unwrapping artefacts introduced in the areas of noise. 3D: outcomes of the 3D 4FT FPU method, arrow A: error-free phase unwrapping of the flow, arrow D: erroneous phase unwrapping (phase has remained wrapped). The colors in the images represent Doppler OCT phase values (red: blood flow direction against the incoming beam of light, and blue: blood flow along the light propagation direction). Increasing color intensities indicate increasing axial flow velocity values as indicated by the color bar. The thresholding of the Doppler OCT images to remove the noise was intentionally avoided to demonstrate how the 4FT FPU algorithms influenced the noise areas. Yellow rectangle denote the region-of-interest used to calculate  $\sigma_{circ}$ . A movie showing all the frames from the data set is presented in [Visualization 2](#).

The plot of  $RMSE(\psi_{exp})$  vs.  $\sigma_{circ}(\varphi_{exp})$  cannot be constructed using the experimental data because the phase distribution that is undisturbed by the wraps that were introduced by the OCT detection is not known. Therefore,  $RMSE(\psi_{exp})$  cannot be reliably calculated. However, we can relate the  $\sigma_{circ}(\varphi_{exp})$  values obtained in the experiments with the use of the flow phantom to the circular standard deviations, and to the  $RMSE$  values estimated based on simulations. Fig. 4(a) shows increasing  $\sigma_{circ}(\varphi_{exp})$  values in subsequent B-scans. The ROI position was approximated by a line that goes from the center of the capillary on the first B-scan in the data set to the last center on the last one. Because a single dataset was used, the dispersion of the data points is high. Therefore, we fitted the linear function  $\sigma'_{circ}(\varphi_{exp})$  to the data points and related in this way the mean values of the circular standard deviation to the simulation results.

Both algorithms yield phase unwrapping errors for lower values of  $\sigma'_{circ}(\varphi_{exp})$  compared to simulations. This may be caused by the simplified noise model used in the simulations. This model does not take into account the few effects present in the experimental data. For example, the reductions of the SNR value owing to the interference signal washout caused by flow, or owing to depth, result in  $\sigma_{circ}$  variations across each B-scan. Nevertheless, the results show that the calculations of  $\sigma'_{circ}(\varphi_{exp})$  in the wrapped Doppler OCT image allow us to predict whether a given version of the algorithm can efficiently unwrap the phase.

To validate whether the 4FT FPU method is able to unwrap multiple phase wraps from experimental data, we have performed OCT experiments, see Fig. 5(a). The imaging parameters listed in Table 2 with  $\Delta t_{max}$  being equal to 20  $\mu$ s. Herein, the value of  $v_{zmax}$  was set to give maximal phase value of approximately 11 rad to generate two phase wraps in the Doppler OCT data as visible in Fig. 5(b). The  $\sigma_{circ}$  calculated from the center of the capillary was equal to 0.45. The results of phase unwrapping are presented in Fig. 5(c,d), whereby the 2D 4FT FPU algorithm results in an increased number of erroneously unwrapped voxels compared to the 3D 4FT FPU algorithm. This result is in agreement with our predictions based on the analysis of the  $RMSE(\psi_{exp})$  vs.  $\sigma_{circ}(\varphi_{exp})$  plots presented in Fig. 3(a, b).

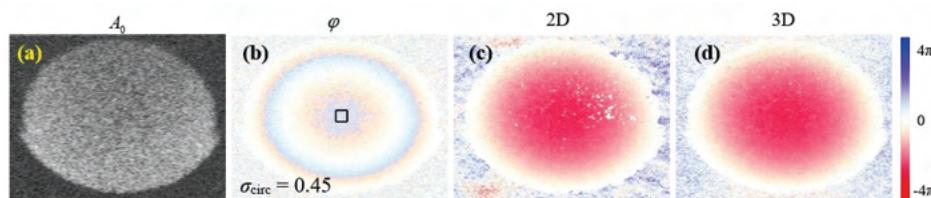


Fig. 5. Comparison of 2D and 3D 4FT FPU methods in the imaging of the flow phantom with the use of multiple phase wraps. (a) Cross-sectional structural OCT image of the glass tube with milk as the circulating fluid. (b) Doppler OCT image with multiple phase wraps within the capillary lumen. Black rectangle denote the region-of-interest used to calculate  $\sigma_{circ}$ . (c) Outcome of the 2D 4FT FPU method. (d) Results of the 3D 4FT FPU method.

### 3.3 Doppler OCT imaging of the human eye in vivo

The imaging of the human volunteer eye *in vivo* was performed in regions within the vicinity of the optic nerve head where a) phase wrapping is most likely to occur owing to the presence of large vessels, and b) fast blood flows and increased inclinations relative to the scanning beam of light occur. Two example datasets were acquired at the same location of the eye, as shown in Fig. 6. In Fig. 6(e–h), the eye was intentionally slightly misaligned as compared to the data in Fig. 6(a–d) to decrease the overall imaging sensitivity. The brightness of the structural image is weaker, especially in the left part of the B-scans. The two datasets were acquired at approximately the same location in the eye. The SNR values calculated from



the mean signal amplitude and noise variance for the data within the yellow rectangles in Fig. 6(a) and Fig. 6(e) are equal to 22 dB and 18 dB, respectively.

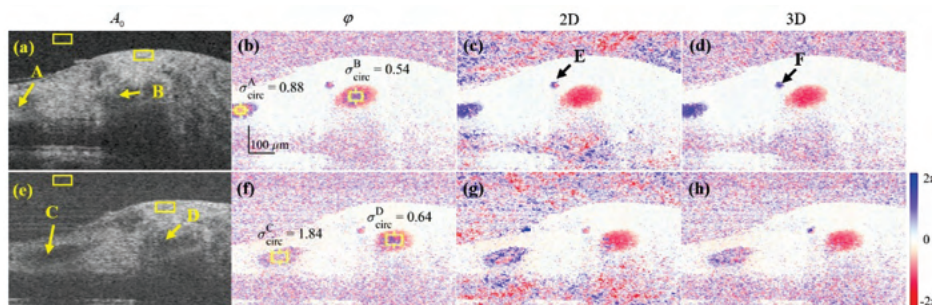


Fig. 6. Comparison of the 2D and 3D 4FT FPU methods in the imaging of the human retina *in vivo* in the vicinity of the head of the optic nerve. (e-h) The eye was intentionally misaligned to decrease the imaging sensitivity as compared to (a-d). (a, e) Structural OCT images of the eye fundus. Arrows A, B, C, and D, indicate large and visible vessels. (b, f) Doppler OCT image with phase wraps within the vessels. (c, g) Results following the use of the 2D 4FT FPU method. (d, h) Results following the use of the 3D 4FT FPU method. Arrows E and F point to small vessels which are not apparent in the structural image but are detected with Doppler OCT. Colors in the images represent the Doppler OCT phase values (red: blood flow direction against the incoming beam of light, blue: flow direction along the light propagation direction). Increasing color intensity indicates increasing axial flow velocity values as indicated by the color bar. The thresholding of the Doppler OCT images to remove the noise was intentionally avoided to demonstrate how the 4FT FPU algorithms influenced the noise areas. Yellow rectangles denote the regions-of-interest used to calculate the signal-to-noise ratio and  $\sigma_{circ}$ . Movies showing all the frames from both datasets are presented in [Visualization 3](#) (top) and [Visualization 4](#) (bottom).

Two large vessels are visible, as indicated by arrows A, C (first vessel) and B, D (second vessel), both with phase wrapping in the Doppler OCT image. A smaller vessel was also revealed as indicated by arrows E and F. In the second vessel, the noise was low ( $\sigma_{circ} = 0.54$  and  $0.64$ ), and the phase was unwrapped with no apparent errors associated with the applications of the 2D and 3D 4FT FPU algorithms. The analysis of the first vessel is more interesting. In Fig. 6(a) the signal strength was high in this area. Therefore, the circular standard deviation of the phase was low ( $\sigma_{circ} = 0.88$ ). Both variants of the algorithm unwrapped the datasets with no apparent errors. However, in Fig. 6(e), the noise was high in this area ( $\sigma_{circ} = 1.84$ ). The 2D 4FT FPU has not only failed but also generated considerable artifacts. The 3D version has only partially removed the phase wraps, thus leaving patches of unwrapped phase in the areas where it has failed. The flow in the small vessel F was correctly unwrapped only by the 3D 4FT FPU algorithm in Fig. 6(d), but was not unwrapped in vessel E by the 2D 4FT FPU algorithm, as observed in Fig. 6(c). Finally, the noise areas in the unwrapped images are not affected by the 3D algorithm, but they show clusters of correlated phase values in the results of the 2D 4FT FPU method. These findings are consistent with the simulations and experiments in the flow phantom.

#### 4. Discussion and conclusions

The fast phase unwrapping algorithm is well suited for applications in Doppler OCT. Its main advantage is the direct access to the complex signal in the cases of Fourier domain OCT techniques. The modification of the FPU algorithm (implemented in the form of the 4FT FPU method) led to the reduction of the number of Fourier transformations from eight – as reported in the original algorithm – to four. The decreased computational burden accelerated the data processing required to generate the phase unwrapped Doppler OCT images. The availability of volumetric data enabled the extension of the algorithm from two to three dimensions. We have demonstrated that the inclusion of additional information on the phase



distribution improved the performance of the 4FT FPU algorithm when it was applied to data with high noise levels. The tests performed on simulated Doppler OCT data obtained from a flow phantom and from the imaging of the human eye *in vivo* indicated that in low-noise data, 2D and 3D 4FT FPU algorithms provided reliable phase unwrapping outcomes. However, at increased noise levels, phase unwrapping errors occurred earlier in the 2D compared to the 3D versions of the algorithm. Additionally, the 3D 4FT FPU method was more immune to noise. However, it required more data processing. Correspondingly, increased computational computer powers were needed for its implementation. The choice between the 2D and 3D versions of the algorithm should thus be dictated by the noise levels of the Doppler OCT data. The measurement of the noise level in the data with phase-wraps required a metric insensitive to these phase ambiguities. We have used a circular standard deviation of phase distribution ( $\sigma_{circ}$ ) as a measure of noise that was insensitive to phase-wraps. We have related this metric to the *RMSE* which was calculated with the use of the unwrapped simulated data. The resultant plots served as reference plots and indicated which  $\sigma_{circ}$  values of the 2D and 3D algorithms were suitable for the phase-sensitive imaging or for the measurements. For  $\sigma_{circ}$  values larger than the noise level of the 2D algorithm, the 3D 4FT FPU method should be used. For noise levels higher than those associated with the 3D algorithm, the 4FT FPU algorithm cannot provide reliable phase unwrapping. The 4FT FPU algorithm applicability plot generated with the simulated data can thus be used to predict the outcomes of the 4FT FPU algorithm based on the data obtained from the experiments.

The analyzed algorithms unwrapped the phase distribution recorded in the data regardless of the origin of the phase wraps. They only required the application of Laplacian operators and adequately high SNR values. As a result, they have been shown to be insensitive to the origins of wraps, and to their spatial and temporal distributions. Phase wraps may appear in the vessels temporarily or locally in the 3D datasets. The temporal occurrence of phase wraps was connected to natural or induced changes in the blood circulation. Accordingly, natural changes can be caused, for example, by the pulsatile blood flow. Changes may also be induced as a part of diagnostic or therapeutic procedures, or as a result of onset of pathology. The local phase wraps may occur owing to vascular tortuosity. Steeper parts of the vessels may exhibit phase wraps, while parts of the same vessels with shallower inclinations relative to the scanning beam of light may be free from phase wraps. Phase can be unwrapped by the 3D phase unwrapping algorithm as long as the phase distribution is correlated in neighboring B-scans. In other words, phase can be unwrapped if the phase distribution does not change abruptly in successive B-scans due to sparse scanning and/or temporal changes in the blood flow when they slower than the acquisition speeds of the B-scans. Typically, scanning in 3D Doppler OCT is performed to ensure B-scan correlations. Additionally, during the typical acquisition of the 3D datasets, ~2–5 cardiac cycles were recorded in more than 300 B-scans. This ensured adequate temporal sampling for the changes in the blood flow along the vessels.

The Doppler OCT images presented in our study were not intensity thresholded to demonstrate the effects of the phase unwrapping in all the areas of interest, including the vessels, stationary tissue, and areas with no OCT signal (noise only). The images can be intensity thresholded to suppress the phase noise. However, thresholding is typically performed subjectively, and care needs to be taken to avoid loss of relevant information. More importantly, intensity thresholding and the resulting noise removal from selected areas of the images prior to the application of the phase unwrapping algorithms should be avoided. Firstly, the thresholding is subjective and may cause loss of information relevant to successful phase unwrapping. Secondly, phase values equal to zero are arbitrarily introduced to the dataset. Both may result in incorrect phase unwrapping and generation of artefacts.

The current overwhelming popularity of the OCT angiography slowed down the advancement of the Doppler OCT technique. However, the possibility of the quantitative analysis of blood flow should not be overlooked in the development of biomedical diagnostic techniques. Limitations often associated with Doppler OCT can be easily bypassed or

eliminated by the application of appropriate experimental and other data analyses methods. In this study, we have introduced a phase unwrapping method which eliminates the phase ambiguity, thus extending the measurable velocity range in the Doppler OCT technique. In addition, we have provided an applicability plot that provides guidance for the use of our method. The 4FT FPU algorithm takes advantage of the specific OCT data acquisition, but can be applied to any phase-sensitive imaging or other measurement technique.

### Funding

Fundacja na rzecz Nauki Polskiej (POIR.04.04.00-00-2070/16-00).

### Acknowledgements

We dedicate this work to our mentor Professor Andrzej Kowalczyk, a creator of the OCT School at the Nicolaus Copernicus University in Torun, Poland, who retired last year from his academic duties.

The project “FreeZEYE Tracker – ultrafast system for image stabilization in biomedical imaging” was conducted within the TEAM TECH Program of the Foundation for Polish Science, co-financed by the European Union under the European Regional Development Fund.

### Disclosures

The authors declare that there are no conflicts of interest related to this article.

### References

1. D. Huang, E. A. Swanson, C. P. Lin, J. S. Schuman, W. G. Stinson, W. Chang, M. R. Hee, T. Flotte, K. Gregory, C. A. Puliafito, and J. G. Fujimoto, “Optical coherence tomography,” *Science* **254**(5035), 1178–1181 (1991).
2. A. F. Fercher, C. K. Hitzenberger, G. Kamp, and S. Y. Elzaiat, “Measurement of Intraocular Distances by Backscattering Spectral Interferometry,” *Opt. Commun.* **117**(1-2), 43–48 (1995).
3. C. L. Chen and R. K. Wang, “Optical coherence tomography based angiography [Invited],” *Biomed. Opt. Express* **8**(2), 1056–1082 (2017).
4. S. Makita, Y. Hong, M. Yamanari, T. Yatagai, and Y. Yasuno, “Optical coherence angiography,” *Opt. Express* **14**(17), 7821–7840 (2006).
5. R. K. Wang, S. L. Jacques, Z. Ma, S. Hurst, S. R. Hanson, and A. Gruber, “Three dimensional optical angiography,” *Opt. Express* **15**(7), 4083–4097 (2007).
6. J. Tokayer, Y. Jia, A. H. Dhalla, and D. Huang, “Blood flow velocity quantification using split-spectrum amplitude-decorrelation angiography with optical coherence tomography,” *Biomed. Opt. Express* **4**(10), 1909–1924 (2013).
7. N. Uribe-Patarroyo, M. Villiger, and B. E. Bouma, “Quantitative technique for robust and noise-tolerant speed measurements based on speckle decorrelation in optical coherence tomography,” *Opt. Express* **22**(20), 24411–24429 (2014).
8. V. J. Srinivasan, S. Sakadzić, I. Gorczynska, S. Ruvinskaya, W. Wu, J. G. Fujimoto, and D. A. Boas, “Quantitative cerebral blood flow with Optical Coherence Tomography,” *Opt. Express* **18**(3), 2477–2494 (2010).
9. V. J. Srinivasan, H. Radhakrishnan, E. H. Lo, E. T. Mandeville, J. Y. Jiang, S. Barry, and A. E. Cable, “OCT methods for capillary velocimetry,” *Biomed. Opt. Express* **3**(3), 612–629 (2012).
10. W. J. Choi, Y. Li, W. Qin, and R. K. Wang, “Cerebral capillary velocimetry based on temporal OCT speckle contrast,” *Biomed. Opt. Express* **7**(12), 4859–4873 (2016).
11. F. Jaillon, S. Makita, and Y. Yasuno, “Variable velocity range imaging of the choroid with dual-beam optical coherence angiography,” *Opt. Express* **20**(1), 385–396 (2012).
12. M. Szkulmowski, A. Szkulmowska, T. Bajraszewski, A. Kowalczyk, and M. Wojtkowski, “Flow velocity estimation using joint Spectral and Time domain Optical Coherence Tomography,” *Opt. Express* **16**(9), 6008–6025 (2008).
13. Y. K. Tao, A. M. Davis, and J. A. Izatt, “Single-pass volumetric bidirectional blood flow imaging spectral domain optical coherence tomography using a modified Hilbert transform,” *Opt. Express* **16**(16), 12350–12361 (2008).
14. J. Walther and E. Koch, “Relation of joint spectral and time domain optical coherence tomography (jSTdOCT) and phase-resolved Doppler OCT,” *Opt. Express* **22**(19), 23129–23146 (2014).
15. A. Bouwens, D. Szlag, M. Szkulmowski, T. Bolmont, M. Wojtkowski, and T. Lasser, “Quantitative lateral and axial flow imaging with optical coherence microscopy and tomography,” *Opt. Express* **21**(15), 17711–17729 (2013).

16. R. A. Leitgeb, R. M. Werkmeister, C. Blatter, and L. Schmetterer, "Doppler optical coherence tomography," *Prog. Retin. Eye Res.* **41**, 26–43 (2014).
17. R. Leitgeb, L. Schmetterer, W. Drexler, A. Fercher, R. Zawadzki, and T. Bajraszewski, "Real-time assessment of retinal blood flow with ultrafast acquisition by color Doppler Fourier domain optical coherence tomography," *Opt. Express* **11**(23), 3116–3121 (2003).
18. B. White, M. Pierce, N. Nassif, B. Cense, B. Park, G. Tearney, B. Bouma, T. Chen, and J. de Boer, "In vivo dynamic human retinal blood flow imaging using ultra-high-speed spectral domain optical coherence tomography," *Opt. Express* **11**(25), 3490–3497 (2003).
19. B. Vakoc, S. Yun, J. de Boer, G. Tearney, and B. Bouma, "Phase-resolved optical frequency domain imaging," *Opt. Express* **13**(14), 5483–5493 (2005).
20. A. Szkulmowska, M. Szkulmowski, A. Kowalczyk, and M. Wojtkowski, "Phase-resolved Doppler optical coherence tomography--limitations and improvements," *Opt. Lett.* **33**(13), 1425–1427 (2008).
21. S. Tozburun, C. Blatter, M. Siddiqui, E. F. J. Meijer, and B. J. Vakoc, "Phase-stable Doppler OCT at 19 MHz using a stretched-pulse mode-locked laser," *Biomed. Opt. Express* **9**(3), 952–961 (2018).
22. R. K. Wang and L. An, "Doppler optical micro-angiography for volumetric imaging of vascular perfusion in vivo," *Opt. Express* **17**(11), 8926–8940 (2009).
23. A. Szkulmowska, M. Szkulmowski, D. Szlag, A. Kowalczyk, and M. Wojtkowski, "Three-dimensional quantitative imaging of retinal and choroidal blood flow velocity using joint Spectral and Time domain Optical Coherence Tomography," *Opt. Express* **17**(13), 10584–10598 (2009).
24. I. Grulkowski, I. Gorczynska, M. Szkulmowski, D. Szlag, A. Szkulmowska, R. A. Leitgeb, A. Kowalczyk, and M. Wojtkowski, "Scanning protocols dedicated to smart velocity ranging in Spectral OCT," *Opt. Express* **17**(26), 23736–23754 (2009).
25. B. J. Vakoc, R. M. Lanning, J. A. Tyrrell, T. P. Padera, L. A. Bartlett, T. Stylianopoulos, L. L. Munn, G. J. Tearney, D. Fukumura, R. K. Jain, and B. E. Bouma, "Three-dimensional microscopy of the tumor microenvironment in vivo using optical frequency domain imaging," *Nat. Med.* **15**(10), 1219–1223 (2009).
26. V. J. Srinivasan, S. Sakadzic, I. Gorczynska, S. Ruvinskaya, W. Wu, J. G. Fujimoto, and D. A. Boas, "Quantitative cerebral blood flow with optical coherence tomography," *Opt. Express* **18**(3), 2477–2494 (2010).
27. A. Bouwens, T. Bolmont, D. Szlag, C. Berclaz, and T. Lasser, "Quantitative cerebral blood flow imaging with extended-focus optical coherence microscopy," *Opt. Lett.* **39**(1), 37–40 (2014).
28. S. Yazdanfar, C. Yang, M. Sarunic, and J. Izatt, "Frequency estimation precision in Doppler optical coherence tomography using the Cramer-Rao lower bound," *Opt. Express* **13**(2), 410–416 (2005).
29. B. Park, M. C. Pierce, B. Cense, S. H. Yun, M. Mujat, G. Tearney, B. Bouma, and J. de Boer, "Real-time fiber-based multi-functional spectral-domain optical coherence tomography at 1.3  $\mu\text{m}$ ," *Opt. Express* **13**(11), 3931–3944 (2005).
30. B. J. Vakoc, G. J. Tearney, and B. E. Bouma, "Statistical properties of phase-decorrelation in phase-resolved Doppler optical coherence tomography," *IEEE Trans. Med. Imaging* **28**(6), 814–821 (2009).
31. E. Koch, J. Walther, and M. Cuevas, "Limits of Fourier domain Doppler-OCT at high velocities," *Sens. Actuators A Phys.* **156**(1), 8–13 (2009).
32. H. C. Hendargo, R. P. McNabb, A. H. Dhalla, N. Shepherd, and J. A. Izatt, "Doppler velocity detection limitations in spectrometer-based versus swept-source optical coherence tomography," *Biomed. Opt. Express* **2**(8), 2175–2188 (2011).
33. A. C. Chan, E. Y. Lam, and V. J. Srinivasan, "Comparison of Kasai autocorrelation and maximum likelihood estimators for Doppler optical coherence tomography," *IEEE Trans. Med. Imaging* **32**(6), 1033–1042 (2013).
34. S. Makita, F. Jaillon, I. Jahan, and Y. Yasuno, "Noise statistics of phase-resolved optical coherence tomography imaging: single-and dual-beam-scan Doppler optical coherence tomography," *Opt. Express* **22**(4), 4830–4848 (2014).
35. R. M. Goldstein, H. A. Zebker, and C. L. Werner, "Satellite radar interferometry: Two-dimensional phase unwrapping," *Radio Sci.* **23**(4), 713–720 (1988).
36. S. Chavez, Q. S. Xiang, and L. An, "Understanding phase maps in MRI: a new outline phase unwrapping method," *IEEE Trans. Med. Imaging* **21**(8), 966–977 (2002).
37. V. S. Jeught, J. Sijbers, and J. J. Dirckx, "Fast Fourier-Based Phase Unwrapping on the Graphics Processing Unit in Real-Time Imaging Applications," *J. Imaging* **1**(1), 31–44 (2015).
38. D. C. Ghiglia and M. D. Pritt, *Two-dimensional phase unwrapping: theory, algorithms, and software* (Wiley, New York, 1998).
39. S. H. Yun, G. Tearney, J. de Boer, and B. Bouma, "Motion artifacts in optical coherence tomography with frequency-domain ranging," *Opt. Express* **12**(13), 2977–2998 (2004).
40. J. Walther, G. Mueller, H. Morawietz, and E. Koch, "Signal power decrease due to fringe washout as an extension of the limited Doppler flow measurement range in spectral domain optical coherence tomography," *J. Biomed. Opt.* **15**(4), 041511 (2010).
41. J. Walther and E. Koch, "Impact of a detector dead time in phase-resolved Doppler analysis using spectral domain optical coherence tomography," *J. Opt. Soc. Am. A* **34**(2), 241–251 (2017).
42. K. Itoh, "Analysis of the phase unwrapping algorithm," *Appl. Opt.* **21**(14), 2470 (1982).
43. M. A. Schofield and Y. Zhu, "Fast phase unwrapping algorithm for interferometric applications," *Opt. Lett.* **28**(14), 1194–1196 (2003).

44. W. Li, A. V. Avram, B. Wu, X. Xiao, and C. Liu, "Integrated Laplacian-based phase unwrapping and background phase removal for quantitative susceptibility mapping," *NMR Biomed.* **27**(2), 219–227 (2014).
45. H. Bagher-Ebadian, Q. Jiang, and J. R. Ewing, "A modified Fourier-based phase unwrapping algorithm with an application to MRI venography," *J. Magn. Reson. Imaging* **27**(3), 649–652 (2008).
46. M. Loecher, E. Schrauben, K. M. Johnson, and O. Wieben, "Phase unwrapping in 4D MR flow with a 4D single-step laplacian algorithm," *J. Magn. Reson. Imaging* **43**(4), 833–842 (2016).
47. E. Barnhill, P. Kennedy, C. L. Johnson, M. Mada, and N. Roberts, "Real-time 4D phase unwrapping applied to magnetic resonance elastography," *Magn. Reson. Med.* **73**(6), 2321–2331 (2015).
48. T. Latychevskaia, P. Formanek, C. T. Koch, and A. Lubk, "Off-axis and inline electron holography: Experimental comparison," *Ultramicroscopy* **110**(5), 472–482 (2010).
49. D. Parshall and M. K. Kim, "Digital holographic microscopy with dual-wavelength phase unwrapping," *Appl. Opt.* **45**(3), 451–459 (2006).
50. H. C. Hendargo, M. Zhao, N. Shepherd, and J. A. Izatt, "Synthetic wavelength based phase unwrapping in spectral domain optical coherence tomography," *Opt. Express* **17**(7), 5039–5051 (2009).
51. Y. Wang, A. A. Fawzi, O. Tan, X. Zhang, and D. Huang, "Flicker-induced changes in retinal blood flow assessed by Doppler optical coherence tomography," *Biomed. Opt. Express* **2**(7), 1852–1860 (2011).
52. Y. Wang, D. Huang, Y. Su, and X. S. Yao, "Two-dimensional phase unwrapping in Doppler Fourier domain optical coherence tomography," *Opt. Express* **24**(23), 26129–26145 (2016).
53. S. Xia, Y. Huang, S. Peng, Y. Wu, and X. Tan, "Robust phase unwrapping for phase images in Fourier domain Doppler optical coherence tomography," *J. Biomed. Opt.* **22**(3), 36014 (2017).
54. T. E. Gureyev and K. A. Nugent, "Phase retrieval with the transport-of-intensity equation. II. Orthogonal series solution for nonuniform illumination," *J. Opt. Soc. Am. A* **13**(8), 1670–1682 (1996).
55. E. Pijewska, I. Gorczynska, and M. Szkulmowski, "Matlab implementation of various forms of the Fast Phase Unwrapping algorithm for 2 and 3 dimensional data," figshare (2019) [retrieved 11 Feb 2019], <https://doi.org/10.6084/m9.figshare.7308413>.
56. H. Sorensen, D. Jones, M. Heideman, and C. Burrus, "Real-valued fast Fourier transform algorithms," *IEEE Trans. Acoust. Speech Signal Process.* **35**(6), 849–863 (1987).
57. M. Frigo and S. G. Johnson, "benchFFT" (2019), accessed on 15–01–2019, <http://www.fftw.org/benchfft/>.
58. N. Uribe-Patarroyo and B. E. Bouma, "Velocity gradients in spatially resolved laser Doppler flowmetry and dynamic light scattering with confocal and coherence gating," *Phys. Rev. E* **94**(2-1), 022604 (2016).
59. N. I. Fisher, *Statistical Analysis of Circular Data* (Cambridge University Press, 1995).
60. D. Ruminski, B. L. Sikorski, D. Bukowska, M. Szkulmowski, K. Krawiec, G. Malukiewicz, L. Bieganowski, and M. Wojtkowski, "OCT angiography by absolute intensity difference applied to normal and diseased human retinas," *Biomed. Opt. Express* **6**(8), 2738–2754 (2015).
61. World Medical Association, "World Medical Association Declaration of Helsinki: ethical principles for medical research involving human subjects," *JAMA* **310**(20), 2191–2194 (2013).





# Blood flow rate estimation in optic disc capillaries and vessels using Doppler optical coherence tomography with 3D fast phase unwrapping

EWELINA PIJEWSKA,<sup>1</sup> MARCIN SYLWESTRZAK,<sup>1</sup>  IWONA GORCZYNSKA,<sup>1</sup> SZYMON TAMBORSKI,<sup>1</sup> MIKOŁAJ A. PAWLAK,<sup>2,3</sup> AND MACIEJ SZKULMOWSKI<sup>1,\*</sup> 

<sup>1</sup>*Institute of Physics, Faculty of Physics, Astronomy and Informatics, Nicolaus Copernicus University in Torun, Grudziądzka 5, 87-100 Torun, Poland*

<sup>2</sup>*Department of Neurology and Cerebrovascular Disorders, Poznan University of Medical Sciences, Fredry 10, 61-701 Poznań, Poland*

<sup>3</sup>*Department of Clinical Genetics, Erasmus MC, PO Box 2040, 3000 CA Rotterdam, The Netherlands*

\**maciej.szkulmowski@fizyka.umk.pl*

**Abstract:** The retinal volumetric flow rate contains useful information not only for ophthalmology but also for the diagnosis of common civilization diseases such as diabetes, Alzheimer's disease, or cerebrovascular diseases. Non-invasive optical methods for quantitative flow assessment, such as Doppler optical coherence tomography (OCT), have certain limitations. One is the phase wrapping that makes simultaneous calculations of the flow in all human retinal vessels impossible due to a very large span of flow velocities. We demonstrate that three-dimensional Doppler OCT combined with three-dimensional four Fourier transform fast phase unwrapping (3D 4FT FPU) allows for the calculation of the volumetric blood flow rate in real-time by the implementation of the algorithms in a graphics processing unit (GPU). The additive character of the flow at the furcations is proven using a microfluidic device with controlled flow rates as well as in the retinal veins bifurcations imaged in the optic disc area of five healthy volunteers. We show values of blood flow rates calculated for retinal capillaries and vessels with diameters in the range of 12–150  $\mu\text{m}$ . The potential of quantitative measurement of retinal blood flow volume includes noninvasive detection of carotid artery stenosis or occlusion, measuring vascular reactivity and evaluation of vessel wall stiffness.

© 2020 Optical Society of America under the terms of the [OSA Open Access Publishing Agreement](#)

## 1. Introduction

Volumetric blood flow (blood flow rate) in the human eye is one of the parameters that characterize blood circulation. It has a wide range of potential applications in the diagnosis of systemic diseases, e.g., diabetes, cerebrovascular disease, hypertensive heart disease, and Alzheimer's disease, with possible links to ocular conditions such as diabetic retinopathy, vessel occlusion, and hypertensive retinopathy [1–6]. Ocular blood flow can also be used to analyze brain perfusion, since the flow to the eye provides direct insight into the internal carotid artery flow dynamics, which provides the majority of the blood flow through the brain. The dynamics of the flow in ocular vessels can be translated into non-invasive flow-based measurement of blood pressure in the cerebrovascular system using a modern computational fluid dynamics approach to signal modeling [7]. Quantitative measurement of blood flow in the brain is currently either expensive, e.g., in the case of magnetic resonance imaging, or invasive, e.g., in the case of computed tomography perfusion. Consequently, this parameter of brain function is rarely considered in routine evaluations. Therefore, fast and noninvasive optical methods for measuring the ocular blood flow rate combined with creative approaches to flow signal processing are required.



Optical coherence tomography (OCT) is a commonly used optical method for 3D structural imaging of the human retina. It has the advantage of providing access to the phase of scattered light, allowing for the detection of small displacements or flows. Therefore, it can be used to provide information about retinal circulatory systems. For example, OCT angiography (OCTA) methods generate images of the blood flow indicating the locations of vessels within the tissues [8–12] and Doppler OCT methods and other OCT velocimetry techniques provide information about blood flow velocity or rate [13,14].

Blood flow rate is defined as the volume of blood flowing through the vessel lumen in a given period of time. There are two approaches to calculating blood flow rates from Doppler OCT data. One requires the knowledge of the mean flow velocity along the vessel and the area of the lumen perpendicular to the blood flow. Multiplication of the two gives the mean flow rate. To determine the volumetric flow the velocity along the vessel has to be measured for each data point across the vessel lumen to account for the change in the velocity from the center to the vessel wall. The flow rate is the integral of the products of velocities and the pixel areas taken over the vessel lumen. The difficulty in this approach lies in the assessment of the vessel orientation in the three-dimensional data set. Several methods have been developed to measure this angle, including segmentation of the vessels in 3D data sets [15], use of circular scan-patterns to determine the local orientation of the vessels [16,17], and two- or three-beam scanning for improved angle measurement accuracy and simultaneous calculation of multiple components of velocity vector [18–20]. The second approach is based on the observation that the flow rate can be calculated from a velocity vector projection in any direction as long as the area of the vessel cross section perpendicular to that direction is also known [21]. In Doppler OCT, the axial projection (Z-component) of the blood flow velocity vector is measured. Multiplication of the Z-component of the velocity and the XY-area of the pixel at which the velocity is measured gives the local flow rate. If the vessel lumen is fully visible in the XY-cross section (C-scan), then the sum of the products of the Z-flow velocity and the XY-pixel area calculated at all the XY-positions in the vessel cross section gives the blood flow rate. In this approach, knowledge of the vessel orientations in the 3D data set is not required. However, segmentation of the vessels in the C-scans is necessary if the flow rate needs to be calculated for each individual vessel. Alternatively, a net flow rate through an entire C-scan of interest can be calculated by summing the products of all the local Z-velocities and XY-pixel areas without the need for vessel segmentation. This approach could be of interest in the analysis of blood flow in the optic nerve head.

The blood flow rate can be calculated from Doppler OCT data provided that the axial flow velocity component can be measured. This may be problematic if the blood flow is too fast compared to the OCT imaging rate. Whenever the axial flow velocity component exceeds the maximum velocity measurable by a given OCT system, the phase change of the complex signal representing the flow exceeds the interval  $(-\pi, \pi)$  and phase-wrapping occurs. The phase wrapping renders characteristic images of flow velocity in the form of concentric rings of opposite flow directions within vessel lumens [22].

Phase unwrapping methods aim to detect the phase wrapping and correct the data such that phase discontinuities (i.e., phase wraps) are removed without the introduction of phase errors. Typically, the correction requires addition or subtraction of multiples of  $2\pi$  when the phase value in a group of neighboring voxels exceeds the  $-\pi$  or  $+\pi$  limit. Many phase unwrapping methods have been introduced to Doppler OCT [23–28]. Recently, we developed a robust and computationally efficient phase unwrapping method, namely four Fourier transform fast phase-unwrapping (4FT FPU) [29], and showed that it is specifically suited for multidimensional Doppler OCT data. Similar method was also presented for 2-dimensional data acquired using stroboscopic interferometry [30].



The focus of our previous article was on the development of algorithms suitable for Fourier-domain OCT imaging [29]. Capability to unwrap the phase was tested in numerical simulation of flow and in a flow phantom for 2-dimensional and 3-dimensional data sets was presented. We have introduced a metric to quantify the phase unwrapping errors and tested the performance of phase unwrapping methods in data with increasing noise level. This analysis enabled us to predict at which phase noise levels the algorithms can be used without introducing errors resulting in incorrect axial flow velocity values. Finally, we have used the phase unwrapping algorithms in Doppler OCT data acquired in the human retina to demonstrate their applicability in calculation of axial blood flow velocity. We have identified the three-dimensional version of the fast phase unwrapping algorithm as better suited for biomedical applications due to its higher immunity to noise than the two-dimensional FPU method.

Although the previous work demonstrated the applicability of the 3D 4FT FPU method to calculate the axial flow velocity in the human retinal vessels, the question still remains whether calculations of volumetric blood flow give reliable results. That is, if they provide correct values of the blood flow on which medical doctors could rely while diagnosing diseases and to what extent they can rely on Doppler OCT measurements. Although it may seem that there is a little difference between calculating the axial flow velocity and volumetric flow rate, there is a considerable difference. Axial component of the flow velocity vector is highly susceptible to variations caused by changing angular orientations of vessels. For example, they may be a result of the anatomy of the vascular system, or alignment of the eye in the OCT device. Because the axial flow velocity does not necessarily reflect only changes in the blood circulation, it is not the best metric for the use in ophthalmic diagnostics. On the other hand, volumetric flow rate, when possible to calculate, is not dependent on the angular orientations of vessels. Although it is not free from possible errors, it is a better choice of metric for ophthalmic applications.

In this article we focus on two questions. First, does the Doppler OCT with the 3D 4FT phase unwrapping method give reasonable values of volumetric blood flow in retinal vessels? Second, can the algorithms be implemented to provide results in real-time or at least within a few minutes after acquiring the data?

Answering the first question isn't an easy task since there is no gold standard to which we could relate our results. That is, there is no scientific consensus as to what are the reference values of blood flow in retinal vessels. Moreover, in the diagnostic practice, medical doctors rarely look for the "ground truths". They relate the results from a specific diagnostic technique or even a specific type of a device to the established norms and pathology classifications. However, only a few papers exist reporting volumetric blood flow values measured with OCT techniques in a limited number of cases [15] [31–35]. Therefore, to answer the first question we have performed two tests, which do not require comparisons with established norms, yet show the reliability of the calculated volumetric flow rate values. In the first test, we check if the additive property of the volumetric flow rate at furcations is fulfilled in the phase-unwrapped Doppler OCT data obtained in a flow phantom (a microfluidic device) and in human retinal vessels (five volunteers). The experiment in the flow phantom also enables us to check if the measured flow values agree with the flow set in the microfluidic pump, thus indicating if phase-unwrapped Doppler OCT generates any offsets in the measured values. In the second test, we measure the blood flow in the human retinal vessels (three volunteers) in a large number of vessels (600) with lumen diameters ranging from 12 to 150  $\mu\text{m}$ . We expect that there should be a well-defined dependence between the vascular lumens diameters and the volumetric blood flow rates [36]. Lack of such dependence would indicate erroneous results of blood flow calculation in the phase-unwrapped Doppler OCT data.

The answer to the second question is important from the perspective of practical clinical applications of the phase-unwrapped Doppler OCT imaging. Efficient and wide-spread use of these methods depends not only on providing reliable results but also on the availability of the



Doppler OCT images and blood flow rate measurement results immediately after the data is acquired in the eyes of visiting patients. To demonstrate that real-time phase-unwrapped Doppler OCT imaging is possible, we have implemented the entire data processing pipeline from basic data processing, through implementation of Doppler OCT methods, to phase unwrapping using graphic processing units (GPU) technology.

## 2. Methods

### 2.1. Materials, subjects, experimental setup, and Doppler OCT imaging methods

Doppler OCT imaging was performed in a flow phantom and in the retinas of five volunteers. The flow phantom was a microfluidic device. A  $300 \times 100 \mu\text{m}$  rectangular microchannel was trifurcated into three  $100 \times 100 \mu\text{m}$  rectangular channels in a polydimethylsiloxane (PDMS) substrate mixed with titanium dioxide ( $\text{TiO}_2$ ) powder, which acted as a light scattering medium. A protein solution consisting of 0.1% cow milk was pumped through the microfluidic device with a syringe pump (neMESYS 290N, CETONI GmbH).

Imaging of the flow phantom was performed with a research-grade spectral-domain optical coherence microscopy (OCM) setup. Light with a center wavelength of 800 nm was emitted by a supercontinuum source (SuperK EXTREME/FIANIUM, NKT). The axial imaging resolution was  $\sim 3 \mu\text{m}$ . The lateral imaging resolution was  $8 \mu\text{m}$ . The A-scan rate was set to 70 kHz by adjusting the repetition time of the camera used in the OCT spectrometer (Basler Sprint spl2048-140km, Basler AG). The imaging protocol (a) is given in Table 1.

**Table 1. Experimental protocols.**

	Microfluidic device (a)	Human eye (b-c)
A-scans $\times$ B-scans $\times$ C-scans	750 $\times$ 300 $\times$ 1024	1024 $\times$ 256 $\times$ 1024
Transverse scan range (x, y)	0.65 $\times$ 0.35 mm	b) 5 $\times$ 5 mm, c) 3 $\times$ 3 mm
Voxel size (x, y, z)	0.9 $\times$ 1.2 $\times$ 1.2 $\mu\text{m}$	b) 4.9 $\times$ 19.5 $\times$ 1.2 $\mu\text{m}$ , c) 2.9 $\times$ 11.7 $\times$ 1.2 $\mu\text{m}$
Lateral imaging resolution	8 $\mu\text{m}$	12 $\mu\text{m}$
Center wavelength	800 nm	830 nm
Axial imaging resolution	3 $\mu\text{m}$	5 $\mu\text{m}$
Camera repetition time $\Delta t_{\text{max}}$	20 $\mu\text{s}$	9.1 $\mu\text{s}$
Maximum velocity $v_{z\text{max}}$	7.5 mm/s	4.2 mm/s

Imaging of the eyes of healthy volunteers was performed in compliance with the Declaration of Helsinki [37] and regulations of the Bioethics Committee of the Nicolaus Copernicus University, Torun, Poland. The fundus of five subjects (age range, 26–40 years) was imaged in the optic nerve head area.

The imaging of volunteers was performed with a commercial spectral-domain OCT device (REVO NX, Optopol Technology, Poland). The light source was a superluminescent diode (center wavelength, 830 nm). The axial imaging resolution in tissue was  $\sim 5 \mu\text{m}$  and the lateral imaging resolution was  $12 \mu\text{m}$ . The A-scan rate was 110 kHz. The imaging protocols (b-c) are given in Table 1.

Doppler OCT imaging in the flow phantom was performed with phase-resolved Doppler OCT method [13] and imaging in the human eyes performed using the joint spectral- and time-domain OCT (STdOCT) method [13]. In Doppler OCT imaging, a series of A-scans is collected from the same spatial location in the object and, in practice, with the change in the beam position between two consecutive OCT spectra acquisitions no larger than half of the beam spot diameter [38,39]. To calculate the blood flow in the human retina, we used groups of four A-scans. The imaging protocols (b-c) are given in Table 1.



## 2.2. Volumetric flow rate calculations

Light back-scattered at moving scatterers, e.g., flowing blood cells, is received by the detector with a frequency shifted by  $\omega_D$  owing to the Doppler effect. For each spatial location in the sample  $\mathbf{r}$ , this shift is proportional to the velocity component parallel to the light beam,  $\omega_D(\mathbf{r}) = 2knv_z(\mathbf{r})$ , where  $k$  is the central wavenumber,  $n$  is the index of refraction of the moving medium, and  $v_z$  is the axial component of the velocity vector  $\mathbf{v}$ . In phase-resolved Doppler OCT (PR-Doppler OCT) imaging, the approximation of the first derivative of the Doppler frequency,  $\varphi_D(\mathbf{r}, \Delta t) = \Delta\omega_D(\mathbf{r})/\Delta t$ , is obtained using the measured phase differences between pairs of A-scans,  $A(\mathbf{r}, t) = |A(\mathbf{r}, t)| \exp(jknv_z(\mathbf{r})t)$ , delayed by  $\Delta t$  [40]:

$$\varphi_D(\mathbf{r}, \Delta t) = \text{Im}\{\ln(A(\mathbf{r}, t)A^*(\mathbf{r}, t + \Delta t))\} = 2knv_z(\mathbf{r})\Delta t. \quad (1)$$

In the STdOCT method, the Doppler frequency  $\omega_D$  is obtained directly by Fourier-transforming groups of A-scans along the time coordinate, which allows for direct use of multiple A-scans to increase the signal-to-noise ratio (SNR) and improve the image quality (Fig. 1) [13].

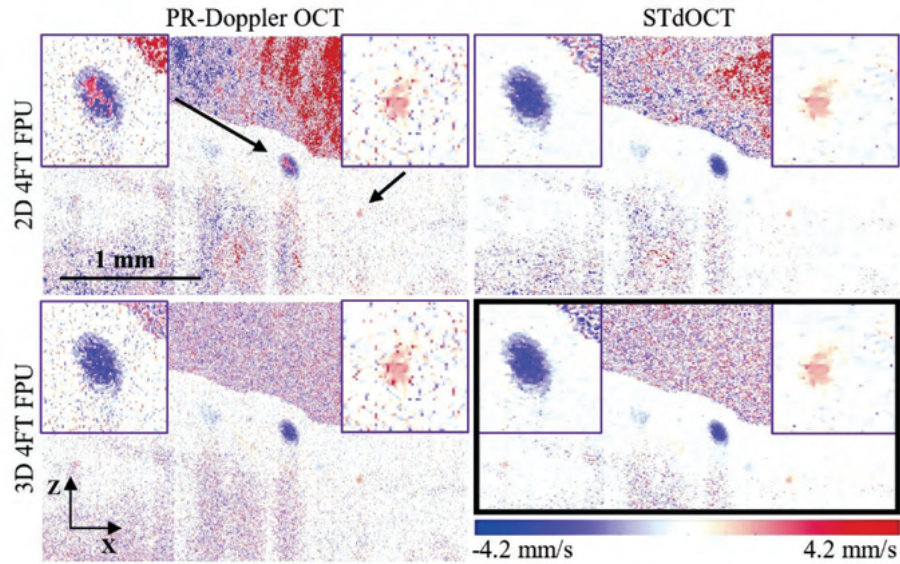


**Fig. 1.** Comparison of B-scans extracted from 3D data processed with the two Doppler OCT methods: phase-resolved (PR) Doppler OCT and joint spectral and time domain OCT (STdOCT). The phase unwrapping was performed with 2D and 3D 4FT FPU. The processing times are listed in Table 2. The insets present zoomed-in vessels. Differences in the noise level (signal-to-noise ratio) and phase-unwrapping outcomes are clearly visible, including the artifacts in the areas with no signal (for the 2D 4FT FPU) and errors in phase unwrapping (phase remained wrapped in one of the vessels in PR-Doppler OCT with 2D 4FT FPU). The black rectangle indicates the result with the best SNR and phase unwrapping outcomes. The colors in the images represent the axial flow velocity values. Blue: flow direction against incoming beam of light; red: along with the light propagation. The increasing color intensity indicates increasing axial flow velocity values as indicated by the color bar.

Knowledge of the Z-component of the flow velocity ( $v_z$ ) and the vessel cross section  $S$  perpendicular to the light beam allows for the calculation of the volumetric flow rate  $Q$  according

**Table 2. Mean computation times and their standard deviations for the implemented Doppler OCT and phase unwrapping algorithms.**

	Microfluidic device (a)		Human eye (b-c)	
A-scans × B-scans × C-scans	750 × 300 × 1024		1024 × 256 × 1024	
A-scan rate	70 kHz		110 kHz	
Data acquisition time <sup>a</sup>	3.3 s		2.7 s	
	GPU computation time	Total processing time <sup>b</sup>	GPU computation time	Total processing time <sup>b</sup>
STdOCT	23 ± 2 s	23 ± 2 s	27 ± 2 s	28 ± 2 s
PR-Doppler OCT	0.40 ± 0.01 s	1.13 ± 0.01	0.50 ± 0.01 s	1.4 ± 0.1 s
2D 4FT FPU	0.63 ± 0.05 s	1.2 ± 0.1 s	0.57 ± 0.06 s	1.3 ± 0.1 s
3D 4FT FPU	0.421 ± 0.002 s	0.9 ± 0.1 s	0.380 ± 0.004 s	1.0 ± 0.1 s

<sup>a</sup>Acquisition time includes all dead times between B-scans.

<sup>b</sup>Processing time includes GPU processing time and all data transfers between PC (host) memory and GPU (device) memory.

to [21]

$$Q = \frac{1}{2kn\Delta t} \sum_{\text{ROI}} \psi(\mathbf{r}) \cdot s, \quad (2)$$

where  $\psi(\mathbf{r})$  is the unwrapped phase difference  $\varphi_D(\mathbf{r}, \Delta t)$ ,  $s$  is the pixel area in the cross section, and ROI is the region of interest for which the flow rate is calculated. In practice, ROI contains the cross section of the vessel lumen perpendicular to the light beam as shown in Fig. 3(a). To obtain  $\psi(\mathbf{r})$ , a phase unwrapping algorithm has to be implemented.

### 2.3. Phase unwrapping

The phase  $\varphi_D(\mathbf{r}, \Delta t)$  measured using the PR-Doppler OCT or STdOCT method is always in the range of  $-\pi$  to  $\pi$ . Phase wrapping occurs when the flow velocity exceeds this limit [22]:

$$v_{z,\text{max}} = \frac{\pi}{2kn\Delta t}. \quad (3)$$

Measurement of velocities exceeding the  $v_{z,\text{max}}$  value requires implementation of numerical phase unwrapping methods. We used our recently developed [29] three-dimensional (3D) fast phase unwrapping (FPU) calculated using four complex Fourier transformations (4FT) (i.e. 3D 4FT FPU). The FPU method calculates the phase correction  $\psi_{\text{est}}$ , in the phase differences distribution  $\varphi$ , which is subsequently used to calculate the unwrapped phase distribution  $\psi(\mathbf{r})$ :

$$\psi_{\text{est}}(\mathbf{r}) = \nabla^{-2} \text{Im}\{\exp(-i\varphi) \nabla^2 \exp(i\varphi)\}, \quad (4)$$

$$\psi(\mathbf{r}) = \varphi(\mathbf{r}) + 2\pi \cdot \text{round}[(\psi_{\text{est}}(\mathbf{r}) - \varphi(\mathbf{r})) \cdot (2\pi)^{-2}]. \quad (5)$$

The Laplace operators  $\nabla^{-2}$  and  $\nabla^2$  are implemented using Fourier transformations [29,30,41].

### 2.4. Implementations of algorithms

We have implemented a processing pipeline consisting of the transformation of OCT spectra into complex A-scans [42,43] followed by one of the two Doppler OCT methods (PR-Doppler OCT [22] or STdOCT [13]), with one of the two versions of the 4FT FPU algorithms [29]. We used the STdOCT method with a window of four A-scans and 128-point Fourier transforms. The 2D and 3D 4FT FPU algorithms were implemented separately and called depending on the dimensionality of the processed data (2D/3D).



The software was developed under the Microsoft Windows 10 operating system. The graphical user interface (GUI) was prepared in LabVIEW 2018. All the processing cores (STdOCT, PR-Doppler OCT, 4FT FPU 2D, and 4FT FPU 3D) were written in C using Microsoft Visual Studio 2017 and compiled into the DLL library. We used a graphics processing unit (GPU) as a data processing accelerator and NVIDIA CUDA compiler 10.1 with the cuFFT library to speed-up the data analysis as described in our previous work [43]. The workstation was equipped with an Intel Core i7-7700K (4.2 GHz) CPU and 32 GB RAM. For data processing, we used NVIDIA GeForce GTX1080 with 8 GB of device memory.

We have measured the computation times of the implemented algorithms: PR-Doppler OCT, STdOCT, 2D 4FT FPU, and 3D 4FT FPU. When unwrapping the 3D data set with 2D 4FT FPU, the algorithm must be used in every B-scan separately. 3D 4FT FPU is called only once to unwrap the phase in the entire 3D data set. When a data processing accelerator is used (as in our system with GPU), there is a need to distinguish between the two processing platforms, i.e., the host and the device. The host is the CPU with RAM and the device consists of the GPU with its on-board memory. The bottleneck of the applications using GPU is the data transfer between the host memory and the device memory. Therefore, we present the computation time on GPU and the total processing time, including the raw OCT data transfer to the GPU memory, the GPU computations, and transfer of the results back to the host memory. Processing with and without data transfer was executed 10 times. The average computation times and standard deviations for protocols (a-c) from Table 1 are listed in Table 2.

### 3. Results

#### 3.1. Comparison of PR-Doppler OCT and STdOCT

We compared the computation times and the axial flow velocity images obtained with PR-Doppler OCT and STdOCT to select the most appropriate method for imaging in the human eye. Figure 1 shows an example B-scan from a 3D data acquired in the human retina using protocol (c) from Table 1 with different combinations of Doppler OCT and 4FT FPU processing techniques. 3D 4FT FPU in combination with STdOCT rendered Doppler OCT images with visibly smaller noise as compared to other combinations and not affected by phase unwrapping artefacts. This observation is in agreement with our previous studies, where we showed that STdOCT offers higher SNR than PR-Doppler OCT [13,44] and, in another study, that 3D 4FT FPU is less likely to generate artifacts than 2D 4FT FPU [29]. It is interesting to relate these observations to the total computation times of the implemented algorithms presented in Table 2. Computations required for phase unwrapping of the entire 3D data sets with both phase unwrapping algorithms take less time than acquisition of the data. When combined with the PR-Doppler OCT, phase-unwrapped Doppler OCT images can be generated in times comparable with the data acquisition. However, computations required in the STdOCT method take half a minute when combined with the 3D 4FT FPU. This suggests possible uses of the two Doppler OCT methods. Real-time images are required during the OCT device alignment procedures, usually performed prior to the acquisition of the data to select the area to be imaged and to optimize the device settings. Typically, a series of 2D data is acquired for this "preview mode" and the images should be of acceptable quality if the highest quality images cannot be generated in real-time. A combination of PR-Doppler OCT and 2D 4FT FPU methods is well suited for this purpose. However, the 3D data acquired to aid the diagnosis of diseases should be processed with methods ensuring the highest signal-to-noise ratio and artifacts-free images. Combination of STdOCT and 3D 4FT FPU meets this requirement while still providing images 30 s after acquiring the 3D data set. Therefore, hereafter, all the results obtained in human eyes are presented for the combination of STdOCT and 3D 4FT FPU.

### 3.2. Flow phantom

The microfluidic device was positioned under the OCT microscope at an angle of  $\sim 45^\circ$ , as schematically illustrated in Fig. 2(a), to introduce a non-zero axial component of the flow velocity and to ensure visibility of the entire channel lumens in the C-scans. Experimental protocol (a) from Table 1 was used. The flow rate of the solution pumped through the microfluidic device was set to three different values, as listed in Table 3, at which a single phase wrap occurred in the Doppler OCT images, as shown in the first column of Fig. 2(b). The solution was injected into the large  $300 \times 100 \mu\text{m}$  channel and the flow then splits into three  $100 \times 100 \mu\text{m}$  channels.

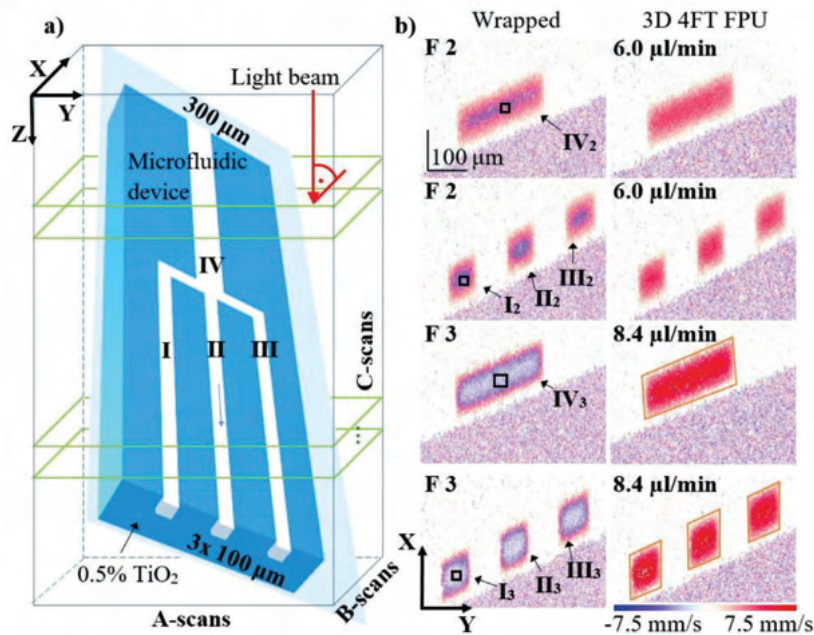


**Fig. 2.** a) Schematic illustration of the flow phantom: a microfluidic device with a protein solution flowing through the trifurcated channels. The light beam propagates from the top. The green rectangles mark sets of  $N = 6$  C-scans before and after trifurcation, which were used to obtain data presented in Table 3. The Roman numerals indicate the channels in the trifurcation. b) STdOCT Doppler C-scans selected from 3D data sets: one pre- and the second post-trifurcation. The two examples show data acquired for different volumetric flow rates, as labelled in the images. First column: wrapped phase. Second column: phase unwrapped with 3D 4FT FPU. The arrows indicate channels (I, II, III, IV), for which the flow rates are listed in Table 3. The noise in the images was intentionally not removed. The orange rectangles indicate the ROIs for volumetric flow rate calculation. The colors in the images represent the axial flow velocity values. Blue: flow direction against incoming beam of light; red: along with the light propagation. The increasing color intensity indicates increasing axial flow velocity values as indicated by the color bar.

The flow rates calculated from the phase-unwrapped data in the regions of interest, marked by orange rectangles in Fig. 2(b), are listed in Table 3. For each flow rate set by the syringe pump (last column of Table 3), six adjacent C-scans were extracted from the data, in which the entire lumens of the channels were visible. The mean flow values were calculated for each channel. The uncertainty of the mean was estimated from t-Student distribution at 0.05 significance level. In a few cases phase unwrapping errors have occurred introducing errors to the calculated values



**Table 3. Mean flow rate values in the flow phantom, in the data unwrapped with 3D 4FT FPU method. The errors were estimated from t-Student distribution at 0.05 significance level.**

<i>F</i>		<i>Channel I</i>	<i>Channel II</i>	<i>Channel III</i>	<i>Channel I + II + III</i>	<i>Channel IV</i>	<i>Pump</i>	
1	$\sigma_{\text{circ}}^a$ [rad]	0.70					0.54	5.4 ± 0.6
	Flow rate [μl/min]	1.87 ± 0.02	1.72 ± 0.06	1.90 ± 0.02	5.50 ± 0.07	5.48 ± 0.08		
2	$\sigma_{\text{circ}}$ [rad]	0.64					0.48	6.0 ± 0.6
	Flow rate [μl/min]	1.92 ± 0.04	1.85 ± 0.04	1.93 ± 0.04	5.70 ± 0.07	5.69 ± 0.07		
3	$\sigma_{\text{circ}}$ [rad]	1.00					1.05	8.4 ± 0.6
	Flow rate [μl/min]	2.75 ± 0.04	2.80 ± 0.06	3.01 ± 0.11	8.58 ± 0.10	8.60 ± 0.02		

<sup>a</sup>Circular standard deviation of the phase distribution defines the noise level of input data [29].

(marked with crosses in Table 3). In the data with no phase unwrapping errors, the flow rates calculated for the large channel (channel IV) are equal to the flow rates set by the pump. This confirms that there are no offsets in the values calculated from the phase-unwrapped Doppler OCT data. As the net flow rate should remain constant, the sums of the flow rates in the trifurcated channels were also calculated. The flow rates calculated for the small channels (I, II, III) sum up to the flow rate in the large channel, except of those with identified phase unwrapping errors. This demonstrates that the phase-unwrapped data allows to reproduce the additive property of the volumetric flow rate.

### 3.3. Flow rates in vessels in the optic disc of the human eye

Doppler OCT imaging of five human volunteers (ID 1 to ID 5) was performed in the optic disc area. Six data sets according to protocol (b) from Table 1 were collected for each subject. Additionally, for subjects ID 1 to ID 3 six data sets according to protocol (c) from Table 1 were collected. Owing to the high blood flow rates and the steep angles between the vessels and the beam of light in this area of the eye, the axial component of the flow velocity vector often exceeds the velocity limit given by Eq. (4), and phase wrapping occurs. The flow rates were calculated in the STdOCT data unwrapped with 3D 4FT FPU method, in the manually fitted elliptical region of interest (ROI) for which we have calculated the flow rate according to Eq. (2). The minor axes of the ellipses were used as estimators of the vessel lumens. The mean values of the flow rates were computed from the six adjacent C-scans. The uncertainty of the mean estimation was calculated from the t-Student distribution at the significance level 0.05.

#### 3.3.1. Vascular bifurcations

We have analyzed blood flow rates in five vascular bifurcations acquired from subjects ID 1 to ID 5 using protocol (b) from Table 1. In each subject we have selected a vascular bifurcation with vessels orientation in the 3D data sets as schematically illustrated in Fig. 3(a). Vessel III splits into two vessels I and II. Doppler OCT C-scans were selected at two different depths as listed in Table 4. Example C-scans proximal and distal to bifurcation are presented in Fig. 3(b). In each of the five subjects six adjacent C-scans pre- and post-bifurcations were selected from which mean values were calculated and their uncertainties estimated from t-Student distribution at 0.05 significance level. Due to the scanning and the tilt of the vessels, branches I, II and III were imaged at different times. To minimize the change of the volumetric flow rate caused by the pulsatile blood flow, the C-scans were selected in such a way that the temporal separation of the sections of vessels I, II and III was less than 20 ms. Phase wrapping occurred in at least one of the branches. After phase-unwrapping, the volumetric flow rates were calculated for each of the branches. The results obtained from all five subjects are presented in Table 4. The additive



property is fulfilled within the standard errors calculated from t-Student distribution at 0.05 significance level.

Having vessels diameters  $d$  and from the elliptical fit we tested whether they fulfill the Murray's law [45], that links vessel diameter proximal to the bifurcation (vessel III) with the distal vessel diameters (vessels I and II) in the following way:  $d_{III}^\alpha = d_I^\alpha + d_{II}^\alpha$ . In the original article  $\alpha = 3$  was found to be optimal value for vascular system that minimizes the power required to maintain and circulate the blood. In another derivation, where mass of the vascular system is minimized,  $\alpha = 3$  was found for laminar flows and  $\alpha = 7/3 = 2.33(3)$  for fully turbulent flows [46]. In both cases the models assumed blood viscosity to be independent on vessel diameter, what is known to be inaccurate. The viscosity of blood depends not only on parameters such as hematocrit, pH, protein content, maturity of the cells (immature are more adhesive) but also depends on vessel diameter. It has the smallest value in the capillaries of diameter around 6-10  $\mu\text{m}$  and increases in larger vessels [47]. In a recent study with almost 500 bifurcations measured with adaptive optics scanning laser ophthalmoscope values of  $\alpha$  were observed to be higher in arteries than in veins and to be lower in smaller vessels than in larger vessels [48]. The authors reported  $\alpha = 2.10$  for arteries with diameters smaller than 50  $\mu\text{m}$  and  $\alpha = 2.74$  for arteries diameters larger than 50  $\mu\text{m}$ . For veins with lumen diameters smaller than 50  $\mu\text{m}$   $\alpha = 1.69$  and  $\alpha = 2.11$  for veins larger than 50  $\mu\text{m}$ . The values calculated for bifurcations reported in the Table 4 for ID 1 ( $\alpha = 2.17$ ), ID 3 ( $\alpha = 2.65$ ) and ID 4 ( $\alpha = 2.43$ ) fall in these ranges, while values for ID 3 ( $\alpha = 7.86$ ) and ID 4 ( $\alpha = 5.39$ ) are outside. The latter is probably caused by the manual method of diameter estimations that is prone to errors if the visible vessel cross-section is not taken in the tubular part of vessel. The reason why the flow rate estimation is more resistant to this kind of error than the estimation of  $\alpha$  is that the integration over erroneous ROI including parts of static tissue has no impact on the calculated flow rate as the static tissue component has zero mean velocity and does not contribute to the flow rate calculation.

### 3.3.2. Correlation between blood flow rates and vascular lumen diameters

Next, we have analyzed the relation between the blood flow rate and the diameters of vessel lumens in the images of subjects ID 1 to ID 3 using six data sets collected with protocol (c) from Table 1. We have identified a total of 600 vessels for which full lumen cross sections were visible in the Doppler OCT C-scans and estimated their diameters and flow rates using manually fitted ellipses as described before and shown in Fig. 4. The diameters were in the range of 12–150  $\mu\text{m}$ . We have excluded capillary vessels with diameters smaller than 12  $\mu\text{m}$ , which is the lateral imaging resolution limit of the OCT system. We have classified the identified vessels as arterioles and veins using Doppler OCT information about flow velocity direction in the center of the optic disc. Next the branching of the vessels was followed in the OCT angiography images as well as in the structural OCT images shown in Fig. 5, generated from the same data sets as Doppler OCT images, where we were able to identify which vessel originated from the main arteriole and which is a vein. Vessels with lumen diameters smaller than 20  $\mu\text{m}$  were classified as capillaries.

In Fig. 6 we have plotted the values of the flow rates vs. lumen diameters in the phase-wrapped and phase-unwrapped data in a linear scale graph for subject ID 1. The blood flow rates calculated in the vessels with phase-wrapping, presented as red dots in Fig. 6(a), seem to be randomly distributed with values below  $\sim 11 \mu\text{l}/\text{min}$  suggesting no relation between the vessels diameters and blood flow rates. In the vessels where no phase-wrapping occurred, presented as blue crosses in Fig. 6(a), the data shows a power dependence  $Q \sim d^\alpha$ , known from literature [36], between the blood flow rate  $Q$  and the lumen diameter  $d$ . After performing the phase-unwrapping with the 3D 4FT FPU all the detected vessels show that dependence between the vascular lumens and the blood flow rates. The fit with a power curve was performed using a weighted least-squares method and is presented in Fig. 6(b). The correlation parameter was found to be  $\alpha = 1.8 \pm 0.2$  for veins and  $\alpha = 2.0 \pm 0.2$  for arterioles.



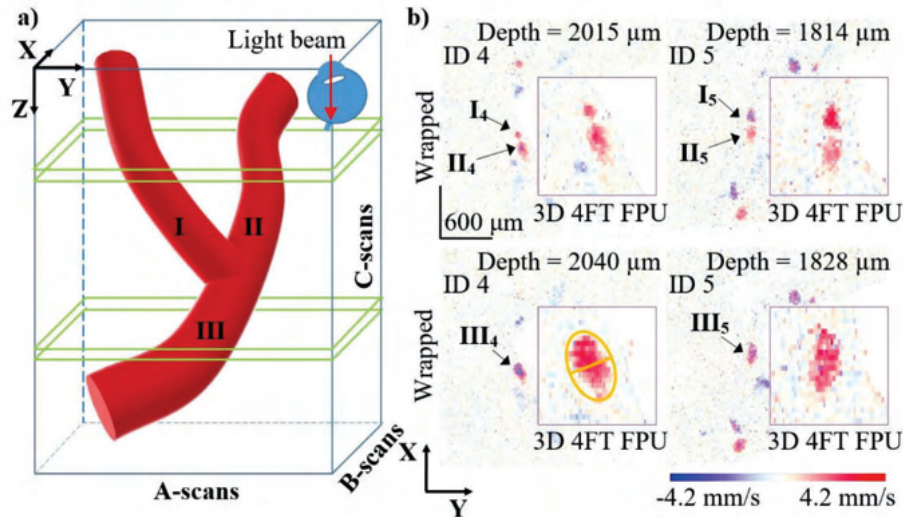


**Fig. 3.** a) Schematic illustration of vessel bifurcation in the human retina. The orange ellipse illustrates an XY-cross section of the vessel. The minor axis of the ellipse is used as the lumen diameter of the vessel. The light beam propagates from the top. The green rectangles mark sets of  $N = 6$  C-scans before and after bifurcations. The Roman numerals indicate the vessels in the bifurcation. b) Example STdOCT Doppler C-scans of the human retina near the optic nerve head at two depths. The images in the background show the data with the wrapped phase while the zoomed-in regions in the foreground show the result of the phase unwrapping. Arrows I, II, III: vessels whose flow rate values are listed in Table 4. The colors in the images represent the axial flow velocity values. Blue: flow direction against incoming beam of light; red: along with the light propagation. The increasing color intensity indicates increasing axial flow velocity values as indicated by the color bar. The orange ellipse illustrates an XY-cross section of the vessel. The minor axis of the ellipse is used as the lumen diameter of the vessel. The Doppler C-scans for the data set for subject ID 4 are presented in Visualization 1.

The results obtained from the 600 vessels identified in 18 data sets of three subjects are presented in Fig. 7 as log-log plots of the flow rates versus the lumen diameters. The calculated flow rates were in the range of 0.16–25.14  $\mu\text{l}/\text{min}$  for the veins and 0.15–18.32  $\mu\text{l}/\text{min}$  for the arterioles. The plots indicate a positive linear correlation in the log-log scale. The slopes of the linear fit (or correlation coefficients  $\alpha$  in the power curve fits) were found to be equal to  $\alpha = 1.8 \pm 0.2$ ,  $\alpha = 1.9 \pm 0.2$ ,  $\alpha = 2.0 \pm 0.2$  in case of veins and  $\alpha = 2.0 \pm 0.2$ ,  $\alpha = 1.8 \pm 0.2$ ,  $\alpha = 2.2 \pm 0.2$  in case of arterioles for subjects ID 1 to ID 3, respectively. In case when the capillaries with diameters less than 20  $\mu\text{m}$  are not taken into account in the fitting procedure, then the above values increase to  $\alpha = 2.0 \pm 0.2$ ,  $\alpha = 1.9 \pm 0.2$ ,  $\alpha = 2.0 \pm 0.2$  in case of veins and  $\alpha = 2.4 \pm 0.2$ ,  $\alpha = 1.9 \pm 0.2$ ,  $\alpha = 2.2 \pm 0.2$  in case of arterioles. This may suggest that either systematic errors appear in vessel diameter estimation and/or the flow mechanics is different in vessels with various diameters as mentioned earlier [47,48]. The above values of slopes are in agreement with values found by other researchers. For example Wang et al. [31] reported slopes in the range 1.52 – 2.54 with mean slope  $1.97 \pm 0.40$ . Higher slopes, closer to Murray's value of three [45] can also be found in the literature. Riva et al. [36] have found slopes 2.76 for arterioles and 2.84 for veins, while Haindl et al. [49] reported  $2.49 \pm 0.09$  for arterioles and  $2.52 \pm 0.06$  for veins. This difference in the results can be partially explained by the results obtained by Luo

**Table 4.** Mean volumetric blood flow rates in bifurcating vessels of the optic nerve head of five volunteers, calculated from six adjacent C-scans in the STdOCT data unwrapped with 3D 4FT FPU method. The errors were estimated from t-Student distribution at 0.05 significance level.

<i>ID</i>		<i>Vessel I</i>	<i>Vessel II</i>	<i>Vessels I + II</i>	<i>Vessel III</i>
1	Depth location [ $\mu\text{m}$ ]		2013–2020 $\mu\text{m}$		2037–2044 $\mu\text{m}$
	$\sigma_{\text{circ}}^a$ [rad]		0.40		0.32
	Flow rate [ $\mu\text{l}/\text{min}$ ]	$-4.6 \pm 0.4$	$-16.3 \pm 1.7$	$-20.9 \pm 1.8$	$-20.7 \pm 0.2$
	Diameter [ $\mu\text{m}$ ]	78	157		172
2	Depth location [ $\mu\text{m}$ ]		2508–2515 $\mu\text{m}$		2579–2586 $\mu\text{m}$
	$\sigma_{\text{circ}}$ [rad]		0.85		0.80
	Flow rate [ $\mu\text{l}/\text{min}$ ]	$-16.1 \pm 1.4$	$-11.4 \pm 2.3$	$-27.5 \pm 2.7$	$-27.8 \pm 0.6$
	Diameter [ $\mu\text{m}$ ]	109	105		117
3	Depth location [ $\mu\text{m}$ ]		1934–1941 $\mu\text{m}$		1833–1840 $\mu\text{m}$
	$\sigma_{\text{circ}}$ [rad]		0.51		0.37
	Flow rate [ $\mu\text{l}/\text{min}$ ]	$-9.3 \pm 0.4$	$-19.7 \pm 2.3$	$-29.0 \pm 2.4$	$-26.8 \pm 0.4$
	Diameter [ $\mu\text{m}$ ]	80	142		153
4	Depth location [ $\mu\text{m}$ ]		1791–1789 $\mu\text{m}$		1833–1840 $\mu\text{m}$
	$\sigma_{\text{circ}}$ [rad]		0.60		0.45
	Flow rate [ $\mu\text{l}/\text{min}$ ]	$-9.3 \pm 0.8$	$12.9 \pm 1.4$	$-22.2 \pm 1.6$	$-20.5 \pm 0.4$
	Diameter [ $\mu\text{m}$ ]	78	119		135
5	Depth location [ $\mu\text{m}$ ]		1808–1815 $\mu\text{m}$		1822–1829 $\mu\text{m}$
	$\sigma_{\text{circ}}$ [rad]		0.90		0.89
	Flow rate [ $\mu\text{l}/\text{min}$ ]	$-10.9 \pm 1.0$	$-11.5 \pm 0.8$	$-22.4 \pm 1.2$	$-20.9 \pm 0.4$
	Diameter [ $\mu\text{m}$ ]	100	107		118

<sup>a</sup>Circular standard deviation of the phase distribution defines the noise level of input data [29].

et al. [48] in their study on retinal bifurcations. If the assumptions made in the derivation of Murray's law are correct [45], then the slope of the linear fit and the power coefficient in the law governing the diameters of bifurcating vessels have the same value. Therefore, as mentioned before in Section 3.3.1 only large arteries with diameters above 50  $\mu\text{m}$  show slopes close to three (2.74), while all the other vessels have slopes around two.

The results presented in Fig. 7 are in agreement with the results presented by other studies and show that phase unwrapping is a necessary step in the flow estimation. The 3D 4FT FPU approach to phase unwrapping is a good candidate to become a standard step in the Doppler OCT data processing pipeline due to its robustness and high computational efficiency. It has to be noted, though, that the weakest point in the current study is the procedure of vessel diameter estimation. First, the precision of this estimation was limited by the transverse imaging resolution of the OCT device equal to 12  $\mu\text{m}$ . Second, the estimation of the lumen diameters was done in C-scans by manually fitting ellipses and using their minor axes as lumen diameters. In this procedure it is not always obvious how the ROI should be placed, especially in the proximities of bifurcations, where the cross-sections of the vessels are not always ellipsoidal, what can be observed in Fig. 4. Although this manual method is prone to errors the general conclusion is visible – the retinal blood flow in the vessels obeys the power dependence on vessel lumen diameter. Development and optimization of procedures yielding more precise values of vessel lumen diameter is outside of the scope of this paper but will be addressed in our future works.



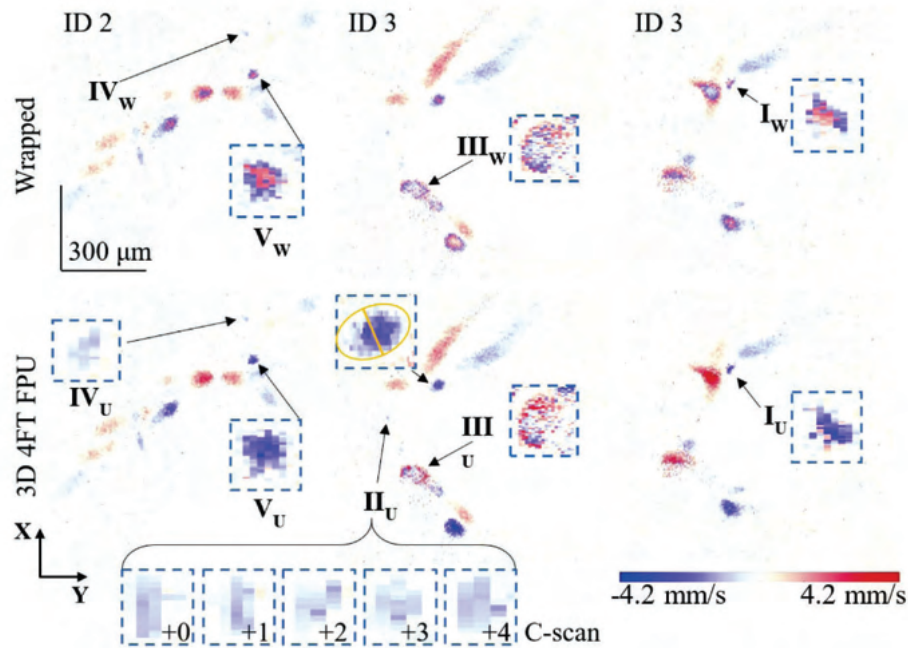


**Fig. 4.** Volumetric blood flow measurement in the vascular bifurcations sets of 3D data obtained in subjects ID 2 and ID 3 (Table 4.). Top: selected cross-sectional images of the wrapped phase. Bottom: outcomes of the 3D 4FT FPU algorithm. The arrows with Roman numerals indicate the selected vessels. The subscript “W” refers to the wrapped phase, while the subscript “U” refers to the same vessels after unwrapping. The figure insets show magnified regions of the indicated vessels.  $I_U$ ,  $III_U$ : errors of the phase unwrapping (phase has remained wrapped). Arrows  $II_U$ ,  $IV_U$ : phase-wrap-free vessel (diameter: 18  $\mu\text{m}$ , 31  $\mu\text{m}$ ). Arrow  $V_U$ : error-free phase unwrapping of the flow for a vessel with diameter of 79  $\mu\text{m}$ . The insets for vessel  $II_U$  present five zoomed regions of adjacent C-scans. The indicated vessels are plotted in Fig. 7. The orange ellipse represents the ROI used for flow calculation. The orange line in the ellipse is the minor axis of the ellipse and indicates the lumen of the vessels. The colors in the images represent the axial flow velocity values. Blue: flow direction against incoming beam of light; red: along with the light propagation. The increasing color intensity indicates increasing axial flow velocity values as indicated by the color bar. A movie showing the Doppler C-scans for subject ID 2 is presented in Visualization 2.

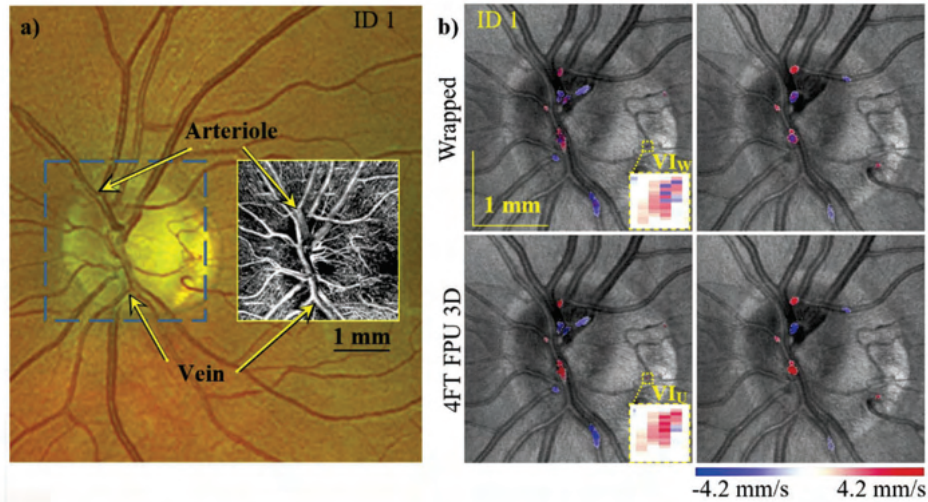


**Fig. 5.** Identification of arterioles and veins in the STdOCT data set. a) Identification of the main vein and arteriole in the OCT angiography image (the grayscale inset) of the optic nerve head by comparison with a fundus photograph (background image). b) Overlay of the STdOCT intensity fundus images with STdOCT Doppler images generated from the same 3D OCT data set. Only areas with blood flow velocity above a threshold are shown from the Doppler images. The two columns show two example data sets from the same subject (ID 1). Top row: STdOCT images with no phase-unwrapping. Bottom row: STdOCT images with phase-unwrapped using 3D 4FT FPU method. The insets show one of the identified vessels before and after phase unwrapping. The colors in the images represent the axial flow velocity values. Blue: flow direction against incoming beam of light; red: along with the light propagation. The increasing color intensity indicates increasing axial flow velocity values as indicated by the color bar.

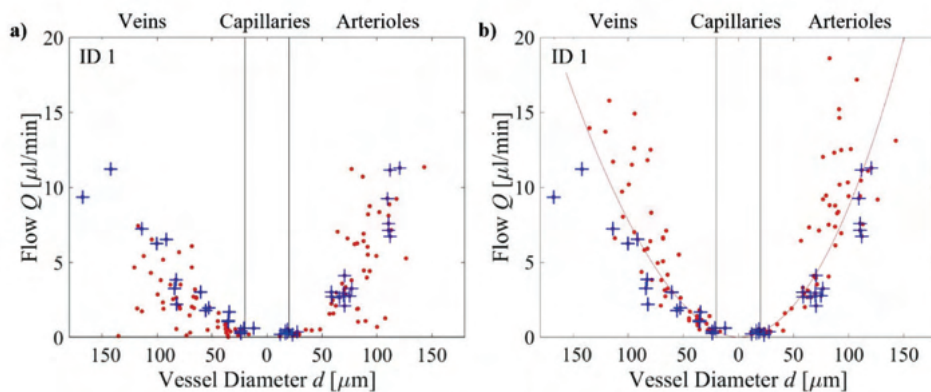


**Fig. 6.** Blood flow rates measured in arterioles, veins and capillaries of the optic nerve head of volunteer ID 1 (Table 4) plotted as a function of vessel lumen diameters (a) prior to phase unwrapping and (b) after phase unwrapping. The blue crosses indicate the flow rates in vessels with no phase-wrapping. The red dots indicate the flow values in vessels with wrapped phase (a) prior to phase unwrapping and (b) after phase unwrapping. Solid line in b: weighted least-square power curve fits. See text for details.



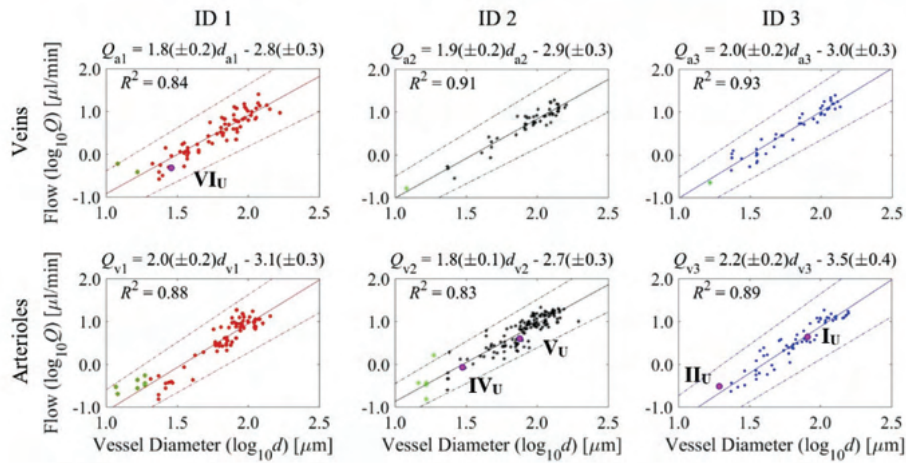


**Fig. 7.** Log-log plots of the blood flow rate versus the vessel lumen diameters. First row: venous blood flow. Second row: arterial blood flow. The green marks indicate capillaries with a diameter smaller than  $20 \mu\text{m}$ . Each column shows combined results from 6 data sets obtained in one of the three subjects (ID 1 to ID 3, Table 4). Solid lines: linear fit (the equations obtained by the least-squares fit are given on the top of each plot). Dashed lines: 95% confidence interval of the fit. Example vessels  $I_U$ ,  $II_U$ ,  $IV_U$ ,  $V_U$ , and  $VI_U$  presented in Fig. 4 are indicated with magenta outlines.

#### 4. Conclusions

Phase unwrapping is a procedure which should be implemented in the Doppler OCT algorithms for calculation of the volumetric blood flow rates in the wide range of flow velocities encountered in the vessels of the human retina and optic nerve head. We have demonstrated that the 3D 4FT FPU algorithm applied to Doppler OCT data gives reliable measurement of the volumetric flow rates. Since there are no “gold standards” for the volumetric blood flow rates in the vessels of the eye fundus to which we could relate our results, we have performed experiments in a flow phantom and tested relative relations between blood flow rates in the eyes of volunteers. The conclusion from the flow phantom experiments is that not only the measured flow rates fulfill the additive property of split-flows but also, they are in an agreement with the flow rates set in the microfluidic pump. The analysis of the blood flow rates in the vascular bifurcations of human subjects demonstrated that the relations between flow rates, measured as the additive property of flow, are preserved. Since there are no offsets between induced and measured flow rates in the flow phantom experiments, it is unlikely that such offsets should be introduced by our methods to the *in vivo* Doppler OCT imaging of the eye. Therefore, the results of the volumetric blood flow rate measurements in the 600 vessels identified in 18 data sets acquired in the eyes of three volunteers may be considered as reasonable estimation of the actual blood flow rates.

As a demonstration of the necessity of the phase-unwrapping in the Doppler OCT, we have analyzed the relation between the blood flow rates and the vessel lumen diameters. We have observed that the phase-wrapping causes large dispersion of flow rates especially for vessels with large diameters. The flow rates included unexpectedly low values for large vessels. Only data free from phase-wrapping (either inherently or after application of the phase-unwrapping methods) reveals the positive power dependence between the blood flow rate and vascular lumen diameters in accordance with theoretical predictions and reports of other researchers.

We also introduced the 4FT FPU methods into the OCT processing pipeline implemented in GPU showing that phase-unwrapped phase-resolved Doppler OCT can be processed in real-time,

and phase-unwrapped joint spectral and time domain OCT images can be generated in less than a minute (Table 2). This is an important result which shows that phase-unwrapped Doppler OCT methods can be used in clinical practice.

### Funding

Fundacja na rzecz Nauki Polskiej (POIR.04.04.00-00-2070/16-00).

### Acknowledgements

The project “FreeZEYE Tracker – ultrafast system for image stabilization in biomedical imaging” is carried out within the TEAM TECH program of the Foundation for Polish Science co-financed by the European Union under the European Regional Development Fund.

### Disclosures

The authors declare that there are no conflicts of interest related to this article.

### References

1. A. P. Cherecheanu, G. Garhofer, D. Schmidl, R. Werkmeister, and L. Schmetterer, “Ocular perfusion pressure and ocular blood flow in glaucoma,” *Curr. Opin. Pharmacol.* **13**(1), 36–42 (2013).
2. S. Frost, Y. Kanagasingam, H. Sohrabi, J. Vignarajan, P. Bourgeat, O. Salvado, V. Villemagne, C. C. Rowe, S. Lance MacAulay, C. Szoce, K. A. Ellis, D. Ames, C. L. Masters, S. Rainey-Smith, and R. N. Martins, “Retinal vascular biomarkers for early detection and monitoring of Alzheimer’s disease,” *Transl. Psychiatry* **3**(2), e233 (2013).
3. J. T. Durham and I. M. Herman, “Microvascular modifications in diabetic retinopathy,” *Curr. Diabetes Rep.* **11**(4), 253–264 (2011).
4. B. Pemp and L. Schmetterer, “Ocular blood flow in diabetes and age-related macular degeneration,” *Can. J. Ophthalmol.* **43**(3), 295–301 (2008).
5. S. A. Fraenkl, M. Mozaffarieh, and J. Flammer, “Retinal vein occlusions: The potential impact of a dysregulation of the retinal veins,” *EPMA J.* **1**(2), 253–261 (2010).
6. Y. W. Tien and R. McIntosh, “Hypertensive retinopathy signs as risk indicators of cardiovascular morbidity and mortality,” *Br. Med. Bull.* **73-74**(1), 57–70 (2005).
7. G. Kissas, Y. Yang, E. Hwuang, W. R. Witschey, J. A. Detre, and P. Perdikaris, “Machine learning in cardiovascular flows modeling: Predicting arterial blood pressure from non-invasive 4D flow MRI data using physics-informed neural networks,” *Comput. Methods Appl. Mech. Eng.* **358**, 112623 (2020).
8. J. A. Izatt, M. D. Kulkarni, J. K. Barton, and A. J. Welch, “In vivo Doppler flow imaging of picoliter blood volumes using optical coherence tomography,” *Conf. Proc. - Lasers Electro-Optics Soc. Annu. Meet.* **11**(18), 212–213 (1997).
9. S. Makita, Y. Hong, M. Yamanari, T. Yatagai, and Y. Yasuno, “Optical coherence angiography,” *Opt. Express* **14**(17), 7821 (2006).
10. J. Fingler, D. Schwartz, C. Yang, and S. E. Fraser, “Mobility and transverse flow visualization using phase variance contrast with spectral domain optical coherence tomography,” *Opt. Express* **15**(20), 12636 (2007).
11. I. Gorczynska, J. V. Migacz, R. J. Zawadzki, A. G. Capps, and J. S. Werner, “Comparison of amplitude-decorrelation, speckle-variance and phase-variance OCT angiography methods for imaging the human retina and choroid,” *Biomed. Opt. Express* **7**(3), 911 (2016).
12. R. F. Spaide, J. G. Fujimoto, N. K. Waheed, S. R. Sadda, and G. Staurengi, “Optical coherence tomography angiography,” *Prog. Retinal Eye Res.* **64**, 1–55 (2018).
13. M. Szkulmowski, A. Szkulmowska, T. Bajraszewski, A. Kowalczyk, and M. Wojtkowski, “Flow velocity estimation using joint Spectral and Time domain Optical Coherence Tomography,” *Opt. Express* **16**(9), 6008 (2008).
14. A. Bouwens, D. Szlag, M. Szkulmowski, T. Bolmont, M. Wojtkowski, and T. Lasser, “Quantitative lateral and axial flow imaging with optical coherence microscopy and tomography,” *Opt. Express* **21**(15), 17711 (2013).
15. C. A. Puliafito, S. Jiao, M. Ruggeri, W. Zhao, G. Gregori, and H. Wehbe, “Automatic retinal blood flow calculation using spectral domain optical coherence tomography,” *Opt. Express* **15**(23), 15193 (2007).
16. B. A. Bower, O. Tan, Y. Wang, J. A. Izatt, and D. Huang, “Retinal blood flow measurement by circumpapillary Fourier domain Doppler optical coherence tomography,” *J. Biomed. Opt.* **13**(6), 064003 (2008).
17. A. S. G. Singh, C. Kolbitsch, T. Schmoll, and R. A. Leitgeb, “Stable absolute flow estimation with Doppler OCT based on virtual circumpapillary scans,” *Biomed. Opt. Express* **1**(4), 1047 (2010).
18. O. Tan, R. Konduru, X. Zhang, S. R. Sadda, and D. Huang, “Dual-Angle Protocol for Doppler Optical Coherence Tomography to Improve Retinal Blood Flow Measurement,” *Transl. Vis. Sci. Technol.* **3**(4), 6 (2014).
19. A. M. Hancock, L. Qi, C. Dai, X. Zhang, R. D. Frostig, Z. Chen, and J. Zhu, “Fully distributed absolute blood flow velocity measurement for middle cerebral arteries using Doppler optical coherence tomography,” *Biomed. Opt. Express* **7**(2), 601 (2016).



20. R. Haindl, W. Trasischker, A. Wartak, B. Baumann, M. Pircher, and C. K. Hitzenberger, "Total retinal blood flow measurement by three beam Doppler optical coherence tomography," *Biomed. Opt. Express* **7**(2), 287 (2016).
21. V. J. Srinivasan, S. Sakadžić, I. Gorczynska, S. Ruvinskaya, W. Wu, J. G. Fujimoto, and D. A. Boas, "Quantitative cerebral blood flow with Optical Coherence Tomography," *Opt. Express* **18**(3), 2477–2494 (2010).
22. A. Szkulmowska, M. Szkulmowski, A. Kowalczyk, and M. Wojtkowski, "Phase-resolved Doppler optical coherence tomography—limitations and improvements," *Opt. Lett.* **33**(13), 1425 (2008).
23. J. Strand, T. Taxt, and A. K. Jain, "Two-dimensional phase unwrapping using a block least-squares method," *IEEE Trans. Image Process.* **8**(3), 375–386 (1999).
24. J. Strand and T. Taxt, "Two-dimensional phase unwrapping using robust derivative estimation and adaptive integration," *IEEE Trans. Image Process.* **11**(10), 1192–1200 (2002).
25. H. C. Hendargo, M. Zhao, N. Shepherd, and J. a Izatt, "Synthetic wavelength based phase unwrapping in spectral domain optical coherence tomography," *Opt. Express* **17**(7), 5039–5051 (2009).
26. Y. I. W. Ang, D. A. H. Ung, and X. S. T. Y. Ao, "Two-dimensional phase unwrapping in Doppler Fourier domain optical coherence tomography," *Opt. Express* **24**(23), 1271–1273 (2016).
27. S. Xia, Y. Huang, S. Peng, Y. Wu, and X. Tan, "Robust phase unwrapping for phase images in Fourier domain Doppler optical coherence tomography," *J. Biomed. Opt.* **22**(3), 036014 (2017).
28. S. Pi, A. Camino, X. Wei, T. T. Hormel, W. Cepurna, J. C. Morrison, and Y. Jia, "Automated phase unwrapping in Doppler optical coherence tomography," *J. Biomed. Opt.* **24**(01), 1 (2019).
29. E. Pijewska, I. Gorczynska, and M. Szkulmowski, "Computationally effective 2D and 3D fast phase unwrapping algorithms and their applications to Doppler optical coherence tomography," *Biomed. Opt. Express* **10**(3), 1365 (2019).
30. J. Martinez-Carranza, K. Falaggis, and T. Kozacki, "Fast and accurate phase-unwrapping algorithm based on the transport of intensity equation," *Appl. Opt.* **56**(25), 7079–7088 (2017).
31. Y. Wang, A. Lu, J. Gil-Flamer, O. Tan, J. A. Izatt, and D. Huang, "Measurement of total blood flow in the normal human retina using Doppler Fourier-domain optical coherence tomography," *Br. J. Ophthalmol.* **93**(5), 634–637 (2009).
32. Y. K. Tao, K. M. Kennedy, and J. A. Izatt, "Velocity-resolved 3D retinal microvessel imaging using single-pass flow imaging spectral domain optical coherence tomography," *Opt. Express* **17**(5), 4177 (2009).
33. A. Wartak, R. Haindl, W. Trasischker, B. Baumann, M. Pircher, and C. K. Hitzenberger, "Active-passive path-length encoded (APPLE) Doppler OCT," *Biomed. Opt. Express* **7**(12), 5233 (2016).
34. T. Tani, Y. S. Song, T. Yoshioka, T. Omae, A. Ishibazawa, M. Akiba, and A. Yoshida, "Repeatability and reproducibility of retinal blood flow measurement using a Doppler optical coherence tomography flowmeter in healthy subjects," *Invest. Ophthalmol. Visual Sci.* **58**(7), 2891–2898 (2017).
35. T. Yoshioka, A. Yoshida, T. Omae, K. Takahashi, T. Tani, A. Ishibazawa, Y. Song, and M. Akiba, "Retinal blood flow reduction after panretinal photocoagulation in Type 2 diabetes mellitus: Doppler optical coherence tomography flowmeter pilot study," *PLoS One* **13**(11), e0207288 (2018).
36. C. E. Riva, J. E. Grunwald, S. H. Sinclair, and B. L. Petrig, "Blood velocity and volumetric flow rate in human retinal vessels," *Invest. Ophthalmol. Vis. Sci.* **26**(8), 1124–1132 (1985).
37. W. M. Association, "World Medical Association Declaration of Helsinki: ethical principles for medical research involving human subjects," *JAMA* **310**(20), 2191–2194 (2013).
38. B. R. White, M. C. Pierce, N. Nassif, B. Cense, B. H. Park, G. J. Tearney, B. E. Bouma, T. C. Chen, and J. F. de Boer, "In vivo dynamic human retinal blood flow imaging using ultra-high-speed spectral domain optical Doppler tomography," *Opt. Express* **11**(25), 3490–3497 (2003).
39. E. Koch, J. Walther, and M. Cuevas, "Limits of Fourier domain Doppler-OCT at high velocities," *Sens. Actuators, A* **156**(1), 8–13 (2009).
40. Y. Zhao, Z. Chen, C. Saxer, S. Xiang, J. F. de Boer, and J. S. Nelson, "Phase-resolved optical coherence tomography and optical Doppler tomography for imaging blood flow in human skin with fast scanning speed and high velocity sensitivity," *Opt. Lett.* **25**(2), 114–116 (2000).
41. M. a Schofield and Y. Zhu, "Fast phase unwrapping algorithm for interferometric applications," *Opt. Lett.* **28**(14), 1194–1196 (2003).
42. M. Sylwestrzak, D. Szlag, P. J. Marchand, A. S. Kumar, and T. Lasser, "Massively parallel data processing for quantitative total flow imaging with optical coherence microscopy and tomography," *Comput. Phys. Commun.* **217**, 128–137 (2017).
43. M. Gora, K. Karnowski, M. Szkulmowski, B. J. Kaluzny, R. Huber, A. Kowalczyk, and M. Wojtkowski, "Ultra high-speed swept source OCT imaging of the anterior segment of human eye at 200 kHz with adjustable imaging range," *Opt. Express* **17**(17), 14880–14894 (2009).
44. J. Walther and E. Koch, "Relation of joint spectral and time domain optical coherence tomography (jSTdOCT) and phase-resolved Doppler OCT," *Opt. Express* **22**(19), 23129 (2014).
45. C. D. Murray, "The Physiological Principle of Minimum Work: I. The Vascular System and the Cost of Blood Volume," *Proc. Natl. Acad. Sci.* **12**(3), 207–214 (1926).
46. H. R. Williams, R. S. Trask, P. M. Weaver, and I. P. Bond, "Minimum mass vascular networks in multifunctional materials," *J. R. Soc., Interface* **5**(18), 55–65 (2008).

47. A. R. Pries, D. Neuhaus, and P. Gaehtgens, "Blood viscosity in tube flow: Dependence on diameter and hematocrit," *Am. J. Physiol. - Hear. Circ. Physiol.* **263**(6), H1770–H1778 (1992).
48. T. Luo, T. J. Gast, T. J. Vermeer, and S. A. Burns, "Retinal vascular branching in healthy and diabetic subjects," *Invest. Ophthalmol. Visual Sci.* **58**(5), 2685–2694 (2017).
49. R. Haindl, W. Trasischker, A. Wartak, B. Baumann, M. Pircher, and C. K. Hitzenberger, "Total retinal blood flow measurement by three beam Doppler optical coherence tomography," *Biomed. Opt. Express* **7**(2), 287–301 (2016).

# PROCEEDINGS OF SPIE

[SPIDigitalLibrary.org/conference-proceedings-of-spie](https://spiedigitallibrary.org/conference-proceedings-of-spie)

## Blood flow rate estimation in optic disc capillaries and vessels using Doppler optical coherence tomography

Pijewska, E., Sylwestrzak, M., Wrobel, K., Gorczynska, I., Tamborski, S., et al.

E. Pijewska, M. Sylwestrzak, K. Wrobel, I. Gorczynska, S. Tamborski, M. A. Pawlak, M. Szkulmowski, "Blood flow rate estimation in optic disc capillaries and vessels using Doppler optical coherence tomography," Proc. SPIE 11359, Biomedical Spectroscopy, Microscopy, and Imaging, 113590Q (22 April 2020); doi: 10.1117/12.2555754

**SPIE.**

Event: SPIE Photonics Europe, 2020, Online Only

Downloaded From: <https://www.spiedigitallibrary.org/conference-proceedings-of-spie> on 21 Oct 2021 Terms of Use: <https://www.spiedigitallibrary.org/terms-of-use>

# Blood flow rate estimation in optic disc capillaries and vessels using Doppler optical coherence tomography

E. Pijewska<sup>a</sup>, M. Sylwestrzak<sup>a</sup>, K. Wrobel<sup>a</sup>, I. Gorczynska<sup>a</sup>, S. Tamborski<sup>a</sup>, M. A. Pawlak<sup>b</sup>  
and M. Szkulmowski<sup>a\*</sup>

<sup>a</sup>Institute of Physics, Faculty of Physics, Astronomy and Informatics, Nicolaus Copernicus University in Toruń, Grudziądzka 5, 87-100 Torun, Poland

<sup>b</sup>Department of Neurology and Cerebrovascular Disorders, Poznan University of Medical Sciences, Fredry 10, 61-701 Poznań, Poland

## ABSTRACT

Ocular blood flow measurement may have a number of potential applications that explore the relationship between blood flow in the eye and diseases such as: diabetic retinopathy, ocular artery obstruction, hypertensive retinopathy and Alzheimer's disease. Reliable and quantitative method for retinal blood flow estimation is still to be created. Doppler OCT is one of candidates for such a method, but suffers from a number of limitations. Recently we proposed a solution to one of the most prominent artefacts in Doppler OCT, which is the phase wrapping problem. This allows for precise recovery of velocity profile the Doppler OCT technique remains sensitive to temporal dependence of the result on the blood flow velocity changing with the pulse during the OCT measurement. In this report we explore this problem and show that the synchronization of the OCT measurement with heart beats only partially gives control over the acquired blood flows.

**Keywords:** Blood flow, optical coherence tomography, phase unwrapping

## 1. INTRODUCTION

Optical Coherence Tomography is a valuable tool for retinal imaging and diagnostics of ophthalmic diseases. It also provides information on functional aspects of the living eye with blood flow being the most prominent example. One of the limits in the blood flow estimation in the eye is that the flow velocity exceeds the maximal detectable velocity value. This manifests in the form of phase wrapping in phase difference signal which is the basis of the Doppler OCT method. This effectively prevents velocity estimation unless an effective phase unwrapping method is applied. In our recent approach to phase unwrapping problem we have shown that three dimensional fast phase unwrapping technique (3D 4FT FPU) is a robust, yet accurate phase wrapping problem solver in OCT, even in case of low signal to noise ratio [1]. We have also shown that this approach allows for calculation of flow in retinal vessels of various diameters ranging from 12 to 150  $\mu\text{m}$  [2]. This allowed us to observe that retinal vessels to follow both: the flow conservation law and the Murray's law stating that the flow and diameter are linked by power law relationship. These results were obtained with a simple assumption that the blood flow is stationary during the OCT measurement time, which is not true in most of cases. Since the standard Doppler OCT measurement protocol lasts for a few seconds (usually 2 to 5) a number of heart beats occur during this time what induces changes in the blood flow velocity. In this report we explore the impact of this effect on the Doppler OCT blood flow measurements and show that even the synchronization of the OCT measurement with pulse recording device, such as transcranial Doppler USG does not solve all the experimental requirements for precise blood flow estimation.

## 2. METHODS

Data was acquired using commercial spectral domain OCT (RevoNX, Optopol Technology, Poland). The light source was a super-luminescent diode (center wavelength: 830 nm). The axial imaging resolution was  $\sim 5 \mu\text{m}$  in tissue and the lateral imaging resolution was 12  $\mu\text{m}$ . Arteriole, veins, and capillaries were segmented by a semiautomatic fitting an ellipse to XY cross-section of the vessel and minor axis of ellipse was considered to be the lumen of the vessel. To obtain axial velocity we used STdOCT which is a more sensitive variation of Doppler OCT [2]. The range of unambiguous velocity estimation, limited by phase wrapping, was extended by phase unwrapping method we recently developed (4FT FPU) [1]. The blood flow rate was calculated using the integration of axial velocity of flow over XY

Biomedical Spectroscopy, Microscopy, and Imaging, edited by Jürgen Popp,  
Csilla Gergely, Proc. of SPIE Vol. 11359, 113590Q · © 2020 SPIE  
CCC code: 0277-786X/20/\$21 · doi: 10.1117/12.2555754

Proc. of SPIE Vol. 11359 113590Q-1

Downloaded From: <https://www.spiedigitallibrary.org/conference-proceedings-of-spie> on 21 Oct 2021  
Terms of Use: <https://www.spiedigitallibrary.org/terms-of-use>



cross-section of vessels. Vascular discrimination between arterioles and veins was supported by angiographic and fundus camera images. We used a GPU as a data processing accelerator and utilized NVIDIA CUDA compiler 10.1 with the cuFFT library. The workstation was equipped with Intel® Core i7-7700K (4.2 GHz) and 32 GB RAM memory. For data processing, we used NVIDIA GeForce® GTX™ 1080 with 8 GB of device memory. 3D data set 1024×1024×256 was processed in GPU in time 1 s or 27 s for standard Doppler OCT and STdOCT, respectively. Unwrapped axial velocities of flow were obtained for all vessels in the 3D data set at the same time. We used transcranial USG (Doppler-BoxX, Compumedics Germany GmbH) to measure cerebral blood velocity during OCT data collection. In order to synchronize the two signals, the USG signal was acquired with I/O card triggered with trigger signal used for OCT camera framegrabber.

We enrolled six healthy volunteers for the study. All the experiments were performed in compliance with the Declaration of Helsinki [37] and regulations of the Bioethics Committee of the Nicolaus Copernicus University in Toruń, Poland. Medical doctor was present during the data acquisition. The measurement protocol consisted of the same steps for all the subjects. To limit the number of OCT experiments to the required minimum, the cerebral flow was located with the use of the transcranial USG before the OCT measurement was started to assure that both signals are recorded. Two datasets were acquired for each subject: (1) the 3D Doppler OCT with 1024 A-scans x 256 B-scans over 3x3 mm area, (2) the time-series Doppler OCT with 1024 A-scans x 512 B-scans over 3 mm at the same retinal location. The two procedures were repeated five times for each subject. After the experiments, the data was processed to extract the phase unwrapped velocity profiles followed by flow calculation over C-scan projection in case of protocol (1) and by integrating the velocity over vessel cross-section in each B-scan to observe the plod pulsatility.

### 3. RESULTS

#### 3.1 Blood flow in human retina using Doppler OCT

The ability to calculate blood flow rate is proven on a microfluidic device with controlled flow and on arteriole bifurcations in data acquired from five healthy subjects was shown in previous paper [3]. For each subject distribution of flow in arterioles, veins and capillaries versus vessel lumen was calculated. The additive character of flow within human retinal vessels are shown [3]. Here, we repeated our measurements for six more volunteers and compared with those previously reported. Again, we obtain parabolic relation between flow and vessel diameter and the log-log dependence of human retinal flow  $Q$  versus vessel lumens  $d$  present linear correlation with a coefficient of determination close to 0.80. Example of the result for one of the (ID 4, see Tab. 1) volunteers there is in the Fig. 1. It allowed us to determine Murray's coefficients presented in the Tab. 1. More details you can find in the paper [3].

Tab. 1. Murray's coefficient  $\alpha$  for six volunteers subject arterioles and veins. The vessel diameter is in the range 12 to 150  $\mu\text{m}$ .

ID	Arterioles	Veins
1	$2.0(\pm 0.2)d^{-3.1(\pm 0.3)}$	$1.8(\pm 0.2)d^{-2.8(\pm 0.3)}$
2	$1.8(\pm 0.2)d^{-2.7(\pm 0.3)}$	$1.9(\pm 0.2)d^{-2.9(\pm 0.3)}$
3	$2.2(\pm 0.2)d^{-3.5(\pm 0.4)}$	$2.0(\pm 0.2)d^{-3.0(\pm 0.3)}$
4	$2.1(\pm 0.3)d^{-3.4(\pm 0.6)}$	$1.9(\pm 0.2)d^{-2.9(\pm 0.4)}$
5	$2.1(\pm 0.3)d^{-3.0(\pm 0.3)}$	$1.9(\pm 0.3)d^{-2.7(\pm 0.3)}$
6	$2.0(\pm 0.2)d^{-3.0(\pm 0.5)}$	$2.0(\pm 0.2)d^{-3.0(\pm 0.5)}$
$\bar{\alpha}$	$2.0(\pm 0.3)$	$1.9(\pm 0.3)$

#### 3.2 Comparison USG cerebral vessel signal with retinal Doppler OCT vessel signal

The blood flow calculation shown above requires phase unwrapped Doppler OCT methods combined with velocity integration over vessel lumen cross-section in the plane perpendicular to the probing beam as described by Srinivasan et al. in Ref. [4]. Such en-face Doppler OCT image is presented in Fig. 2(a). The results presented in the previous section assume that the blood flow is constant during acquisition of the vessel cross-section in the en-face plane (or C-scan), see Fig. 2(a). This is hardly possible to fulfill in standard Doppler OCT protocol such as protocol (1). The total measurement time is equal to approximately 2.5s and, as shown in Fig. 2(b), the time required to acquire the example cross-section is equal to 0.139s. In this example the acquisition time is equal to approx. one third of heart beat period, see Fig. 2(c).

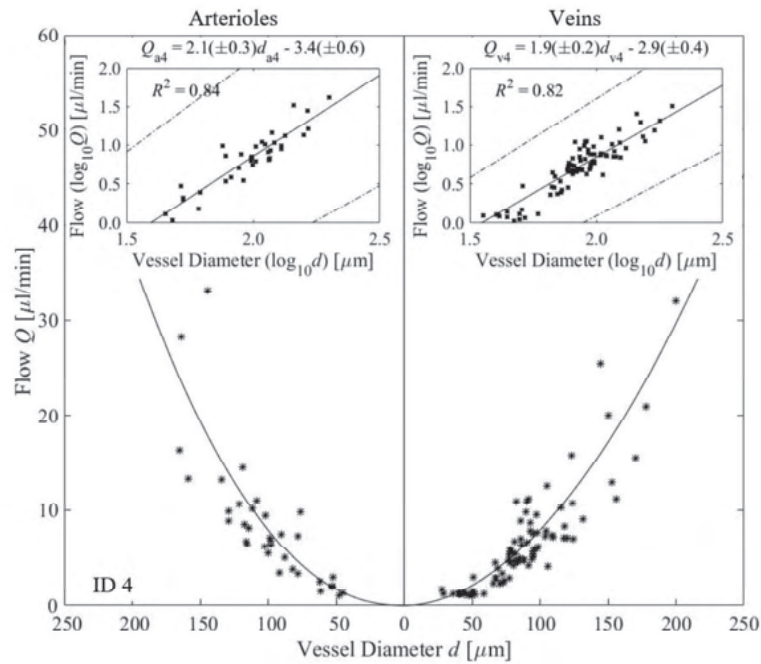


Fig. 1. Blood flow rates measured in arterioles, veins and capillaries of the optic nerve head of volunteer ID 4 (Tab. 1) plotted as a function of vessel lumen diameters. Solid line is a weighted least-square power curve fit. The log-log plots of the same data are presented in the insets at the top of the figure. Linear coefficient  $\alpha$  corresponds to Murray's coefficient in the Table. 1. See text for details.

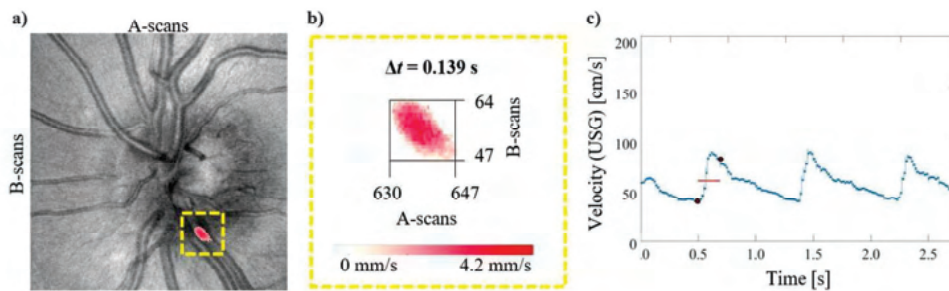


Fig. 2. Problem with data collection in Doppler OCT. a) En face image of the proximity of the optics head acquired with protocol (1) for subject ID 4. A yellow rectangle indicate Doppler-OCT axial velocity cross section from selected depth. b) Zoom of the selected with A-scans and B-scans numbers in the OCT dataset. Total acquisition time between the first and last B-scan with the vessel is equal to 0.139 s. c) Transcranial Doppler USG signal acquired during the OCT data acquisition (in blue). The red line indicate scanning time of the vessel during Doppler OCT detection. The red points show start and end of the OCT data collection on the plot of the heart rate.

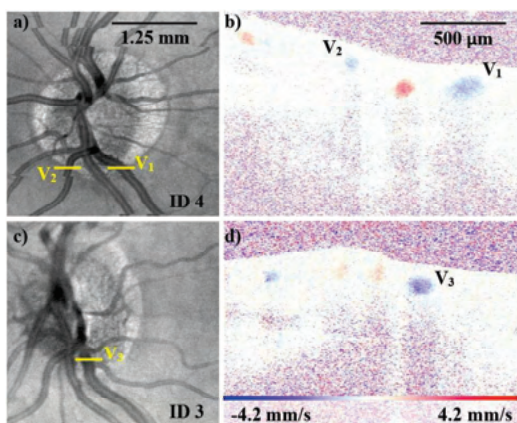


Fig. 3. a) & c) Location of vessels  $V_1$  to  $V_3$  measured with protocol (2) overlaid on the en-face projection from OCT data acquired with protocol (1) from subjects ID 4 and ID 3. b) & d) Doppler OCT images extracted from protocol (2) measurement at location of the vessels  $V_1$  to  $V_3$ .

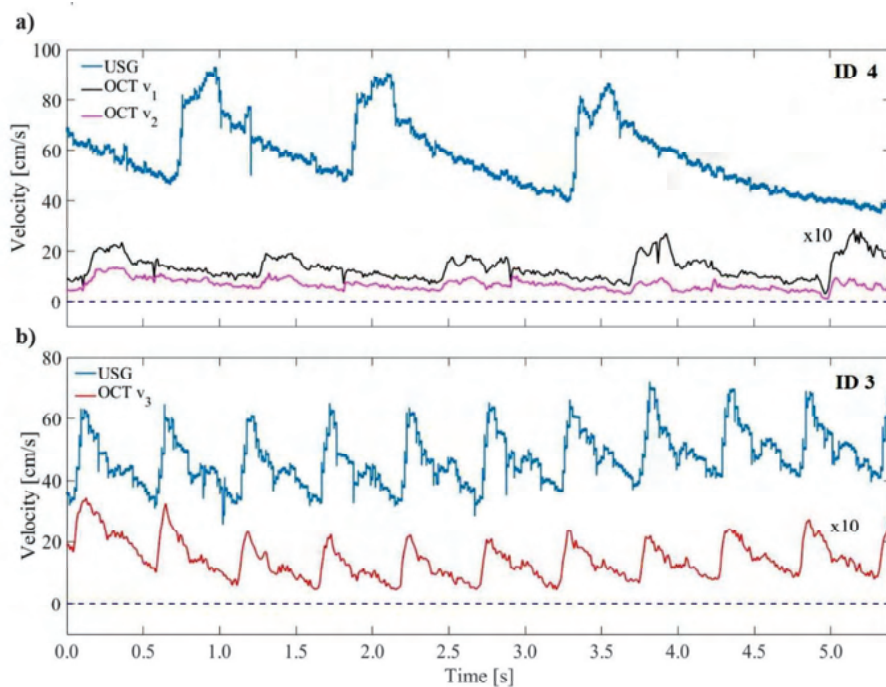


Fig. 4. a) Doppler USG signal from cerebral vessel (blue) and Doppler OCT axial velocity profiles for retinal vessels  $V_1$  and  $V_2$  (black and magenta) for subject ID 4. b) Doppler USG signal from cerebral vessel (blue) and Doppler OCT axial velocity profiles for retinal vessels  $V_3$  (red) for subject ID 3.

If the blood velocity changes during this time, the calculated flow will be disturbed. Therefore, it is important to synchronize the Doppler OCT signal with the pulse at each retinal location. In order to check whether the cerebral pulse can be used to synchronize the OCT data acquisition we used the signal from transcranial Doppler USG. We used protocol (2) to acquire Doppler OCT tomograms with frequency comparable to the Doppler USG. We have chosen vessels from the proximity of the optic nerve head as shown on Fig. 3(a, c). Selected vessels, as visible in Fig. 3(b, d) were manually segmented and the integral of axial velocity and vessel lumen was calculated. Next the two signals, Doppler USG and Doppler OCT, were compared, see Fig. 4(a) for results from vessel  $V_1$  and  $V_2$  from subject ID 4 and Fig. 4(b) for results from vessel  $V_3$  subject ID 3. It can be seen that the phase difference for the two subjects is different and equal to 10ms for subject ID 3 and approx. 500ms for subject ID 4.

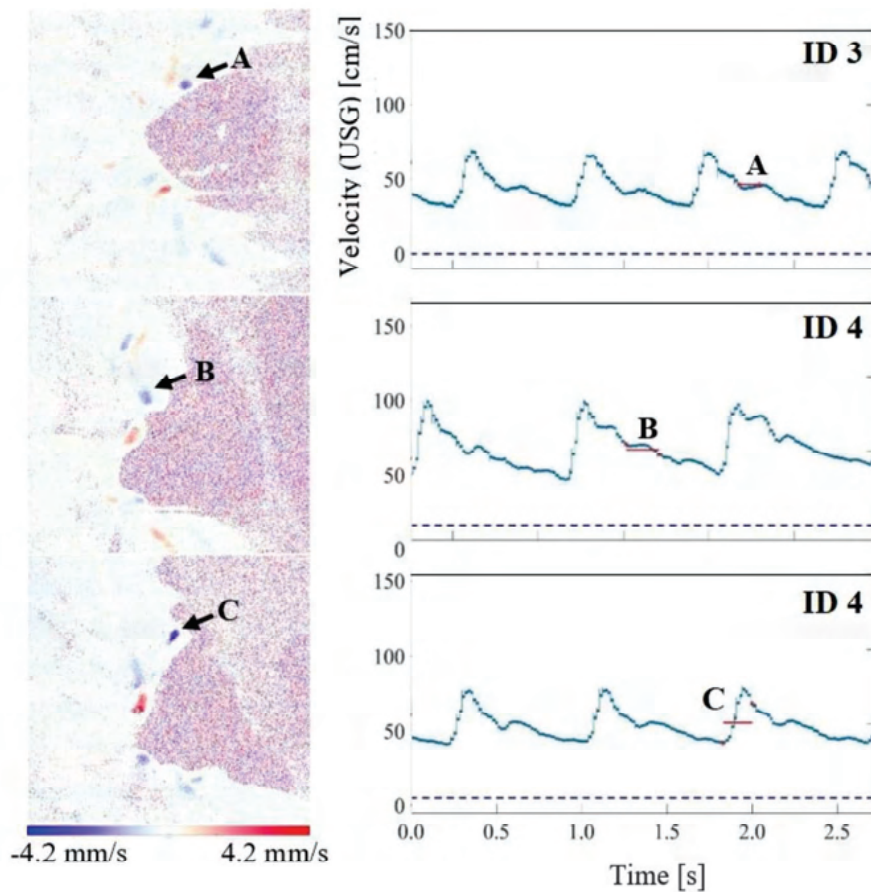


Fig. 5. (left) Selected en-face Doppler OCT images for subjects ID 3 and ID 4. (right) Blood flow velocity from cerebral vessel measured with transcranial Doppler USG. The red lines indicate scanning time of the vessels A-C during Doppler OCT detection. The red points show start and end of the OCT data collection on the plot of the heart rate.

#### 4. CONCLUSIONS

The results show that the Doppler OCT method with the unwrapping 3D 4FT FPU method is able to provide blood flow rate for arterioles, veins, and capillaries in the optic disc area and for vessel lumens as low as 12  $\mu\text{m}$ . Since the retinal flow can be used as indicator of pathological changes in the vessels in the course of systemic disorders, the proposed technique should be insensitive to the blood flow velocity changes during the acquisition of the Doppler OCT signal. Unfortunately, for larger vessels, the data acquisition time may be equal to a significant fraction of the heart rate. Although it is possible to find periods with quasi constant blood velocity long enough to measure the whole vessel cross-section, it is possible to be done only with external heart rate measurement. An example of such signal source can be transcranial Doppler USG, but care must be taken as phase delay between pulse registered by Doppler OCT and Doppler USG vary from subject to subject. Currently, we are investigating the relations between the two and methods to exploit them for improved retinal blood flow estimation.

#### ACKNOWLEDGEMENTS

The project "FreezEYE Tracker – ultrafast system for image stabilization in biomedical imaging" (POIR.04.04.00-00-2070/16-00) is carried out within the TEAM TECH program of the Foundation for Polish Science co-financed by the European Union under the European Regional Development Fund.

#### REFERENCES

1. E. Pijewska, I. Gorczynska, and M. Szkulmowski, "Computationally effective 2D and 3D fast phase unwrapping algorithms and their applications to Doppler optical coherence tomography," *Biomed. Opt. Express* (2019).
2. E. Pijewska, M. Sylwestrzak, I. Gorczynska, S. Tamborski, M. A. Pawlak, and M. Szkulmowski, "Blood flow rate estimation in optic disc capillaries and vessels using Doppler optical coherence tomography with 3D fast phase unwrapping," *Biomed. Opt. Express* (2020).
3. M. Szkulmowski, A. Szkulmowska, T. Bajraszewski, A. Kowalczyk, and M. Wojtkowski, "Flow velocity estimation using joint Spectral and Time domain Optical Coherence Tomography.," *Opt. Express* (2008).
4. M. Szkulmowski, I. Gorczynska, and E. Pijewska, "Complex fast phase unwrapping method for Doppler OCT," in *Optical Coherence Tomography and Coherence Domain Optical Methods in Biomedicine XXIII*, J. A. Izatt and J. G. Fujimoto, eds. (SPIE, 2019), **10867**, p. 87.
5. World Medical Association, "World Medical Association Declaration of Helsinki: ethical principles for medical research involving human subjects," *JAMA* **310**(20), 2191–2194 (2013).
6. V. J. Srinivasan, S. Sakadžić, I. Gorczynska, S. Ruvinskaya, W. Wu, J. G. Fujimoto, and D. A. Boas, "Quantitative cerebral blood flow with Optical Coherence Tomography," *Opt. Express* (2010).



# Extraction of phase-based optoretinograms (ORG) from serial B-scans acquired over tens of seconds by mouse retinal raster scanning OCT system

EWELINA PIJEWSKA,<sup>1</sup> PENGFEI ZHANG,<sup>2,3</sup>  MICHAŁ MEINA,<sup>1</sup>   
RATHEESH K. MELEPPAT,<sup>2</sup>  MACIEJ SZKULMOWSKI,<sup>1</sup>  AND  
ROBERT J. ZAWADZKI<sup>2,4,\*</sup> 

<sup>1</sup>*Institute of Physics, Faculty of Physics, Astronomy and Informatics, Nicolaus Copernicus University in Toruń, Grudziądzka 5, 87-100 Toruń, Poland*

<sup>2</sup>*UC Davis Eyepod Imaging Laboratory, Dept. of Cell Biology and Human Anatomy, University of California Davis, 4320 Tupper Hall, Davis, CA 95616, USA*

<sup>3</sup>*School of Optoelectronic Engineering and Instrumentation Science, Dalian University of Technology, No. 2 Linggong Road, Ganjingzi District, Dalian City, Liaoning Province 116024, China*

<sup>4</sup>*Department of Ophthalmology & Vision Science, University of California Davis, 4860 Y Street Suite 2400 Sacramento, CA 95817, USA*

\*[rjzawadzki@ucdavis.edu](mailto:rjzawadzki@ucdavis.edu)

**Abstract:** Several specialized retinal optical coherence tomography (OCT) acquisition and processing methods have been recently developed to allow *in vivo* probing of light-evoked photoreceptors function, focusing on measurements in individual photoreceptors (rods and cones). Recent OCT investigations in humans and experimental animals have shown that the outer segments in dark-adapted rods and cones elongate in response to the visible optical stimuli that bleach fractions of their visual photopigment. We have previously successfully contributed to these developments by implementing OCT intensity-based “optoretinograms” (ORG), the paradigm of using near-infrared OCT (NIR OCT) to measure bleaching-induced back-scattering and/or elongation changes of photoreceptors in the eye *in vivo*. In parallel, several groups have successfully implemented phase-based ORGs, mainly in human studies, exploiting changes in the phases of back-scattered light. This allowed more sensitive observations of tiny alterations of photoreceptors structures. Applications of the phase-based ORG have been implemented primarily in high speed and cellular resolution AO-OCT systems that can visualize photoreceptor mosaic, allowing phase measurements of path length changes in outer segments of individual photoreceptors. The phase-based ORG in standard resolution OCT systems is much more demanding to implement and has not been explored extensively. This manuscript describes our efforts to implement a phase analysis framework to retinal images acquired with a standard resolution and raster scanning OCT system, which offers much lower phase stability than line-field or full-field OCT detection schemes due to the relatively slower acquisition speed. Our initial results showcase the successful extraction of phase-based ORG signal from the B-scans acquired at ~100 Hz rate and its favorable comparison with intensity-based ORG signal extracted from the same data sets. We implemented the calculation of phase-based ORG signals using Knox-Thompson paths and modified signal recovery by adding decorrelation weights. The phase-sensitive ORG signal analysis developed here for mouse retinal raster scanning OCT systems could be in principle extended to clinical retinal raster scanning OCT systems, potentially opening doors for clinically friendly ORG probing.

© 2021 Optical Society of America under the terms of the [OSA Open Access Publishing Agreement](#)



## 1. Introduction

OCT is an optical imaging method relying on the interference of a reference light with light back-scattered from the sample allowing depth-resolved measurements of back-scattering profiles (A-scans). Acquisition of many A-scans mapped over imaged region allows three-dimensional (3D) visualization of semitransparent tissue [1–3]. Over the last decade, OCT became a gold standard in the non-invasive evaluation of the volumetric structure of the eye. With the increasing need for improved sensitivity of ocular diagnostic, the simple measurements of tissue morphology, based on light scattering intensity alone, are often insufficient. Several functional extensions of OCT have been developed, over the years, that offer different contrast, greatly improving sensitivity for ocular diagnosis. These include Doppler OCT [4–7], OCTA [8], STdOCT [9], OCE [10,11], polarization-sensitive OCT [12], and spectroscopic OCT [13]. However, all these methods do not directly measure tissue functions but rather higher-order optical properties of tissue beyond simple scattering potential (blood flow, birefringence, absorption).

There are several functional objective tests of ocular tissue that extract light-evoked responses of the retina. These measurements include electroretinograms (ERGs) that measure light-evoked changes in the electrical activity of the retina. Following the same paradigm, there have been many successful attempts to observe light-evoked changes in the retina using optical imaging only [14–26]. This paper uses the term “optoretinogram” (ORG) to describe the light-evoked photoreceptor function measured by OCT. The term ORG was initially coined by Don MacLeod [27] and recently adopted by other investigators [28–32] for the paradigm of using NIR OCT to measure bleaching-induced back-scattering and/or elongation changes in the eye in vivo noninvasively. The name ORG draws an instructive parallel to the ERG, which has long been used to assess retinal function in vivo. Specifically, the ORG, like the ERG, comprises multiple components arising from distinct cells and mechanisms. Moreover, both ERG and ORG require an explanation of the underlying cellular and molecular mechanisms to achieve their full scientific and clinical utility. The most recent measurements of light-evoked intrinsic signals in photoreceptors can be divided into two categories, one extracting changes in retinal/photoreceptors reflectivity [33–36] and the other extracting changes in photoreceptors morphology. The latter splits into sub-categories: phase-based methods [17,26,28–31,37–41] and intensity-based methods [32,42,43]. Application of the phase-based ORG has been implemented mostly in cellular resolution AO-OCT systems that can visualize the photoreceptor mosaic allowing phase measurements of path length changes in outer segments of individual photoreceptors. All these methods required dedicated image acquisition systems (cellular resolution (3–4  $\mu\text{m}$ ) or ultrahigh acquisition speed (MHz)), often not available in the current generation of clinical retinal imaging systems. However, the ultimate goal for this work should result in the implementation of light-evoked functional retinal tests using commercial OCT setups. In the OCT systems with standard clinical resolution (10–15  $\mu\text{m}$ ) and acquisition speed ( $\sim 100$  kHz), the phase-based ORG is much more demanding to implement and explore because the systems cannot resolve individual photoreceptors and show instead speckle pattern corresponding to groups of cells [44], with no meaningful phase information due to temporal speckle decorrelation. However, a framework implemented to study phase-based light-evoked photoreceptor activity (ORG) with full-field swept-source optical coherence tomography (FF-SS-OCT) [29] proves that phase comparison between decorrelated speckle patterns is still possible by utilizing a series of images acquired before full decorrelation.

The main problem in implementing such a framework to raster scanning systems with standard acquisition speed is that the signal decorrelates very fast (tens of ms) due to saccadic and axial eye movements [41], which results in loss of phase-based ORG signals. Many groups have made a substantial effort to develop eye tracking and eye motion correction to reduce or remove tissue motion, allowing phase-sensitive measurements over seconds [45]. In intensity-based ORG measurements on mice, we observed that the light-evoked changes of the retina morphology continue over several seconds to minutes (an order of magnitude longer than in human studies).

Therefore, phase-based analysis in mice faces challenges such as tissue movements caused by breathing, heartbeat, and eye drift, which are inevitable even after anesthesia.

In this paper, we describe the application of the modified Knox-Thompson method [46], where the cross-correlation of the phase difference between the measured layers of the object allows identification of the areas in which phase decorrelation occurs. In general, the method assembles the ORG signal from the most correlated elements of the inter-layer differential phase signal measured over time [47]. This work presents an evaluation of noise in phase-based length measurements in the sample consisting of a microscope coverslip and in a mouse retina *in vivo*. We also show that the ORG measurements, despite the relatively slow acquisition speed (equal to 100 kHz for A-scans and 100 Hz for B-scans), combined with the modified Knox-Thompson method, allow reconstruction of the phase-based ORG signal of the retina in an anesthetized mouse.

Several anatomical differences between mouse and human photoreceptors (both rods and cones) result in different appearances of the photoreceptor bands as measured by OCT. In human retinal imaging, cones reflectance provides a dominant signal and thus is naturally investigated for ORGs. On the other hand, human rods are much more challenging to image and analyze due to their lower reflectivity and size, but there are efforts to measure ORGs in rods [38]. There is no distinct difference between rods and cones reflectivity in mice, making the separation of two classes of photoreceptors very challenging. Additionally, due to the composition of the mouse retina (rod dominant), the measured ORG signal is believed to come mostly from rods. There are, however, efforts to measure cone ORGs in mice, and proposed phase-based analysis might provide access to the cone-based ORGs in mice [32].

The phase-sensitive ORG signal analysis presented here could be in principle extended to clinical retinal raster scanning OCT systems, potentially opening doors for clinically friendly ORG probing.

## 2. Methods

This paragraph will briefly describe details of our experimental system, including ORG data acquisition procedure and presentation of the main components of phased-based ORG processing.

### 2.1. Experiments in the living mice

All mouse husbandry and handling were in accord with protocols approved by the University of California Animal Care and Use Committee, which strictly adheres to all National Institutes of Health guidelines. Mice (B6-albinos (B6(Cg)-Tyr<sup>c</sup>-2J/J)) were obtained from Jackson Labs. A contact lens and gel (GelTeal Tears, Alcon) were used to maintain corneal transparency. All ORG experiments were performed in a darkroom. During the experiment's mice were anesthetized with 2% isoflurane delivered in O<sub>2</sub>, and maintained on a heated, adjustable platform adjacent to the imaging apparatus, as described previously [48].

### 2.2. Experimental system

For *in vivo* imaging of the mouse retina, we used a custom multimodal system with OCT and SLO sharing the same scanning system for simultaneous imaging of the retina. In the experiments here, only horizontal scanning is on without vertical scanning. Each horizontal scan collects 1024 pixels for SLO and 1024 A-scans for OCT at a 100 kHz rate. The SLO subsystem is equipped with a 488-nm laser (Coherent, 488-30FP) with an external trigger that enables precise control of light delivery during scanning. The SLO was used to deliver precisely calibrated 488-nm bleaching exposures. The SLO laser power was set to 4.7  $\mu$ W at the mouse pupil. A single SLO scan (50 degrees) at this power bleaches  $\sim$ 10% of the rhodopsin. The NIR Fourier domain-OCT system has a superluminescent diode light source (Superlum, T-860-HP) with an 82-nm bandwidth (effective fullwidth at half maximum [FWHM] after Hann windowing) centered at 860 nm and



delivers 600  $\mu\text{W}$  at the mouse pupil. The total 860 nm light exposure during an imaging session produced negligible bleaching or activation of rhodopsin. The lateral resolution of the system was characterized as  $\sim 3 \mu\text{m}$  for SLO [49] and  $\sim 5 \mu\text{m}$  for OCT, respectively.

The timing protocol for the experiment described in this paper is different from our standard protocol for *in vivo* imaging of the rod ORG, consisting of a series of scanning cycles (each taking about  $\sim 0.92$  seconds) with 4 B-scans collected in each cycle. Standard ORG protocol, used in our previous work relying on intensity-based light-evoked signal extraction, includes repeated raster scanning of the retina over field-of-view (FOV) of  $50 \times 25$  degrees and a pixel sampling of  $512 \times 128$  pixels at 100 kHz A-scan rate; the OCT signal is collected only from 4 centered adjacent B-scans in each raster scan. Considering the scanner fly-back time and the software resetting time, the time interval between two raster scans is about 0.92 s [32] which is  $\sim 100$  times slower than what we present here. Instead, the data is collected in a BM-scan mode, where consecutive B-scans are acquired over the same spatial location at a 100 Hz frame acquisition rate. For the “stimulus ON” experiment, the 488 nm laser was triggered to deliver the bleaching exposure for  $\sim 1.4$  s between B-scans 129 to 270. The scanning continued for an additional  $\sim 40$  s (4,000 B-scans) to record the ORG response. The “stimulus ON” scanning protocol was designed to analyze the phase stability between B-scans and ensure all the rhodopsin is bleached during light stimulation.

### 2.3. Initial OCT signal processing

The OCT interferometer acquires back-scattered light from the sample arm and allows its interference with the reference arm light. A line camera detects the spectrally modulated spectrum of light that undergoes the typical A-scan reconstruction steps: fixed pattern noise subtraction followed by wavenumber linearization, dispersion mismatch compensation, and spectral shaping. Finally, the Fourier transformation produces a complex-valued A-scan [50]. Several such complex A-scans acquired by moving the imaging beam with a fast  $x$ -scanner are combined to create a two-dimensional complex OCT B-scan:

$$I(x, z, t) = FFT[I(x, k, t)] = A(x, z, t)\exp(-i\varphi(x, z, t)), \quad (1)$$

where FFT is Fourier Transformation,  $z$  – depth coordinate of the pixel,  $x$  – lateral pixel position defined by  $x$ -scanner position,  $A$  – signal amplitude,  $\varphi$  – signal phase.

### 2.4. Intensity-based processing of ORG signals in mice

The intensity-based processing of ORG signals in mice has been described in detail previously [32]. Here we just highlight its major components: the center 60%–80% (600–800 A-scans) portion of the BM-Stack was manually selected, then it was divided into sub-stacks, each with 20 A-scans widths, they were cross-correlated, axial position corrected and averaged, then, the averaged A-scans were interpolated axially to increase digital sampling to  $0.1 \mu\text{m}/\text{pixel}$  and further cross-correlated, and axial position corrected in the time direction to form a kymography flatten to BrM. Finally, the peak positions and peak intensities of BrM, ELM, ISOS, and other layers of interest were calculated using gaussian fit of individual layers to allow comparison with ORG extracted using phase-based processing. Note that the axial peak position estimation method is similar to the centroiding methods used in photoactivated localization microscopy (PALM), one of the super-resolution microscopy techniques [51]. Therefore, we can achieve sub-micron sensitivity of peak position shifts between individual OCT layers.

### 2.5. Phase-based processing of ORG signals

The phase-based processing of ORG signals in mice has been implemented to improve the sensitivity of ORG measurements (change in thickness of photoreceptor structures). In general,

we expect phase-based position detection methods to be more sensitive in OCT processing than intensity-based position detection methods. Figure 1. shows an outline of phase-based processing of ORG signals with visualization of intermediate results. In the first step to extract phase information from layers of interest, an intensity-based OCT segmentation is performed by semi-automatic procedure derived from the work of Yin [52]. Initially, manual segmentation is performed on one specific Intensity B-scan to define the layer of interest. For all other B-scans, segmentation is performed automatically by an iterative Monte-Carlo method minimizing a cost function based on intensity changes between the line and its envelope (so-called double-line algorithm). After this intensity segmentation, we obtain reference positions for the phase processing. We refer to them as lay1 and lay2 for two retinal layers, respectively. To observe phase changes between two segmented layers in time  $t$ , we adopted the method of cross-spectra analysis first proposed by Spahr et al. [47]. Cross-spectrum is a two-dimensional representation of time-dependent phase-correlation between complex numbers. We calculate the cross-spectrum of the time evolution of a point with coordinates  $x$  and  $z$ , as:

$$U_{lay}(x, z, t, \Delta t) = I(x, z, t) \cdot I(x, z, t + \Delta t)^*, \quad (2)$$

where \* represents complex conjugate,  $\Delta t$ – the time interval between two B-scans (reference one, at time  $t$ , and time-shifted one at  $t + \Delta t$ ). An example visualization of the time evolution of the cross-spectrum phase from a single point in the retina (lay) is shown in Fig. 1(b).

Next, a phase difference between two spatially separated points (in our case, two layers of interest separated by a distance along the  $z$ -axis on an A-scan) is calculated by multiplying the cross-spectrum of the first layer with conjugation of cross-spectrum of the second layer, see Fig. 1(c):

$$U_{lay1/lay2}(x, t, \Delta t) = U_{lay1}(x, z_1, t, \Delta t) \cdot U_{lay2}(x, z_2, t, \Delta t)^*. \quad (3)$$

The difference signal between two layers  $U_{lay1/lay2}$  is averaged in space (over multiple A-scans) over window of size  $M$ , to improve the accuracy of phase difference estimation for ORG, see Fig. 1(d):

$$U_{lay1/lay2}^M(t, \Delta t) = \frac{1}{M} \sum_{x \in M} U_{lay1/lay2}(x, t, \Delta t), \quad (4)$$

$M$  – number of pixels used for averaging. The main advantage of cross-spectrum is the opportunity to separate less correlated speckle from a well-defined phase signal easily. We achieve that by use of the weights  $w$  defined below and visualized in Fig. 1(e):

$$w(t, \Delta t) = \frac{\left| \sum_{x, z \in M} U_{lay1/lay2}(x, t, \Delta t) \right|}{\sum_{x, z \in M} |U_{lay1/lay2}(x, t, \Delta t)|}. \quad (5)$$

The weights  $w$  can be interpreted as the phase correlation between points within the window  $M$ . The weights  $w$  has the value of 0 for totally random phase shifts and 1 for fully coherent phase shifts. Next, we calculate  $w^2$  for easier visualization of phase correlations, and we use it for thresholding of the  $U_{lay1/lay2}^M$ . The threshold was selected experimentally on the level  $th = 0.02$ . In our experiments, this thresholding removed  $\sim 55\%$  of the most decorrelated pairs of B-scans (separated by  $\Delta t$ ) in mouse data and  $\sim 14\%$  of the final phase ORG signal. A real-valued weights  $b$ , shown in Fig. 1(f), used to extract well-defined regions of phase cross-spectrum are defined below:

$$b(t, \Delta t) = \begin{cases} 1 & \text{for } w^2(t, \Delta t) > th \\ 0 & \text{for } w^2(t, \Delta t) \leq th. \end{cases} \quad (6)$$

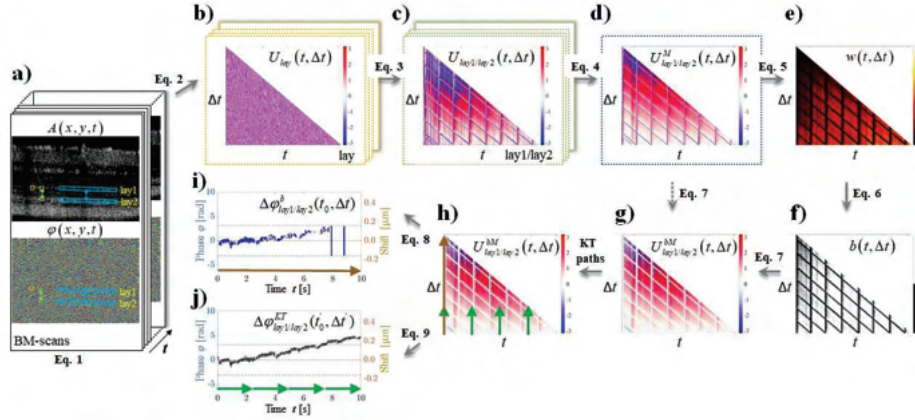


**Fig. 1.** Outline of the processing steps for phase-based ORG signal extraction, with visualization of intermediate results. (a) OCT BM-Scans. (b) Time evolution of the cross-spectrum phase from single point in the retina (lay), representative position of point is marked by orange rectangle in (a). (c) Time evolution of a phase difference of the cross spectrum between two spatially separated points from two layers (lay1 & lay2), representative position of points is marked by two green rectangles in (a). (d) Time evolution of a phase difference of the averaged cross spectrum, over window of size  $M$ , between two spatially separated layers (lay1 & lay2), representative position of windows is marked by two blue rectangles in (a). (e) Weights  $w$  showing phase correlation between points within the window  $M$ . (f) Binary-valued weights  $b$ , calculated to extract well-defined regions of phase cross-spectrum. (g) Reduced weighted time evolution of a phase difference of the averaged cross spectrum from (d). (h) Visualization of phase extraction paths from g, brown arrow (along the first (left) vertical line) and green arrows (using the Knox-Thompson paths). (i) Time-dependent phase difference between two layers extracted using single path. (j) Time-dependent phase difference between two layers extracted using the Knox-Thompson paths. See Eq. (1–9) in text for details regarding mathematical operations.

Providing the reduced weighted cross spectra between layers 1 and 2 over window  $M$ , see examples in Fig. 1(g), Fig. 7(c), Fig. 9(c), Fig. 10(c), and Fig. 11(a,d,g,j):

$$U_{lay1/lay2}^{bM}(t, \Delta t) = b(t, \Delta t) \cdot U_{lay1/lay2}^M(t, \Delta t). \quad (7)$$

The regions where  $U_{lay1/lay2}^{bM}$  was reduced to zero (created by zeros in the weights  $b$  (Eq. (6)) were interpolated using an averaged value from ten nearest points ( $\pm 5 \Delta t$ ), resulting in weighted corrected cross-spectra  $U_{lay1/lay2}^{cM}$ . This worked well for the  $U_{lay1/lay2}^{cM}$  values near the base ( $\Delta t = 0$ ), which is sufficient for Knox-Thompson reconstruction.

To extract time-dependent phase difference between two layers using weighted corrected cross spectra, which is needed for ORG signal extraction, one needs to define the reference time  $t_0$ . Once this is done, the ORG signal can be reconstructed using:

$$\Delta\varphi_{lay1/lay2}^b(t_0, \Delta t) = \arg(U_{lay1/lay2}^{cM}(t_0, \Delta t)), \quad (8)$$

where  $t_0$  is the reference time when phase measurements start, see Fig. 1(i). Designation “arg” is the operation to extract phase from complex signals or complex numbers. This represents the phase extraction along the first (left) vertical column in the weighted corrected cross-spectra. This method of ORG extraction produced good results for short time intervals  $\Delta t$ , but it is not sufficient for long-term monitoring of ORG.

In order to improve ORG signal fidelity over larger time intervals, the final phase signal  $\Delta\varphi_{lay1/lay2}^{KT}$  was computed using the Knox-Thompson paths [46,47]. The number of paths has been selected in such a way that allowed phase wrapping and decorrelated region (Fig. 1(h)). Signal reconstruction was done by assembling Knox-Thompson paths of length  $p$  between B-scans indicated with arrows. The total number of Knox-Thompson paths  $\Pi$  is given by:  $\Pi = Z_{quotient}(\Delta t_{max}/(p \cdot \Delta t_{min}))$ , where  $\Delta t_{max}$  is the total measurement time. Current Knox-Thompson path number  $\delta$  for time difference  $\Delta t$  is defined as  $\delta = Z_{quotient}(\Delta t/(p \cdot \Delta t_{min}))$  where  $\Delta t_{min}$  is the time step between two consecutive B-scans. Then we define  $\Delta\varphi_{lay1/lay2}^{KT}$  as a phase difference at the end of  $\delta$ -th of Knox-Thompson paths, see Fig. 1(j):

$$\Delta\varphi_{lay1/lay2}^{KT}(t'_0, \Delta t') = \begin{cases} \arg[U_{lay1/lay2}^M(t'_0, \Delta t')], & \text{for } t'_0 < \Delta t' \leq \Delta t'_{KT} \\ \arg[U_{lay1/lay2}^M(t'_0 + \delta \cdot \Delta t'_{KT}, \Delta t' - \delta \cdot \Delta t'_{KT})] + \\ \frac{1}{t_N} \sum_{m=0}^{\delta-1} \sum_{j=\Delta t'_{KT}-t_N}^{\Delta t'_{KT}} \arg[U_{lay1/lay2}^M(t'_0 + m \cdot \Delta t'_{KT}, j)], & \\ \text{for } \delta \cdot \Delta t'_{KT} < \Delta t' \leq (\delta + 1) \cdot \Delta t'_{KT}, \delta = 1, \dots, \Pi - 1, \end{cases} \quad (9)$$

where  $t'_0$ ,  $\Delta t'$ ,  $\Delta t'_{KT}$  are the indices of continuously varied times  $t_0$ ,  $\Delta t$ ,  $\Delta t_{KT}$ . Note that  $\Delta t_{KT} = p$ , and  $t_N$  is the number of pixels taken at the end of the previous arrow to obtain an average value to be added to consecutive Knox-Thompson paths.  $t_N$  should be small so that it does not extend towards  $U_{lay1/lay2}^{cM}$  dominated by zeros, which would change the final calculated phase. In our measurement, we took five pixels  $t_N$  at the end of each KT arrow, and we added the mean value from these pixels to the next arrow of the Knox-Thompson path;  $m$  indicates consecutive phase arrows with signal extracted from previous  $(\delta-1)$ -th Knox-Thompson paths. This ensured a reduction in phase bias.

Binarization function  $b$  was computed the similar way as  $\Delta\varphi_{lay1/lay2}^{KT}$  by path collection from  $\Pi$  Knox-Thompson paths:

$$b(t'_0, \Delta t') = \begin{cases} b(t'_0, \Delta t'), & \text{for } t'_0 < \Delta t' \leq \Delta t'_{KT} \\ b(t'_0 + \delta \cdot \Delta t'_{KT}, \Delta t' - \delta \cdot \Delta t'_{KT}), & \\ \text{for } \delta \cdot \Delta t'_{KT} < \Delta t' \leq (\delta + 1) \cdot \Delta t'_{KT}, \delta = 1, \dots, \Pi - 1. \end{cases} \quad (10)$$

The phase differences with weights are then defined as:

$$\Delta\varphi_{lay1/lay2}^{b,KT}(t'_0, \Delta t') = b(t'_0, \Delta t') \cdot \Delta\varphi_{lay1/lay2}^{KT}(t'_0, \Delta t'). \quad (11)$$

Finally, the time-dependend layer displacement can be calculated from:

$$\Delta_{lay1/lay2}(t) = \lambda_0 \cdot \frac{\Delta\varphi_{lay1/lay2}^{b,KT}(t)}{4\pi n}, \quad (12)$$

where  $n$  – refractive index of tissue,  $\lambda_0$  – light source central wavelength. In our experiments, we assigned BrM to layer 1 and ELM to layer 2 to extract time-dependent phase-based ORG signals.

## 2.6. Phase-based distance measurements error

The theoretical sensitivity of phase difference measurements depends on two components. The first component is defined by the signal-to-noise ratio of OCT data [53,54]. In the case of the ORG measurements, since we compare phases between two layers, SNR of each layer needs to

be taken into account:

$$\sigma_{\Delta\text{ph,ORG}} = \sqrt{\frac{1}{2\text{SNR}_{\text{lay1}}} + \frac{1}{2\text{SNR}_{\text{lay2}}}} = \sqrt{\frac{1}{\text{SNR}_{\text{lay12}}}}. \quad (13)$$

where  $\text{SNR}_{\text{lay}} = 20 \cdot \log(\text{lay}/\sigma_{\text{noise}})$ . The SNR was calculated from segmented layers 1 and 2 (signal) and pixels outside the sample (noise) using amplitudes in a region of interest.

The second component is defined by a reduction in coherence between two phase measurements. In classical Doppler measurements, the reduction of coherence is simulated by phase error caused by lateral displacement,  $\Delta x$  between two consecutive phase measurements acquired with the beam of diameter  $d$  [53,54]:

$$\sigma_{\Delta x} = \sqrt{\frac{4\pi}{3} \left( 1 - \exp\left(-2\left(\frac{\Delta x}{d}\right)^2\right)\right)}. \quad (14)$$

This results in the total phase sensitivity estimation of:

$$\sigma_{\text{phase, Doppler}} = \sqrt{\sigma_{\Delta\text{ph, Doppler}}^2 + \sigma_{\Delta x}^2}. \quad (15)$$

Note that from Eq. (14), the maximum value of Doppler phase error calculated between two totally decorrelated measurements ( $d \gg \Delta x$ ) should be equal to  $\sqrt{4\pi/3}$  rad. Considering Eq. (12) and our central wavelength of 860 nm, this translates to  $\sigma_{\Delta x, \text{max}} \sim 105$  nm. In the ORG measurements, the phase difference is calculated between two points separated in space, not in time. This means that the phase variance of the ORG signal calculated between two positions should depend on how correlated the two fields are. Resulting in the experimental values consistently higher than theoretical phase variance estimation  $\sigma_{\Delta\text{ph, ORG}}$  for correlated fields:

$$\sigma_{\text{phase, ORG}} = \sqrt{\sigma_{\Delta\text{ph, ORG}}^2 + \sigma_{\text{incoherence}}^2}. \quad (16)$$

In the phase estimation presented here, two random independent speckle fields are used to calculate phase difference. Thus, we should expect to have the phase error  $\sigma_{\text{incoherence}}$  in the range of  $\sigma_{\Delta x, \text{max}}$ .

Another consequence of this phase decorrelation between two layers is that ORG signal averaging between different A-scans will not follow simple SNR-dependent improvement of phase sensitivity (with the square root of the number of averaged signals  $M$ ). Therefore, we decided to use a more elaborate Kernel to investigate the effect of averaging on ORG signal variance. We found experimentally that the following equation describes the improvement of differential phase error, due to A-scan averaging, very accurately (see Fig. 3):

$$\sigma_{\text{the/exp}} = \frac{\sigma}{a_{\text{the/exp}}\sqrt{M} + b_{\text{the/exp}}} + c_{\text{the/exp}}, \quad (17)$$

where  $\sigma$  is a phase sensitivity of a single ORG measurement for  $M = 1$  (theoretical “the”:  $\sigma_{\Delta\text{ph, ORG}}$  or experimental “exp”:  $\sigma_{\text{phase, ORG}}$ ),  $a_{\text{the/exp}}$ ,  $b_{\text{the/exp}}$ ,  $c_{\text{the/exp}}$  – fitting parameter from the least square method,  $M$  – number of averaged phase differences in space (over multiple A-scans). This ORG phase error estimation should not apply to the adaptive optics (AO) based ORG measurements where the ORGs from individual photoreceptors are measured, and one expects to have a good phase correlation between two axial positions within the same photoreceptor.

### 3. Results

#### 3.1. System stability characterization

The system was characterized by signal-to-noise ratio (SNR) and temporal phase stability. A measure of phase sensitivity or stability is given by the standard deviation of the measured phase



differences. Figure 2 showcases the effect of the galvo-scanner jitter quantified by measurements of phase sensitivity under three conditions: (cond. I) galvo-scanner powered off, 4000 BM-scans of a coverslip glass plate, (cond. II) galvo-scanner powered on, and linear scan of a coverslip glass plate, 4000 BM-scans, and (cond. III) a galvo-scanner powered on and linear scan of the living mouse retina. The first column of the Fig. 2 shows an example of OCT intensity B-scans for three experiments. The following two columns show the time-varying phase extracted from the OCT data over the whole duration of the experiment (40 s) and the zoomed-in portion (2 s). The fourth column shows temporal Phase Power Spectrum (FFT of phase signals from layers 1–2 and the phase difference between layers), and the fifth column shows a phase histogram for corresponding data sets. For absolute phase variation, the phase on the front surface of coverslip over time was obtained for conditions (cond. I) and (cond. II) in a BM-scan. For (cond. III), the phase in the same spatial location on a layer in mouse retina in each BM-scan was obtained along the time. Note, that cond. I and cond. II represent static sample, while cond. III represent moving sample (living mouse retina). The theoretical sensitivity  $\sigma_{\text{the}}$  (calculated using SNR) of the raw phase for one A-scan was equal to 0.04, 0.19, and 0.24 radians respectively for the three conditions (cond. I), (cond. II) and (cond. III). The standard deviation of the measured raw unreferenced phase over time was equal to 0.20, 1.03, and 1.30 radians, respectively for the three conditions (cond. I), (cond. II), and (cond. III), confirming deviation from shot-noise limited detection of the phase.

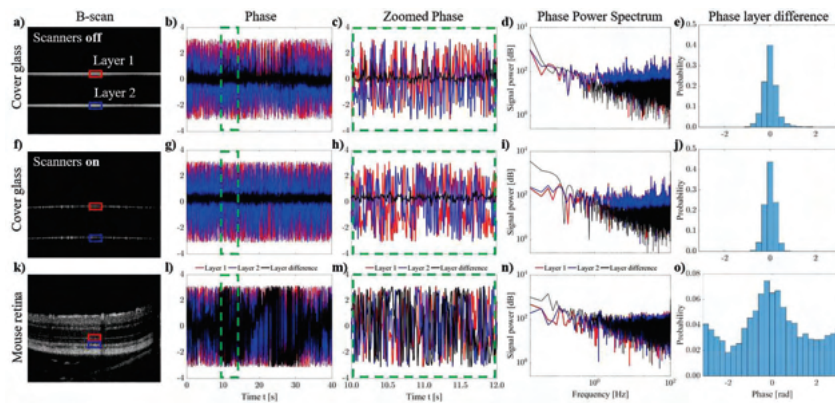


**Fig. 2.** Signal analysis of the temporal phase stability. The first column presents an example of one OCT B-scan, from series of BM-scans, for glass plate (a, f) and mouse retina (k). The second column presents phase stability for edges of the coverslip glass in the sample channel with the scanners off (b) and on (g), and for layers in a scanned mouse retina (l). Red and blue colors correspond to phase calculated from layers 1 & 2 marked by rectangles with corresponding colors in (a, f, k). The black line shows the phase difference between the signal from layers 1 and 2. The third column presents the magnified phase results from (b, g, l) - seconds 10 to 12 marked by a dashed green line. The fourth column shows temporal Phase Power Spectrum (FFT of phase signals from layers 1–2 and the phase difference between layers). The fifth column shows a phase histogram for corresponding data sets.

In order to showcase that our phase stability was not negatively affected by the time interval between phase measurements and to show that our system is phase stable, we compared our previously measured temporal phase stability between B-scans to temporal phase stability between A-scans. This resulted in two orders of magnitude reduction in the time interval between phase measurements. Figure 3 shows an analysis of differential phase stability in this case for the microscope coverslip and both galvo scanners powered off (cond. I). Note that Fig. 3(c) shows



virtually the same differential phase histogram as shown previously for longer time intervals in Fig. 2(e,j) for conditions (cond. I) and (cond. II).

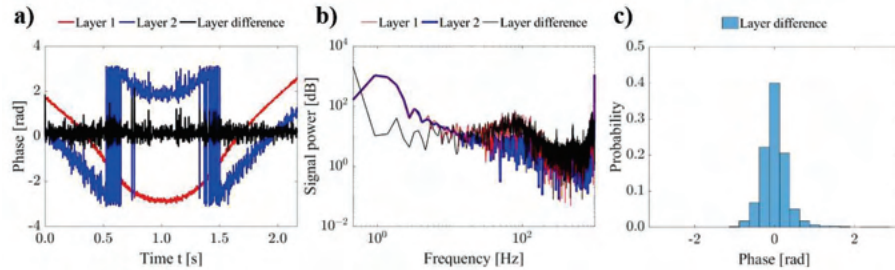


**Fig. 3.** Signal analysis of temporal phase stability for 100 kHz A-scan acquisition (cond. I). (a) Phase stability for edges of the coverslip glass in the sample channel with the scanners off. Red and blue colors correspond to phase calculated from layers 1 & 2 marked by rectangles with corresponding colors in Fig. 1(a). The black line shows the phase difference between layers 1 and 2. (b) Temporal Phase Power Spectrum (FFT of phase signals from layers 1–2 and for the phase difference between layers). (c) Histogram for phase difference.

### 3.2. Effect of averaging on phase-based processing

To estimate the effect of averaging on differential phase measurement error, we evaluated data acquired with cond. I) galvo-scanner powered off, acquired at coverslip glass plate, and cond. III) a galvo powered and linear galvo scan of the mouse retina. The changes in phase stability as a function of number averaged A-scans were measured and fitted using Eq. (17). Figure 4 summarizes these results for both theoretical (SNR based:  $\sigma_{\Delta\text{ph, ORG}}$ ) and experimental (direct:  $\sigma_{\text{phase, ORG}}$ ) differential phase error estimation.

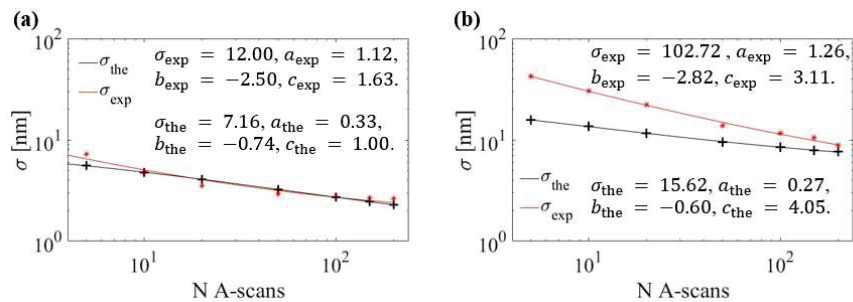


**Fig. 4.** Estimation of phase noise theoretically – SNR-based (red line) and experimentally (black line) for a glass plate with scan off (a) and mouse retina with scan on (b). Coefficient of determination for (a) and (b) is equal  $R^2 = 0.99$ .

The results shown in Fig. 4 allow us to estimate the phase error  $\sigma_{\text{incoherence}}$  using Eq. (16), due to decorrelation between two layers. This error is equal to  $\sim 9.6$  nm and  $\sim 102$  nm for glass plate and mouse retina differential phase measurements, respectively. This result is expected since reflections of two surfaces of a glass plate should be well correlated while scattering between two retinal layers should be decorrelated. Another interesting observation is that averaging of A-scans allows a very efficient reduction of the differential phase error bringing the

theoretical limit of improvement by averaging to the same range (see from (Eq. (17))  $c_{\text{exp}}$  and  $c_{\text{the}}$  for both measurements). This also showcases the need for averaging of differential phase measurements between A-scan when extracting light-evoked changes in layer thickness. The similar values of fitting parameters  $a_{\text{the/exp}}$ , and  $b_{\text{the/exp}}$  (both in SNR-based estimation and direct phase measurements) suggest that degree of differential phase decorrelation does not affect the averaging process.

### 3.3. Measurements of phase-based ORG signal

In our ORG measurements, the light-evoked changes in retinal activity are measured as the relative swelling of the outer retina, which is extracted by measuring a change in relative distance between the BrM and ELM directly proportional to the phase difference (Eq. (12)). However, a simple calculation of the phase change between the first and subsequent B-scans is not feasible due to the OCT signal decorrelation (within the same layer) over time. This signal decorrelation (due to the eye movements and tissue internal dynamics) causes the measured phase differential signal to disappear, as shown in [Visualization 1.avi](#) and [Visualization 2.avi](#). Selected frames are shown in Fig. 5 and Fig. 8, where we can see that for a time difference of  $\Delta t = 0.01$  s, the phase difference between two B-scans is well defined. After 11 seconds, the common phase information between the same structures in the 1<sup>st</sup> and 1060<sup>th</sup> B-scan has decreased, manifested by a low phase difference signal (phase difference becomes random). This is why the use of periodic signal self-referencing is necessary to allow the comparison of successive phase differences over a longer time.

#### 3.3.1. Control experiment (no light stimulation)

ORG control experiment measured changes in the relative swelling of the outer retina (distance between the BrM and ELM) without any visible light stimulation. The only source of bleaching is the imaging OCT light itself. Figure 5 showcases the phases stability during the experiment performed over 40 s acquisition window.

The problem of time-dependent signal decorrelation observed in Fig. 5. can be solved using phase analysis employing Knox-Thompson paths [46]. The light-induced retinal activity in the mouse retina was mapped as the time-dependent change in outer retina thickness (between ELM and BrM). These reference layers were presented in Fig. 2, Fig. 5, and Fig. 8. For comparison, we measured the light-evoked activity using our previously developed intensity-based methods and newly developed phase-based method, as described in section §2.7. In order to allow phase-based ORG signal extraction, we calculated cross-spectra differences  $U_{\text{lay1/lay2}}^{M=150}$  from 150 A-scans (from 350<sup>th</sup> A-scan to 500<sup>th</sup> A-scan). The number of the A-scans that need to be averaged will depend on the OCT signal intensity and phase stability of the optical system. Figure 4 shows the change of the phase noise level depending on the number of averaged A-scans. According to Eq. (17), we can estimate the theoretical phase error depending on the number of averaged A-scans, corresponding to the accuracy of the phase-based ORG signal. We have chosen the number of A-scans to be averaged based on the difference between the experimental standard deviation of phase and the theoretical phase error levels. We found that the number of A-scans around 150 (see  $c_{\text{exp}}$  and  $c_{\text{the}}$  in Fig. 4(b)) provide the smallest difference. Figure 6(a) and Fig. 9(a) show examples of the cross-spectrum before averaging. Based on this, we conclude that solid ORG responses could be traced with a low number of averaged A-scans, while weak ORG responses would require a large number of averaged A-scans.

The range of A-scans used to extract the ORG signal is indicated in Fig. 5(a). As a control experiment, the results of phase-based ORG signal extracted from 40 sec. acquisition without light stimulation are presented in Fig. 6. The phase difference signal from a single A-scan was characterized by a standard deviation  $\sigma_{\text{in}}$ . The  $\sigma_{\text{in}}$  varied from A-scan to A-scan in the range of 1.0–2.1 rad (51–107 nm). This variation in  $\sigma_{\text{in}}$  is probably due to the local tissue properties of

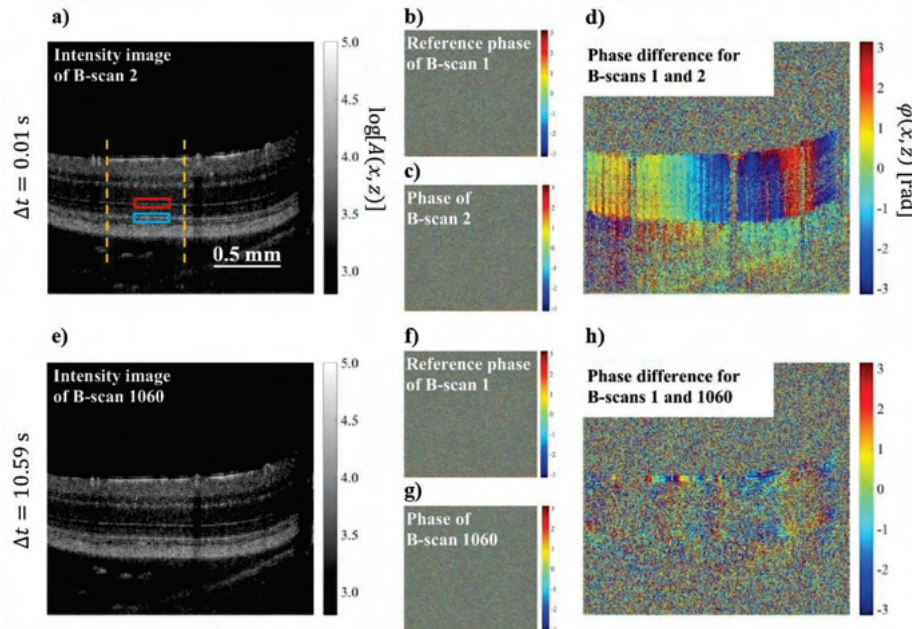


**Fig. 5.** Phase stability during measurement of a mouse retina. (a & e) The OCT intensity in  $\log_{10}$  scale of B-scan #2 and #1060 was collected in time 0.01 s and 10.59 s from the first reference B-scan. The red and blue rectangles indicate ELM and BrM layers accordingly. The yellow dashed lines presented a range of A-scans that were taken to analyze with Knox-Thompson paths. (b & f) Reference phase of first B-scan in radians. The color scale bars (b-d & f-h) indicate values of phase from  $-\pi$  to  $\pi$  from blue to red, respectively. (c & g) The phase of B-scans collected in time 0.01 s and 10.59 s from the first reference B-scan, respectively. (d & h) The phase difference between phases of first reference B-scan and B-scan collected after time interval  $\Delta t$ . The phase stability over time is presented in Visualization 1.avi.

ELM and BrM and represents a varying contribution of back-scattering and back-reflection from these structures. Low  $\sigma_{\text{lin}}$  corresponds to reflection dominant signal, and high  $\sigma_{\text{lin}}$  corresponds to scattering dominant signal (see a change in ELM and BrM brightens depending on the lateral position of A-scans in Fig. 5(a,e)). This is why spatial signal averaging was needed to reduce the phase variance, as presented in Fig. 6(b). The spatial averaging over  $M = 150$  A-scans reduced the standard deviation of phase difference to  $\sigma_{\text{lin}} = 0.19\text{--}0.39$  rad (10–20 nm), depending on the specific A-scans used for averaging. The initially constant phase difference (before light stimulation) is associated with the baseline “dark adapted” state of the retina and can be visible in the averaged image Fig. 6(d), better depicted in the portion of the experiment acquired during the first 10 s Fig. 7(d).

The phase ORG signal in Fig. 6 was reconstructed using  $\Pi = 5$  Knox-Thompson paths corresponding to  $\Delta t_{\text{KT}} = 8$  s. The phase ORG signal in Fig. 7 was reconstructed using  $\Pi = 10$  Knox-Thompson paths corresponding to  $\Delta t_{\text{KT}} = 4$  s. The thresholding on  $\Delta\varphi_{\text{lay1/lay2}}^{\text{KT}}$  signal for  $\Delta t_{\text{KT}} = 8$  s removed 3% of the least correlated phase and 26% of data from a total phase of  $U_{\text{lay1/lay2}}^{M=150}$ . The thresholding on zoomed  $\Delta\varphi_{\text{lay1/lay2}}^{\text{KT}}$  signal for  $\Delta t_{\text{KT}} = 4$  s removed 2% of the least correlated phase and 5% of data from a total phase of  $U_{\text{lay1/lay2}}^{M=150}$ . The phase-based ORG

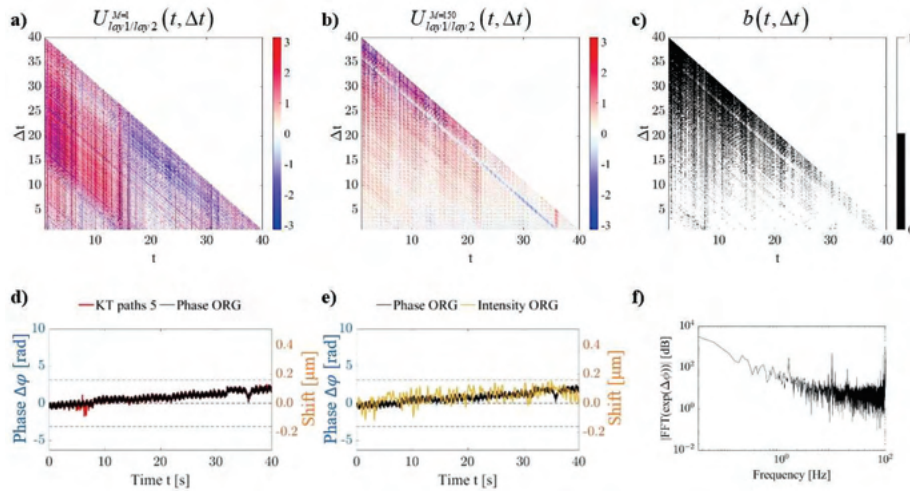


**Fig. 6.** The results of the control experiment (no visible light stimulation) in the mouse retina with a distance between ELM and BrM layers followed over 40 s. (a) The phase of  $U_{lay1/lay2}^{M=1}$  cross-spectra layer differences for one A-scan. (b) Result of averaging  $M = 150$  cross-spectra differences  $U_{lay1/lay2}^{M=150}$  for ELM and BrM layers. A-scan range taken to average is shown in Fig. 4(a,c). (c) The binary map  $b$  was used to threshold and remove less correlated phasors. The white region indicates a well-defined phase signal that could be taken to analyze. (d) Comparison of Knox-Thompson signal without thresholding (red line) and with weights (black line). (e) Comparison ORG phase-based signal with ORG intensity-based signal. The ORG phase signal was reconstructed from  $\Pi=5$  Knox-Thompson paths. (f) Power spectrum (FFT of phase signals from ELM and BrM layers).

results are compared with averaged intensity-based ORG calculations for the same data set in Fig. 6(d,e) and Fig. 7(d,e) for shorter time evaluation. For comparison, the standard deviation for the phase-based ORG method, the variance of position difference between ELM and BrM intensity maxima, was  $\sigma_{lin} \sim 12$  nm (Fig. 7(e)). The standard deviation for the intensity-based ORG method, the variance of position difference between ELM and BrM intensity maxima, was  $\sigma_{lin} = 45$  nm ( $\sim 4$  times higher than for phase-based ORG method).

The increase in distance between ELM and BrM layers in this experiment represents the unwanted activation of photoreceptors by the NIR OCT imaging beam bleaching 0.01% of rhodopsin during the whole imaging session ( $\sim 12000$  B-scans ( $\sim 2$  min) in total, including the alignment, the pre-imaging scans, and the imaging acquisition). The method to calculate the bleach levels in mice was described in detail previously [55], and includes formulas for pigmented and albino mice. Briefly, the spectral power distribution function (W/nm) of the OCT light at the pupil was determined from the spectrometer, and the total power was measured by Thorlabs S120C photodiode with its wavelength setting at 860 nm. For calculation of bleaching, the spectral energy density was converted into rhodopsin-equivalent units, using a Lamb–Govardovskii [56,57], template for mouse rhodopsin, assuming the axial density of rhodopsin in mouse rods to be 0.35. Note that total elongation of ELM and BrM due to this continuous stimulation equaled 100 nm over 40 s and that it can be only seen on phase-based ORG analysis. Also, note that in this paper, we use serial B-scans for fast ORG signal measurement rather than serial volumes used in our standard intensity-based ORG signal measurements [32,43], when local bleaching by OCT light is 100x lower, and thus its effects are negligible. The periodic pattern seen on magnified,



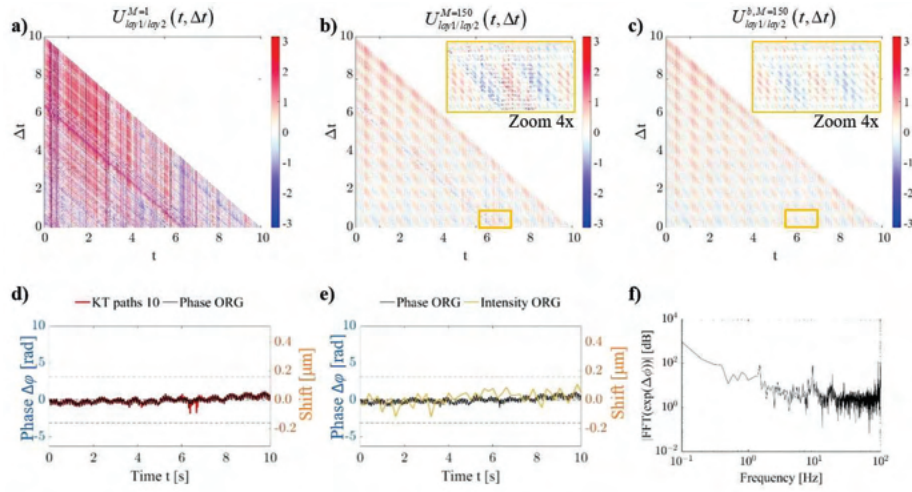


**Fig. 7.** Magnified results of the distance between ELM and BrM layers in the first 10 s without light stimulus. (a) The phase of  $U_{lay1/lay2}^{M=1}$  cross-spectra layer differences for one A-scan. (b) Result of averaging  $M = 150$  cross-spectra differences  $U_{lay1/lay2}^{M=150}$  for ELM and BrM layers. A-scan range taken to average is shown in Fig. 4(a). (c) The averaged  $U_{lay1/lay2}^{b,M=150}$  signal after thresholding to remove less correlated phasors. The yellow rectangles in (b-c) indicate a region where we can see decorrelated signal reduction using weights. (d) Comparison of Knox-Thompson signal without thresholding (red line) and with weights (black line). (e) Comparison ORG phase-based signal with ORG intensity-based signal. The ORG phase signal was reconstructed from  $\Pi=10$  Knox-Thompson paths. (f) The power spectrum for phase difference signal (FFT of time-varying phase signals from ELM and BrM layers).

and A-scan averaged cross-spectra in Fig. 7(c) is depicted by the power frequency analysis seen on Fig. 7(f) and corresponds to the modulations of 1.3 Hz and 9.5 Hz. The potential origins of these modulations are breathing and heartbeat, respectively. Their effect on phase-based ORG signal variance will be briefly discussed in the discussion and conclusions section.

### 3.3.2. Light evoked ORG experiment

After our baseline experiment (no visible light stimulation) present in the previous section, here we want to present our phase-based ORG analysis of ELM-BrM distance changes due to visible light stimulation. The bleaching light was introduced after 1.29 s from the start of the OCT acquisition. The stimulus continued for  $\sim 1.41$  s. Similar to previously observed time-dependent signal decorrelation depicted in Fig. 5 in our baseline experiment, here as well the same effect is evident as showcased in Fig. 8. To resolve this problem, we used the same phase analysis employing Knox-Thompson paths and mapping light-induced retinal activity as the time-dependent change in outer retina thickness (between ELM and BrM). Here as well the phase-based extraction of ORG signals was compared with the intensity-based method. To allow phase-based ORG signal extraction, we calculated cross-spectra differences  $U_{lay1/lay2}^{M=150}$  from 150 A-scans (from 350<sup>th</sup> A-scan to 500<sup>th</sup> A-scan). The range of A-scans used for our analysis is indicated in Fig. 8(a).

The results of the phase-based ORG signal extracted in the experiment with light stimulation are presented in Fig. 9 for the whole duration of the experiment. Here the ORG was reconstructed

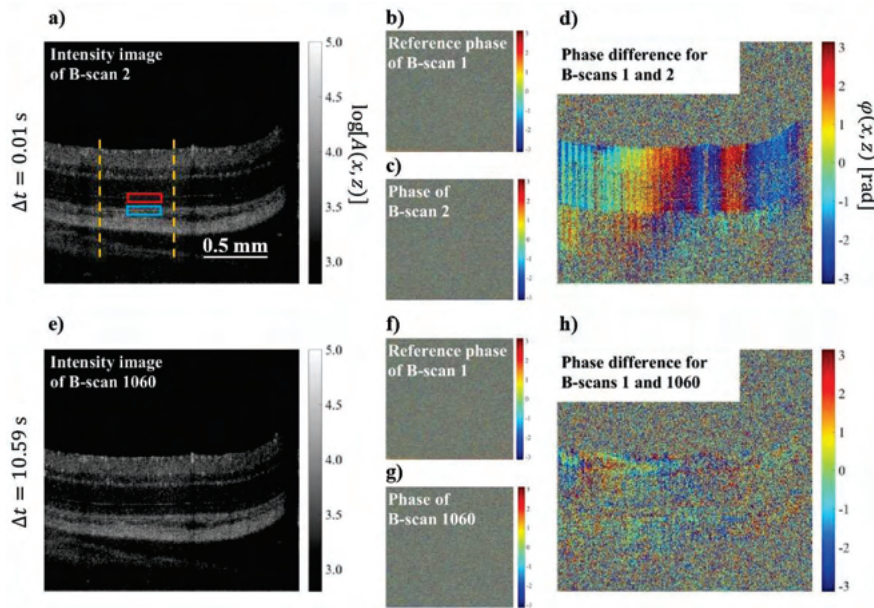


**Fig. 8.** Phase stability during measurement of the light-evoked responses of the mouse retina. (a & e) The OCT intensity in  $\log_{10}$  scale of B-scan #2 and #1060 was collected in time 0.01 s and 10.59 s from the first reference B-scan. The red and blue rectangles indicate ELM and BrM layers accordingly. The yellow dashed lines presented a range of A-scans that were taken to analyze with Knox-Thompson paths. (b & f) Reference phase of first B-scan in radians. The color scale bars (b-d & f-h) indicate values of phase from  $-\pi$  to  $\pi$  from blue to red, respectively. (c & g) The phase of B-scans collected in time 0.01 s and 10.59 s from the first reference B-scan, respectively. (d & h) The phase difference between phases of first reference B-scan and B-scan collected after time interval  $\Delta t$ . The phase stability over time is presented in [Visualization 2.avi](#).

using  $\Pi = 20$  Knox-Thompson paths corresponding to  $\Delta t_{KT} = 2$  s. The phase ORG signal in Fig. 10 was reconstructed using  $\Pi = 10$  Knox-Thompson paths corresponding to  $\Delta t_{KT} = 4$  s. The thresholding on  $\Delta\varphi_{lay1/lay2}^{KT}$  signal  $\Delta t_{KT} = 2$  s removed 15% of the least correlated phase and 58% of data from a total phase of  $U_{lay1/lay2}^{M=150}$ . The thresholding on zoomed  $\Delta\varphi_{lay1/lay2}^{KT}$  signal for  $\Delta t_{KT} = 4$  s removed 10% of the least correlated phase and 29% of data from a total phase of  $U_{lay1/lay2}^{M=150}$ . Figure 9(e) and Fig. 10(e) show the comparison of the ORG signals extracted with phase-based and intensity-based calculations. Here as well, the phase difference signal from a single A-scan was characterized by a standard deviation  $\sigma_{lin}$ . The  $\sigma_{lin}$  varied from A-scan to A-scan in the range of 1.0–2.4 rad (51–123 nm). After spatial signal averaging, the phase variance was reduced, as presented in Fig. 9(b) and Fig. 10(b). The spatial averaging over  $M = 150$  A-scans reduced the standard deviation of phase difference to  $\sigma_{lin} = 0.29$ – $0.67$  rad (15–34 nm), depending on the specific A-scans used for averaging. Note that the constant slope was removed to estimate the standard deviation of phase difference during light stimulation. The initial brief constant phase difference (before visible light stimulation) can be visible in the averaged image Fig. 9(d,e), better depicted in the magnified portion of the experiment acquired during the first 10 s Fig. 10(d,e). The standard deviation for phase-based ORG method, the variance of position difference between ELM and BrM intensity maxima, was  $\sigma_{lin} \sim 15$  nm (Fig. 10(e)). The standard deviation for



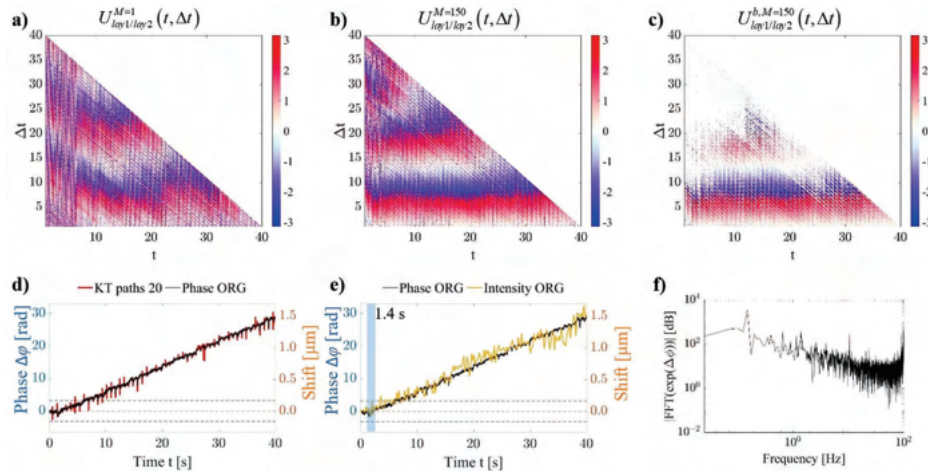


**Fig. 9.** The light-evoked activity of the mouse retina for ELM and BrM layers. (a) The phase of  $U_{lay1/lay2}^{M=1}$  cross-spectra layer differences for one A-scan with light stimulus. (b) Result of averaging  $M = 150$  cross-spectra differences  $U_{lay1/lay2}^{M=150}$  for ELM and BrM layers. A-scan range taken to average is shown in Fig. 8(a). (c) The averaged  $U_{lay1/lay2}^{b,M=150}$  signal after thresholding to remove less correlated phasors. (d) Comparison of Knox-Thompson signal without thresholding (red line) and with weights (black line). (e) Comparison ORG phase-based signal with ORG intensity-based signal. The ORG phase signal was reconstructed from  $\Pi=20$  Knox-Thompson paths. (f) The power spectrum for phase difference signal (FFT of phase signals from ELM and BrM layers).

the intensity-based ORG method, the variance of position difference between ELM and BrM intensity maxima, was  $\sigma_{lin} = 68$  nm,  $\sim 4$  times higher than for the phase-based ORG method.

The increase in distance between ELM and BrM layers in this experiment is much more evident than in our baseline studies due to the estimated total bleaching (100%) of photoreceptors rhodopsin during 1.41 s visible light exposure. Total elongation of ELM and BrM due to this stimulation equaled  $1.5 \mu\text{m}$  over 40 s (15 times more than in our baseline experiment), and that it can be easily seen on both phase-based and intensity-based ORG analysis. Note that here as well, the periodic pattern can be seen on zoomed and A-scan averaged cross spectra in Fig. 10(c), and that it is clearly depicted by the power frequency analysis seen on Fig. 10(f) and corresponds to the modulations of 1.3 Hz and 10.4 Hz, similar to the values observed in control experiment presented in section §3.3.1 and assigned to breathing and heartbeat, respectively.

### 3.3.3. Repeatability of phase-based ORG signal extraction

To showcase the repeatability of the phase-base ORG signal extraction, Fig. 11 shows the results of four more representative experiments (two without light stimulation and two with light stimulation).

These results confirm the improved accuracy of phased-based ORG signal extraction compared to our standard intensity-based ORG analysis.

Note that decorrelation between B-scans can be estimated by evaluating the averaged  $U_{lay1/lay2}^{b,M=150}$  signals after thresholding. In all experiments, phase variations corresponding to breathing and heartbeat can be easily identified, further confirming similar phase sensitivity with previous data.

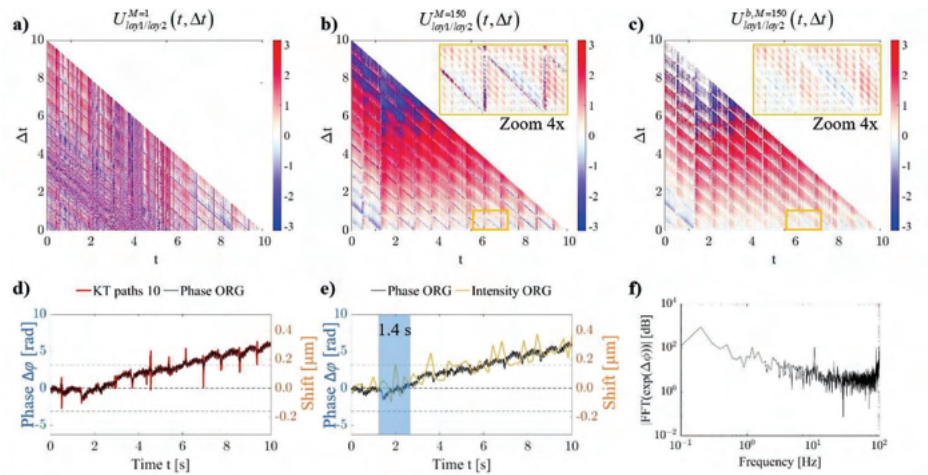


**Fig. 10.** Magnified results of the light-evoked activity of the mouse retina for ELM and BrM layers in the first 10 s in response to 1.41 s of light stimulation. (a) The phase of  $U_{lay1/lay2}^{M=1}$  cross-spectra layer differences for one A-scan with light stimulus. (b) Result of averaging  $M = 150$  cross-spectra differences  $U_{lay1/lay2}^{M=150}$  for ELM and BrM layers. A-scan range taken to average is shown in Fig. 7(a). (c) The averaged  $U_{lay1/lay2}^{b,M=150}$  signal after thresholding to remove less correlated phasors. The yellow rectangles in (b-c) indicate a region where we can see decorrelated signal reduction using weights. (d) Comparison of Knox-Thompson signal without thresholding and (red line) with weights (black line). (e) Comparison ORG phase-based signal with ORG intensity-based signal. The ORG phase signal was reconstructed from  $\Pi=10$  Knox-Thompson paths. The blue rectangle indicates light exposure time. (f) The power spectrum for phase difference signal (FFT of phase signals from ELM and BrM layers).

As an example, “Experiment 2” data shows a breathing artifacts-free dataset. In all experiments, phase-based ORG signal extraction resulted in much less noisy estimation of the ORG signals, see Fig. 11(c, f, i, l). Application of the Knox-Thompson paths allowed reliable extraction of the ORG signal even in Experiment 4 (Fig. 11(j-l)), where the OCT signal becomes decorrelated after about 5 seconds from the start of the acquisition.

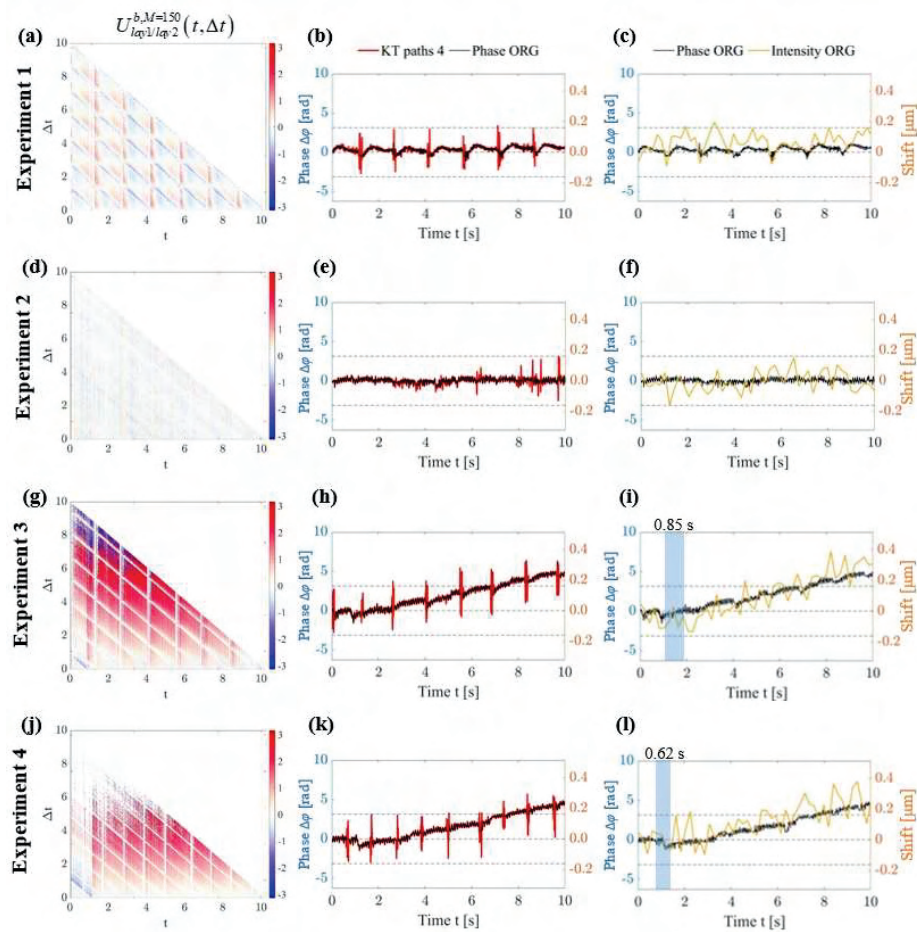


**Fig. 11.** The results of additional control experiment (Experiment 1 & 2) and light-evoked activity experiment (Experiment 3 & 4) of the mouse retina showing the distance between ELM and BrM layers in the first 10 s in response to 0.85 s (Experiment 3) and 0.62 s (Experiment 4) light stimulation. (a, d, g, j) The averaged  $U_{lay1/lay2}^{b,M=150}$  signals after thresholding to remove less correlated phasors are shown for each experiment. (b, e, h, k) Comparison of Knox-Thompson signal without thresholding (red line) and with weights (black line) for each experiment, respectively. (c, f, i, l) Comparison between ORG phase-based signal with ORG intensity-based signal. The ORG phase-based signal was reconstructed from  $\Pi=4$  Knox-Thompson paths and threshold  $b = 0.03$ . The blue rectangle indicates blue light exposure time.

#### 4. Discussion and conclusions

OCT is a coherent detection technique that carries not only information about scattering intensity but also about the axial position of the scattering object encoded in both the peak position of the signal and in a relative phase of its interferometric fringe. The FFT amplitude of the fringes allows for obtaining information about the structure of the object. Evaluation of the FFT phase of spectral fringes allows access to information about axial shifts smaller than the axial resolution of the OCT system. The work presented here described the practical implementation of the framework to use phase-based OCT signal analysis to measure axial displacement between two randomly scattering structures generating time-varying, uncorrelated speckle fields.

Lack of melanin in albino mice allows clear visualization of OCT signal back-scattered from ROS tips (ROST) and from BrM, therefore only B6-albinos (B6(Cg)-Tyrc-2J/J) mice, which are congenic with B6 mice (C57BL/6(J)) save for the null mutation in the tyrosinase gene that eliminates melanin, were used for this study. However, the methodology developed here could be applied to pigmented mice as well. We intend to work in the future on extending our phase-based ORG method analysis to mouse models with varying pigmentation levels [58].

Our previous work [43] has shown that intensity-based processing can be applied to measure the light-evoked response of the retina in an anesthetized mouse. These methods allow the extraction of time-dependent changes in the thickness of the retinal layers using simple and fast data processing. Additionally, intensity-based processing was relatively not sensitive to the eye motion artifacts. Alternatively, in OCT data, changes in the relative position of retinal layers can be measured using phase-based processing [39]. The phase-based position detection in interferometric methods is in general more sensitive than intensity-based peak position detection. However, phase-based measurement is more sensitive to bulk motion artifacts, which makes it particularly vulnerable to the eye motion artifacts mainly caused by saccades, heartbeat, and breath. One way to avoid these artifacts is to increase the acquisition speed. Publications [17,40,41] show that with an A-scan acquisition rate of 1 MHz and motion correction, it is possible to measure the phase shifts within individual photoreceptors caused by swelling of photoreceptors outer segments using direct phase analysis methods using flying spot AO-OCT datasets. The standard approach is to subtract consecutive A-scans from the reference A-scan, then measure the signal change over time.

However, as shown in this paper, during the measurement lasting from a few to several dozens of seconds, and in the presence of speckles, there are time varying changes in signal correlation. Here, we have visualized the mutual correlation of each B-scan by implementation of the cross-spectra analysis allowing for easy separation of highly correlated regions from weakly correlated ones. Using the Knox-Thompson method with the path analysis (folding arrows in Fig. 1(h,j)), it is possible to perform the phase analysis of the retina during light stimulation for systems with an A-scan acquisition rate in the range of 100 kHz and multiple scattering dominant (presence of speckle) of OCT signal. The threshold providing the reduced weighted cross spectra between layers 1 and 2 over window  $M$  was set so that to remove artifacts related primarily to the breath of the mice. The breath of the mice can be observed by phase jumps, as shown in Fig. 7(d) and Fig. 10(d) and Fig. 11(b, h, k). The red line in Fig. 7(d) and Fig. 10(d) show the ORG signal without thresholding compared to the final threshold signal drawn in the black line. Overestimating the threshold value could include the decorrelated signal of the mouse breathing in ORG calculations. The standard deviation of the measured ORG signal might increase, and the accuracy of the calculation decreases. On the other hand, the threshold should be chosen to retain useful phase information. Underestimating the threshold might demote the precision of the ORG measurement.

We have shown that for a 100 Hz serial B-scan acquisition, and in the case of an immobilized animal (mouse), we are able to reconstruct the phase-based ORG signal from the BrM and ELM layers using the Knox-Thompson path analysis. We achieved compliance of the phase-based



ORG signal with the amplitude-based ORG signal. As expected, the phase signal shows a higher sensitivity depending on the number of averaged A-scans and signal SNR. As the sensitivity of the phase method is higher, we could observe a decrease in the ELM-BrM distance with the onset of the light stimulus (Fig. 10(d)), plausibly caused by the contraction of the photoreceptor OS. This effect was not visible in the amplitude measurement. The relatively high value of phase difference variance in the *in vivo* ORG experiment is due to residual phase shifts in the retina. A closer look at the power spectrum of the phase-based ORG signals shown in Fig. 6(f) and Fig. 7(f) for control and Figs. 9(f) and 10(f) for light stimulus case reveal the presence of slow ( $\sim 1.3$  Hz for both experiments) and fast ( $\sim 9.5$  Hz and  $\sim 10.4$  Hz for control and light stimulus experiments respectively) phase modulations. We have confirmed that this corresponds to mouse breathing and heart bit frequency, respectively. This showcase that our phase-based ORG measurements are more sensitive than our current intensity-based distance analysis, offering about 10 times improvement in sensitivity of phase-based ORG estimation.

Since the distance between the ELM-BrM boundary rather than individual compartments of this band (RPE, SRS, OS, IS) were measured in the present study, we cannot directly attribute our observations with photoreceptor swelling. One alternative possibility is that ELM-BrM distance change could correspond to light-induced subretinal space (SRS) expansion caused by mitochondrial respiration [59], where SRS is defined as the extracellular fluid space between RPE cells and photoreceptors, with the growing body of work researching this topic [60–63]. We have, however, previously studied the light-evoked SRS changes [32], and did not find any SRS expansion after a visible light stimulus. One noticeable difference between these experiments is the type of anesthesia used in the study. Other groups often use a mix of ketamine (100 mg/kg) and xylazine (6 mg/kg) as injectable anesthetics, while our mice are always anesthetized with 1.5–2% isoflurane mixed with oxygen. Taking into account how different methods of anesthesia affects mouse physiology, such as blood flow [64], intraocular pressure (IOP) [65], or eye movements and electroretinogram (ERG) [66], it is possible that it could affect the light-evoked response of the retina in general and of the SRS in particular, despite some reports suggesting no difference [61]. Therefore, future ORG studies in animal models should include evaluating the different effects anesthesia could have on the extracted signals.

Over the last few years there has been rapid progress in development of the non-invasive, optical measurement of neural function in the retina. These functions have been investigated using imaging systems already used in the clinic or intended for clinical and translational use. While the most success in ORG signal extraction has been achieved with a phase-based analysis of data acquired with optical coherence tomography (OCT) with adaptive optics (AO), its broader application in clinical settings remains limited mostly due to high cost of AO-OCT systems and difficulty of its use in truly clinical settings. The work presented here contributes to developing sensitive phase-based methods to extract ORG signal from clinical-grade non-AO OCT systems. The ORG methodology has demonstrated the ability to detect responses to stimuli isomerizing less than 0.01% of photopigment. Therefore it has the potential to prove a quick, non-invasive, and objective way to measure subtle disease-related dysfunction and thus to provide an entirely new and complementary biomarker for retinal disease and recovery [67]. Using the presented cross-correlation spectrum analysis framework, the use of phase-based ORG signal extraction should be possible in the current clinical systems operating at B-scan acquisition rates of 0.1 Hz and without active eye-tracking systems or AO correction. Presented data processing was performed after the acquisition of serial B-scans, and lateral and axial displacement of tissue was waited by cross-spectra decorrelation and Knox-Thompson paths calculations. Thus, phase errors caused by large transverse or axial displacements were removed from the analysis. This development of a phase-sensitive analysis method that is insensitive to speckle signal decorrelation due to the eye movements represents an important step towards implementing non-invasive procedures of measuring the light-evoked retinal function in the human clinic.



**Funding.** Fundacja na rzecz Nauki Polskiej (POIR.04.04.00-00-2070/16-00); National Eye Institute (EY012576, EY026556, EY031098); University of California Davis School of Medicine (UC Davis Eye Center Departmental Fund).

**Acknowledgments.** We gratefully acknowledge the contributions of UC Davis EyePod and VSRI labs members, including Profs. Edward N. Pugh Jr., Ravi S. Jonnal, and John S. Werner. This work was supported in part by Foundation for Polish Science co-financed by the European Union under the European Regional Development Fund (POIR.04.04.00-00-2070/16-00) (MS), NIH EY026556 (RJZ); NIH EY031098 (RJZ); UC Davis NEI Vision Center Core Grant NIH EY012576 (RJZ) and UC Davis Eye Center Departmental Fund (RJZ).

**Disclosures.** The authors declare that there are no conflicts of interest related to this article.

**Data availability.** Data underlying the results presented in this paper are not publicly available at this time but may be obtained from the authors upon reasonable request.

## References

1. J. A. Izatt, E. A. Swanson, J. G. Fujimoto, M. R. Hee, and G. M. Owen, "Optical coherence microscopy in scattering media," *Opt. Lett.* **19**(8), 590–592 (1994).
2. M. Wojtkowski, V. J. Srinivasan, T. H. Ko, J. G. Fujimoto, A. Kowalczyk, and J. S. Duker, "Ultra-high-resolution, high-speed, Fourier domain optical coherence tomography and methods for dispersion compensation," *Opt. Express* **12**(11), 2404 (2004).
3. D. Huang, E. A. Swanson, C. P. Lin, J. S. Schuman, W. G. Stinson, W. Chang, M. R. Hee, T. Flotte, K. Gregory, C. A. Puliafito, and J. G. Fujimoto, "Optical coherence tomography," *Science* **254**(5035), 1178–1181 (1991).
4. A. Szkulmowska, M. Szkulmowski, A. Kowalczyk, and M. Wojtkowski, "Phase-resolved Doppler optical coherence tomography—limitations and improvements," *Opt. Lett.* **33**(13), 1425 (2008).
5. J. A. Izatt and S. Yazdanfar, "Self-referenced Doppler optical coherence tomography," *Opt. Lett.* **27**(23), 2085–2087 (2002).
6. A. Bouwens, D. Szlag, M. Szkulmowski, T. Bolmont, M. Wojtkowski, and T. Lasser, "Quantitative lateral and axial flow imaging with optical coherence microscopy and tomography," *Opt. Express* **21**(15), 17711 (2013).
7. A. S. G. Singh, C. Kolbitsch, T. Schmoll, and R. A. Leitgeb, "Stable absolute flow estimation with Doppler OCT based on virtual circumpapillary scans," *Biomed. Opt. Express* **1**(4), 1047 (2010).
8. S. Makita, Y. Hong, M. Yamanari, T. Yatagai, and Y. Yasuno, "Optical coherence angiography," *Opt. Express* **14**(17), 7821 (2006).
9. M. Szkulmowski, A. Szkulmowska, T. Bajraszewski, A. Kowalczyk, and M. Wojtkowski, "Flow velocity estimation using joint Spectral and Time domain Optical Coherence Tomography," *Opt. Express* **16**(9), 6008 (2008).
10. K. M. Kennedy, C. Ford, B. F. Kennedy, M. B. Bush, and D. D. Sampson, "Analysis of mechanical contrast in optical coherence elastography," *J. Biomed. Opt.* **18**(12), 121508 (2013).
11. J. M. Schmitt, "OCT elastography: imaging microscopic deformation and strain of tissue," *Opt. Express* **3**(6), 199–211 (1998).
12. J. De Boer, S. Srinivas, A. Malekafzali, Z. Chen, and J. Nelson, "Imaging thermally damaged tissue by Polarization Sensitive Optical Coherence Tomography," *Opt. Express* **3**(6), 212–218 (1998).
13. U. Morgner, W. Drexler, X. Li, F. X. Kartner, C. Pitris, S. A. Boppart, E. P. Ippen, and J. G. Fujimoto, "Spectroscopic optical coherence tomography," *IQEC, Int. Quantum Electron. Conf. Proc.* (1999).
14. T. Schmoll, C. Kolbitsch, and R. A. Leitgeb, "In vivo functional retinal optical coherence tomography," *J. Biomed. Opt.* **15**(4), 041513 (2010).
15. A. A. Moayed, S. Hariri, V. Choh, and K. Bizheva, "In vivo imaging of intrinsic optical signals in chicken retina with functional optical coherence tomography," *Opt. Lett.* **36**(23), 4575 (2011).
16. J. J. Hunter, W. H. Merigan, and J. B. Schallek, "Imaging Retinal Activity in the Living Eye," *Annu. Rev. Vis. Sci.* **5**(1), 15–45 (2019).
17. F. Zhang, K. Kurokawa, A. Lassoued, J. A. Crowell, and D. T. Miller, "Cone photoreceptor classification in the living human eye from photostimulation-induced phase dynamics," *Proc. Natl. Acad. Sci. U. S. A.* **116**(16), 7951–7956 (2019).
18. A. Messner, R. M. Werkmeister, G. Seidel, H. Stegmann, L. Schmetterer, and V. Aranha dos Santos, "Light-induced changes of the subretinal space of the temporal retina observed via optical coherence tomography," *Sci. Rep.* **9**(1), 13632–10 (2019).
19. W. Suzuki, K. Tsunoda, G. Hanazono, and M. Tanifuji, "Stimulus-induced changes of reflectivity detected by optical coherence tomography in macaque retina," *Investig. Ophthalmol. Vis. Sci.* **54**(9), 6345–6354 (2013).
20. P. Bedggood and A. Metha, "Optical imaging of human cone photoreceptors directly following the capture of light," *PLoS One* **8**(11), e79251 (2013).
21. Q. Zhang, R. Lu, B. Wang, J. D. Messinger, C. A. Curcio, and X. Yao, "Functional optical coherence tomography enables in vivo physiological assessment of retinal rod and cone photoreceptors," *Sci. Rep.* **5**(1), 9595 (2015).
22. Y. Lu, B. Wang, D. R. Pepperberg, and X. Yao, "Stimulus-evoked outer segment changes occur before the hyperpolarization of retinal photoreceptors," *Biomed. Opt. Express* **8**(1), 38 (2017).
23. X. Yao, T. Son, T. H. Kim, and Y. Lu, "Functional optical coherence tomography of retinal photoreceptors," *Exp. Biol. Med.* **243**(17-18), 1256–1264 (2018).

24. I. Erchova, A. R. Tumlinson, J. Fergusson, N. White, W. Drexler, F. Sengpiel, and J. E. Morgan, "Optophysiological characterisation of inner retina responses with high-resolution optical coherence tomography," *Sci. Rep.* **8**(1), 1813 (2018).
25. Y. Lu, J. Benedetti, and X. Yao, "Light-induced length shrinkage of rod photoreceptor outer segments," *Transl. Vis. Sci. Technol.* **7**(6), 29 (2018).
26. C. Pfäffle, H. Spahr, L. Kutzner, S. Burhan, F. Hilge, Y. Miura, G. Hüttmann, and D. Hillmann, "Simultaneous functional imaging of neuronal and photoreceptor layers in living human retina," *Opt. Lett.* **44**(23), 5671 (2019).
27. J. B. Mulligan and D. I. A. Macleod, "In Search of an optoretinogram," in *Vision Science and Its Application Topical Meeting* (1994).
28. V. P. Pandiyan, A. M. Bertelli, J. A. Kuchenbecker, B. Hyle Park, D. V. Palanker, A. Roorda, and R. Sabesan, "Optoretinogram: stimulus-induced optical changes in photoreceptors observed with phase-resolved line-scan OCT," *Invest. Ophthalmol. Vis. Sci.* **6**(37), 1426 (2020).
29. V. P. Pandiyan, X. Jiang, A. Maloney-Bertelli, J. A. Kuchenbecker, U. Sharma, and R. Sabesan, "High-speed adaptive optics line-scan OCT for cellular-resolution optoretinography," *Biomed. Opt. Express* **11**(9), 5274 (2020).
30. V. P. Pandiyan, A. Maloney-Bertelli, J. A. Kuchenbecker, K. C. Boyle, T. Ling, Z. C. Chen, B. Hyle Park, A. Roorda, D. Palanker, and R. Sabesan, "The optoretinogram reveals the primary steps of phototransduction in the living human eye," *Sci. Adv.* **6**(37), eabc1124 (2020).
31. M. Azimipour, D. Valente, K. V. Vienola, J. S. Werner, R. J. Zawadzki, and R. S. Jonnal, "Optoretinography: Optical measurements of human cone and rod photoreceptor responses to light," *bioRxiv* 760306 (2019).
32. P. Zhang, B. Shibata, G. Peinado, R. J. Zawadzki, P. FitzGerald, and E. N. Pugh, "Measurement of diurnal variation in rod outer segment length in vivo in mice with the OCT optoretinogram," *Investig. Ophthalmol. Vis. Sci.* **61**(3), 9 (2020).
33. T. Son, T. H. Kim, G. Ma, H. Kim, and X. Yao, "Functional intrinsic optical signal imaging for objective optoretinography of human photoreceptors," *Exp. Biol. Med.* **246**(6), 639–643 (2021).
34. T.-H. Kim, B. Wang, Y. Lu, T. Son, and X. Yao, "Functional optical coherence tomography enables in vivo optoretinography of photoreceptor dysfunction due to retinal degeneration," *Biomed. Opt. Express* **11**(9), 5306 (2020).
35. G. Ma, T. Son, T. H. Kim, and X. Yao, "In vivo optoretinography of phototransduction activation and energy metabolism in retinal photoreceptors," *J. Biophotonics* **14**(5), e202000462 (2021).
36. R. F. Cooper, D. H. Brainard, and J. I. W. Morgan, "Optoretinography of individual human cone photoreceptors," *Opt. Express* **28**(26), 39326 (2020).
37. F. Zhang, K. Kurokawa, M. T. Bernucci, H. W. Jung, A. Lassoued, J. A. Crowell, J. Neitz, M. Neitz, and D. T. Miller, "Revealing how color vision phenotype and genotype manifest in individual cone cells," *Investig. Ophthalmol. Vis. Sci.* **62**(2), 8 (2021).
38. M. Azimipour, D. Valente, K. V. Vienola, J. S. Werner, R. J. Zawadzki, and R. S. Jonnal, "Optoretinogram: optical measurement of human cone and rod photoreceptor responses to light," *Opt. Lett.* **45**(17), 4658 (2020).
39. D. Hillmann, H. Spahr, C. Pfäffle, H. Sudkamp, G. Franke, and G. Hüttmann, "In vivo optical imaging of physiological responses to photostimulation in human photoreceptors," *Proc. Natl. Acad. Sci. U. S. A.* **113**(46), 13138–13143 (2016).
40. M. Azimipour, J. V. Migacz, R. J. Zawadzki, J. S. Werner, and R. S. Jonnal, "Functional retinal imaging using adaptive optics swept-source OCT at 1.6 MHz," *Optica* **6**(3), 300–303 (2019).
41. M. Azimipour, J. V. Migacz, R. J. Zawadzki, J. S. Werner, and R. S. Jonnal, "Functional retinal imaging using adaptive optics swept-source OCT at 1.6 MHz (Conference Presentation)," in *Proceedings Volume 10867, Optical Coherence Tomography and Coherence Domain Optical Methods in Biomedicine XXIII* (2019).
42. C. D. Lu, B. Lee, J. Schottenhamml, A. Maier, E. N. Pugh, and J. G. Fujimoto, "Photoreceptor layer thickness changes during dark adaptation observed with ultrahigh-resolution optical coherence tomography," *Investig. Ophthalmol. Vis. Sci.* **58**(11), 4632–4643 (2017).
43. P. Zhang, R. J. Zawadzki, M. Goswami, P. T. Nguyen, V. Yarov-Yarovoy, M. E. Burns, and E. N. Pugh, "In vivo optophysiology reveals that G-protein activation triggers osmotic swelling and increased light scattering of rod photoreceptors," *Proc. Natl. Acad. Sci. U. S. A.* **114**(14), E2937–E2946 (2017).
44. G. Ma, T. Son, T.-H. Kim, and X. Yao, "Functional optoretinography: concurrent OCT monitoring of intrinsic signal amplitude and phase dynamics in human photoreceptors," *Biomed. Opt. Express* **12**(5), 2661 (2021).
45. M. M. Bartuzel, K. Wróbel, S. Tamborski, M. Meina, M. Nowakowski, K. Dalasiński, A. Szkulmowska, and M. Szkulmowski, "High-resolution, ultrafast, wide-field retinal eye-tracking for enhanced quantification of fixational and saccadic motion," *Biomed. Opt. Express* **11**(6), 3164 (2020).
46. K. T. Knox and B. J. Thompson, "Recovery of images from atmospherically degraded short-exposure photographs," *Astrophys. J.* **193**, L45 (1974).
47. H. Spahr, C. Pfäffle, S. Burhan, L. Kutzner, F. Hilge, G. Hüttmann, and D. Hillmann, "Phase-sensitive interferometry of decorrelated speckle patterns," *Sci. Rep.* (2019).
48. P. Zhang, A. Zam, Y. Jian, X. Wang, Y. Li, K. S. Lam, M. E. Burns, M. V. Sarunic, E. N. Pugh, and R. J. Zawadzki, "In vivo wide-field multispectral scanning laser ophthalmoscopy–optical coherence tomography mouse retinal imager: longitudinal imaging of ganglion cells, microglia, and Müller glia, and mapping of the mouse retinal and choroidal vasculature," *J. Biomed. Opt.* **20**(12), 126005 (2015).

49. P. Zhang, M. Goswami, A. Zam, E. N. Pugh, and R. J. Zawadzki, "Effect of scanning beam size on the lateral resolution of mouse retinal imaging with SLO," *Opt. Lett.* **40**(24), 5830 (2015).
50. M. Szkulmowski, M. Wojtkowski, and S. Tamborski, "Spectrometer calibration for spectroscopic Fourier domain optical coherence tomography," *Biomed. Opt. Express* **7**(12), 5042–5054 (2016).
51. L. Schermelleh, A. Ferrand, T. Huser, C. Eggeling, M. Sauer, O. Biehlmaier, and G. P. C. Drummen, "Super-resolution microscopy demystified," *Nat. Cell Biol.* **21**(1), 72–84 (2019).
52. X. Yin, J. R. Chao, and R. K. Wang, "User-guided segmentation for volumetric retinal optical coherence tomography images," *J. Biomed. Opt.* **19**(8), 086020 (2014).
53. B. Hyle Park, M. C. Pierce, B. Cense, S.-H. Yun, M. Mujat, G. J. Tearney, B. E. Bouma, and J. F. de Boer, "Real-time fiber-based multi-functional spectral-domain optical coherence tomography at 13  $\mu\text{m}$ ," *Opt. Express* **13**(11), 3931 (2005).
54. B. Braaf, K. V. Vienola, C. K. Sheehy, Q. Yang, K. A. Vermeer, P. Tiruveedhula, D. W. Arathorn, A. Roorda, and J. F. de Boer, "Real-time eye motion correction in phase-resolved OCT angiography with tracking SLO," *Biomed. Opt. Express* **4**(1), 51 (2013).
55. P. Zhang, M. Goswami, R. J. Zawadzki, and E. N. Pugh, "The photosensitivity of rhodopsin bleaching and light-induced increases of fundus reflectance in mice measured in vivo with scanning laser ophthalmoscopy," *Invest. Ophthalmol. Vis. Sci.* **57**(8), 3650–3664 (2016).
56. T. D. Lamb, "Photoreceptor spectral sensitivities: common shape in the long-wavelength region," *Vision Res.* **35**(22), 3083–3091 (1995).
57. V. I. Govardovskii, N. Fyhrquist, T. Reuter, D. G. Kuzmin, and K. Donner, "In search of the visual pigment template," *Vis. Neurosci.* **17**(4), 509–528 (2000).
58. R. K. Meleppat, P. Zhang, M. J. Ju, S. K. K. Manna, Y. Jian, E. N. Pugh, and R. J. Zawadzki, "Directional optical coherence tomography reveals melanin concentration-dependent scattering properties of retinal pigment epithelium," *Biomed. Opt. Express* **24**(06), 1 (2019).
59. B. A. Berkowitz and H. Qian, "OCT imaging of rod mitochondrial respiration in vivo," *Exp. Biol. Med.* **246**(20), 2151–2158 (2021).
60. Y. Li, R. N. Fariss, J. W. Qian, E. D. Cohen, and H. Qian, "Light-induced thickening of photoreceptor outer segment layer detected by ultra-high resolution OCT imaging," *Investig. Ophthalmol. Vis. Sci.* **57**, 105 (2016).
61. B. A. Berkowitz, R. H. Podolsky, H. Qian, Y. Li, K. Jiang, J. Nellissery, A. Swaroop, and R. Roberts, "Mitochondrial respiration in outer retina contributes to light-evoked increase in hydration in vivo," *Invest. Ophthalmol. Vis. Sci.* **59**(15), 5957–5964 (2018).
62. B. A. Berkowitz, R. H. Podolsky, K. L. Childers, A. Saadane, T. S. Kern, R. Roberts, H. Olds, J. Joy, C. Richards, T. Rosales, M. Schneider, B. Schilling, A. Orchanian, E. Graffice, K. Sinan, H. Qian, and L. Harp, "Sildenafil-evoked photoreceptor oxidative stress in vivo is unrelated to impaired visual performance in mice," *PLoS One* **16**(3), e0245161 (2021).
63. B. A. Berkowitz, E. M. Grady, N. Khetarpal, A. Patel, and R. Roberts, "Oxidative Stress and Light-Evoked Responses of the Posterior Segment in a Mouse Model of Diabetic Retinopathy," *Invest. Ophthalmol. Vis. Sci.* **56**(1), 606–615 (2015).
64. E. R. Muir and T. Q. Duong, "MRI of retinal and choroidal blood flow with laminar resolution," *NMR Biomed.* **24**(2), 216–223 (2011).
65. F. E. Cone, M. R. Steinhart, E. N. Oglesby, G. Kalesnykas, M. E. Pease, and H. A. Quigley, "The effects of anesthesia, mouse strain and age on intraocular pressure and an improved murine model of experimental glaucoma," *Exp. Eye Res.* **99**(1), 27–35 (2012).
66. C. Ding, P. Wang, and N. Tian, "Effect of general anesthetics on IOP in elevated IOP mouse model," *Exp. Eye Res.* **92**(6), 512–520 (2011).
67. R. S. Jonnal, "Toward a clinical optoretinogram: a review of noninvasive, optical tests of retinal neural function," *Ann. Transl. Med.* **9**(15), 1270 (2021).

# Analysis of strain estimation methods in phase-sensitive compression optical coherence elastography

JIAYUE LI,<sup>1,2,3,5,\*</sup> EWELINA PIJEWSKA,<sup>4,5</sup> QI FANG,<sup>1,2</sup>  
MACIEJ SZKULMOWSKI,<sup>4</sup> AND BRENDAN F. KENNEDY<sup>1,2,3</sup>

<sup>1</sup>BRITelab, Harry Perkins Institute of Medical Research, QEII Medical Centre Nedlands and Centre for Medical Research, The University of Western Australia, Crawley, Western Australia 6009, Australia

<sup>2</sup>Department of Electrical, Electronic & Computer Engineering, School of Engineering, The University of Western Australia, Crawley 6009, Australia

<sup>3</sup>Australian Research Council Centre for Personalized Therapeutics Technologies, Australia

<sup>4</sup>Institute of Physics, Faculty of Physics, Astronomy and Informatics, Nicolaus Copernicus University in Toruń, Grudziądzka 5, 87-100 Toruń, Poland

<sup>5</sup>These authors contributed equally to this work

\*jiayue.li@research.uwa.edu.au

**Abstract:** In compression optical coherence elastography (OCE), deformation is quantified as the local strain at each pixel in the OCT field-of-view. A range of strain estimation methods have been demonstrated, yet it is unclear which method provides the best performance. Here, we analyze the two most prevalent strain estimation methods used in phase-sensitive compression OCE, *i.e.*, weighted least squares (WLS) and the vector method. We introduce a framework to compare strain imaging metrics, incorporating strain sensitivity, strain signal-to-noise ratio (SNR), strain resolution, and strain accuracy. In addition, we propose a new phase unwrapping algorithm in OCE, fast phase unwrapping (FPU), and combine it with WLS, termed WLS<sub>FPU</sub>. Using the framework, we compare this new strain estimation method with both a current implementation of WLS that incorporates weighted phase unwrapping (WPU), termed WLS<sub>WPU</sub>, and the vector method. Our analysis reveals that the three methods provide similar strain sensitivity, strain SNR, and strain resolution, but that WLS<sub>FPU</sub> extends the dynamic range of accurate, measurable local strain, *e.g.*, measuring a strain of 2.5 mε with ~4% error, that is ×11 and ×15 smaller than the error measured using WLS<sub>WPU</sub> and the vector method, respectively. We also demonstrate, for the first time, the capability to detect sub-resolution contrast in compression OCE, *i.e.*, changes in strain occurring within the strain axial resolution, and how this contrast varies between the different strain estimation methods. Lastly, we compare the performance of the three strain estimation methods on mouse skeletal muscle and human breast tissue and demonstrate that WLS<sub>FPU</sub> avoids strain imaging artifacts resulting from phase unwrapping errors in WLS<sub>WPU</sub> and provides improved contrast over the other two methods.

© 2022 Optica Publishing Group under the terms of the [Optica Open Access Publishing Agreement](#)

## 1. Introduction

Optical coherence elastography (OCE) is an imaging technique that maps mechanical parameters (*e.g.*, strain, stress, transverse-wave velocity, and resonance frequency) and mechanical properties of tissue (*e.g.*, elasticity and viscoelasticity) into micro-scale images, termed micro-elastograms [1–6]. Phase-sensitive compression OCE is one of the most prominent variants of OCE, providing rapid image acquisition with micro-scale resolution over millimeter-scale fields-of-view. This approach has shown promise in a number of applications, particularly in oncology [7–11] and mechanobiology [12–14]. In addition, as the compressive load is co-axially aligned with the optical axis, phase-sensitive compression OCE is readily implemented in compact imaging probes [15–19], which holds promise for translation of OCE to pre-clinical and clinical

applications. Phase-sensitive compression OCE comprises three main steps: measuring sample deformation (*i.e.*, displacement) using phase-sensitive optical coherence tomography (OCT), calculating local strain as the spatial derivative of displacement, and relating strain to elasticity via a mechanical model. Thus, a key factor in determining the image quality of compression OCE is the method used to estimate local strain.

A main challenge in compression OCE is obtaining accurate strain estimation in the presence of noise in the measured displacement. In an optimally configured OCE system, displacement sensitivity is determined by shot noise [20] and, also, as has recently been shown, speckle brightness [21]. The most straightforward approach to estimating strain is the finite difference method [22], *i.e.*, the calculation of the change in displacement with depth between two discrete depth locations. However, this results in noisy strain as the noise in measured displacement is amplified in the estimated strain [23,24]. To alleviate this, several more sophisticated strain estimation methods have been proposed [5,24]. In particular, in the last decade, linear regression methods have been extensively utilized [19,24–28]. For instance, in an early demonstration of vibrational OCE [25], which is effectively a variant of compression OCE, ordinary least squares (OLS) was used to estimate the slope of vibration amplitude with depth. In this approach, a range of consecutive vibration or displacement measurements in depth are used to estimate strain, often referred to as the fitting range (typically, 5-10 times larger than the OCT axial resolution). As OCT signal-to-noise ratio (SNR) is one of the main determinants of the accuracy and precision of the measured displacement at a given depth [20], weighted least squares (WLS) was then proposed, with larger weights given to pixels corresponding to higher OCT SNR [24]. However, phase wrapping (occurring when the phase difference exceeds  $2\pi$ ) imposes a limit on the maximum measurable displacement and, by extension, the maximum measurable local strain, requiring the additional step of phase unwrapping to extend the strain dynamic range. Phase unwrapping techniques are inherently sensitive to noise, which can cause artifacts in strain micro-elastograms. Alternatively, a variant of the finite difference method implemented in the complex plane, referred to as the vector method [29,30], has been proposed to estimate local strain by calculating the phase gradient (*i.e.*, the gradient in phase difference calculated between consecutive pixels in the axial direction). As this phase gradient is typically smaller than  $2\pi$  and the intermediate steps for calculating phase gradients are implemented in the complex plane, this method avoids phase unwrapping. Importantly, the vector method performs vector summation, *i.e.*, a type of spatial averaging to increase phase stability by summing a set of complex OCT signals, providing improved image quality over the finite difference and OLS methods [29].

Whilst both WLS and the vector method have been demonstrated in the majority of recent compression OCE studies [5,13,24,28–30], a systematic comparison of these two methods has yet to be performed. Consequently, it is difficult to determine which method is optimal for a given application. A main challenge is that, until now, each method has been demonstrated on different samples and using specific parameters that are difficult to compare between the methods, *e.g.*, the fitting range and size of the phase averaging window are main determinants of spatial resolution in WLS and the vector method, respectively, but it is not clear how they compare. To address this, we introduce a framework to quantitatively compare strain imaging metrics (*e.g.*, strain sensitivity [24,31,32], strain SNR [24,31,33], strain resolution [34–36], and strain accuracy [21,32]) calculated on the same data acquired from phantoms. In addition, we demonstrate the utility of the framework by comparing the performance of a new phase unwrapping algorithm for WLS, fast phase unwrapping (FPU), to both the existing WLS method and the vector method. The existing implementation of WLS applies a phase unwrapping algorithm that corrects phase discontinuities in depth by subtracting an integer multiple of  $2\pi$  from the weighted phase difference [37], termed weighted phase unwrapping (WPU). Whilst WPU accounts for the dependence of phase sensitivity on OCT SNR, it is sensitive to phase noise in regions of low OCT SNR, resulting in phase unwrapping errors that manifest as prominent,



streak-like artifacts in strain micro-elastograms [15]. This issue is addressed by FPU, which identifies phase discontinuities by calculating phase gradients using Laplace operators that can be calculated using Fourier transforms to improve computational efficiency [38]. The three-dimensional (3-D) version of the algorithm was initially developed and implemented in a graphics processing unit for quantitative retinal blood flow measurements in Doppler OCT [39,40]. Here, we propose iterative-based 3-D FPU combined with Volkov symmetrization [38,41] to fulfill periodic boundary conditions of Fourier transforms so that the accuracy of the approach is optimum for OCE. We then perform a comparison between the existing WLS method, termed  $WLS_{WPU}$ , the vector method, and the new implementation of WLS, termed  $WLS_{FPU}$ . Our results show that whilst these three methods provide similar strain sensitivity, strain SNR, and strain resolution,  $WLS_{FPU}$  provides improved dynamic range of accurate strain estimation with an error of  $\sim 4\%$  that is  $\times 11$  and  $\times 15$  times smaller than the error measured for  $WLS_{WPU}$  and the vector method, respectively, for an expected strain of  $2.5 \text{ m}\epsilon$ . We also provide preliminary analysis of sub-resolution contrast in compression OCE, *i.e.*, the capability to detect changes in strain occurring within the strain axial resolution and, also, how this varies for the different strain estimation methods. Furthermore, we present strain micro-elastograms of mouse skeletal muscle and human breast tissue. We demonstrate that strain imaging artifacts caused by phase unwrapping errors in  $WLS_{WPU}$  are avoided in the other two methods and that the higher dynamic range of accurate strain estimation provided by  $WLS_{FPU}$  translates to improved contrast in strain micro-elastograms.

## 2. Theory: strain estimation methods in phase-sensitive compression OCE

Consistent with the broader field of elastography, in compression OCE, the sample is commonly assumed to be linearly elastic and mechanically isotropic. Under these assumptions, the elasticity of the sample can be represented by Young's modulus,  $E$ , which is defined as the ratio between the normal uniaxial stress,  $\sigma_{zz}$ , and the normal uniaxial strain,  $\epsilon_{zz}$ ,

$$E = \frac{\sigma_{zz}}{\epsilon_{zz}}. \quad (1)$$

Assuming that each pixel within the OCT field-of-view is mechanically isolated,  $E$  estimated at each pixel, *i.e.*, local elasticity, is independent throughout the micro-elastogram. In early demonstrations of compression OCE, the assumption of uniform stress was commonly made [1,5,42], whereby strain is inversely proportional to elasticity. More recently, techniques have been developed to estimate local stress, providing a more direct estimate of elasticity [43–45]. In both cases, developing accurate strain estimation methods is a crucial determinant of image quality in compression OCE. In this section, we describe in detail the two most prominent methods, WLS and the vector method.

### 2.1. Weighted least squares regression

#### 2.1.1. Displacement measurement

In phase-sensitive compression OCE, the OCT phasor difference B-scan,  $b(x, z)$ , can be calculated using the Kasai estimator [46,47] from complex OCT B-scans of the sample in unloaded,  $a_U(x, z)$ , and loaded,  $a_L(x, z)$  states,

$$\begin{aligned} b(x, z) &= a_U^*(x, z) \cdot a_L(x, z) \\ &= A_U(x, z)A_L(x, z) \exp[i \cdot (\phi_L(x, z) - \phi_U(x, z))] \\ &= B(x, z) \exp[i \cdot \Delta\phi(x, z)], \end{aligned} \quad (2)$$

where  $a_U^*(x, z)$  denotes the complex conjugate of  $a_U(x, z)$ ,  $A_U(x, z)$  and  $A_L(x, z)$  are the amplitude of  $a_U(x, z)$  and  $a_L(x, z)$ , respectively,  $\phi_U(x, z)$  and  $\phi_L(x, z)$  are the corresponding phase of  $a_U(x, z)$

and  $a_L(x, z)$ , respectively,  $\Delta\phi(x, z)$  represents the phase difference, and  $B(x, z)$  represents the amplitude of  $b(x, z)$ . In phase-sensitive compression OCE, the axial displacement,  $u_z(x, z)$ , is directly proportional to  $\Delta\phi(x, z)$ ,

$$u_z(x, z) = \frac{\lambda\Delta\phi(x, z)}{4\pi n}, \quad (3)$$

where  $\lambda$  and  $n$  represent the central wavelength of the light source and the bulk refractive index of the sample (often assumed to be 1.3-1.4), respectively. Assuming that noise is purely from the optical and electronic components of the OCT system, and ignoring other sources of displacement noise (e.g., environmental vibration), the minimum measurable change in phase difference, i.e., the phase difference sensitivity,  $S_{\Delta\phi}$  is [20],

$$S_{\Delta\phi} = \frac{1}{\sqrt{SNR_{OCT}}}, \text{ when } SNR_{OCT} \gg 1. \quad (4)$$

Combining Eqs. (3) and (4), the displacement sensitivity,  $S_{u_z}$ , is

$$S_{u_z} = \frac{\lambda}{4\pi n\sqrt{SNR_{OCT}}}. \quad (5)$$

However, phase difference is a circular variable and wraps when the phase difference exceeds  $2\pi$ , creating ambiguity in the measured displacement. Thus, to increase the dynamic range of displacement and, therefore, strain estimated using WLS, phase unwrapping is required.

#### 2.1.2. Weighted phase unwrapping (WPU) algorithm

The WPU algorithm has been described in detail in a previous study [37]. Here, we provide a brief summary. The algorithm was initially proposed for a common-path phase-sensitive compression OCE configuration [37], where the back surface of the imaging window in contact with the sample is used as a reference reflector. Furthermore, the imaging window is affixed to an annular PZT actuator and acts as a compression plate. In this configuration, the phase difference at the surface of the sample is zero, as the window and sample surface have the same displacement. For a sample under uniform compression, as the resulting magnitude of phase difference increases with depth, i.e., as the change in displacement between the imaging window and the sample increases, the direction of required phase unwrapping is known. In addition, as highlighted in Eq. (4), phase difference sensitivity is dependent on OCT SNR, which allows the phase difference at each pixel to be weighted by the corresponding OCT SNR.

The weighted phase differences at the first  $n_z$  pixels in depth are assumed to be free of wrapping events, where the mean of weighted phase difference in these pixels,  $\mu_{\Delta\phi,z}$ , is used as a reference to determine if a wrapping discontinuity has occurred. Then, for subsequent depths, starting from  $n_z+1$ , each pixel is unwrapped by subtracting an integer multiple of  $2\pi$  such that the difference between each weighted phase difference and  $\mu_{\Delta\phi,z}$  calculated from the preceding  $n_z$  pixels is minimized. Similar to the axial phase unwrapping, in the subsequent lateral phase unwrapping, a sliding window with a size of  $(2m+1) \times (2m+1)$  in the  $xy$  plane is specified to calculate the mean of weighted phase difference in the *en face* plane,  $\mu_{\Delta\phi,xy}$ , used as a reference to determine if lateral phase unwrapping is needed. Each pixel in the *en face* plane is laterally unwrapped by subtracting an integer multiple of  $2\pi$  to minimize the difference between the axially unwrapped phase difference at each pixel and  $\mu_{\Delta\phi,xy}$ .

#### 2.1.3. Fast phase unwrapping algorithm

Here, we propose to use 3-D FPU algorithm as an alternative phase unwrapping algorithm [39] for use in phase-sensitive compression OCE. The algorithm was initially developed for unwrapping

blood velocity profiles in retinal vessels imaged with Doppler OCT [39,40] and a complete derivation of the method can be found there. The method can be regarded as one of the transport of intensity equation solvers described in detail in [38,48]. Compared to the original FPU method, we introduce two modifications here. The first is the use of iterative error correction as described in [38], and the second is the use of Volkov symmetrization [41] in the FPU algorithm. FPU calculates the estimated unwrapped phase,  $\Delta\psi_{est}(\mathbf{r})$ , by solving the Poisson equation,

$$\Delta\psi_{est}(\mathbf{r}) = \nabla^{-2} \text{Im} \{P(\mathbf{r})^{-1} \nabla^2 P(\mathbf{r})\}, \quad (6)$$

where  $\mathbf{r}$  denotes the spatial coordinates,  $\nabla^{-2}$  and  $\nabla^2$  are the inverse and forward Laplace operators. In the above equation,  $P(\mathbf{r})$  is the complex-valued function of both wrapped phase  $\Delta\phi(\mathbf{r})$  and unwrapped phase  $\Delta\psi(\mathbf{r})$ ,

$$P(\mathbf{r}) = \exp(j\Delta\psi(\mathbf{r})) = \exp(j\Delta\phi(\mathbf{r})), \quad (7)$$

where  $j^2 = -1$ , and  $P(\mathbf{r})$  can be obtained directly from complex OCT A-scans [39] using all B-scans of the sample in unloaded and loaded states, as described by Eq. (2):

$$P(\mathbf{r}) = \frac{b(\mathbf{r})}{|b(\mathbf{r})|}, \quad (8)$$

where  $\mathbf{r}$  denotes the spatial coordinates ( $x, y, z$ ). To improve the computational efficiency, Eq. (6) can be expressed with Fourier transformations instead of Laplace operators as [38,39]

$$\Delta\psi_{est}(\mathbf{r}) = -(2\pi)^{-2} F^{-1} \{ \mathbf{K}^{-2} F [\text{Im}(-P(\mathbf{r})^{-1} (2\pi)^2 F^{-1} [\mathbf{K}^2 F(P(\mathbf{r}))])] \}, \quad (9)$$

where  $\mathbf{K}$  is the Fourier space conjugate of the vector  $\mathbf{r}$ , and  $F$  and  $F^{-1}$  are forward and inverse transformation operators. In contrast to Doppler OCT, the periodic boundary conditions of the OCE data are usually not fulfilled due to a phase ramp and discontinuities on the tissue boundaries, which lead to phase unwrapping errors. Therefore, it is reasonable to utilize Volkov symmetrization to improve the accuracy of unwrapped phase difference, as shown by Martinez-Carranza *et al.* [38]. In this paper, we extend their work by performing the Volkov symmetrization on 3-D data prior to the estimation of unwrapped phase difference in Eq. (9).

Figure 1 presents an illustrative diagram of the modified FPU algorithm using experimental data acquired from a silicone inclusion phantom. After the calculations of  $\Delta\psi_{est}(\mathbf{r})$  from the enlarged data, we extract one part (represented by a solid black frame in Fig. 1) for the subsequent steps of the FPU algorithm. As it is common that  $\Delta\psi_{est}(\mathbf{r})$  may not be fully unwrapped from the first estimation, the phase unwrapping errors can be minimized by iterating Eq. (9) based on the condition that  $\Delta\phi(\mathbf{r})$  and  $\Delta\psi_{est}(\mathbf{r})$  should be the same in the complex plane, as highlighted in Eq. (7). Therefore, we define the error function for the estimation of the unwrapped phase difference,  $Q(\mathbf{r})$ , as

$$Q(\mathbf{r}) = \text{angle}[\exp(j\Delta\phi(\mathbf{r})) \cdot \exp(-j\Delta\psi_{est}(\mathbf{r}))]. \quad (10)$$

$Q(\mathbf{r})$  is likely to be wrapped, which also can be unwrapped using Eq. (9) by replacing  $P(\mathbf{r})$  with  $\exp(jQ(\mathbf{r}))$ . Similar to  $\Delta\psi_{est}(\mathbf{r})$ , we also perform Volkov symmetrization for the estimation of the unwrapped phase difference error,  $Q_{est}^{iter}(\mathbf{r})$ , and iteratively update  $\Delta\psi_{est}^{iter}(\mathbf{r})$  with the addition of  $Q_{est}^{iter}(\mathbf{r})$ ,

$$\Delta\psi_{est}^{iter+1}(\mathbf{r}) = \Delta\psi_{est}^{iter}(\mathbf{r}) + Q_{est}^{iter}(\mathbf{r}). \quad (11)$$

As the number of iterations in Eq. (11) increases,  $Q_{est}^{iter}(\mathbf{r})$  is reduced towards zero. When  $Q_{est}^{iter+1}(\mathbf{r})$  is equal to zero, the iterations stop and  $\Delta\psi_{est}^{iter+1}(\mathbf{r})$  represents the final estimation of unwrapped phase difference. In practical implementation, the FPU algorithm faces two main problems when using  $Q(\mathbf{r})$  as the stop criterion. The first is that  $\Delta\psi_{est}(\mathbf{r})$  can have different phase offset equal to an integer multiple of  $2\pi$ , leading to an ambiguity of applying Eq. (10). The

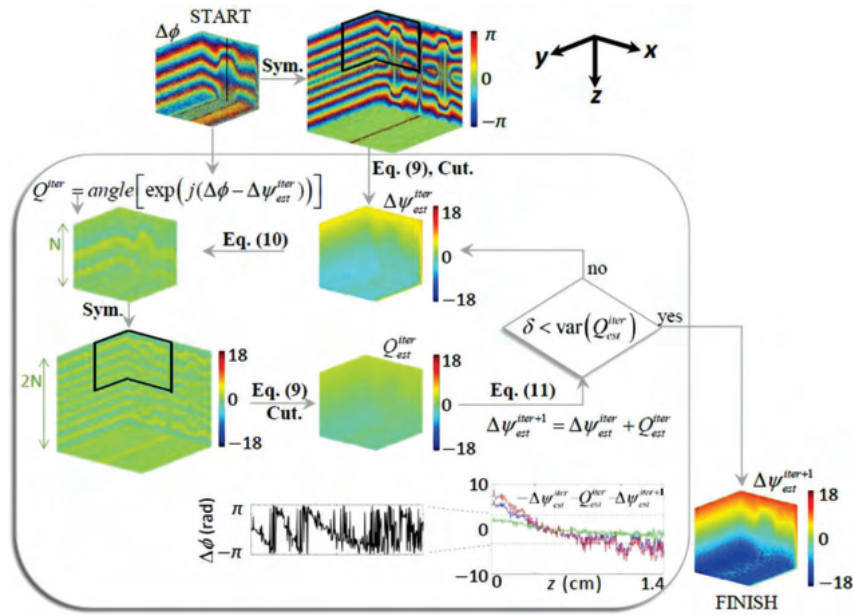


**Fig. 1.** Illustrative diagram of the FPU algorithm for phase-sensitive compression OCE on a silicone inclusion phantom. “Sym.” is the Volkov symmetrization that precedes Eq. (9). “Cut.” is the operation of cutting off data that was marked as a solid black frame on enlarged symmetrized data. “Angle” is the operator to extract phase difference from complex functions.

second is variation in noise that still exists after a number of iterations. Thus, we instead compute spatial variance of  $Q_{est}^{iter}(\mathbf{r})$  as the stop criterion since it is insensitive to constant value difference between  $\Delta\phi(\mathbf{r})$  and  $\Delta\psi_{est}(\mathbf{r})$ . Then, the iteration only stops when the variance of  $Q_{est}^{iter}(\mathbf{r})$  reaches a threshold accuracy  $\delta$ , which is obtained by measuring the noise floor of (wrapped) phase difference in the deep regions of experimental OCT scans.

#### 2.1.4. WLS strain estimation

After disambiguating the relationship between phase difference and displacement using phase unwrapping, strain can be estimated using WLS. WLS has been shown to improve strain sensitivity over OLS by accounting for spatially varying OCT SNR at each pixel [24] over the fitting range  $\Delta z$ , which determines the axial resolution of strain estimation [24,34]. Specifically, WLS assigns a weight,  $w_i$ , to each displacement measurement,  $u_{z_i}$ , where  $w_i$  is defined as the inverse variance of each displacement measurement,

$$w_i = \frac{1}{S_{u_{z_i}}^2} \tag{12}$$

A complete derivation of the analytical expression for WLS strain estimation is provided in [24]. Here, we directly provide the expression,

$$\epsilon_{zz}^w = \frac{\left( \sum_{i=j}^{j+m-1} w_i \right) \left( \sum_{i=j}^{j+m-1} w_i u_{z_i} \Delta z \right) - \left( \sum_{i=j}^{j+m-1} w_i \Delta z \right) \left( \sum_{i=j}^{j+m-1} w_i u_{z_i} \right)}{\left( \sum_{i=j}^{j+m-1} w_i \right) \left( \sum_{i=j}^{j+m-1} w_i (\Delta z)^2 \right) - \left( \sum_{i=j}^{j+m-1} w_i \Delta z \right)^2}, \tag{13}$$

where  $u_{z_i}$  and  $m$  are the displacement measurements at each depth location  $z_i$  and the number of displacement points, respectively, over the fitting range  $\Delta z$ . By combining WLS with the WPU and FPU algorithms, respectively, we consider two WLS-based strain estimation methods, namely  $\text{WLS}_{\text{WPU}}$  and  $\text{WLS}_{\text{FPU}}$ .

## 2.2. Vector method

Here, we provide a brief description of the vector method. A more detailed description can be found elsewhere [30]. In the vector method, strain is estimated from the finite difference between two OCT phasor differences from consecutive depths within  $b(x, z)$ . We refer to this finite difference as the OCT phasor gradient,  $c(x, z)$ . This method removes the need for phase unwrapping as the computation is performed in the complex plane, and the phase angle of  $c(x, z)$ ,  $\Delta\phi'(x, z_i) = [\Delta\phi(x, z_i) - \Delta\phi(x, z_{i+1})]$ , referred to as the phase gradient, is typically smaller than  $2\pi$ . From Eq. (3), as  $u_z(x, z)$  is proportional to  $\Delta\phi(x, z)$ , it follows that since  $\varepsilon_{zz} = \Delta u_z / \Delta z$ , then  $\varepsilon_{zz}(x, z)$  is proportional to the  $\Delta\phi'(x, z)$ ,

$$\begin{aligned} c(x, z_i) &= b^*(x, z_i) \cdot b(x, z_{i+1}) \\ &= B(x, z_i)B(x, z_{i+1}) \exp[i \cdot (\Delta\phi(x, z_i) - \Delta\phi(x, z_{i+1}))] \\ &= C(x, z_i) \exp[i \cdot \Delta\phi'(x, z_i)], \end{aligned} \quad (14)$$

where  $C(x, z)$  is the amplitude of  $c(x, z)$  in units of squared intensity.  $\Delta\phi'(x, z)$  is in units of radians per pixel and, more importantly, is proportional to  $\varepsilon_{zz}(x, z)$ ,

$$\varepsilon_{zz}^v = \frac{\lambda \Delta\phi'}{4\pi \delta z}, \quad (15)$$

where  $\delta z$  is the pixel size in the axial direction. Analogously to the finite difference method demonstrated in previous studies [22,24], the finite difference of phasor differences along the  $z$ -axis is inherently noisy, resulting in low strain sensitivity. To improve strain sensitivity, the vector method incorporates spatial averaging known as “vector summation” [29,30]. By summing a set of complex OCT signals, *i.e.*,  $b(x, z)$  and  $c(x, z)$ , the stability of the resulting phase angles, *i.e.*,  $\Delta\phi(x, z)$  and  $\Delta\phi'(x, z)$ , is considerably improved, corresponding to an improved phase sensitivity. Briefly, from the displacement measured using Eq. (2), a small preliminary vector summation window, typically, with a size of  $\sim 2$ -3 pixels in  $x$  and  $z$ , is used to smooth  $b(x, z)$ . As the amplitude of  $b(x, z)$  is proportional to the OCT SNR, summing a small region of OCT phasor differences effectively weights  $b(x, z)$  at each pixel. The spatially averaged  $b(x, z)$  is then used to calculate  $c(x, z)$ , as illustrated in Eq. (14). Subsequently, a larger vector summation window with a size of  $N_x \times N_z$  (typically  $16 \times 16$  pixels) is used to smooth the normalized  $c(x, z)$  that is obtained by dividing  $c(x, z)$  with  $C(x, z)$ . This is effectively unweighted averaging of the estimated  $\varepsilon_{zz}$ . It should be noted that, to improve SNR of  $c(x, z)$ , the vector method typically calculates  $c(x, z)$  from the finite difference between  $b(x, z_i)$  and  $b(x, z_{i+n})$  at a step of  $n$  pixels ( $n = 2$  used in [29,30]). To provide a reasonable comparison between the vector method,  $\text{WLS}_{\text{WPU}}$ , and  $\text{WLS}_{\text{FPU}}$ , in Section 4, we demonstrate these three methods under the same processing conditions.

## 3. Experimental setup and procedure

### 3.1. Phantom fabrication, tissue preparation and histology

The bulk material of the inclusion phantom (Phantom 1) is a 3 mm thick cylinder with a diameter of 10 mm, which was made from Elastosil P7676 (Wacker, Germany) with Young’s modulus of  $\sim 19$  kPa, as measured by a compression testing device. To minimize the out-of-plane deformation which could reduce the accuracy of strain estimation in OCE [49], the inclusion was designed to be a strip with dimensions of  $\sim 8 \times 0.6 \times 0.5$  mm ( $xyz$ ), and was made from Elastosil RT601



(Wacker, Germany) with measured Young's modulus of  $\sim 327$  kPa. To provide optical contrast, titanium dioxide ( $\text{TiO}_2$ ) particles (refractive index = 2.3, Sigma-Aldrich, Germany) with a mean diameter of  $1 \mu\text{m}$  were mixed in the bulk and inclusion silicone materials (both of refractive index = 1.4) at concentrations of 2 mg/ml and 10 mg/ml, respectively. Separately, to investigate the accuracy of strain estimation methods, a mechanically homogeneous phantom (Phantom 2) with a thickness of  $\sim 1$  mm and a diameter of 10 mm was made from Elastosil P7676 (Wacker, Germany). A 2 mg/ml concentration of  $\text{TiO}_2$  particles was incorporated in the silicone mixture for Phantom 2.

In addition, we performed OCE experiments on data acquired from freshly excised mouse skeletal muscle and human breast tissue. An extensor digitorum longus (EDL) muscle with dimensions of  $\sim 10 \times 3 \times 1$  mm was excised from a 10-month-old male wild-type (WT) mouse sacrificed via cervical dislocation under anesthetic, as per institutional ethics requirements. Similar to a previous OCE study [50], we encapsulated the EDL muscle in 3-D methacrylated gelatin (GelMA [51]), a clear photopolymerizable hydrogel ( $\sim 15 \times 15 \times 3$  mm), to keep the tissue hydrated during scan acquisition, and more importantly, to reduce image artifacts induced by non-uniform compression due to uneven surface topology [52]. The small size of the EDL muscle made it challenging to obtain meaningful co-registration between histology and micro-elastograms. When we attempted this, we observed freeze artifacts that caused staining issues in tissue histology. Thus, the corresponding histology is not provided here. In addition, we scanned a human breast tissue specimen excised during a mastectomy surgery. Informed consent was obtained from the patient and ethics was approved by the Sir Charles Gairdner and Osborne Park Health Care Group Human Research Ethics Committee (HREC No: 2007-152). This specimen had approximate dimensions of  $4 \times 4 \times 2$  cm and was scanned within an hour of excision. After data acquisition, the specimen was marked by ink for orientation, dissected, placed in two cassettes, and fixed in 10% neutral-buffered formalin for at least one day before histology processing was performed. Paraffin embedding was performed prior to sectioning and staining with hematoxylin and eosin, following the standard histology protocols at the hospital.

### 3.2. Phase-sensitive compression OCE system

The compression OCE system used has been detailed in previous studies [8,32]. Hence, a brief summary is provided here. Compression OCE measurements were performed using a fiber-based spectral-domain OCT system (Telesto 220; Thorlabs Inc., USA) with a central wavelength of 1300 nm and a 3 dB bandwidth of 170 nm. The measured full-width-at-half-maximum (FWHM) OCT axial resolution is  $4.8 \mu\text{m}$  (in air). For imaging tissue-mimicking phantoms and the encapsulated muscle tissue, a scan lens (LSM03; Thorlabs Inc., USA) with a measured lateral resolution of  $7.2 \mu\text{m}$  (FWHM in air) and a maximum field-of-view of 10 mm was used. A scan lens (LSM04; Thorlabs Inc., USA) with a measured lateral resolution of  $13 \mu\text{m}$  (FWHM in air) and a maximum field-of-view of 16 mm was used to image the relatively larger breast specimen for cancer margin assessment. An imaging window (Edmund Optics Inc., USA) with a diameter of 75 mm was bonded with wax to a ring actuator (Piezomechanik GmbH, Germany) with an internal aperture of 65 mm, enabling imaging and compression to be introduced from the same side of the sample. The OCT system was implemented in a common-path configuration where the bottom side of the imaging window that contacts the sample during scanning provides the reference reflection. Silicone oil was applied between the sample and the imaging window to reduce surface friction. For biological tissue scans, a compliant silicone layer (made from Elastosil P7676) with a thickness of  $\sim 500 \mu\text{m}$  was placed between the imaging window and the underlying tissue sample to improve the uniformity of compressive loading throughout the sample [43,52]. To ensure uniform contact, a pre-strain (*i.e.*, a bulk strain prior to actuation) of 20% was imparted to the layer-sample system via a motorized vertical translation stage (MLJ150; Thorlabs Inc., USA). At this pre-strain, the ring actuator was driven collinearly with the imaging

beam and synchronized with the OCT B-scan rate, delivering a maximum stroke of 10  $\mu\text{m}$ . The A-scan acquisition time was 20  $\mu\text{s}$ . A single B-scan consisting of 1000 A-scans was recorded in an acquisition time of 20 ms.

To characterize the strain sensitivity, strain SNR, and strain resolution, we utilized methods defined previously [31,32,34]. Specifically, in this study, 1,000 A-scans per B-scan, and 1,000 B-scan pairs (unloaded and loaded) per C-scan were acquired from Phantom 1 over a 2.5 mm field-of-view with a lateral sampling density of 2.5  $\mu\text{m}$ . To enable a more accurate characterization of strain accuracy, denser lateral sampling was performed to include more OCT realizations; 2,000 A-scans per B-scan were acquired over a 2 mm lateral extent (1  $\mu\text{m}$  per pixel in  $x$ ) and a total of 256 B-scans were acquired at the same spatial location in Phantom 2. Similarly, to reduce the effect of optical noise on strain accuracy measurement, temporal averaging of 16 phasor difference B-scans was performed, which resulted in a total of 8 averaged phasor difference B-scans. The middle B-scan (the 4<sup>th</sup> B-scan) was used to characterize the accuracy of the strain estimation methods, described in Section 4.2. Scans of the encapsulated EDL muscle were acquired by taking 1,000 A-scans per B-scan, and 1,000 B-scan pairs (unloaded and loaded) per C-scan over a 10 mm field-of-view at a lateral sampling density of 10  $\mu\text{m}$ . Additionally, for the breast tissue scans, 808 A-scans per B-scan and 808 B-scan pairs (unloaded and loaded) per C-scan were acquired over a 16 mm field-of-view at a lateral sampling density of 19.8  $\mu\text{m}$ . We note that the OCT lateral resolution was sub-sampled for measurements on biological tissues to allow for rapid data acquisition by trading off resolution to reduce the impact of temporal factors (*e.g.*, dehydration [53] or viscoelastic creep [54]) that could alter the mechanical response of tissue in the process of data acquisition. The imaging specifications used in this study are summarized in Table 1.

**Table 1. Phase-sensitive compression OCE scanning parameters and FPU parameters used in this study.**

	Inclusion phantom (Phantom 1)	Homogeneous phantom (Phantom 2)	EDL muscle	Breast tissue
A-scans $\times$ B-scans	1000 $\times$ 1000	2000 $\times$ 256	1000 $\times$ 1000	808 $\times$ 808
Field-of-view (mm)	2.5 $\times$ 2.5	2 $\times$ 0.001	10 $\times$ 10	16 $\times$ 16
Lateral OCT resolution	7.2 $\mu\text{m}$	7.2 $\mu\text{m}$	7.2 $\mu\text{m}$	13 $\mu\text{m}$
Axial OCT resolution	4.8 $\mu\text{m}$	4.8 $\mu\text{m}$	4.8 $\mu\text{m}$	4.8 $\mu\text{m}$
FPU – threshold accuracy $\delta$ ( $\text{rad}^2$ )	0.3	0.02-2.9	0.2	0.1
FPU - number of iterations	150	10-150	150	120

To unwrap the phase difference using the WPU algorithm,  $n_z = 7$  axial pixels were utilized to calculate the phase unwrapping reference along the axial direction ( $\mu_{\Delta\phi,z}$ ). After axial phase unwrapping, a window of  $9 \times 9$  lateral pixels ( $m = 4$ ) was specified to calculate the phase unwrapping reference along the lateral direction ( $\mu_{\Delta\phi,xy}$ ). To determine the optimal number of iterations in FPU, a threshold accuracy of  $\delta$  was measured from the standard deviation of phase difference calculated within a spatial window in the  $xz$  plane (typically  $20 \times 30$  pixels) at a depth of 1.4 mm in OCT scans. The measured  $\delta$  and the corresponding number of iterations for different datasets are also summarized in Table 1. We note that different values of  $\delta$  in Table 1 correspond to varying sample deformation that increases strain-induced decorrelation and amplifies the spatial variation of phase difference in the strain accuracy experiment. Based on Eq. (3), the axial displacement at each pixel was then calculated from the unwrapped phase difference using the WPU and FPU algorithms, respectively, prior to WLS strain estimation. In terms of the computational cost, using the homogenous OCT data as an example, it requires  $146.43 \pm 0.38$  s,  $142.39 \pm 0.86$  s, and  $22.62 \pm 0.43$  s for reconstructing 3-D strain from phasor difference using  $\text{WLS}_{\text{WPU}}$ ,  $\text{WLS}_{\text{FPU}}$ , and the vector method, respectively, in MATLAB (R2016a)

with a workstation that has two Intel Xeon E5-2690 8-core CPUs, 192 GB of RAM, and a 1 TB solid-state drive.

### 3.3. Comparison of strain estimation methods

Figure 2 provides a comparison of strain micro-elastograms generated using  $WLS_{WPU}$  and the vector method from data acquired on Phantom 1, using processing parameters previously reported for both methods [30,37]. For  $WLS_{WPU}$ , a 1-D axial fitting range of 100  $\mu\text{m}$ , corresponding to 30 axial pixels, was implemented to estimate strain. For the vector method, a pre-filtering window with a size of  $3 \times 3$  pixels ( $xz$ ) was applied to OCT phasor differences, followed by vector summation over 16 pixels of normalized phasor gradients in  $x$  and a subsequent vector summation over 16 pixels of normalized, laterally-averaged phasor gradients in  $z$ . In addition, the phasor gradient at each pixel was calculated between two pre-filtered phasor differences at a step of 2 pixels (*i.e.*,  $n = 2$ ).

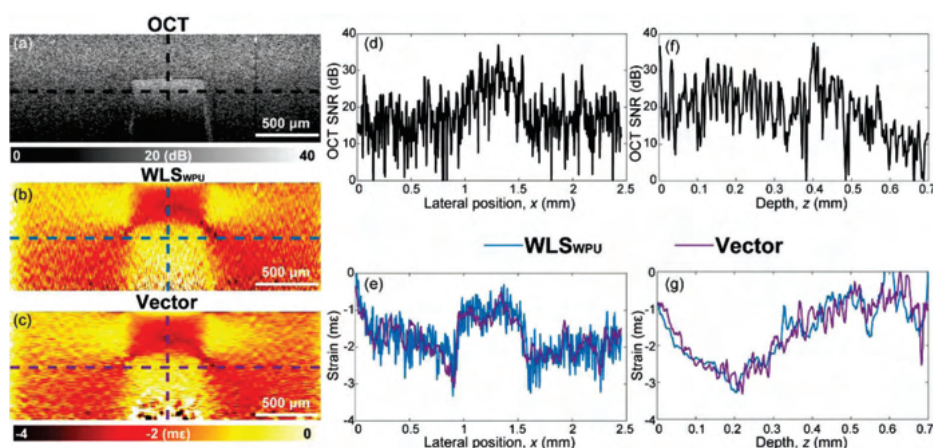


**Fig. 2.** Comparison of strain micro-elastograms generated with  $WLS_{WPU}$  and the vector method using typical parameters described in previous studies for both techniques. (a) OCT B-scan ( $xz$  plane), and the corresponding strain micro-elastograms generated using (b)  $WLS_{WPU}$  with a 1-D axial fitting range of 100  $\mu\text{m}$  and (c) the vector method with a pre-filtered window size of  $3 \times 3$  pixels ( $xz$ ) and a main processing window size of  $16 \times 16$  pixels ( $xz$ ). The OCT SNR plotted as a function of (d) lateral position in  $x$  and (f) axial position in  $z$ , respectively. The strain estimated using  $WLS_{WPU}$  (blue) and the vector method (purple) as a function of (e) lateral position in  $x$  and (g) axial position in  $z$ , respectively.

Figure 2(a) shows the OCT B-scan of Phantom 1, and the corresponding strain micro-elastograms obtained with  $WLS_{WPU}$  and the vector method are presented in Figs. 2(b) and 2(c), respectively, where the difference in the strain texture is pronounced due to the different spatial averaging techniques used in both methods. Figures 2(d)–2(g) show the variation of OCT SNR and strain over the lateral and axial ranges indicated by dashed black lines in Figs. 2(a)–2(c), respectively. Compared to  $WLS_{WPU}$  (Fig. 2(b)), the lateral boundaries of the inclusion are more blurred in the strain micro-elastogram obtained using the vector method (Fig. 2(c)) due to the incorporation of lateral averaging. Consequently, in Fig. 2(e), the strain estimated by  $WLS_{WPU}$  along the  $x$ -axis is noisier than that of the vector method. Similarly, as the axial averaging window size of  $WLS_{WPU}$  is larger than that of the vector method, the axial boundary of the inclusion is more blurred in the case of  $WLS_{WPU}$  in Fig. 2(b), and the corresponding strain along the  $z$ -axis shown in Fig. 2(g) is relatively smoother, compared to the case of the vector method.

From Fig. 2, it can be seen that differences in the averaging techniques and window size used for different strain estimation methods make it challenging to analyze and compare performance. To enable a fair comparison, for the results presented in Section 4, we modified both strain estimation methods and, importantly, aimed to preserve the advantages of each method, by restricting the processing to two layers of spatial averaging: (1) pre-filtering OCT phasor difference using a 3-D vector summation window ( $2 \times 2 \times 7$  pixels,  $xyz$ ), which has been typically incorporated in the vector method in previous studies [30,45], and (2) estimating strain over a  $100 \mu\text{m}$  axial range of consecutive displacement and phasor gradient ( $n = 1$  herein) data points for WLS-based methods and the vector method, respectively. To facilitate a numerical comparison of imaging performance between the different strain estimation methods, we define the following imaging metrics: strain sensitivity, strain SNR, strain resolution, and strain accuracy, as summarized in Table 2.

**Table 2. Imaging metrics used to compare strain estimation methods**

Imaging metric	Definition	Approach
Strain sensitivity ( $S_{\varepsilon}$ )	The precision of estimated strain.	The standard deviation of strain measurements, $S_{\varepsilon}$ , within a spatial window in a strain micro-elastogram [24,31,32].
Strain SNR ( $\text{SNR}_{\varepsilon}$ )	The ratio of the mean strain and the strain sensitivity.	$\text{SNR}_{\varepsilon} = 20 \log_{10}(\mu_{\varepsilon}/S_{\varepsilon})$ [24,31,33].
Strain resolution	The measured resolution of features in a strain micro-elastogram.	The FWHM of the point spread function provided by the derivative of the step response in axial strain across axial and lateral feature boundaries [34].
Strain accuracy	The deviation of strain from a known true value.	Compare the mean of strain measurements, $\mu_{\varepsilon}$ , within a spatial window against the “ground truth” (defined in Section 4.2).

## 4. Experimental results

### 4.1. Strain sensitivity, strain SNR, and strain resolution

Figure 3(a) shows an experimental OCT B-scan acquired from Phantom 1, where the top surface of the embedded stiff inclusion can be observed at a depth of  $380 \mu\text{m}$ . The corresponding strain micro-elastograms generated using the vector method,  $\text{WLS}_{\text{WPU}}$ , and  $\text{WLS}_{\text{FPU}}$  are presented in Figs. 3(b)–3(d), respectively. We note that there are variations in strain different between the homogeneous regions of Phantom 1, *i.e.*, at the top left and top right of Figs. 3(b)–3(d). This is most likely caused by the non-uniform deformation in the sample due to sample imperfections (*e.g.*, uneven surface topology [55]) arising from the phantom fabrication process. The quality of the strain micro-elastogram obtained using  $\text{WLS}_{\text{FPU}}$  (Fig. 3(d)) is similar to  $\text{WLS}_{\text{WPU}}$  (Fig. 3(c)). However, the texture of the strain micro-elastogram obtained using the vector method in Fig. 3(b) is distinct to that of the WLS-based methods, where the strain at each pixel estimated by the vector method appears to be less stretched along the  $z$ -axis (*i.e.*, the fitting direction), despite the same axial range for strain estimation being used. This is attributed to the difference between weighted (*i.e.*, WLS) and unweighted averaging (*i.e.*, the vector method) in strain estimation. Because of weighted averaging, the linear regression in WLS tends to fit towards those displacement pixels with high OCT SNR (*i.e.*, large weights) over the axial range. In contrast, the second layer of vector summation in the vector method is performed on the normalized phasor gradients, which means that each pixel over the axial range contributes equally to the estimated strain. This effect caused by weighting can also result in distinct features in strain micro-elastograms generated using WLS and the vector method, respectively. For example, Fig. 3(e) shows the magnified OCT image of a feature, a clump of  $\text{TiO}_2$  particles, highlighted by the dashed blue



box in Fig. 3(a). This feature extends over an axial range of  $30\ \mu\text{m}$ , *i.e.*, it is smaller than the axial resolution of the OCE system (FWHM,  $\sim 71\ \mu\text{m}$  [34]). The corresponding magnified region in the strain micro-elastograms obtained using the vector method,  $\text{WLS}_{\text{WPU}}$ , and  $\text{WLS}_{\text{FPU}}$  are shown in Figs. 3(f)–3(h), respectively. Noticeably, using the WLS-based methods, the feature is identified as a region of low strain, indicating a stiff “inclusion”. However, this feature is not present in the micro-elastogram obtained with the vector method. Figures 3(i) and 3(j) present the OCT SNR and displacement profiles from a single A-scan through the middle of the bright feature. Importantly, the depth range where the slope of the displacement is close to zero (*i.e.*, zero strain), marked by dashed black lines in Fig. 3(j), corresponds to the location of the highest OCT SNR, indicating that, in this case, the WLS-based methods correctly detect the presence of the stiff feature, whilst the vector method does not. The locations of the dashed lines in Figs. 3(i) and 3(j) represent the top and bottom boundaries of the aggregate determined from the abrupt changes of OCT SNR ranging from 30 dB to 41 dB and 37 dB to 26 dB, respectively. This result demonstrates a coupling between optical and mechanical contrast brought about by the weighting used in WLS-based methods. For a stiff and highly scattering feature that is smaller than the fitting range ( $\times 3$  smaller in this case), the fitting can be biased towards the bright region, resulting in the detection of the feature whilst the absence of this weighting precludes the detection of the feature using the vector method. It should be noted, however, that although the feature is detected using the WLS-based methods, as it extends over an axial length that is lower than the fitting length, it is not resolved, as can be observed by its elongation over a larger axial range than is the case in the OCT image. This phenomenon will be further discussed in Section 5.

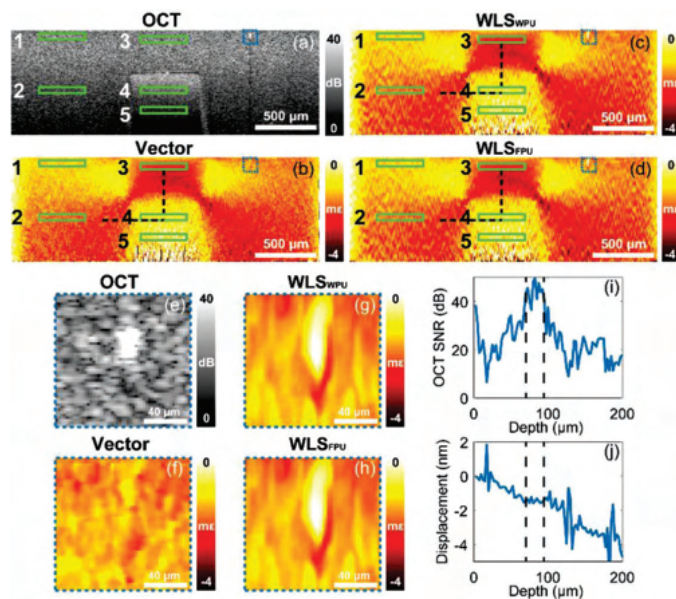


**Fig. 3.** Characterizations of strain sensitivity and strain SNR using the vector method,  $\text{WLS}_{\text{WPU}}$  and  $\text{WLS}_{\text{FPU}}$  using a B-scan acquired from Phantom 1. (a) OCT image. The corresponding strain micro-elastograms obtained using (b) the vector method, (c)  $\text{WLS}_{\text{WPU}}$  and (d)  $\text{WLS}_{\text{FPU}}$ . (e) The magnified region-of-interest where a  $\text{TiO}_2$  aggregate is resolved, marked by the dashed blue box in (a). The corresponding magnified strain obtained using (f) the vector method, (g)  $\text{WLS}_{\text{WPU}}$  and (h)  $\text{WLS}_{\text{FPU}}$ . The depth profiles of (i) OCT SNR and (j) displacement across the middle of the  $\text{TiO}_2$  aggregate. The dashed black lines in both (i) and (j) indicate the location of the aggregate.



To quantify the comparative performance of the three strain estimation methods, we used the imaging metrics defined in Table 2. We measured the strain sensitivity ( $S_{me}$ ), mean strain ( $\mu_{me}$ ), and strain SNR ( $SNR_{me}$ ) from five different regions (each  $\sim 375 \times 50 \mu\text{m}$  in area, 3,000 pixels in total) in Phantom 1, indicated by the green boxes in Figs. 3(a)–3(d). The imaging metrics corresponding to the regions are summarized in Table 3. Overall, in the regions of high OCT SNR (R1-R4), the measured strain sensitivity is similar (<5% difference), whereas in the region of low OCT SNR (R5), the strain sensitivity of the WLS-based methods is slightly superior ( $\sim 12\%$  improvement) to that of the vector method. The improved strain sensitivity of WLS is likely due to the advantage of weighted averaging over unweighted averaging in regions of low OCT SNR. Similar to strain sensitivity, the mean strain is also comparable between each method, within 5%. As such, the measured strain SNR, in general, is close between the three different methods except in region R5 where the strain SNR of both  $WLS_{WPU}$  and  $WLS_{FPU}$  is slightly higher than that of the vector method due to the higher strain sensitivity. In addition, we reported the resolution (mean  $\pm$  standard deviation) of strain micro-elastograms for all three methods, as shown in Table 3. As indicated by the dashed black lines in Figs. 3(b)–3(d), the axial resolution for each method was measured from the middle A-scan across the inclusion axial boundary, and the lateral resolution was measured from the strain step response over the inclusion lateral boundary at a depth location of  $\sim 134 \mu\text{m}$  from the inclusion surface. The mean and standard deviation were computed from three resolution measurements. Although the texture in the strain micro-elastograms gives the appearance of different resolution, as shown in Figs. 3(b)–3(d), the measured lateral and axial strain feature resolutions for three different methods are close:  $181 \mu\text{m}$  and  $182 \mu\text{m}$ , respectively. Overall, both lateral and axial strain resolution for the three different methods are similar:  $181 \mu\text{m}$  and  $182 \mu\text{m}$ , respectively. As the same number of pixels were used to estimate strain from Phantom 1 and the same OCT system was used, it is expected that the strain resolution is similar for the three different methods.

**Table 3. Strain sensitivity, mean strain, strain SNR, and strain resolution (mean  $\pm$  standard deviation) for the three strain estimation methods.**

R	OCT SNR (dB)	Strain sensitivity, $S_{me}$			Mean strain, $\mu_{me}$			Strain SNR, $SNR_{me}$ (dB)		
		Vector	$WLS_{WPU}$	$WLS_{FPU}$	Vector	$WLS_{WPU}$	$WLS_{FPU}$	Vector	$WLS_{WPU}$	$WLS_{FPU}$
1	24.9	0.16	0.16	0.16	-1.27	-1.27	-1.27	17.99	17.99	17.99
2	17.7	0.25	0.24	0.24	-1.82	-1.82	-1.80	17.24	17.60	17.50
3	25.5	0.22	0.20	0.20	-2.22	-2.22	-2.22	20.08	20.91	20.91
4	24.1	0.23	0.24	0.24	-0.87	-0.86	-0.88	11.56	11.09	11.29
5	12.4	0.41	0.36	0.36	-0.78	-0.79	-0.82	5.59	6.83	7.15
Strain estimation method		Lateral feature resolution ( $\mu\text{m}$ )				Axial feature resolution ( $\mu\text{m}$ )				
Vector		181 $\pm$ 3				182 $\pm$ 2				
$WLS_{WPU}$		181 $\pm$ 3				182 $\pm$ 3				
$WLS_{FPU}$		180 $\pm$ 3				183 $\pm$ 3				

#### 4.2. Strain accuracy

In this section, we investigate the accuracy of strain estimation for the different methods over a range of strains imparted to Phantom 2, a homogeneous silicone phantom. Figure 4(a) shows the OCT image of Phantom 2. To determine strain accuracy, we require a method to measure the strain introduced to the phantom independently of the three strain estimation methods under analysis. To achieve this, we defined the expected strain using a method previously implemented in quantitative micro-elastography (QME) [43] where strain is calculated as the displacement introduced to the phantom using a PZT actuator (as described in Section 3.2) divided by the

unloaded phantom thickness, measured from the OCT intensity image. In a common-path system, the displacement is calculated from the phase difference at the phantom boundary distal from the imaging plate, *i.e.*, at the back plate, importantly, for the specific case of Phantom 2, it was possible to image through the entire phantom. This allowed us to calculate strain without using one of the strain estimation methods typically used in OCE. Also, as described below, this method provided a strain accuracy far superior to that achievable using the strain estimation methods, providing a “ground truth” strain measurement. It is important to note that this method is not generally applicable in OCE, as it is only suited to samples whose thickness can be determined directly from an OCT image, which is not typically the case in turbid samples. Another critical aspect is that the boundaries should be well lubricated to ensure uniform axial strain throughout the sample. Using this approach, phase-sensitive detection was used to measure the displacement of the phantom at the distal back plate, with the number of wrapping events manually counted and added to the phase difference measured at the interface, avoiding any inaccuracies introduced by phase unwrapping. The phantom thickness was measured from the distance between the first pixel in the OCT image (Fig. 4(a)) and a pixel of high OCT SNR ( $\sim 58$  dB) at the sample-plate interface. The error in the strain measured using this method is the combination of errors in the displacement measurement at the interface and errors in the phantom thickness measurement. For the case of a specular reflection, it can be assumed that the phase difference error measured from any specular reflection (*e.g.*, a bright interface) is inversely proportional to OCT SNR [20,21,56] and, thus, the displacement error is 3.7 nm for a corresponding OCT SNR of 58 dB. For the phantom thickness measurement, the maximum error of the measured peak intensity is determined by the axial pixel size, corresponding to  $\sim 2.4$   $\mu\text{m}$  in the phantom (assuming a bulk refractive index of 1.4). Applying the law of error propagation, the error of expected strain is  $\sim 7.2$   $\mu\epsilon$ , which is more than an order of magnitude higher strain sensitivity than that reported in Table 3.

$S_{m\epsilon}$ ,  $\mu_{m\epsilon}$  and  $\text{SNR}_{m\epsilon}$  at different expected strain were measured from the  $\sim 1000 \times 250$   $\mu\text{m}$  white box indicated in Fig. 4(a) in the strain micro-elastograms of Phantom 2 obtained using the three different methods. Figures 4(b)–4(d) show the strain micro-elastograms at 2.5  $m\epsilon$  for the vector method,  $\text{WLS}_{\text{WPU}}$  and  $\text{WLS}_{\text{FPU}}$ , respectively. Figure 4(e) shows the measured strain sensitivity of the different strain estimation methods plotted as a function of expected strain measured. Within the low strain regime (*i.e.*,  $< 1.1$   $m\epsilon$ ), the strain sensitivity of all three methods is similar, but degrades slowly as the expected strain increases. The degradation of strain sensitivity is attributed to strain-induced phase decorrelation, which invalidates the assumption that the unloaded and loaded scans are fully correlated [31]. Within the strain regime 1.4–2.5  $m\epsilon$ , the strain sensitivity of all three methods degrades more rapidly, particularly for the vector method. This is likely due to the positive strain artifacts (*i.e.*, vertical bright lines indicated by a black arrow in Fig. 4(b)), which start to appear in the strain micro-elastogram obtained using the vector method at  $\sim 1.4$   $m\epsilon$ . Compared to WLS-based methods, these positive strain artifacts occur at lower expected strain and introduce spatial variation to the strain micro-elastogram of a mechanically homogeneous phantom, decreasing the precision (*i.e.*, strain sensitivity) of strain micro-elastograms generated using the vector method. The formation of this artifact results from the accumulated errors in the unweighted vector summation over a set of normalized phasor gradients (*i.e.*, only phase angles retained) including some noisy phase signals, which are likely to be inaccurate in regions of dark speckle [21]. As both strong and weak signals are normalized to unity, these weak and inaccurate phase values reduce the accuracy of the averaged phase gradient after vector summation.

Figure 4(f) shows the mean strain estimated using the different methods plotted against the expected strain, overlaid with a solid black line that indicates the ideal result where expected strain and estimated strain are equal. Up to the expected strain of 1.4  $m\epsilon$ , the strain estimated using all three methods is similar and shows good agreement with the ground truth. Above 1.4

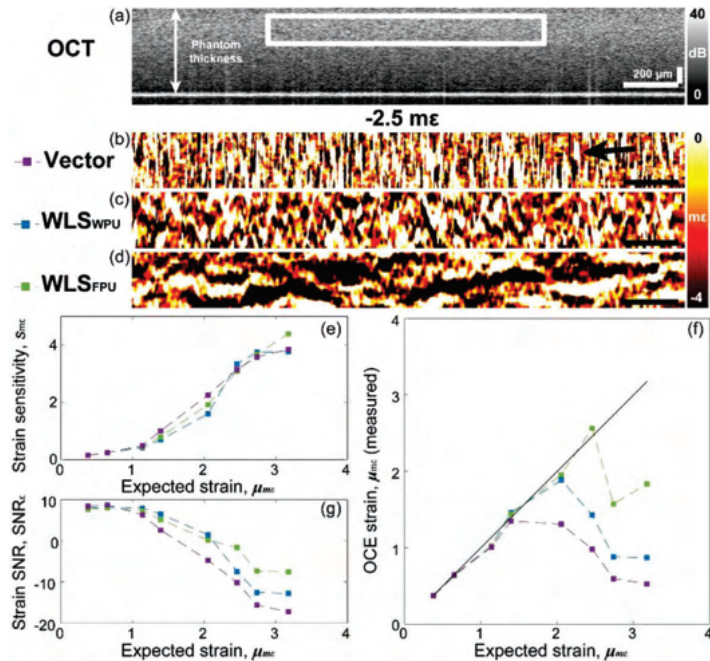


**Fig. 4.** Accuracy of strain estimation using the vector method, WLS<sub>WPU</sub> and WLS<sub>FPU</sub>, respectively. (a) OCT B-scan of Phantom 2, where a spatial window (marked by a white box) with a size of  $\sim 1000 \times 250 \mu\text{m}$  is used to quantify strain sensitivity ( $S_{m\epsilon}$ ), strain accuracy ( $\mu_{m\epsilon}$ ) and strain SNR ( $SNR_{m\epsilon}$ ). Magnified views of the window in the strain micro-elastograms at  $2.5 m\epsilon$  obtained using (b) the vector method, (c) WLS<sub>WPU</sub> and (d) WLS<sub>FPU</sub>, respectively. Scale bars in (b)-(d) represent  $100 \mu\text{m}$ . The black arrow in (b) highlights a line artifact corresponding to positive strain in the case of the vector method. (e)  $S_{m\epsilon}$ , (f)  $\mu_{m\epsilon}$  and (g)  $SNR_{m\epsilon}$  as a function of expected strain. The black line in (f) represents the ideal strain measurements where OCE strain matches expected strain.

$m\epsilon$ , the vector method significantly underestimates the expected strain. For instance, at  $2.1 m\epsilon$ , the error of strain estimation using the vector method is approximately 5 and 7 times larger than WLS<sub>WPU</sub> and WLS<sub>FPU</sub>, respectively. Analogously to the degradation of strain sensitivity using the vector method, the accuracy is also reduced due to a significant underestimation of expected strain resulting from the formation of positive strain line artifacts. Above  $2.1 m\epsilon$ , WLS<sub>WPU</sub> also significantly underestimates the strain. At  $2.5 m\epsilon$ , the vector method and WLS<sub>WPU</sub> deviate by  $\sim 42\%$  and  $\sim 60\%$  from the expected value, respectively. In contrast, at this point, the error of strain estimation using WLS<sub>FPU</sub> is  $\sim 4\%$ , which is nearly 11 and 15 times smaller than WLS<sub>WPU</sub> and the vector method, respectively. The underestimation of strain using WLS<sub>WPU</sub> is attributed to increased strain-induced decorrelation resulting in decreased phase difference sensitivity, causing errors in the calculation of the axial phase unwrapping reference in WPU. We observed that, as strain increases above  $2.5 m\epsilon$ , a high spatial frequency noise due to phase decorrelation occurs at local depth locations, resulting in zero strain (*i.e.*, a flattened unwrapped phase difference-depth profile) in these locations. This suggests that the unwrapped phase difference using WPU no longer reflects the true displacement in the sample, as indicated in Eq. (3). This ultimately leads to the reduction of strain accuracy using WLS<sub>WPU</sub>, setting an upper limit to its dynamic range of accurate strain estimation. Compared to WPU, by performing Volkov symmetrization in

3-D space, FPU incorporates more data points (*i.e.*, eight duplicates of the whole data volume), providing a more accurate estimation of unwrapped phase difference in the presence of noise. In addition, FPU is implemented in an iterative manner in which phase unwrapping errors are further reduced by iterating  $Q(\mathbf{r})$  (*i.e.*, the phase unwrapping error function) until its spatial variance meets  $\delta$  (*i.e.*, the threshold accuracy), leading to a larger dynamic range of accurate displacement estimation and, by extension, strain estimated by  $WLS_{FPU}$ , in comparison to the other two methods. More importantly, as highlighted in Fig. 4(f), the extended strain dynamic range of  $WLS_{FPU}$  could potentially lead to improved strain contrast. For instance, for expected strains of  $1.4 m\epsilon$  and  $2.5 m\epsilon$ , the strain contrast (*i.e.*, strain ratio) between these two points measured by  $WLS_{FPU}$  is  $\times 2$  larger than that of the vector method, suggesting the suitability of  $WLS_{FPU}$  for imaging strain in mechanically heterogeneous samples. Figure 4(g) presents the measured strain SNR for the three different methods, with  $WLS_{FPU}$  providing the highest strain SNR when the expected strain is above  $2.1 m\epsilon$ .

#### 4.3. Comparison of the performance of strain estimation methods in biological tissue

To compare the performance of the three strain estimation techniques on biological tissue, we first imaged a mouse muscle, as such tissue has previously been shown to provide large variations in strain across muscle fibers [57]. Figure 5 presents the results of the encapsulated EDL muscle using the different strain estimation methods. An *en face* OCT image of the tissue at a depth of  $\sim 340 \mu\text{m}$  below the tissue surface is presented in Fig. 5(a). Figures 5(b)–5(d) demonstrate the corresponding strain micro-elastograms. To better visualize the difference in image quality between the different methods, we selected a local region ( $\sim 3 \times 1 \text{ mm}$ ) that contains a characteristic feature showing a muscle striation close to the highly scattering tendon, which is highlighted by a white arrow in the magnified OCT image shown in Fig. 5(e). The corresponding magnified strain micro-elastograms are shown in Figs. 5(f)–5(h). Similar to a previous study [57], striation patterns manifest in both the OCT image and the strain micro-elastograms. Noticeably, the striation is much more clearly delineated by  $WLS_{FPU}$  in Fig. 5(h), in comparison to the other two methods, especially for the case of the vector method where the striation is hardly visible (Fig. 5(f)). The improved contrast of muscle striation provided by  $WLS_{FPU}$ , corresponding to larger compressive strains in the micro-elastogram of  $WLS_{FPU}$  (Fig. 5(h)), likely results from the extended dynamic range of  $WLS_{FPU}$  (Fig. 4(f)).

Figures 5(i) and 5(j) show the *en face* unwrapped phase difference images obtained using the WPU and FPU algorithms, respectively. Interestingly, distinctive imaging artifacts (highlighted by a dashed black arrow in Fig. 5(i)) that propagate from the tissue boundary can be observed in the unwrapped phase difference image generated using WPU, which result in streak-like imaging artifacts appearing in the corresponding strain micro-elastogram obtained with  $WLS_{WPU}$  (highlighted by a dashed black arrow in Fig. 5(c)). As the tissue is encapsulated within clear hydrogel with correspondingly low OCT SNR, the phase difference sensitivity in the hydrogel is low. As such, the axial phase unwrapping reference calculated from the preceding  $n_z$  (*i.e.*,  $n_z = 7$  herein) axial pixels is inaccurate. As highlighted in the unwrapped phase difference B-scan obtained using WPU in Fig. 5(k), this error is then propagated in the axial phase unwrapping of the subsequent axial pixels, followed by the lateral phase unwrapping [15]. In contrast, owing to the advantage of using an enlarged data volume through Volkov symmetrization and 150 iterations for the estimation of unwrapped phase difference, such an artifact is not present in the unwrapped phase difference images in the same plane generated using FPU (Figs. 5(j) and 5(l)) and the corresponding strain micro-elastograms (Figs. 5(d) and 5(h)). Similarly, since the vector method avoids the need for phase unwrapping, the strain micro-elastogram is free of this imaging artifact in Figs. 5(b) and 5(f), as expected.

In addition, we analyzed the performance of each strain estimation method on excised human breast tissue. Figure 6(a) shows an *en face* OCT image at a depth of  $100 \mu\text{m}$  from the tissue



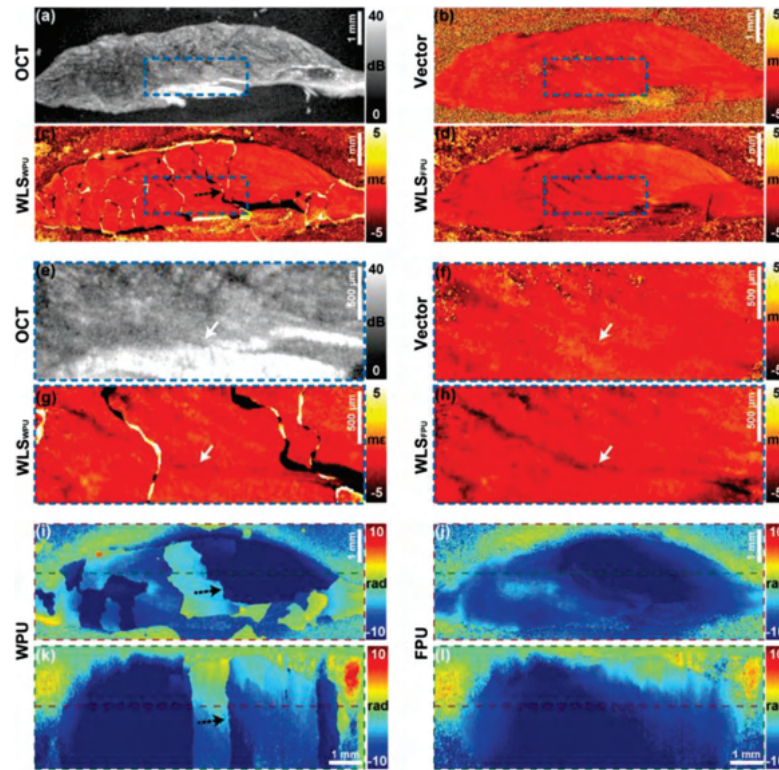


**Fig. 5.** Excised mouse EDL muscle encapsulated in the hydrogel. *En face* (a) OCT image at a depth of  $\sim 340 \mu\text{m}$  below the tissue surface. The corresponding strain micro-elastograms obtained using (b) the vector method, (c)  $\text{WLS}_{\text{WPU}}$  and (d)  $\text{WLS}_{\text{FPU}}$ , respectively. Magnified regions-of-interest (marked by dashed blue boxes in (a)-(d)) for (e) OCT, (f) the vector method, (g)  $\text{WLS}_{\text{WPU}}$  and (h)  $\text{WLS}_{\text{FPU}}$ . White arrows indicate a location where additional strain contrast of a muscle striation can be observed in (h) using  $\text{WLS}_{\text{FPU}}$ . *En face* unwrapped phase difference images obtained using (i) WPU and (j) FPU, respectively. Unwrapped phase difference B-scans obtained using (k) WPU and (l) FPU, respectively. Cross-sections in the B-scan plane and *en face* plane are represented by dashed green and red boxes. The dashed black arrows in (i) and (k) indicate a streak-like phase unwrapping artifact caused by WPU, corresponding to an artifact in the strain micro-elastogram generated using  $\text{WLS}_{\text{WPU}}$  in (c) and (g).

surface. Analogously to Fig. 5, we selected a  $\sim 4 \times 4 \text{ mm}$  region-of-interest (highlighted by a dashed blue box in Fig. 6(a)) in OCT, for better visualization of differences in micro-elastogram quality, and the magnified OCT image of this region is presented in Fig. 6(b). The co-registered histology and the corresponding strain micro-elastograms of the vector method,  $\text{WLS}_{\text{WPU}}$  and  $\text{WLS}_{\text{FPU}}$  are presented in Fig. 6(c)–6(f), respectively. In contrast to the OCT image in Fig. 6(b) where the optical contrast between the tumor and benign tissue is limited, the tumor is clearly delineated by distinctive mechanical contrast provided by all three strain estimation methods in Figs. 6(d)–6(f), showing a close correspondence with the co-registered histology in Fig. 6(c). The strain estimated by each method presents a heterogeneous pattern in regions corresponding to tumor, which is consistent with previous OCE studies [7–9]. Whilst the improvement in contrast provided by  $\text{WLS}_{\text{FPU}}$  is lower here than the case of the mouse muscle shown in Fig. 5, additional



contrast in the tumor region is still visible in the  $WLS_{FPU}$  strain micro-elastogram (Fig. 6(f)), highlighted by white arrows, particularly with respect to the vector method (Fig. 6(d)). The relatively low improvement in contrast observed in Fig. 6(f) is likely attributed to lower strain induced in this much thicker breast tissue ( $\times 7$  thicker than the mouse muscle demonstrated in Fig. 5) under compression. As such, the advantage of larger dynamic range of accurate strain estimation using  $WLS_{FPU}$  is less pronounced. Similar to Fig. 5(c), in Fig. 6(e), streak-like artifacts in the  $WLS_{WPU}$  strain micro-elastogram can be seen, which are attributed to phase unwrapping errors in WPU.

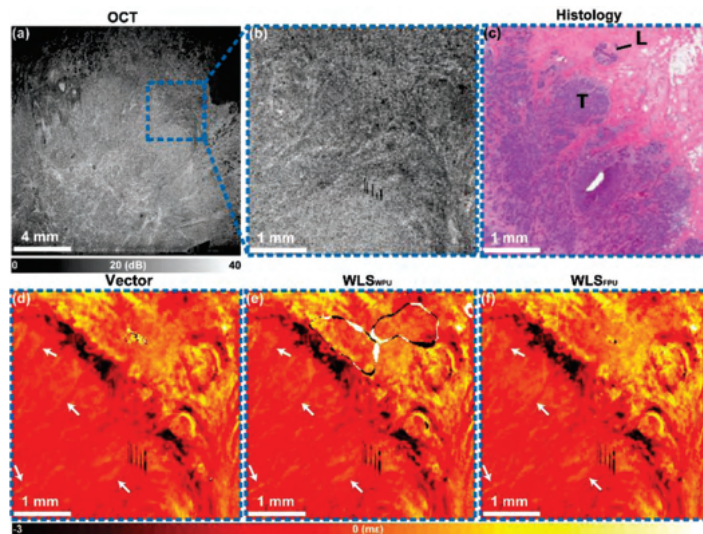


**Fig. 6.** Excised human breast tissue containing invasive tumor. (a) *En face* OCT image and (b) the magnified region-of-interest marked by the dashed blue box in (a) ( $\sim 4 \times 4$  mm in area). (c) The corresponding co-registered histology. L: Lobules, T: Tumor. The corresponding zoomed-in strain micro-elastograms for (d) the vector method, (e)  $WLS_{WPU}$  and (f)  $WLS_{FPU}$ . White arrows showing additional strain contrast provided by  $WLS_{FPU}$ .

## 5. Discussion

In this paper, we have presented the first framework that provides a comprehensive comparison between WLS and the vector method: the two most prevalent strain estimation methods. In addition, we proposed a new implementation of WLS, *i.e.*,  $WLS_{FPU}$ , by implementing FPU in OCE for the first time. We demonstrated that  $WLS_{FPU}$  provides comparable strain sensitivity and resolution to the existing methods, but an increased dynamic range of accurate strain estimation with  $\sim 4\%$  error that is approximately 11 and 15 times lower than  $WLS_{WPU}$  and the vector method, respectively, for an expected strain of  $2.5 \text{ m}\epsilon$ . Through a qualitative comparison of tissue results, we have demonstrated that the improved dynamic range of accurate strain translates to a noticeable improvement in strain contrast of tissue provided by  $WLS_{FPU}$ . In addition,  $WLS_{FPU}$  removes phase unwrapping errors in  $WLS_{WPU}$  that result in imaging artifacts in strain micro-elastograms.

In Fig. 3, we demonstrated that a highly scattering, stiff feature with dimensions below the system resolution of the OCE system presents differently in the WLS-based methods and the vector method, respectively. In the example shown in Fig. 3, whilst the WLS fitting range is  $\times 3$  larger than the size of the bright feature, the corresponding strain of the feature is detected using WLS, demonstrating the detection of sub-resolution mechanical features in OCE for the first

time. However, as the feature size is below the system resolution, the strain in the soft region adjacent to the feature is significantly underestimated by WLS (Figs. 3(g) and 3(h)). Furthermore, it can be inferred that, in the case that a soft or stiff feature is less scattering than the surrounding region, the weighting used in WLS may result in a feature being masked by the surrounding region. Whilst this effect has been demonstrated here to provide useful contrast, it should be highlighted that these scenarios are examples where the assumption used in WLS that a more accurate fitting is enabled by accounting for OCT SNR is violated. This coupling between OCT SNR and mechanical contrast suggest that it is prudent to analyze the OCT image before deciding on the optimal strain estimation technique to use for a given sample.

In Fig. 4(f), we demonstrated the effect of applied strain on the accuracy of strain estimation for three different methods. Compared to the WLS-based methods, in particular to WLS<sub>FPU</sub>, the results suggest that the vector method is less tolerant to strain-induced decorrelation noise, where the “line” artifacts (Fig. 4(b)) corresponding to positive strain becoming dominant in the micro-elastogram at an expected strain of  $2.1 \text{ m}\epsilon$ , resulting in an underestimation of strain by  $\sim 36\%$ . As detailed in Section 4.2, the formation of this artifact is attributed to the accumulated errors of strain estimation arising from the weak and inaccurate phasor gradients within the axial range of unweighted vector summation. In addition, as the phasor gradient in the vector method is calculated from the finite difference of two adjacent phasor difference in depth, it is subject to errors caused by optical noise. As such, simply increasing axial range of the unweighted vector summation worsens the strain image quality. One solution is to assign a weight of OCT SNR or, ideally, speckle brightness [21] to the phasor gradient at each pixel over the axial range of vector summation, which should improve the sensitivity and accuracy of strain estimation using the vector method. Besides, it is straightforward to increase the size of the pre-filter window of the weighted averaging for improved strain sensitivity and strain accuracy at the expense of strain resolution. For the calculation of the phasor gradient, one could calculate the finite difference between two discrete depth locations at a step of  $n$  ( $n \geq 2$ ) pixels. This essentially improves the SNR of the phasor gradient since it increases  $n$ -fold the angle of the phasor gradient (*i.e.*, the phase gradient) with a constant phase noise at each pixel. However, as it skips several pixels in depth, phase wrapping may occur within the step when the applied strain imparted to a sample is very high, making it difficult to choose an appropriate step size for the optimal strain SNR in mechanically heterogeneous biological tissues where phase wrapping could vary significantly. In addition, we note that both strain sensitivity and strain accuracy should be taken into account in OCE image interpretation. Whilst the mean strain measured in a local region could be close to the true value, the low strain sensitivity corresponding to larger spatial variation of strain measurements makes it challenging to differentiate a real mechanical feature from the noise. Thus, strain SNR (the ratio of mean strain to strain sensitivity), as illustrated in Table 2, can be used to assess the reliability of strain micro-elastograms. Separately, to trace the origin of the strain imaging artifact at various reconstruction steps, the images of OCT intensity, wrapped phase difference, unwrapped phase difference (if needed), and strain can be displayed at the same plane, and the artifacts can be identified from the comparison between these images, as shown in Fig. 5.

In Sections 4.1 and 4.2, we demonstrated the numerical comparisons of strain imaging metrics from one inclusion phantom and one homogeneous phantom. In general, to demonstrate the repeatability and reproducibility of each method, the experimental results of both intra-sample comparison and inter-sample comparison should be performed. However, previous studies suggested that, in addition to the contribution of strain estimation that we specifically focus on here, the strain micro-elastogram quality is determined by mechanical deformation [31–34]. As such, intra-sample variations (*e.g.*, inconsistent frictional conditions [32,52,55]) and inter-sample variations (*e.g.*, sample geometries and stiffness [33,34]) would obscure variations between strain estimation methods that we are targeting in this paper. A robust compression OCE setup and a

framework to enable meaningful inter-sample comparison of strain imaging metrics are worth investigating in the future.

In this paper, we demonstrated that incorporating a robust phase unwrapping algorithm into WLS can provide improved strain dynamic range over the vector method, which leads to additional imaging contrast, as demonstrated by the results in Section 4.3. However, the necessity of phase unwrapping and the varying weights in WLS make it challenging to implement this method rapidly. A main advantage of the vector method is its computational efficiency as no phase unwrapping is required. This means that the computation can readily be accelerated using complex convolution rather than vector summation and the computation of phasor difference and phasor gradients can be parallelized. This suggests that, despite the improved dynamic range of accurate strain achievable using WLS<sub>FPU</sub>, in applications requiring real-time visualization of strain, *e.g.*, imaging strain dynamics induced by thermal heating [58–62], it may be preferable to implement the vector method. This highlights the need to take a considered approach in deciding which strain estimation method to use in a given application. We believe the analysis performed in this study can assist in making that decision.

## 6. Conclusion

We have presented a framework for analyzing strain estimation in phase-sensitive compression OCE. We have demonstrated the use of this framework by proposing a new strain estimation method, WLS<sub>FPU</sub>, and more importantly, we have presented a quantitative comparison between this new method and the two most prevalent methods in compression OCE, *i.e.*, WLS<sub>WPU</sub> and the vector method. Our experimental results indicate that WLS<sub>FPU</sub> provides an increased dynamic range of accurate strain estimation by reducing errors to ~4% that is approximately 11 and 15 times smaller relative to WLS<sub>WPU</sub> and the vector method, respectively, for an expected strain of 2.5 m $\epsilon$ . Through a qualitative comparison of tissue results, we have shown that this increased dynamic range translates to higher mechanical contrast in strain micro-elastograms of heterogeneous tissue. We have also shown that imaging artifacts caused by phase unwrapping in WLS<sub>WPU</sub> can be avoided using WLS<sub>FPU</sub>. Furthermore, we have demonstrated the detection of sub-resolution mechanical features using WLS-based strain estimation. We believe that our framework provides a useful mechanism to compare strain estimation methods that could be adapted to compare different signal processing methods used in other OCE techniques such as transient OCE.

**Funding.** Cancer Council Western Australia; Fundacja na rzecz Nauki Polskiej (POIR.04.04.00-00-2070/16-00); Department of Jobs, Tourism, Science and Innovation, Government of Western Australia; Australian Research Council Industrial Transformation Training Centre; Department of Health, Government of Western Australia.

**Acknowledgements.** The authors thank Erin M. Lloyd and Matt S. Hepburn for providing experimental data of mouse muscle tissue for assessing the comparative performance of strain estimation methods in this paper.

**Disclosures.** BFK: OncoRes Medical (F, I). The other authors declare that there are no conflicts of interest related to this article.

**Data availability.** Data underlying the results presented in this paper are not publicly available at this time but may be obtained from the authors upon reasonable request.

## References

1. B. F. Kennedy, K. M. Kennedy, and D. D. Sampson, "A review of optical coherence elastography: fundamentals, techniques and prospects," *IEEE J. Sel. Top. Quantum Electron.* **20**(2), 272–288 (2014).
2. J. A. Mulligan, G. R. Untracht, S. N. Chandrasekaran, C. N. Brown, and S. G. Adie, "Emerging approaches for high-resolution imaging of tissue biomechanics with optical coherence elastography," *IEEE J. Sel. Top. Quantum Electron.* **22**(3), 246–265 (2016).
3. K. V. Larin and D. D. Sampson, "Optical coherence elastography – OCT at work in tissue biomechanics [Invited]," *Biomed. Opt. Express* **8**(2), 1172–1202 (2017).
4. S. Wang and K. V. Larin, "Optical coherence elastography for tissue characterization: A review," *J. Biophotonics* **8**(4), 279–302 (2015).

5. V. Y. Zaitsev, A. L. Matveyev, L. A. Matveev, A. A. Sovetsky, M. S. Hepburn, A. Mowla, and B. F. Kennedy, "Strain and elasticity imaging in compression optical coherence elastography: the two-decade perspective and recent advances," *J. Biophotonics* **14**(2), e202000257 (2021).
6. B. F. Kennedy, *Optical Coherence Elastography: Imaging Tissue Mechanics on the Micro-Scale* (AIP Publishing, 2021).
7. B. F. Kennedy, R. A. McLaughlin, K. M. Kennedy, L. Chin, P. Wijesinghe, A. Curatolo, A. Tien, M. Ronald, B. Latham, C. M. Saunders, and D. D. Sampson, "Investigation of optical coherence microelastography as a method to visualize cancers in human breast tissue," *Cancer Res.* **75**(16), 3236–3245 (2015).
8. W. M. Allen, L. Chin, P. Wijesinghe, R. W. Kirk, B. Latham, D. D. Sampson, C. M. Saunders, and B. F. Kennedy, "Wide-field optical coherence micro-elastography for intraoperative assessment of human breast cancer margins," *Biomed. Opt. Express* **7**(10), 4139–4153 (2016).
9. W. M. Allen, K. Y. Foo, R. Zilkens, K. M. Kennedy, Q. Fang, L. Chin, B. F. Dessauvagie, B. Latham, C. M. Saunders, and B. F. Kennedy, "Clinical feasibility of optical coherence micro-elastography for imaging tumor margins in breast-conserving surgery," *Biomed. Opt. Express* **9**(12), 6331–6349 (2018).
10. K. M. Kennedy, R. Zilkens, W. M. Allen, K. Y. Foo, Q. Fang, L. Chin, R. W. Sanderson, J. Anstie, P. Wijesinghe, A. Curatolo, H. E. I. Tan, N. Morin, B. Kunjuraman, C. Yeomans, S. L. Chin, H. DeJong, K. Giles, B. F. Dessauvagie, B. Latham, C. M. Saunders, and B. F. Kennedy, "Diagnostic accuracy of quantitative micro-elastography for margin assessment in breast-conserving surgery," *Cancer Res.* **80**(8), 1773–1783 (2020).
11. A. A. Plekhanov, M. A. Sirotkina, A. A. Sovetsky, E. V. Gubarkova, S. S. Kuznetsov, A. L. Matveyev, L. A. Matveev, E. V. Zagaynova, N. D. Gladkova, and V. Y. Zaitsev, "Histological validation of in vivo assessment of cancer tissue inhomogeneity and automated morphological segmentation enabled by optical coherence elastography," *Sci. Rep.* **10**(1), 11781 (2020).
12. W. J. Hadden, J. L. Young, A. W. Holle, M. L. McFetridge, D. Y. Kim, P. Wijesinghe, H. Taylor-Weiner, J. H. Wen, A. R. Lee, K. Bieback, B. N. Vo, D. D. Sampson, B. F. Kennedy, J. P. Spatz, A. J. Engler, and Y. S. Cho, "Stem cell migration and mechanotransduction on linear stiffness gradient hydrogels," *Proc. Natl. Acad. Sci. U. S. A.* **114**(22), 5647–5652 (2017).
13. M. S. Hepburn, P. Wijesinghe, L. G. Major, J. Li, A. Mowla, C. Astell, H. W. Park, Y. Hwang, Y. S. Choi, and B. F. Kennedy, "Three-dimensional imaging of cell and extracellular matrix elasticity using quantitative micro-elastography," *Biomed. Opt. Express* **11**(2), 867–884 (2020).
14. L. G. Major, A. W. Holle, J. L. Young, M. S. Hepburn, K. Jeong, I. L. Chin, R. W. Sanderson, J. H. Jeong, Z. M. Aman, B. F. Kennedy, Y. Hwang, D. W. Han, H. W. Park, K. L. Guan, J. P. Spatz, and Y. S. Choi, "Volume adaptation controls stem cell mechanotransduction," *ACS Appl. Mater. Interfaces* **11**(49), 45520–45530 (2019).
15. Q. Fang, A. Curatolo, P. Wijesinghe, Y. L. Yeow, J. Hamzah, P. B. Noble, K. Karnowski, D. D. Sampson, R. Ganss, J. K. Kim, W. M. Lee, and B. F. Kennedy, "Ultrahigh-resolution optical coherence elastography through a micro-endoscope: towards in vivo imaging of cellular-scale mechanics," *Biomed. Opt. Express* **8**(11), 5127–5138 (2017).
16. R. W. Sanderson, A. Curatolo, P. Wijesinghe, L. Chin, and B. F. Kennedy, "Finger-mounted quantitative micro-elastography," *Biomed. Opt. Express* **10**(4), 1760–1773 (2019).
17. Q. Fang, B. Krajancich, L. Chin, R. Zilkens, A. Curatolo, L. Frewer, J. D. Anstie, P. Wijesinghe, C. Hall, B. F. Dessauvagie, B. Latham, C. M. Saunders, and B. F. Kennedy, "Handheld probe for quantitative micro-elastography," *Biomed. Opt. Express* **10**(8), 4034–4049 (2019).
18. Q. Fang, L. Frewer, R. Zilkens, B. Krajancich, A. Curatolo, L. Chin, K. Y. Foo, D. D. Lakhiani, R. W. Sanderson, P. Wijesinghe, J. D. Anstie, B. F. Dessauvagie, B. Latham, C. M. Saunders, and B. F. Kennedy, "Handheld volumetric manual compression-based quantitative microelastography," *J. Biophotonics* **13**(6), e201960196 (2020).
19. X. Wang, Q. Wu, J. Chen, and J. Mo, "Development of a handheld compression optical coherence elastography probe with a disposable stress sensor," *Opt. Lett.* **46**(15), 3669–3672 (2021).
20. B. Hyle Park, M. C. Pierce, B. Cense, S.-H. Yun, M. Mujat, G. J. Tearney, B. E. Bouma, and J. F. de Boer, "Real-time fiber-based multi-functional spectral-domain optical coherence tomography at 1.3  $\mu\text{m}$ ," *Opt. Express* **13**(11), 3931 (2005).
21. M. S. Hepburn, K. Y. Foo, P. Wijesinghe, P. R. T. Munro, L. Chin, and B. F. Kennedy, "Speckle-dependent accuracy in phase-sensitive optical coherence tomography," *Opt. Express* **29**(11), 16950–16968 (2021).
22. J. M. Schmitt, "OCT elastography: imaging microscopic deformation and strain of tissue," *Opt. Express* **3**(6), 199–211 (1998).
23. F. Kallel and J. Ophir, "A least-squares strain estimator for elastography," *Ultrason. Imaging* **19**(3), 195–208 (1997).
24. B. F. Kennedy, S. H. Koh, R. A. McLaughlin, K. M. Kennedy, P. R. T. Munro, and D. D. Sampson, "Strain estimation in phase-sensitive optical coherence elastography," *Biomed. Opt. Express* **3**(8), 1865–1879 (2012).
25. B. F. Kennedy, M. Wojtkowski, M. Szkulmowski, K. M. Kennedy, K. Karnowski, and D. D. Sampson, "Improved measurement of vibration amplitude in dynamic optical coherence elastography," *Biomed. Opt. Express* **3**(12), 3138 (2012).
26. F. Zvietcovich, G. R. Ge, H. Mestre, M. Giannetto, M. Nedergaard, J. P. Rolland, and K. J. Parker, "Longitudinal shear waves for elastic characterization of tissues in optical coherence elastography," *Biomed. Opt. Express* **10**(7), 3699–3718 (2019).



27. A. Nair, M. Singh, S. Aglyamov, and K. V. Larin, "Heartbeat optical coherence elastography: corneal biomechanics in vivo," *J. Biomed. Opt.* **26**(02), 020502 (2021).
28. M. Singh, A. Nair, S. R. Aglyamov, and K. V. Larin, "Compressional optical coherence elastography of the cornea," *Photonics* **8**(4), 111 (2021).
29. V. Y. Zaitsev, A. L. Matveyev, L. A. Matveev, G. V. Gelikonov, A. A. Sovetsky, and A. Vitkin, "Optimized phase gradient measurements and phase-amplitude interplay in optical coherence elastography," *J. Biomed. Opt.* **21**(11), 116005 (2016).
30. A. L. Matveyev, L. A. Matveev, A. A. Sovetsky, G. V. Gelikonov, A. A. Moiseev, and V. Y. Zaitsev, "Vector method for strain estimation in phase-sensitive optical coherence elastography," *Laser Phys. Lett.* **15**(6), 065603 (2018).
31. L. Chin, A. Curatolo, B. F. Kennedy, B. J. Doyle, P. R. T. Munro, R. A. McLaughlin, and D. D. Sampson, "Analysis of image formation in optical coherence elastography using a multiphysics approach," *Biomed. Opt. Express* **5**(9), 2913–2930 (2014).
32. J. Li, M. S. Hepburn, L. Chin, A. Mowla, and B. F. Kennedy, "Analysis of sensitivity in quantitative micro-elastography," *Biomed. Opt. Express* **12**(3), 1725–1745 (2021).
33. K. M. Kennedy, C. Ford, B. F. Kennedy, M. B. Bush, and D. D. Sampson, "Analysis of mechanical contrast in optical coherence elastography," *J. Biomed. Opt.* **18**(12), 121508 (2013).
34. M. S. Hepburn, P. Wijesinghe, L. Chin, and B. F. Kennedy, "Analysis of spatial resolution in phase-sensitive compression optical coherence elastography," *Biomed. Opt. Express* **10**(3), 1496–1513 (2019).
35. N. Leartprapun, R. R. Iyer, C. D. Mackey, and S. G. Adie, "Spatial localization of mechanical excitation affects spatial resolution, contrast, and contrast-to-noise ratio in acoustic radiation force optical coherence elastography," *Biomed. Opt. Express* **10**(11), 5877 (2019).
36. M. A. Kirby, K. Zhou, J. J. Pitre, L. Gao, D. S. Li, I. M. Pelivanov, S. Song, C. Li, Z. Huang, T. T. Shen, R. K. Wang, and M. O'Donnell, "Spatial resolution in dynamic optical coherence elastography," *J. Biomed. Opt.* **24**(09), 1 (2019).
37. B. F. Kennedy, R. A. McLaughlin, K. M. Kennedy, L. Chin, A. Curatolo, A. Tien, B. Latham, C. M. Saunders, and D. D. Sampson, "Optical coherence micro-elastography: mechanical-contrast imaging of tissue microstructure," *Biomed. Opt. Express* **5**(7), 2113–2124 (2014).
38. J. Martinez-Carranza, K. Falaggis, and T. Kozacki, "Fast and accurate phase-unwrapping algorithm based on the transport of intensity equation," *Appl. Opt.* **56**(25), 7079 (2017).
39. E. Pijewska, I. Gorczynska, and M. Szkulmowski, "Computationally effective 2D and 3D fast phase unwrapping algorithms and their applications to Doppler optical coherence tomography," *Biomed. Opt. Express* **10**(3), 1365 (2019).
40. E. Pijewska, M. Sylwestrzak, I. Gorczynska, S. Tamborski, M. A. Pawlak, and M. Szkulmowski, "Blood flow rate estimation in optic disc capillaries and vessels using Doppler optical coherence tomography with 3D fast phase unwrapping," *Biomed. Opt. Express* **11**(3), 1336 (2020).
41. V. V. Volkov, Y. Zhu, and M. De Graef, "A new symmetrized solution for phase retrieval using the transport of intensity equation," *Micron* **33**(5), 411–416 (2002).
42. B. F. Kennedy, K. M. Kennedy, A. L. Oldenburg, S. G. Adie, S. A. Boppart, and D. D. Sampson, "Optical coherence elastography," in *Optical Coherence Tomography: Technology and Applications, Second Edition* (Springer Reference, 2015), pp. 1007–1054.
43. K. M. Kennedy, L. Chin, R. A. McLaughlin, B. Latham, C. M. Saunders, D. D. Sampson, and B. F. Kennedy, "Quantitative micro-elastography: Imaging of tissue elasticity using compression optical coherence elastography," *Sci. Rep.* **5**(1), 15538 (2015).
44. Y. Qiu, Y. Wang, Y. Xu, N. Chandra, J. Haorah, B. Hubbi, B. J. Pfister, and X. Liu, "Quantitative optical coherence elastography based on fiber-optic probe for in situ measurement of tissue mechanical properties," *Biomed. Opt. Express* **7**(2), 688–700 (2016).
45. A. A. Sovetsky, A. L. Matveyev, L. A. Matveev, D. V. Shabanov, and V. Y. Zaitsev, "Manually-operated compressional optical coherence elastography with effective aperiodic averaging: Demonstrations for corneal and cartilaginous tissues," *Laser Phys. Lett.* **15**(8), 085602 (2018).
46. C. Kasai, K. Namekawa, A. Koyano, and R. Omoto, "Real-time two-dimensional blood flow imaging using an autocorrelation technique," *IEEE Trans. Sonics Ultrason.* **32**(3), 458–464 (1985).
47. V. X. D. Yang, M. L. Gordon, A. Mok, Y. Zhao, Z. Chen, R. S. C. Cobbold, B. C. Wilson, and I. A. Vitkin, "Improved phase-resolved optical Doppler tomography using the Kasai velocity estimator and histogram segmentation," *Opt. Commun.* **208**(4-6), 209–214 (2002).
48. Z. Zhao, H. Zhang, C. Ma, C. Fan, and H. Zhao, "Comparative study of phase unwrapping algorithms based on solving the Poisson equation," *Meas. Sci. Technol.* **31**(6), 065004 (2020).
49. E. Brusseau, J. Kybic, J. F. Déprez, and O. Basset, "2-D locally regularized tissue strain estimation from radio-frequency ultrasound images: theoretical developments and results on experimental data," *IEEE Trans. Med. Imaging* **27**(2), 145–160 (2008).
50. G. Guan, "Quantitative evaluation of degenerated tendon model using combined optical coherence elastography and acoustic radiation force method," *J. Biomed. Opt.* **18**(11), 111417 (2013).
51. J. W. Nichol, S. T. Koshy, H. Bae, C. M. Hwang, S. Yamanlar, and A. Khademhosseini, "Cell-laden microengineered gelatin methacrylate hydrogels," *Biomaterials* **31**(21), 5536–5544 (2010).



52. V. Y. Zaitsev, A. L. Matveyev, L. A. Matveev, E. V. Gubarkova, A. A. Sovetsky, M. A. Sirotkina, G. V. Gelikonov, E. V. Zagaynova, N. D. Gladkova, and A. Vitkin, "Practical obstacles and their mitigation strategies in compressional optical coherence elastography of biological tissues," *J. Innov. Opt. Health Sci.* **10**(06), 1742006 (2017).
53. S. Nicolle and J. F. Palierne, "Dehydration effect on the mechanical behaviour of biological soft tissues: observations on kidney tissues," *J. Mech. Behav. Biomed. Mater.* **3**(8), 630–635 (2010).
54. P. Wijesinghe, R. A. McLaughlin, D. D. Sampson, and B. F. Kennedy, "Parametric imaging of viscoelasticity using optical coherence elastography," *Phys. Med. Biol.* **60**(6), 2293–2307 (2015).
55. P. Wijesinghe, D. D. Sampson, and B. F. Kennedy, "Computational optical palpation: A finiteelement approach to micro-scale tactile imaging using a compliant sensor," *J. R. Soc. Interface* **14**(128), 20160878 (2017).
56. J. W. Goodman, *Statistical Optics*, 2nd ed., Wiley Series in Pure and Applied Optics (Wiley, 2015).
57. L. Chin, B. F. Kennedy, K. M. Kennedy, P. Wijesinghe, G. J. Pinniger, J. R. Terrill, R. A. McLaughlin, and D. D. Sampson, "Three-dimensional optical coherence micro-elastography of skeletal muscle tissue," *Biomed. Opt. Express* **5**(9), 3090–3102 (2014).
58. V. Y. Zaitsev, A. L. Matveyev, L. A. Matveev, G. V. Gelikonov, A. I. Omelchenko, D. V. Shabanov, O. I. Baum, V. M. Svistushkin, and E. N. Sobol, "Optical coherence tomography for visualizing transient strains and measuring large deformations in laser-induced tissue reshaping," *Laser Phys. Lett.* **13**(11), 115603 (2016).
59. V. Y. Zaitsev, A. L. Matveyev, L. A. Matveev, G. V. Gelikonov, A. I. Omelchenko, O. I. Baum, S. E. Avetisov, A. V. Bolshunov, V. I. Siplivy, D. V. Shabanov, A. Vitkin, and E. N. Sobol, "Optical coherence elastography for strain dynamics measurements in laser correction of cornea shape," *J. Biophotonics* **10**(11), 1450–1463 (2017).
60. V. Y. Zaitsev, A. L. Matveyev, L. A. Matveev, G. V. Gelikonov, O. I. Baum, A. I. Omelchenko, D. V. Shabanov, A. A. Sovetsky, A. V. Yuzhakov, A. A. Fedorov, V. I. Siplivy, A. V. Bolshunov, and E. N. Sobol, "Revealing structural modifications in thermomechanical reshaping of collagenous tissues using optical coherence elastography," *J. Biophotonics* **12**(3), e201800250 (2019).
61. O. I. Baum, V. Y. Zaitsev, A. V. Yuzhakov, A. P. Sviridov, M. L. Novikova, A. L. Matveyev, L. A. Matveev, A. A. Sovetsky, and E. N. Sobol, "Interplay of temperature, thermal-stresses and strains in laser-assisted modification of collagenous tissues: speckle-contrast and OCT-based studies," *J. Biophotonics* **13**(1), e201900199 (2020).
62. Y. M. Alexandrovskaya, O. I. Baum, A. A. Sovetsky, A. L. Matveyev, L. A. Matveev, E. N. Sobol, and V. Y. Zaitsev, "Observation of internal stress relaxation in laser-reshaped cartilaginous implants using OCT-based strain mapping," *Laser Phys. Lett.* **17**(8), 085603 (2020).

### **Co-authorship declarations**

The substantive contribution of all the authors of the [Pub. 1-5](#) has been included in this chapter.

dr hab. Iwona Gorczynska, prof. UMK  
Institute of Physics  
Faculty of Physics, Astronomy and Informatics  
Nicolaus Copernicus University in Torun  
Grudziadzka 5, 87-100 Torun, Poland

### Statement of coauthorship

1. I hereby declare that my contribution to the paper

Ewelina Pijewska, Iwona Gorczynska, and Maciej Szkulmowski. "Computationally effective 2D and 3D fast phase unwrapping algorithms and their applications to Doppler optical coherence tomography." *Biomedical Optics Express* 10.3 (2019): 1365-1382. <https://doi.org/10.1364/BOE.10.001365>

**included:** participation in the development of the research problem and concept of the paper, consultations in planning and execution of the experiments, critical editing of the manuscript, training PhD student Ewelina Pijewska in work with optical clinical setups.

2. I hereby declare that my contribution to the paper

Ewelina Pijewska, Marcin Sylwestrzak, Iwona Gorczynska, Szymon Tamborski, Mikołaj Pawlak, Maciej Szkulmowski. "Blood flow rate estimation in optic disc capillaries and vessels using Doppler optical coherence tomography with 3D fast phase unwrapping". *Biomedical Optics Express* 11.3 (2020): 1336-1353. <https://doi.org/10.1364/BOE.382155>

**included:** participation in the development of the research problem, consultations in planning and execution of the experiments, critical editing of the paper.

3. I hereby declare that my contribution to the paper

Ewelina Pijewska, Marcin Sylwestrzak, Krystian Wróbel, Iwona Gorczynska, Szymon Tamborski, Mikołaj Pawlak, Maciej Szkulmowski. "Blood flow rate estimation in optic disc capillaries and vessels using Doppler optical coherence tomography." *Biomedical Spectroscopy, Microscopy, and Imaging*. Vol. 11359. International Society for Optics and Photonics, 2020. <https://doi.org/10.1117/12.2555754>

**included:** participation in the development of the research problem of the paper, consultations in planning and execution of the experiments, critical editing of the manuscript.



**Iwona Gorczynska, PhD, prof. NCU**  
Institute of Physics  
Faculty of Physics, Astronomy and Informatics  
Nicolaus Copernicus University in Torun, Poland

Toruń, 11-01-2022

dr inż. Marcin Sylwestrzak  
Instytut Fizyki UMK  
ul. Grudziądzka 5/7  
87-100 Toruń

### Statement of coauthorship

I hereby declare that my contribution to the paper:

Ewelina Pijewska, Marcin Sylwestrzak, Iwona Gorczynska, Szymon Tamborski, Mikołaj Pawlak, Maciej Szkulmowski. "Blood flow rate estimation in optic disc capillaries and vessels using Doppler optical coherence tomography with 3D fast phase unwrapping". Biomedical Optics Express 11.3 (2020): 1336-1353. <https://doi.org/10.1364/BOE.382155>

it included the development of software (ustilising CUDA technology) for OCT data processing from optical fringes to structural and phase information incorporating spectral and temporal OCT processing, consultations on the implementation of the phase unwrapping algorithm in CUDA, assistance in the preparation of the CUDA library.

I hereby declare that my contribution to the paper:

Ewelina Pijewska, Marcin Sylwestrzak, Krystian Wróbel, Iwona Gorczynska, Szymon Tamborski, Mikołaj Pawlak, Maciej Szkulmowski. "Blood flow rate estimation in optic disc capillaries and vessels using Doppler optical coherence tomography." Biomedical Spectroscopy, Microscopy, and Imaging, Vol. 11359. International Society for Optics and Photonics, 2020. <https://doi.org/10.1117/12.2555754>

it included the development of software (ustilising CUDA technology) for OCT data processing from optical fringes to structural and phase information incorporating spectral and temporal OCT processing, consultations on the implementation of the phase unwrapping algorithm in CUDA, assistance in the preparation of the CUDA library.



(coauthor signature)



Toruń, 11-01-2022

dr Szymon Tamborski  
Institute of Physics  
Nicolaus Copernicus University in Toruń  
ul. Grudziądzka 5/7  
87-100 Toruń

### **Statement of coauthorship**

I hereby declare that my contribution to the paper:

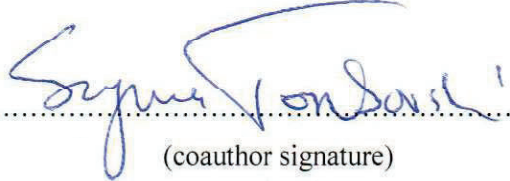
Ewelina Pijewska, Marcin Sylwestrzak, Iwona Gorczynska, Szymon Tamborski, Mikołaj Pawlak, Maciej Szkulmowski. "Blood flow rate estimation in optic disc capillaries and vessels using Doppler optical coherence tomography with 3D fast phase unwrapping". Biomedical Optics Express 11.3 (2020): 1336-1353. <https://doi.org/10.1364/BOE.382155>

included design and building of the optical setup to experiments with flow phantoms, consultation on the realization of the experiments with flow phantom, support given to Ph.D. student Ewelina Pijewska in preparing OCT setup to experiments with flow phantom.

I hereby declare that my contribution to the paper:

Ewelina Pijewska, Marcin Sylwestrzak, Krystian Wróbel, Iwona Gorczynska, Szymon Tamborski, Mikołaj Pawlak, Maciej Szkulmowski. "Blood flow rate estimation in optic disc capillaries and vessels using Doppler optical coherence tomography." Biomedical Spectroscopy, Microscopy, and Imaging. Vol. 11359. International Society for Optics and Photonics, 2020. <https://doi.org/10.1117/12.2555754>

included design and building of the optical setup to experiments with flow phantoms, consultation on the realization of the experiments with flow phantom, support given to Ph.D. student Ewelina Pijewska in preparing OCT setup to experiments with flow phantom.

  
.....  
(coauthor signature)



Poznań, 11-01-2022

dr n. med. Mikołaj Pawlak  
Department of Neurology and Cerebrovascular Disorders  
University of Medical Sciences  
Fredry 10, 61-701 Poznań, Poland

### **Statement of coauthorship**

I hereby declare that my contribution to the paper:


Ewelina Pijewska, Marcin Sylwestrzak, Iwona Gorczynska, Szymon Tamborski, Mikołaj Pawlak, Maciej Szkulmowski. "Blood flow rate estimation in optic disc capillaries and vessels using Doppler optical coherence tomography with 3D fast phase unwrapping". Biomedical Optics Express 11.3 (2020): 1336-1353. <https://doi.org/10.1364/BOE.382155>

included assisting during experiments in vivo with human retina, medical and science consultation of selected blood flow parameters, and an indication of the significance of this project in medical application in the future.

I hereby declare that my contribution to the paper:

Ewelina Pijewska, Marcin Sylwestrzak, Krystian Wróbel, Iwona Gorczynska, Szymon Tamborski, Mikołaj Pawlak, Maciej Szkulmowski. "Blood flow rate estimation in optic disc capillaries and vessels using Doppler optical coherence tomography." Biomedical Spectroscopy, Microscopy, and Imaging. Vol. 11359. International Society for Optics and Photonics, 2020. <https://doi.org/10.1117/12.2555754>

included assisting during experiments in vivo with human retina, medical and science consultation of selected blood flow parameters, creating of the idea of comparing results of blood flow velocities from transcranial USG with OCT, and an indication of the significance of this project in medical application in the future.

  
.....  
(coauthor signature)

Toruń, 11-01-2022

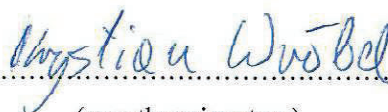
mgr inż. Krystian Wróbel  
Instytut Fizyki UMK  
ul. Grudziądzka 5/7  
87-100 Toruń

### Statement of coauthorship

I hereby declare that my contribution to the paper:

Ewelina Pijewska, Marcin Sylwestrzak, Krystian Wróbel, Iwona Gorczynska, Szymon Tamborski, Mikołaj Pawlak, Maciej Szkulmowski. "Blood flow rate estimation in optic disc capillaries and vessels using Doppler optical coherence tomography." Biomedical Spectroscopy, Microscopy, and Imaging. Vol. 11359. International Society for Optics and Photonics, 2020. <https://doi.org/10.1117/12.2555754>

included preparing software to acquire USG signal and synchronization with OCT measurement, help with experiments in vivo on human volunteers.



(coauthor signature)



Eye Center

4860 Y Street, Suite 2400  
Sacramento, CA 95817-2307  
916-734-6602 tel  
[health.ucdavis.edu/eyecenter](http://health.ucdavis.edu/eyecenter)

Vision Science and Advanced Retinal Imaging Laboratory (VSRI)  
UC Davis Eye Center  
4860 Y Street Suite 2400  
Sacramento, California 95817

UC Davis EyePod  
Department of Cell Biology and Human Anatomy  
4304 Tupper Hall  
Davis, California 95616

Phone: (916) 734-5839  
Cell: (916)-233-8240  
Fax: (916) 734-4543  
e-mail: [rjzawadzki@ucdavis.edu](mailto:rjzawadzki@ucdavis.edu)

Robert J. Zawadzki  
Associate Professor  
Department of Ophthalmology & Vision Science  
and  
Department of Cell Biology and Human Anatomy

January 11th, 2022

### Statement of co authorship

To whom it may concern,

I hereby declare that my contribution to the paper:

Ewelina Pijewska, Pengfei Zhang, Michał Meina, Ratheesh K. Meleppat, Maciej Szkulmowski, and Robert J. Zawadzki, "Extraction of phase-based optoretinograms (ORG) from serial B-scans acquired over tens of seconds by mouse retinal raster scanning OCT system," *Biomed. Opt. Express* 12.12 (2021): 7849-7871. <https://doi.org/10.1364/BOE.439900>

included determination of the research problem for this paper, consultations on the idea of the experiments, consultation on the idea of the phase-based method application in optoretinography, dissemination of the result and editing manuscript.

(co author signature)

Sincerely,

Robert J. Zawadzki, Ph.D.

Associate Professor of Ophthalmology and Vision Science  
University of California, Davis

Toruń, 19-01-2022

Ph.D. Pengfei Zhang

School of Optoelectronic Engineering and Instrumentation Science

Dalian University of Technology

No. 2 Linggong Road, Ganjingzi District, Dalian City, Liaoning Province 116024, China

### Statement of co authorship

I hereby declare that my contribution to the paper:

Ewelina Pijewska, Pengfei Zhang, Michał Meina, Ratheesh K. Meleppat, Maciej Szkulmowski, and Robert J. Zawadzki, "Extraction of phase-based optoretinograms (ORG) from serial B-scans acquired over tens of seconds by mouse retinal raster scanning OCT system," Biomed. Opt. Express 12.12 (2021): 7849-7871. <https://doi.org/10.1364/BOE.439900>

included design and implementation of the mouse retinal imaging system, OCT-ORG data acquisition and processing, data analysis to extract intensity-based optoretinograms, editing manuscript.



.....  
(coauthor signature)

Davis, 11-01-2022

Ph.D. Ratheesh K. Meleppat

UC Davis Eyepod Imaging Laboratory, Dept. of Cell Biology and Human Anatomy,  
The University of California, Davis,  
4320 Tupper Hall, Davis, CA 95616, USA.

### Statement of co authorship

I hereby declare that my contribution to the paper:

Ewelina Pijewska, Pengfei Zhang, Michał Meina, Ratheesh K. Meleppat, Maciej Szkulmowski, and Robert J. Zawadzki, "Extraction of phase-based optoretinograms (ORG) from serial B-scans acquired over tens of seconds by mouse retinal raster scanning OCT system," Biomed. Opt. Express 12.12 (2021): 7849-7871. <https://doi.org/10.1364/BOE.439900>

included maintenance of the mouse retinal imaging system, consultation on the optical design of the ORG setup, application of modified phase-based method to extract light-evoke changes, editing manuscript.

A handwritten signature in black ink, appearing to be 'Ratheesh K. Meleppat', written over a horizontal dotted line.

(coauthor signature)



Toruń, 11-01-2022

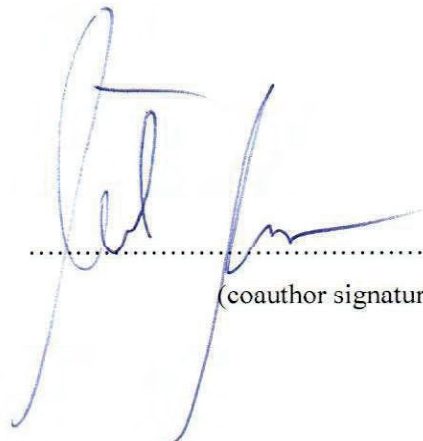
mgr Michał Meina  
Instytut Fizyki UMK  
ul. Grudziądzka 5/7  
87-100 Toruń

### **Statement of coauthorship**

I hereby declare that my contribution to the paper:

Ewelina Pijewska, Pengfei Zhang, Michał Meina, Ratheesh K. Meleppat, Maciej Szkulmowski, and Robert J. Zawadzki, "Extraction of phase-based optoretinograms (ORG) from serial B-scans acquired over tens of seconds by mouse retinal raster scanning OCT system," Biomed. Opt. Express 12.12 (2021): 7849-7871. <https://doi.org/10.1364/BOE.439900>

included preparing algorithm to retinal layers segmentation and consultation in the field of Python programming.



(coauthor signature)

Crawley, 19-03-2022

Prof. Brendan Kennedy

BRITelab, Harry Perkins Institute of Medical Research, QEII Medical Centre Nedlands and Centre for Medical Research, The University of Western Australia, Crawley, Western Australia 6009 Australia

Department of Electrical, Electronic & Computer Engineering, School of Engineering, The University of Western Australia, Crawley 6009, Australia

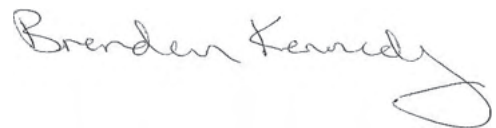
Australian Research Council Centre for Personalized Therapeutics Technologies, Australia

### Statement of coauthorship

I hereby declare my contribution to the paper:

Jiayue Li, Ewelina Pijewska, Qi Fang, Maciej Szkulmowski, Brendan Kennedy, "Analysis of strain estimation methods in phase-sensitive compression optical coherence elastography", *Biomed. Opt. Express* **13**(4), p. 2224-2246 (2022), <https://doi.org/10.1364/BOE.447340>

included supervision of Ph.D. student Jiayue Li, determination of the research problem of this paper, dissemination of the result and editing manuscript, consultations of the idea of the experiments, help in the interpretation of elastography results.



.....  
(coauthor signature)

Crawley, 11-01-2022

MSc Jiayue Li

BRITelab, Harry Perkins Institute of Medical Research, QEII Medical Centre Nedlands and Centre for Medical Research,

The University of Western Australia, Crawley, Western Australia 6009 Australia

Department of Electrical, Electronic & Computer Engineering, School of Engineering,

The University of Western Australia, Crawley 6009, Australia

Australian Research Council Centre for Personalized Therapeutics Technologies, Australia

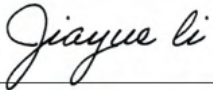
### **Statement of coauthorship**

I hereby declare that my contribution to the paper:

Jiayue Li (35%), Ewelina Pijewska (35%), Qi Fang (10%), Maciej Szkulmowski (10%), Brendan Kennedy (10%), "Analysis of strain estimation methods in phase-sensitive compression optical coherence elastography", *Biomed. Opt. Express* **13**(4), p. 2224-2246 (2022),

<https://doi.org/10.1364/BOE.447340>

JL and EP were the joint principal authors of this article. JL designed and performed the experiments, processed the strain OCE data, analyzed the results, generated figures, and led the writing of the manuscript.

  
(coauthor signature)

Crawley, 11-01-2022

Ph.D. Qi Fang

BRITelab, Harry Perkins Institute of Medical Research, QEII Medical Centre Nedlands and Centre for Medical Research, The University of Western Australia, Crawley, Western Australia 6009 Australia

Department of Electrical, Electronic & Computer Engineering, School of Engineering, The University of Western Australia, Crawley 6009, Australia

### **Statement of coauthorship**

I hereby declare that my contribution to the paper:

Jiayue Li, Ewelina Pijewska, Qi Fang, Maciej Szkulmowski, Brendan Kennedy, "Analysis of strain estimation methods in phase-sensitive compression optical coherence elastography", *Biomed. Opt. Express* **13**(4), p. 2224-2246 (2022): <https://doi.org/10.1364/BOE.447340>

includes performing the experiments, helping in data analysis and implementation of the strain estimation algorithm, reviewing the draft and response letter to reviewers.



.....  
(coauthor signature)

Toruń, 18-03-2022

dr hab. Maciej Szkulmowski, prof. UMK  
Instytut Fizyki UMK  
ul. Grudziądzka 5/7  
87-100 Toruń

### **Statement of coauthorship**

I hereby declare that my contribution to the publication :

Ewelina Pijewska, Iwona Gorczynska, and Maciej Szkulmowski. "Computationally effective 2D and 3D fast phase unwrapping algorithms and their applications to Doppler optical coherence tomography." *Biomedical Optics Express* 10(3), 1365-1382 (2019), <https://doi.org/10.1364/BOE.10.001365> included direct supervision of the Ph.D. student Ewelina Pijewska, determination of the research problem of this paper, help with data analysis, dissemination of the result, and editing the manuscript.

I hereby declare that my contribution to the publication:

Ewelina Pijewska, Marcin Sylwestrzak, Iwona Gorczynska, Szymon Tamborski, Mikołaj Pawlak, Maciej Szkulmowski. "Blood flow rate estimation in optic disc capillaries and vessels using Doppler optical coherence tomography with 3D fast phase unwrapping". *Biomedical Optics Express* 11(3), 1336-1353 (2020), <https://doi.org/10.1364/BOE.382155>,

included direct supervision of the Ph.D. student Ewelina Pijewska, determination of the research problem of this paper, help with data analysis, dissemination of the result, and editing the manuscript.

I hereby declare that my contribution to the publication:

Ewelina Pijewska, Marcin Sylwestrzak, Krystian Wróbel, Iwona Gorczynska, Szymon Tamborski, Mikołaj Pawlak, Maciej Szkulmowski. "Blood flow rate estimation in optic disc capillaries and vessels using Doppler optical coherence tomography." *Biomedical Spectroscopy, Microscopy, and Imaging*. Vol. 11359. International Society for Optics and Photonics, 2020.  
<https://doi.org/10.1117/12.2555754>

included direct supervision of the Ph.D. student Ewelina Pijewska, determination of the research problem of this paper, help with data analysis, dissemination of the result, and editing the manuscript.



I hereby declare that my contribution to the publication:


Ewelina Pijewska, Pengfei Zhang, Michał Meina, Ratheesh K. Meleppat, Maciej Szkulmowski, and Robert J. Zawadzki, "Extraction of phase-based optoretinograms (ORG) from serial B-scans acquired over tens of seconds by mouse retinal raster scanning OCT system," Biomed. Opt. Express 12(12), 7849-7871 (2021), <https://doi.org/10.1364/BOE.439900>

included supervision of the PhD student Ewelina Pijewska, consultation of the idea of the phase-based method application in a new field of OCT.

I hereby declare that my contribution to the publication:

Jiayue Li, Ewelina Pijewska, Qi Fang, Maciej Szkulmowski, Brendan Kennedy, "Analysis of strain estimation methods in phase-sensitive compression optical coherence elastography", Biomed. Opt. Express 13(4), 2224-2246 (2022), <https://doi.org/10.1364/BOE.447340>

included supervision of the PhD student Ewelina Pijewska, advice on the simulations and data analysis, consultation of the idea of the unwrapping method application in a new field of OCT.

  
.....  
(coauthor signature)